COMPUTATIONAL AND EXPERIMENTAL TIME DOMAIN, ONE DIMENSIONAL MODELS OF AIR WAVE PROPAGATION IN HUMAN AIRWAYS

A thesis submitted for the degree of Doctor of Philosophy

By

Francesco Clavica

Brunel Institute for Bioengineering

Brunel University

February 2012

Declaration of Authenticity

I hereby declare that the work presented in this thesis, except where otherwise indicated, is my own.

Francesco Clavica

Abstract

The scientific literature on airflow in the respiratory system is usually associated with rigid ducts. Many studies have been conducted in the frequency domain to assess respiratory system mechanics. Time-domain analyses appear more independent from the hypotheses of periodicity, required by frequency analysis, providing data that are simpler to interpret since features can be easily associated to time. However, the complexity of the bronchial tree makes 3-D simulations too expensive computationally, limiting the analysis to few generations. 1-D modelling in space-time variables has been extensively applied to simulate blood pressure and flow waveforms in arteries, providing a good compromise between accuracy and computational cost. This work represents the first attempt to apply this formulation to study pulse waveforms in the human bronchial tree. Experiments have been carried out, in this work, to validate the model capabilities in modelling pressure and velocity waveforms when air pulses propagate in flexible tubes with different mechanical and geometrical properties. The experiments have shown that the arrival of reflected air waves occurs in correspondence of the theoretical timing once the wave speed is known. Reflected backward compression waves have generated an increase of pressure (P) and decrease of velocity (U) while expansion backward waves have produced a decrease of P and increase of U according to the linear analysis of wave reflections. The experiments have demonstrated also the capabilities of Wave intensity analysis (WIA), an analytical technique used to study wave propagation in cardiovascular system, in separating forward and backward components of pressure and velocity also for the air case. After validating the 1-D modelling in space and time variables, several models for human airways have been considered starting from simplified versions (bifurcation trachea- main bronchi, series of tubes) to more complex systems up to seven generations of bifurcations according to both symmetrical and asymmetrical models. Calculated pressures waveforms in trachea are shown to change accordingly to both peripheral resistance and compliance variations, suggesting a possible non-invasive assessment of peripheral conditions. A favourable comparison with typical pressure and flow waveforms from impulse oscillometry system, which has recently been introduced as a clinical diagnostic technique, is also shown. The results suggested that a deeper investigation of the mechanisms underlying air wave propagation in lungs could be a useful tool to better understand the differences between normal and pathologic conditions and how pathologies may affect the pattern of pressure and velocity waveforms.

Acknowledgements

The writing of this thesis would not have been possible without the support of many people that I would like to mention.

I wish to express my gratitude first of all to my supervisor Dr Ashraf Khir for his guidance and encouragements throughout the PhD experience.

Special thanks to Prof Spencer Sherwin and Dr Jordi Alastruey for their availability to answer my questions and for sharing with me the numerical tools of this project.

I am grateful to Prof Colin Clark and Prof Kim Parker for their incommensurable advices, to Dr Hans-Juegen Smith for kindly providing IOS pressure and flow data and Roger Paton for the help with electrical equipment.

I would like to thank Jenny and Caroline for their kindness and everyone at Brunel Institute for Bioengineering for contributing to my personal and professional development.

Special thanks to Alessandra and Gianpaolo for sharing unforgettable moments together; Masoud, Philippe, Karnal, Samantha, Flavio, Marcel, Jakub, Ye, Lukasz, Yi, Hao for being colleagues and great friends in the same time.

I could not have survived my PhD without the support of special people that have characterized the overall experience in London, starting from Lucia and her big support while I wrote this thesis, Luigi and Carmen for sharing since the beginning this big adventure, Chiara and the travelling period, Francesco, Christian and Marta for being always part of the crew.

Last, but not the least I would like to thank my mother and my brother for being always a constant source of incredible inspiration and support. Thank you.

This thesis is dedicated
to the memory of my father

Table of contents

Nomenclature

Literature review

C	airway compliance
C_{ve}	tissue viscolelastic compliance
C_w	compliance of the chest wall
C_l	lung compliance
D	internal airway diameter
I_{aw}	airwy inertance
L	airway length
P_{alv}	alveolar pressure
P_{AO}	pressure at airway opening
P_{br}	bronchial pressure
P_{RS}	pressure applied to respiratory system
P_{RS}	pressure generated by respiratory muscles
P_{pl}	pleural pressure
P_{tr}	pressure measure at trachea
R_c	central airway resistance
R_L	total airway resistance
R_p	peripheral airway resistance
R_{ve}	tissue viscoelastic resistance
V_p	phase velocity
z	Weibel's generation

Variables of the computational model

A	cross sectional area
A_0	initial cross sectional area
C	peripheral compliance
c	wave speed
c_β	modified wave speed to account of C_S limitation
c_k	wave speed determined with Korteweg's formula
Cs	sound speed in free air
D	internal airway diameter
D_{FRC}	internal airway diameter at FRC
D_{FRC}	internal airway diameter at TLC
D_s	tube distensibility
dI	wave intensity
E	Young's modulus
h	wall thickness
f	friction coefficient per unit length
f_r	resonance frequency
K	bulk modulus of the fluid
P	average pressure over the cross section
P_{ext}	external pressure
Q	flow rate
R	peripheral airway resistance (gen. 8-23)
R_f	reflection coefficient
R_t	terminal reflection coefficient
T	number of end branches supplied
U	average velocity over the crosssection
$W_\pm$	characteristic variables
Δt	time step
Δx	distance between two subsequent quadrature points
Z_0	characteristic impedance
ρ	fluid density
ρ_w	wall density
μ	fluid viscosity
γ	ratio of specific heats
φ	cartilage content
υ	Poisson's ratio
$+$	forward direction
$-$	backward direction

Experimental setup

E_1, E_2	voltages from the velocity sensors
c_{foot}	wave speed determined by the foot to foot method
Rc	cable electrical resistance
R_L	probe led resistance
R_0	probe electrical resistance
P_{comp}	computational pressure
P_{exp}	experimental pressure
PI	wave intensity peak
U_{comp}	computational velocity
U_{exp}	experimental velocity
t_{foot}	time of the onset of the pressure incindent wave
Δt_{theor}	theoretical time delay between the foot of the incident wave and the onset of the reflected wave

Abbreviations

CI cumulative wave intensity (or wave area)
COPD chronic obstructive pulmonary diseases
CTA constant temperature anemometry
FCW forward compression wave
FEW forward expansion wave
FOT forced oscillation technique
FRC functional residual capacity
FVC forced expiratory volume
FVC_1 forced expiratory volume in the first second
FVC_3 forced expiratory volume in the first three seconds
IOS impulse oscillometry system
LXT latex tube
PEFR peak expiratory flow rate
PMC proportion of muscle in airways
R resistance model
R_m characteristic impedance of the terminal segment of 1-D model
RC two parameters Windkessel model
R_mCR three parameters Windkessel model
RT rubber tube
ST silicon tube
TLC total lung capacity
WIA wave intensity analysis

Chapter 1

Background

1.1 Introduction

One person in every seven is affected by lung disease in UK (British Lung Foundation website). **Figure 1.1** shows the mortality rate due to respiratory diseases in most of the Western countries where for respiratory diseases are intended: asthma, emphysema, bronchiolitis, tuberculosis, cystic fibrosis, influenza, and pneumonia. Since a very early diagnosis is required due to this big impact on the population, an increasingly role in improving diagnosis and the treatment of respiratory diseases has been played by numerical models in the last few decades. The present work aims to introduce a new approach in time domain for the modelling of respiratory system that could help to improve the diagnosis of the early stage chronic pulmonary diseases.

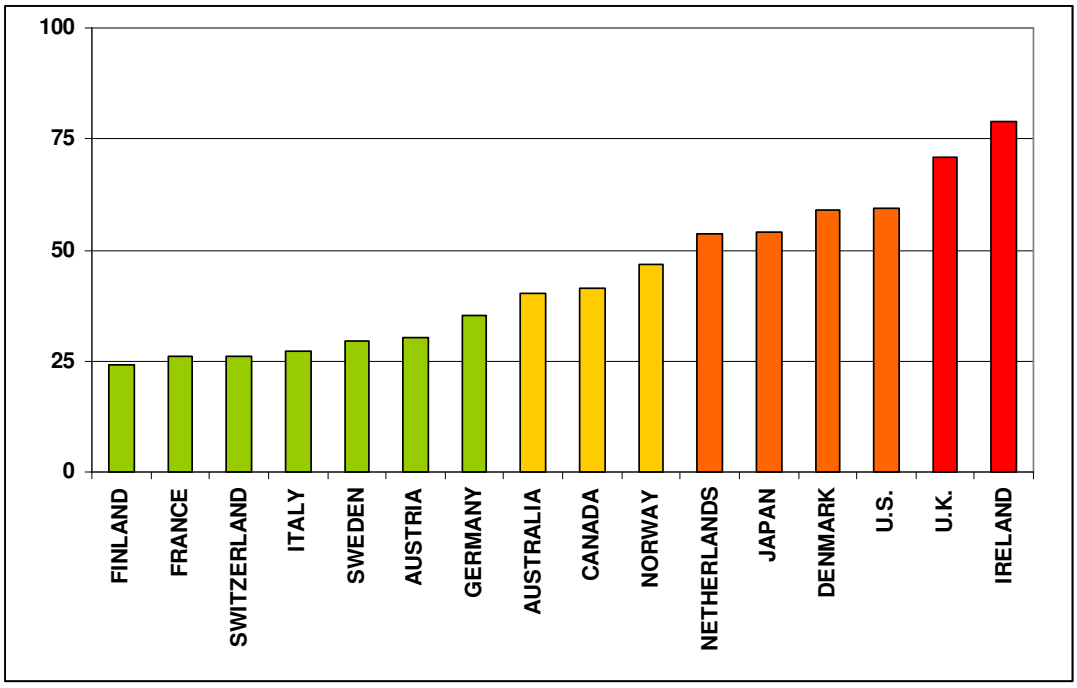

Figure 1.1 Mortality due to respiratory diseases, deaths per 100,000 population (website of Conference Board of Canada)

Even if the airway walls are distensible structures, with increasing distensibility passing from trachea to alveoli, most of the suggested models for airways have assumed the walls to be rigid. (Chang and Elmasry, 1982; Jackson et al., 1977; Liu et al., 2002; Liu et al., 2003; Luo and Liu, 2008; Schroter and Sudlow, 1969). The flexibility of airway wall has been considered mostly for studying the airway input impedance in the frequency domain (Fredberg and Hoenig, 1978; Habib et al., 1994). The analysis in frequency domain allows short time for computations but the required hypothesis of periodicity makes it potentially limiting. Time-domain analysis appears more

independent from the above hypothesis. However, the complexity of the bronchial tree (approximately 23 generations of bifurcations from trachea down to alveoli) makes 3-D simulations too expensive computationally, limiting the analysis to few generations (Liu et al., 2002; Luo and Liu, 2008).

The choice of time domain 1-D modelling has therefore been suggested as a good compromise between computational cost and accuracy (Matthys et al., 2007). This work accounts of the airway distensibility and introduces a one-dimensional (1-D) model in time domain to investigate the propagation of air waves in flexible vessels, with the specific application to human central airways models. This formulation has been extensively applied, for cardiovascular studies, to investigate pulse waves generated by the heart and propagating in the arterial tree (Alastruey et al., 2008; Alastruey et al., 2009; Matthys et al., 2007a; Sherwin et al., 2003; Wan et al., 2002). Pulses are generated also in the respiratory tree either naturally, during normal respiration, or artificially through diagnostic techniques or artificial ventilation. During a normal inspiration as the diaphragm and intercostal muscles move to increase the size of the thorax, the pressure within alveoli decreases below atmospheric pressure and air moves into the lungs. The inspiration can be therefore interpreted as a sum of expansion waves propagating from the alveoli to the mouth. On the contrary using artificial ventilation or forced oscillation technique (FOT) and impulse oscillometry (IOS) (Oostveen et al., 2003; Smith et al., 2005) compression or expansion waves are generated externally from the body and transmitted inside the lungs through a mouthpiece connected to the patient.

The following literature review will examine the existing morphological models of airways and a variety of techniques that have been developed for the clinical assessment of the lung mechanics, enhancing the related advantages and disadvantages. A theoretical and experimental analysis of the existing scientific literature regarding the propagation of pressure waves in the lungs is also presented. This will introduce the importance and the potentiality that the understanding of the wave propagation mechanism in lung may have for the diagnosis and treatment of respiratory disease.

1.2 Pulmonary diseases

Pulmonary diseases can be generally classified into two groups even if, in some cases, components of both categories can be present (Hicks, 2000; Lumb and Nunn, 2005; Ward, 2002).

- **Restrictive pulmonary diseases** are characterized by a reduction in lung volume and lung compliance, while flows are preserved. Generally a person with restrictive lung disease is not able to reach a deep inspiration but has no difficulties in exhaling all the volume inspired. Lung cancer, pneumonia, pulmonary fibrosis and interstitial diseases are included in this classification.
- **Obstructive pulmonary diseases** are characterized by a reduced expiratory flow and an increased work of breathing due to the increase of respiratory resistances. Generally a person with obstructive lung disease is able to take a full inspiration but can not exhale the inspired air completed, demonstrating air trapping. Generally the so called "Chronic Obstructive pulmonary diseases (COPD)" like asthma, chronic bronchitis and emphysema are included in this category.

1.3 Respiratory anatomy and physiology

The respiratory system starts at the mouth and nose, it continues through the pharynx, larynx, trachea, bronchi down to the alveoli. Its main function is to provide oxygen to the cells and to remove carbon dioxide from the circulation. Two distinct mechanisms are involved: gas transport down the airways and gas exchange. Horsfield and Cumming (1967) have shown that the bronchial tree morphology appears appropriately designed to the gas transport in its upper part and to molecular diffusion in the distal and terminal part, occupying the minimal volume inherently for these functions. Gas transport is relevant within the conduction region (that includes upper and central airways) where mass movement is the dominant process and where the inspired air is humidified and thermo regulated to reach the body temperature. While the gas exchange occurs in the terminal airways, where the physical process involved is the gaseous diffusion.

On the lung surface fissures divide the lung in lobes. There are three lobes (upper, middle and lower) in the right lung and two (upper and lower) in the left one with a subdivision in the upper lobe called lingual as shown in **Figure 1.2** (Hicks, 2000).

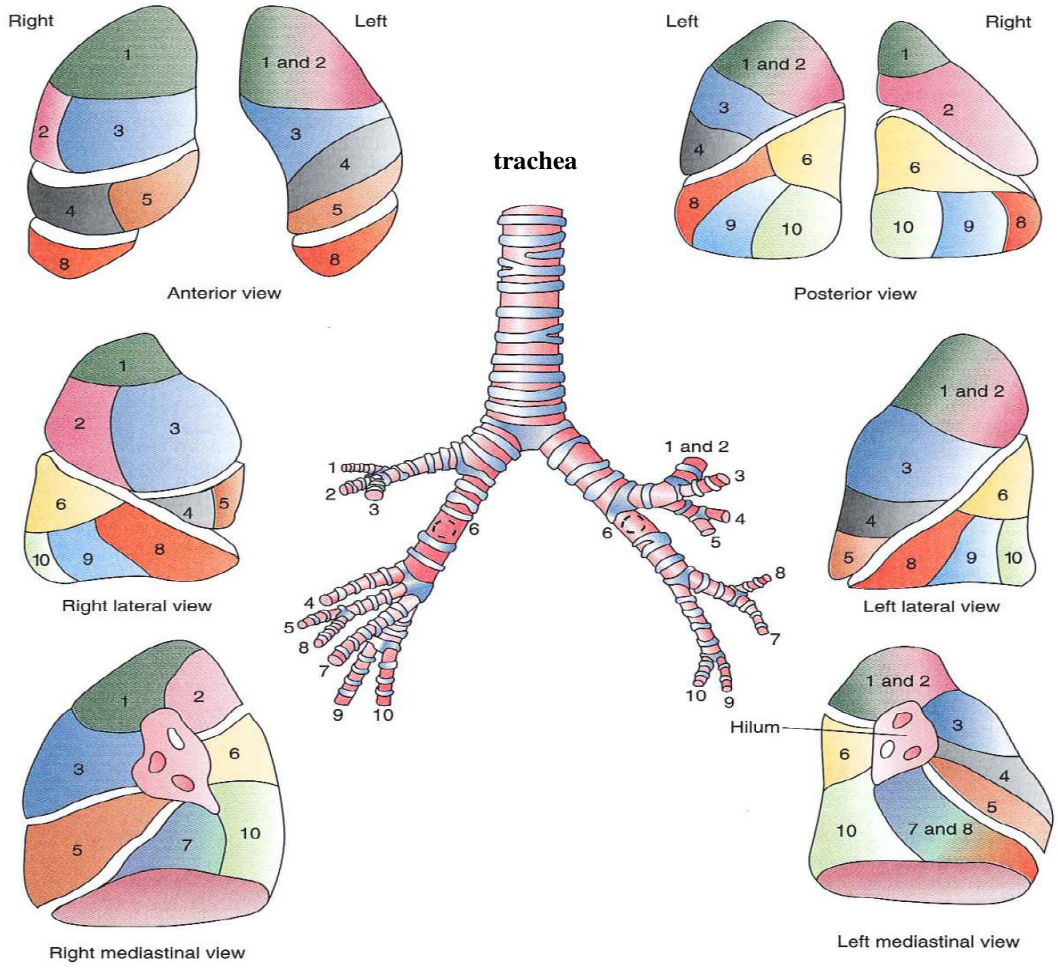

RIGHT LUNG		LEFT LUNG	
RIGHT UPPER LOBE		**LEFT UPPER LOBE**	
Apical	1	Apical- posterior	1 and 2
Posterior	2	Anterior	3
Anterior	3		
RIGHT MIDDLE LOBE		**LINGULAR DIVISION**	
Lateral	4	Superior lingula	4
Medial	5	Inferior lingula	5
RIGHT LOWER LOBE		**LEFT LOWER LOBE**	
Superior	6	Superior	6
Medal basal	7	Anteromedial	7 and 8
Anterior basal	8	Lateral basal	9
Lateral basal	9	Posterior basal	10
Posterior basal	10		

Figure 1.2 Respiratory airways and lobes (Reproduced from Hicks, 2000)

1.3.1 Respiratory tree

The tracheobronchial tree is a very complex bifurcating asymmetrical network (**Figure 1.4**) that starts with trachea, just after larynx, and extends down to the airways involved

in the gas exchange (alveoli). At each bifurcation each segment gives rise to two daughter branches producing smaller airways of the subsequent generation. Therefore progressing from trachea to alveoli both the velocity and diameter fall. Three flow regimes can be identified based on Reynold number (Re) (Shroter and Sudlow, 1969). The first is a turbulent region that includes the trachea and the first few generations of bronchi; the second is a laminar region that extends from the the first region to bronchi where $1<Re<10$ and, finally the Stokes region that includes all the airways (bronchi, ducts and alveoli) where $Re<1$. Usually the airways from generation 0 to 15 are called "the conducting airways" (conduction region), beyond the generation 15^{th} airways are usually called "respiratory airways". The classifications of the airways is described in the next sections (Hicks, 2000; Lumb and Nunn, 2005).

1.3.2 Trachea (generation 0) and main bronchi (generation 1)

The trachea starts at the end of larynx and divides in two main bronchi (right and left bronchus) in correspondence of the 6^{th} thoracic vertebra. The length of trachea is around 11cm but it can change according to the movement of the neck; the diameter (around 1.8cm) is influenced by the tracheal muscle contraction. The tracheal wall is supported by typical U-shaped cartilage rings (usually 16-20) that prevent the tracheal collapse. These rings are joined, in the posterior part, by smooth muscle bands and elastic connective tissue. **Figure 1.3** shows the main tissues of a tracheal cross section. Carina is the last ring of trachea and characterizes the bifurcation with main bronchi. The U-shaped cartilage rings are also characteristic of the main bronchi .

1.3.3 Lobar and segmental bronchi (generations 2-4)

In these ducts the thickness of airway wall decrease by increasing the number of generation as well as the cartilaginous content that assumes more irregular and helical shapes with smooth muscle in between. In correspondence of the third generation the total cross sectional area reaches a minimum; this is the region in which the collapse of the airways wall occurs at a transmural pressure around 5kPa; this phenomenon is responsible of the flow limitation during a forced expiration.

1.3.4 Small bronchi (generations 5-11) and bronchioles (generations 12-14)

Small bronchi are representative of the region between generations 5 and 11; the cartilage is still present in the wall. In bronchioles the cartilage content disappears from the wall, the smooth muscle is still present. In this region the number of airways increases much more per generation than the lumen decreases therefore the total cross sectional area increases significantly, reaching 100 times the cross sectional area of the main bronchi.

1.3.5 Respiratory bronchioles (generations 15-18)

The gas exchange takes place starting from respiratory bronchioles. In this region alveoli start to appear on the wall with muscle band between them.

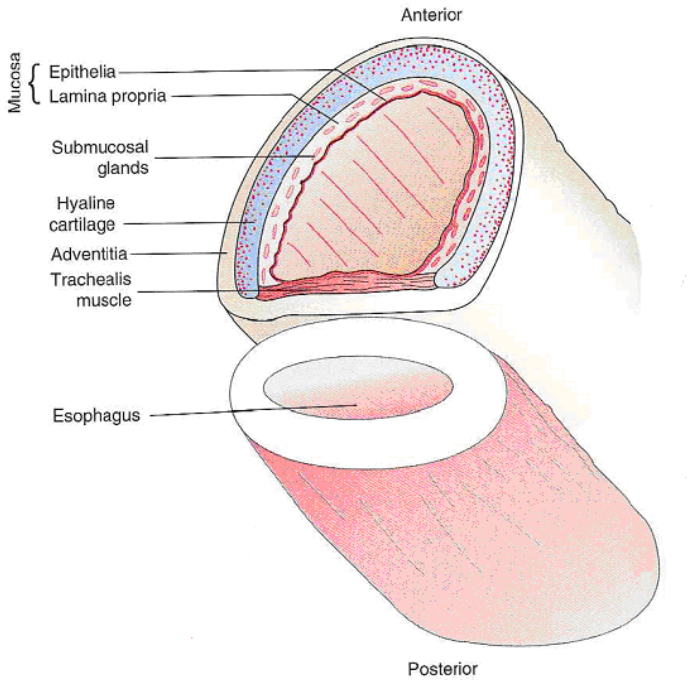

Figure 1.3 Schematic of tracheal cross section with the typical U shaped cartilage rings (Reproduced from Hicks, 2000)**.**

1.3.6 Alveolar ducts (generations 9-22), sacs (generation 23) and alveoli

Alveolar ducts and sacs are very similar to each other and their walls are fully composed by alveoli. Around 300 million alveoli are present in a normal lung. The

mean diameter is 0.2mm even if the size is influenced by lung volume and by the position in the lungs; usually they are bigger in the upper part than in lower part.

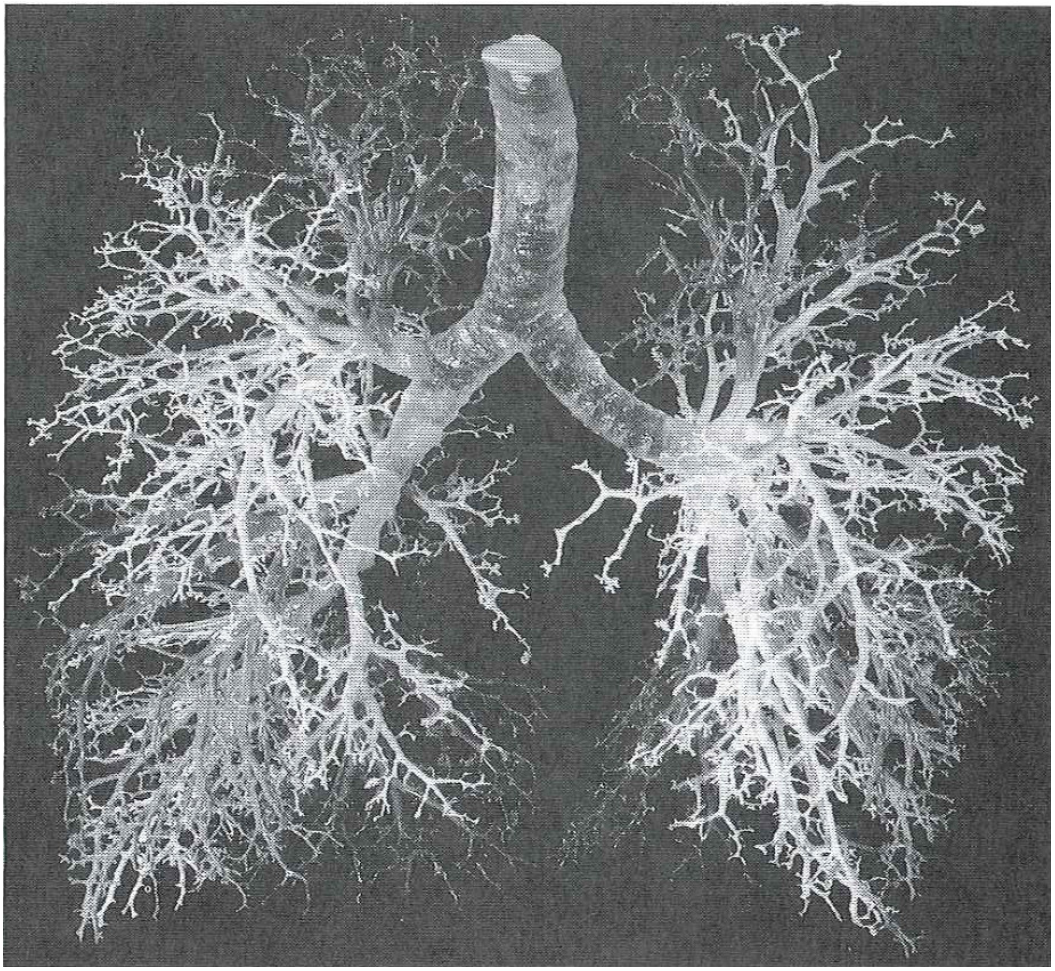

Figure 1.4 Cast of human airways (Reproduced from West, 2005)

1.4 Generation and orders in tree structures

According to Horsfield et al. (1971) a dichotomous bifurcation is when a branch defined "parent" divides into two branches. The two new branches are called "daughter" branches and they can in turn divide. This process can be repeated a number of times to generate a tree like structure. The "stem" is the original branch that gives rise to all the others; the trachea represents therefore the stem for the bronchial tree. There are different methods for branch numbering to indicate the relative position and size in the tree:

- In the numbering of generation (Weibel, 1963) the number of each branch is defined accordingly to the number of dichotomous divisions, generally down, from the stem branch that is defined as generation 0 (**Figure 1.5**).

- On the contrary the numbering of orders commonly starts from periphery and proceeds towards the stem (**Figure 1.6**). There are different ways of counting orders:
    - The first method was introduced and used by Horsfield (Horsfield and Cumming, 1968b; Horsfield et al., 1971; Horsfield, 1990). The first order is assigned to the most distal branches, if two distal branches merge together a second order branch is generated and so on. If branches of different order meet together, the parent branch is numbered using one order greater than the higher order of the two daughter branches (**Figure 1.6a**) .
    - The second method for numbering orders was introduced by Strahler (Strahler, 1963) to describe rivers and was also applied to airways by Horsfield. In Strahler's method when two branches of different orders encounter each other, the parent branch takes the higher order between the two daughter branches (**Figure 1.6b**). If the two daughter branches have the same order, Stahler's method is same as Horsfield's method (Horsfield and Thurlbeck, 1981; Yeh, 1979).

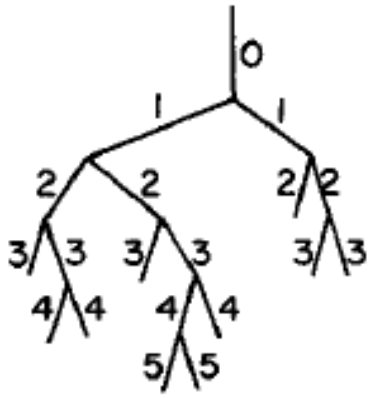

Figure 1.5 Branch numbering by generation down (Yeh, 1979)

In the study of biological tree structure two types of dichotomous bifurcation are usually considered (Horsfield and Cumming, 1968a):

- ***Symmetrical bifurcation***: the parent vessel generates, at each bifurcation, two smaller daughter vessels, which have the same length and cross sectional area. If the stem is defined as generation 0, the number of branches per generation will be 2^z, where z denotes the considered generation.

- *Asymmetrical bifurcation*: the parent vessels generates daughter vessels different in length or diameters. Applying a branch numbering by generation to an asymmetrical system, each generation will include branches with difference in size and functions.

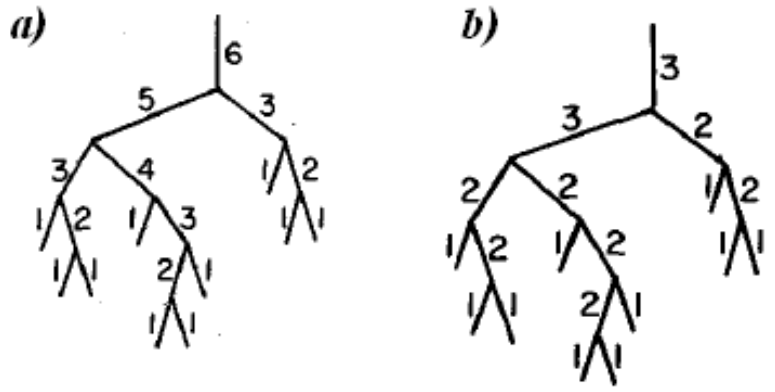

Figure 1.6 Branch numbering according to a) Horsfield's method and b) Straheler's method (Reproduced from Yeh, 1979)

1.4.1 Asymmetry of human airways

The bronchial tree can be considered as dichotomous branching tree starting from trachea (the original stem) and generating two new daughter vessels at each bifurcation. The division is usually asymmetrical in terms of size and lung volumes that each daughter vessel supplies. Because of this asymmetry the shortest path from trachea to terminal bronchioles consists of only about nine generations, while the longest path has about three times more bifurcations. For this reason Horsfield pointed out that the use of generations for classifying such asymmetrical trees has a poor meaning from the functional point of view suggesting the classification by orders as more suitable for the purpose (Horsfield and Cumming, 1968b). Extreme cases of asymmetry are considered the monopody that are associated to a situation in which the diameter of one of the two daughter vessels does not differ from the parent vessel or the trichotomy if one of the two daughter vessel is very short (Weibel, 1963).

1.4.2 Geometrical Models for human bronchial tree

The published data regarding the morphology of human bronchial airways rely on measurements conducted on few lung casts. An extensive description of thr human bronchial tree in forms of raw morphometric data was conducted by Raabe et al.

(Raabe, 1976). In most cases models were introduced to describe the huge amount of data; some classification schemes were applied to group the airways and average dimensions were estimated for each group. As it was mentioned before, generations were used by Weibel (1963), orders by Horsfield (Horsfield and Cumming, 1968b; Horsfield et al., 1971; Horsfield, 1990). There are also other ways of classifications, Yeh (1979), for example, removed the hypothesis of dichotomous bifurcation and Phillips (Phillips et al., 1994a; Phillips et al., 1994b) used a statistical technique to reconstruct the airways using a classification based on the diameter applied to Raabe's partial cast. In this thesis only Weibel and Horsfield's models have been considered for human central airways.

1.4.2.1 Weibel's models

Detailed measurement of the geometry of both the conducting and the respiratory airways were conducted by Weibel (1963). He presented his data in forms of two models: a model A that assumes symmetrical dichotomy and a model B that takes into account the irregular dichotomy.

Model A or 'regular dichotomy model' is the typical symmetrical model in which airways are classified by generation: an average diameter and length were assigned to each of the 23 generations (**Figure 1.7**). In this model the conductive zone is referred to the range from 0 to 16^{th} generation, respiratory bronchioles to the range 17-19 and alveolar ducts/sac zone from generation 20^{th} to 23^{rd}. The dimensions of the symmetrical model, for the first 10 generations, were derived from measurements on a plastic partial cast of the human airways. The cast was complete till the 5^{th} generation; from 6^{th} to 10^{th} generation (incomplete part) a binomial distribution was used to estimate diameters in each generation. Measurements on histological sections were used to derive average diameters and lengths for the generations in the range 17-23. In the region of generations between 11 and 16 (not involved either in the histological specimens or the cast) an interpolating curve was used (Phillips et al., 1994a).

z	n	D (mm)	l (mm)
0	1	18.000	120.000
1	2	12.200	47.600
2	4	8.300	19.000
3	8	5.600	7.600
4	16	4.500	12.700
5	32	3.500	10.700
6	64	2.800	9.000
7	128	2.300	7.600
8	256	1.860	6.400
9	512	1.540	5.400
10	1024	1.300	4.600
11	2048	1.090	3.900
12	4096	0.950	3.300
13	8192	0.820	2.700
14	16384	0.740	2.300
15	32768	0.660	2.000
16	65536	0.600	1.650
17	131072	0.540	1.410
18	262144	0.500	1.170
19	524288	0.470	0.990
20	1048576	0.450	0.830
21	2097152	0.430	0.700
22	4194304	0.410	0.590
23	8388608	0.410	0.500

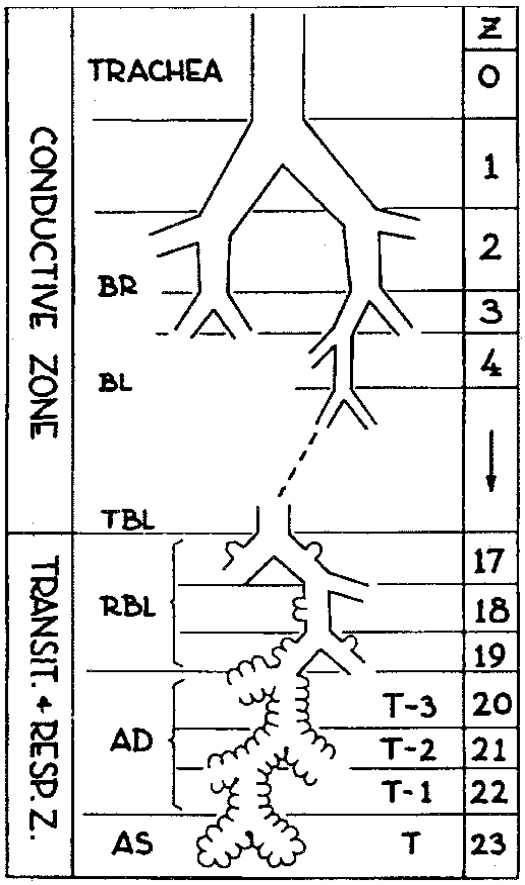

Figure 1.7 Weibel's model: each generation (z) is represented by the total number of airways (n) and the corresponding length (l) and diameter (D). Reproduced from (Weibel, 1963).

Contrary to Model A, Model B enhances the existing variability of the path lengths. The lung is supposed to be divided in '*n*' units supplied by a defined diameter (entrance bronchus). The distribution of probability of the path length, in order to reach each defined diameter, was suggested to be Gaussian for which mean and variance were deducted. In contrast of the extensively applied symmetrical model, only few workers have adopted model B in subsequent studies (Phillips et al., 1994a).

1.4.2.2 Horsfield's models

Horsfield's models are considered the most important and popular asymmetrical models of human airways. A nearly complete resin cast of the conducting airways was used for measurements. According to the first Horsfield's study about respiratory morphological modelling (Horsfield and Cumming, 1968b), the length of each branch was measured as the distance between two points of bifurcation (**Figure 1.8a**), the diameter was evaluated at the midpoint of the length of each branch (**Figure 1.8b**); for elliptic cross sections the arithmetic mean value was applied to both major and minor axes (**Figure**

1.8c). The measurements were completed till the value for diameter was equal or less 0.07 cm; distally the measurements followed a sampling technique.

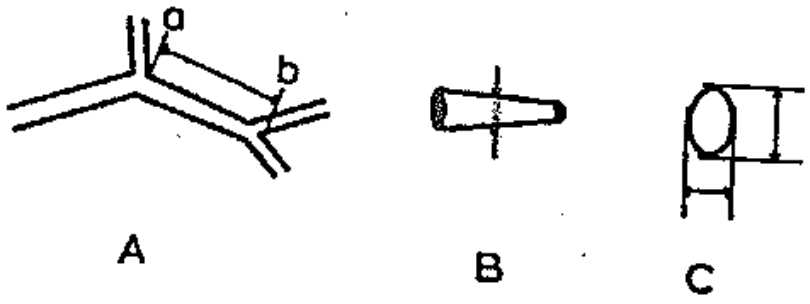

Figure 1.8 Measurements of bronchial branch dimension (see text) (Horsfield and Cumming, 1968b)

A range between 10 and 32 bifurcations was found between trachea and respiratory bronchioles, enhancing the asymmetrical nature of the bronchial tree. A first preliminary model was suggested similarly to a reversed Weibel's model counting the division up instead of down. For each order the following data were provided: total number of observed airways, the number of distal respiratory bronchioles supplied and the average values for lengths and diameters. Diameters (D) were computed following regression equations between D and the orders; average lengths were first evaluated through regression equations with D and then consequently with order. One of the main advantages of Horsfield's first model is the ability to characterise many of the properties of asymmetrical trees in an easy way. On the contrary, as suggested by Phillips (Phillips et al., 1994a; Phillips et al., 1994b), the main limitation of the model is to understand how to compose the whole lung by combining together airway with different orders. In 1971, Horsfield et al. tried to introduce a higher level of detail to the previous model formulating two new mathematical models of the bronchial tree (*Model 1 and Model 2*); original data and other data obtained from subsequent analysis were used in formulating these models.

Model 1

In model 1, Horsfield et al. (1971) established the branching patterns to describe asymmetrical bifurcations; these patterns were simplified in subsequent works by other authors introducing the concept of 'recursion index Δ' (Habib et al., 1994). It was assumed that a parent vessel of *order n* generates two daughters vessel at each bifurcation respectively of *order n-1* and *order n-1-Δ(n)*; therefore the recursion index is

associated to the degree of asymmetry of the bifurcation: $\Delta(n)=0$ establish indeed a symmetrical bifurcation. 31 orders were identified in *Model 1*: in central bronchi (approximately from order 28 to 31, noting that 31 is the tracheal order) the data referred to direct measurements on the cast. After central bronchi, the following recursion indexes are used:

- from order 11 to order 27, $\Delta(n)=3$
- order 9 and 10 branch with $\Delta(n)=2$
- order 8 branch with $\Delta(n)=1$
- from order 2 to 7, $\Delta(n)=0$ that means that at bronchioles level there is a symmetrical dichotomy

Model 2

In Model 2 (the one considered as asymmetrical model in this thesis), similarly to Model 1, the data from central airways refer to direct measurements made on cast (Horsfield et al. 1971). Central branches are shown in **Figure 1.9** according to Horsfield's model 2. The principal difference and novelty introduced by this model is that each bronchopulmonary segment (BPS) is considered independently. The data for each BPS (all the terminal segments in **Figure 1.9**) were described separately to provide average values of lengths and diameters for all the orders between 7 and 24 that the considered BPS supplies. In this way each BPS is characterized by a unique series of lengths and diameters according to corresponding orders. The bronchioles (from order 1 to 6) were modelled, identically to model 1, as symmetrical structures with average values assigned to each order.

branch number	order	D (mm)	l (mm)	T
0	31	16	100	216544
1	28	12	50	98432
2	27	7.5	16	44416
3	26	7.3	1	30592
4	25	5	9	13760
5	24	5.5	11	13824
6	27	8	11	54016
7	26	6.5	18	43840
8	25	7	4.5	27008
9	24	5.5	7.5	16832
10	30	11.1	22	118112
11	26	7.3	15.6	47008
12	25	8.5	6.4	23776
13	29	8.9	26	71104
14	25	5.2	21	20800
15	28	6.4	8	50304
16	27	6	8.4	35392
17	26	6.2	14.8	27520
20	24	5.3	13.5	16832
23	23	3.5	11.5	7872
24	22	3.5	7.5	5952
25	20	5.5	8.5	10176
26	24	5	11.5	16832
28	20	5	8.5	10176
30	24	4	2	16832
31	19	4	13.4	6944
32	25	5.5	17	23232
33	24	4	10	10400
34	24	4.4	9.6	10400
35	21	4.4	6.2	14912
36	23	3.2	6.2	7872
37	25	4.8	6.8	13760
38	25	5.8	10.6	13760

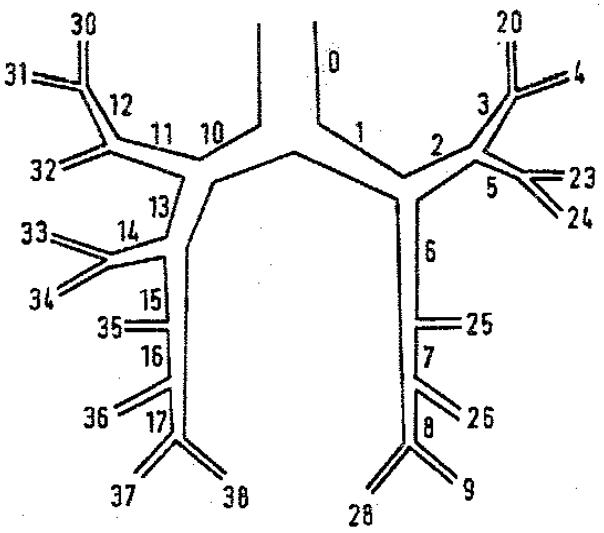

Figure 1.9 Horsfield's model 2: central branches of human bronchial tree. Each branch is identified by the numbers (branch number) to which is assigned an order, diameter (D) and length (l). T is the number of end branches supplied (Reproduced from Horsfield et al., 1971).

1.5 Lumped parameter models for the respiratory system

In the previous sections one dimensional data (diameters and lengths) were provided for single airways according to the models (Weibel and Horsfield) that have been mostly used in the scientific literature. Other ways of modelling have been introduced in literature to model the whole respiratory system impedance and to analyze its behaviour particularly in frequency domain. In fact the possibility to investigate non invasively the mechanics of the human respiratory system, by sampling flow and pressure at airway openings, has encouraged the development of mathematical and computational lumped parameters modelling based on the system identification analysis (or inverse modelling) (Bates and Suki, 2008). Since many lumped parameter models are available in literature, for the respiratory impedance, in the next sections only the most common will be presented.

1.5.1 Single compartment models

1.5.1.1 RC model or pipe balloon model

The RC model is the simplest model used to describe the respiratory mechanics. It considers two elements: a resistance (R) to model the airways flow resistance and a compliance (C), used to model the compliance of the lungs and the chest (**Figure 1.10a**).

1.5.1.2 RIC model

The main limit of the previous model was associated with the difficulties in modelling the respiratory impedance at higher frequencies because both the air inertia and tissue inertance were neglected. The RIC model (**Figure 1.10b**) takes into account also the inertance, modelling the respiratory impedance as series of airways resistance (R), lung inertance (I) and alveolar compliance (C) (Diong et al., 2007; Schmidt et al., 1998).

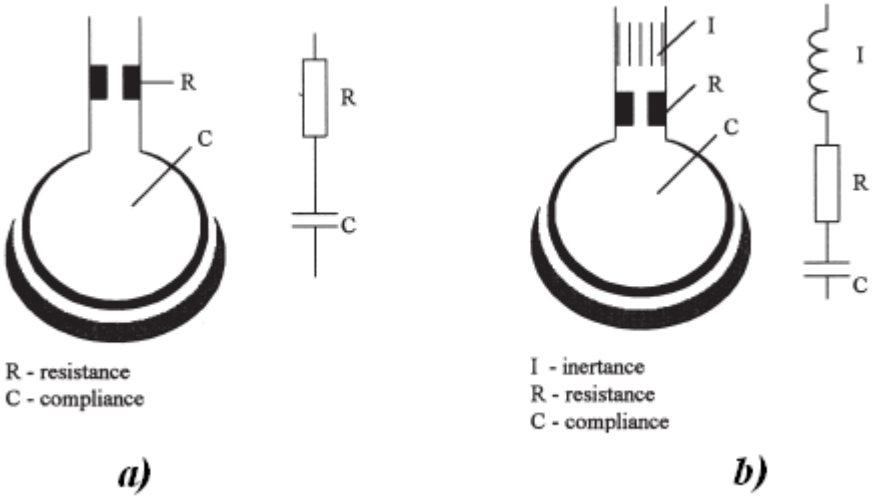

Figure 1.10 a) RC and b) RIC model (Reproduced from Schmidt et al., 1998)

1.5.1.3 Viscoelastic model

This model takes into account that the wall tissue of the chest and the lungs behave as viscoelastic structures. As shown in **Figure 1.11a** R_{aw} represents the airway resistance, C_s is the respiratory system static compliance while R_{ve} and C_{ve} are referred respectively to the viscoelastic resistance and compliance of the tissues (Bates et al., 1986; Lutchen and Costa, 1990).

1.5.2 Multi compartment models

1.5.2.1 Dubois's model

In the electric analogue for the respiratory system suggested by Dubois et al. (1956), different compartments are associated to airways, tissue and alveoli as shown in **Figure 1.11b**. R_{aw} and I_{aw} are respectively the airways resistance and inertance; R_t, I_t and C_t are the tissue resistance, inertance and compliance while C_g refers to alveolar compliance (Diong et al., 2007).

1.5.2.2 Mead's model

In Mead's model (Mead, 1961) seven parameters are considered to simulate the mechanics of lungs and the chest wall (**Figure 1.11c**). In the model, R_c and R_p are the central and peripheral resistance, I is the inertance while C_w, C_l, C_b, C_e are respectively the compliance of the chest wall, lungs, bronchial conduit and thorax (Mead, 1961; Schmidt et al., 1998).

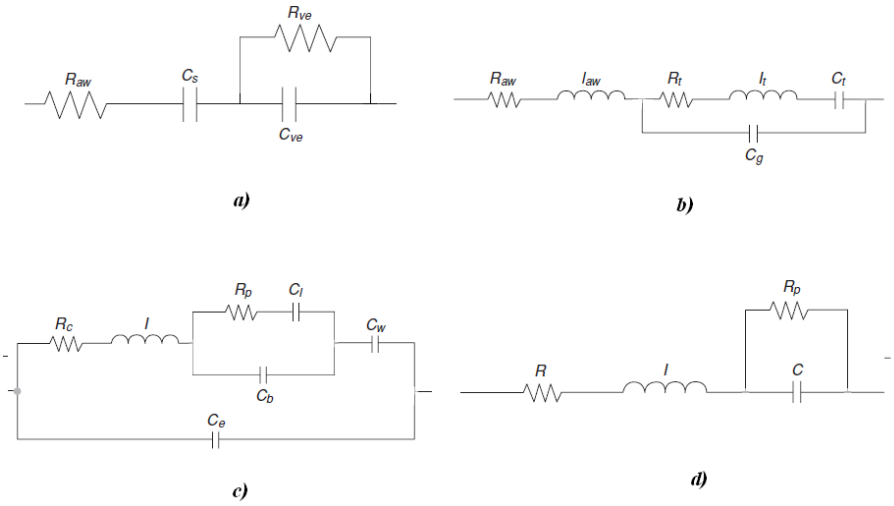

Figure 1.11 a) Viscoelastic model; b) Dubois's model; c) Mead's model; d) Extended RIC model (Diong et al., 2007)

1.5.2.3 Extended RIC model

The extended RIC model, shown in **Figure 1.11d**, has been introduced by Diong (Diong et al., 2007) as an improvement of the RIC model; it is, in the same time, a simplification of Dubois's model (with $C_t = \infty$ and I_t=0) or Mead's model (with C_e=0 and $C_l, C_w = \infty$). The only difference with the RIC model is the appearance of the peripheral resistance (R_p) in parallel with the alveolar compliance (C). It separates therefore central from peripheral airways.

1.6 Non invasive assessment of lung mechanics

There are different existing diagnostic techniques used to assess the lung function and mechanics in the common clinical practise and different models have been suggested to reproduce the respiratory behaviour associated to these techniques. Most of the clinical analysis are referred to the pressure and flow at the airway openings because of the need of non invasive diagnosis. In the next sections the most important are presented.

1.6.1 Spirometry

Spirometry represents one of the first and most common tests to evaluate the pulmonary function consisting, as the same name suggests, in measuring the breath through a device called spirometer. The spirometry is commonly used to measure, in time domain, the lung volumes (**Figure 1.12**) and to test the lung functionality through a forced expiration.

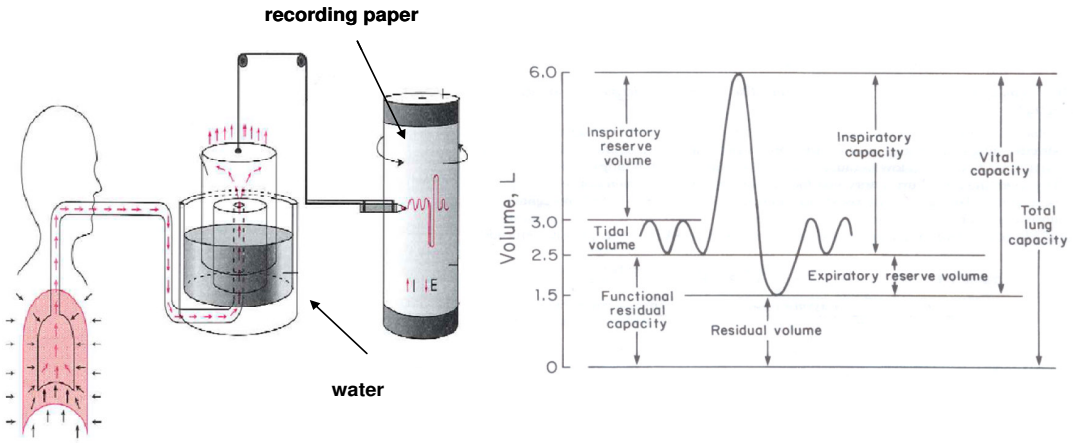

Figure 1.12 Spirometry used for lung volumes recording (Reproduced from Hicks, 2000)

Different parameters can be evaluated using this technique, the most important ones are the forced vital capacity (FVC), the forced expiratory volume in one or three seconds (FEV_1, FEV_3), and the peak expiratory flow rate (PEFR). FVC is the total amount of air that the patient can blow after a full inspiration. FEV_1 and FEV_3 refer respectively to the amount of air forcibly blown by the patient in the first second and in the first three seconds of forced expiration starting from full inspiration. The ratios FEV_1/ FVC (FEV_1%) is used to distinguish between obstructive and restrictive pulmonary diseases. As it was mentioned in Section 1.2, in the obstructive diseases the flow rates are usually

decreased because of the increase in airway resistance with some air trapping. While restrictive diseases are commonly associated to reductions in the lung capacities and volumes leaving normal values for flow rates. According to this, severe obstructions cause commonly the reduction of FEV% while severe restrictive pathologies provoke an increase of it (Hicks, 2000). The major limitations associated to this technique are related to the patient cooperation, it appears therefore a difficult diagnostic tool for preschool children (Arets and van der Ent, 2004; Oostveen et al., 2003)

1.6.2 Body plethysmography

The body plethysmograph measures the total volume of gas in the lung. It consists of a large airtight box where the subject sits. A shutter closes the mouthpiece at the end of a normal expiration and the patient is required to make inspiratory efforts. Due to the efforts, the pressure and volume in the box change from P_1 and V_1 (before the inspiratory effort) to P_2 and $V_1+\Delta V$ (after the effort), where ΔV is the change in the volume of the box (or lung). It is therefore valid: $P_1V_1 = P_2(V_1 - \Delta V)$, from which ΔV can be calculated. The Boyle's Law is then applied to determine the volume (V_2) inside the lung: $P_3V_2 = P_4(V_2 - \Delta V)$, where P_3 and P_4 are respectively the pressure at the mouth before and after the inspiratory effort. Using this procedure, the only unknown (V_2) can be easily determined (Hicks, 2000; West, 2005).

1.6.3 Mechanical ventilation

The process of normal inspiration begins when the movement of diaphragm generates negative intrapleural pressure. This phenomenon creates a pressure difference between the mouth (at atmospheric pressure) and the alveoli (at negative pressure) and consequently an inflow. During mechanical ventilation the process is artificially inverted and the cause of the pressure difference is due to the application of a positive pressure at airway openings. In a ventilated patient the pressure that is applied to the respiratory system (P_{RS}), considering the single compartment model (**Figure 1.10a**), is given by (Guerin and Richard, 2007; Lucangelo et al., 2005):

$$P_{RS} = P_{AO} + P_{mus} = P_{res} + P_{el} + k \qquad (1.1)$$

Where P_{AO} is the pressure at the airway opening (the pressure generated by the ventilator), P_{mus} is the pressure generated by respiratory muscles (negligible when the

patient is entirely passive). $P_{res} = \dot{V} R$ is the pressure dissipation due to the inflation flow ($\dot{V}$) across the endotracheal tube and airways resistance (R). $P_{el} = \frac{V}{C}$ is the pressure that is required to overcome the elastic force depending by the volume (V) and the compliance of respiratory system (C) while the term 'k' is referred to the P_{AO} value when both flow and volume are zero (positive end expiration pressure).

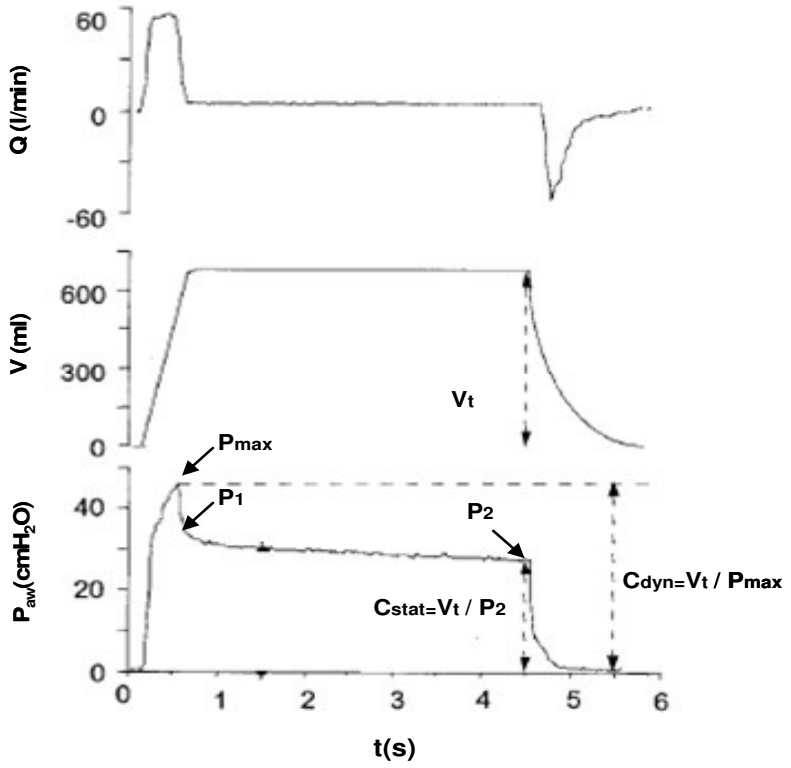

Figure 1.13 Measured Airway pressure (P_{aw}), volume (V) and flow (Q) during end inspiratory occlusion (Reproduced from Lucangelo et al., 2005)

The mechanics of airways can be derived both dynamically and statically. In the dynamic analysis, linear least square or multiple regression analysis are used to find the value of R and C that match the measured P_{AO}, V and $\dot{V}$ in Equation (1.1). The static analysis uses the so called 'end –inspiratory occlusion technique' during a constant flow ventilation (Don and Robson, 1965). From **Figure 1.13** once the flow is stopped, the airway pressure (P_{AW}) decreases instantaneously from P_{MAX} to P_1 and then it asymptotically decreases to P_2. Dividing P_{MAX}-P_1 by the flow $\dot{V}$ (immediately before the occlusion) the resistance (R) can be calculated. By dividing P_1-P_2 by the flow $\dot{V}$ (immediately before the occlusion) it is possible to calculate also the additional

viscoelastic resistance (Guerin and Richard, 2007). The static compliance accounts for the respiratory system elastic features and it is given by $C_{stat}=V_t/P_2$ while the dynamic compliance considers also the resistive component of airways and is given by $C_{dyn}=V_t/P_{max.}$(Lucangelo et al., 2005).

1.6.4 Forced oscillation technique

Forced oscillation technique (FOT), was introduced by Dubois et al. (1956) and has the main advantage of being a non invasive tool, in clinical practise, for respiratory mechanics investigations, requiring minimal cooperation from the patient (Oostveen et al., 2003). The basic concept for FOT concerns the use of an external forcing signals that can be mono or multifrequency, generated by a loud speaker and superimposed on the normal breathing. The investigations of respiratory mechanics consist in the evaluation of impedance, the spectral ratio (in frequency domain) of pressure and airflow; real and imaginary part of respiratory impedance are measured in the frequency domain. Real part is associated to respiratory resistance; imaginary part (or reactance) is associated to the elastic properties of respiratory system (capacitance) and inertive properties of the moving air (inertance). Variations of the curves (resistance-frequency and reactance –frequency) compared to control situations, as shown in **Figure 1.14**, are often associated to pathologic conditions of airways (Arets and van der Ent, 2004; Oostveen et al., 2003; Smith et al., 2005). The fact that requirement of linearity is needed by this technique only oscillation of small amplitudes can be applied (Oostveen et al., 2003). The impulse oscillometry system (IOS) is functionally similar to FOT. The main characteristic of the IOS is in the forcing signals: an aperiodic single impulse-shaped of alternating direction (Smith et al., 2005).

Being frequency domain techniques, one of the main limitations of FOT and IOS is the difficulty to associate features to time.

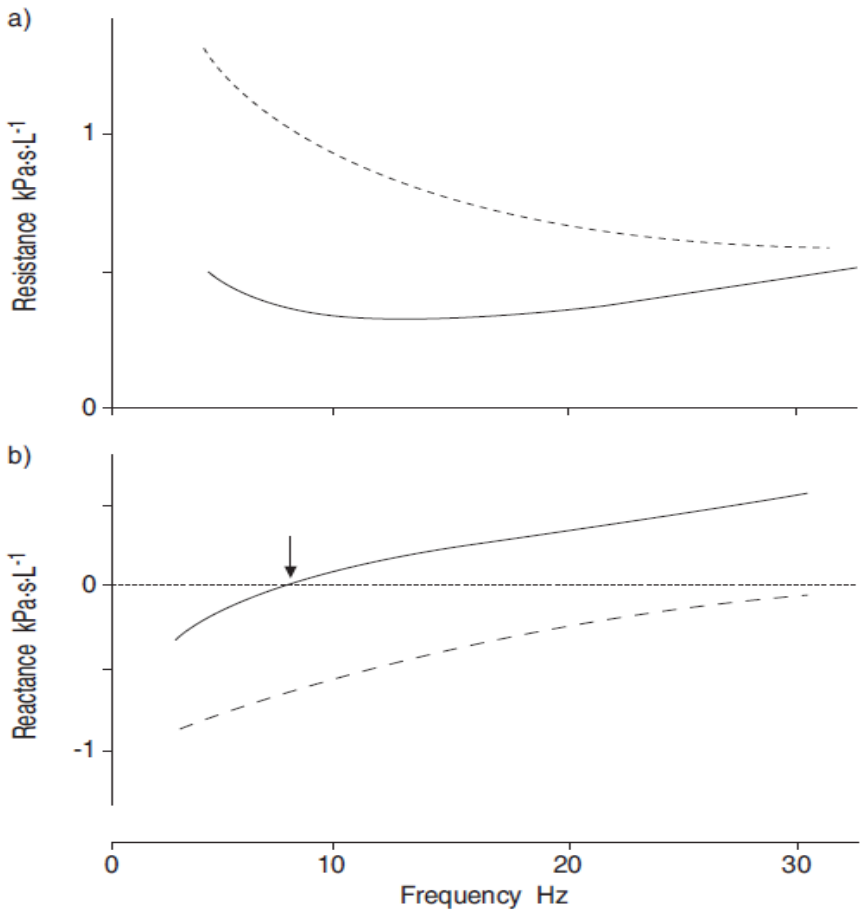

Figure 1.14 a) Resistance and b) reactance frequency dependence in normal (-) and obstructed (- - -) airways. The arrow indicates the resonance frequency (Reproduced from Oostveen et al., 2003).

1.7 Invasive assessment of peripheral lung mechanics

1.7.1 Retrograde catheter

The retrograde catheter technique was first introduced in 1967 (Macklem and Mead, 1967). In essence, a flexible catheter is pulled through a hole passing the pleural surface, parenchyma and bronchial wall until it wedges in an airway of about 2mm diameter. The main advantage of this technique is the possibility to measure the bronchial pressure without obstructing the airway in which the pressure measurement takes place, as it can happen when the catheter is inserted from trachea (Hogg et al., 1968). Using this technique and the system shown in **Figure 1.15** Macklem and Mead were able to separate the contribution of central (R_C) from peripheral (R_P) airways

resistance. The total pulmonary flow resistance R_L was calculated considering R_C and R_P as two resistances in series:

$$R_L = R_C + R_P = \frac{P_{tr} - P_{alv}}{\dot{V}} \tag{1.2}$$

Where P_{tr} is the pressure measured in trachea, P_{alv} is the alveolar pressure (obtained subtracting from the pleural pressure (P_{pl}) the pressure due to the elastic recoil) and $\dot{V}$ is the flow recorded in trachea. R_C and R_P were respectively calculated:

$$R_C = \frac{P_{tr} - P_{br}}{\dot{V}} \tag{1.3}$$

$$R_P = \frac{P_{br} - P_{alv}}{\dot{V}} \tag{1.4}$$

Denoting with P_{br} the bronchial pressure measured with the catheter. The measurements were made with lungs oscillating at their resonance frequency in order to obtain the only resistive component (at resonant frequency the pressure required to overcome elastic recoil balances the pressure required to overcome inertia).

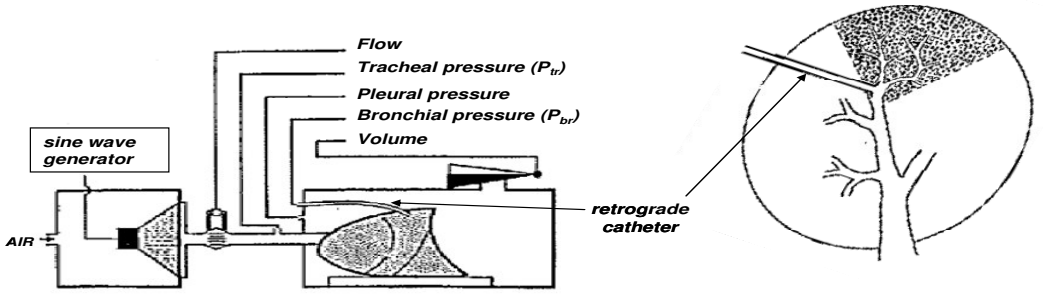

Figure 1.15 Setup for retrograde catheter technique (Reproduced from Macklem and Mead, 1967).

The main limitations of the retrograde technique were related to the frequency response of the catheter and the limited applicability to only isolated lungs. This technique underlined in particular the concept of peripheral airways as a 'silent zone': due to the huge total cross sectional area of the whole peripheral region, the peripheral contribution to the total R_L was found to be small compared to the central region. According to this, only relevant narrowing of peripheral airways can affect the overall lung function (Bates and Suki, 2008).

1.7.2 Wedged catheter

This technique was first introduced in 1971 (Woolcock and Macklem, 1971) and it consists of a catheter (bronchoscope) that is introduced from trachea with the tip stably wedged inside an airway. Compared to the retrograde catheter (Section 1.7.1) the application are not only restricted to isolated lungs but it can be applied to intact animals and even patients (Bates and Suki, 2008). For the most common applications a catheter with a double lumen is used. An airflow ($\dot{V}$) is imposed through one lumen of the catheter while the other lumen is for measuring the pressure at the tip of the catheter (P_B). An estimation of peripheral airways resistance (R'_P), according to this technique, is calculated as $R'_P = \frac{P_B}{\dot{V}}$. The wedged catheter has been used to evaluate the change of peripheral lung resistance in smokers, normal and asthmatic patients (Wagner et al., 1990; Wagner et al., 1992). Because of existence of collateral ventilation among airways (collateral ventilation refers to any ventilation in which the air comes from a " neighbouring airway", instead of the normal path), the calculated R'_P includes the resistance of the whole path from the tip of the wedges catheter, the alveolar duct, the collateral connections and finally back to trachea (Bokulic, 1992).

1.7.3 Lung explants

The lung explants consist of isolating a portion of lung that is maintained in an organ bath under physiological condition in order to evaluate the in vitro properties of the small peripheral airways and their responsiveness to chemical stimulation (Bates and Suki, 2008). This technique has been particularly applied to slices of animal lungs to obtain information about the airway wall pharmaco-mechanics dependence (Bergner and Sanderson, 2003) or the contribution that peripheral airways can have on the mechanics of the whole lung in asthmatic condition (Adler et al., 1998). Using lung explants, Tiddens et al. (1999) were able to test the compliance, collapsibility and hysteresis of human peripheral airways isolated from smokers, with different level of chronic obstructive pulmonary disease (COPD), by inflating and deflating them cyclically with a pressure of ±15cmH_2O.

1.7.4 Alveolar capsule

Alveolar capsule is an invasive technique first introduced in 1977 (Sasaki et al., 1977) and subsequently improved by Fredberg et al. (1984) and applied on animals. It consists of measuring the alveolar pressure (P_A): a small capsule is glued to the pleural surface, small holes on the pleural surface just under the capsule allow the access of a miniature pressure sensor to the alveolar gas. Applying small oscillations to the airway opening it was possible to study the regional distribution of P_A in different lobes of the lungs. The use of alveolar capsule underlined that the measured P_A, at different locations of the lung, are almost the same when the applied oscillations are in the normal breathing frequency range (Bates et al., 1995; Bates and Suki, 2008).

1.8 Propagation of pressure air waves in flexible tubes and airways

A wave is a disturbance propagating in space and time. It is important to distinguish between two definitions of propagation velocity of pressure waves: if the speed of propagation of pressure waves is constant for all the frequencies the term wave speed (c) is used; if the speed varies according to the frequency there is not a unique speed and the speed at which the phase of each frequency of the wave travels is called phase velocity (V_p) (Winter and Pimmel, 1980).

1.8.1 Determination of wave speed

Different methodologies have been introduces to measure the speed of wave propagation

1.8.1.1 Impedance technique

In frequency domain the phase velocity is determined from the distance between crests in presence of standing waves or the gradient of the phase angle along the tube if standing waves were not observable (Guelke and Bunn, 1981). The main limitation of this technique is that the determination of phase velocity might be affected by the reflections (Guelke and Bunn, 1981; Latham et al., 1987; Winter and Pimmel, 1980).

1.8.1.2 Foot to foot method

It is the most common method for determining the wave speed with two pressure measurements in two different locations at a known distance (ΔL) from each other. It consists in measuring the time interval (Δt) required by a wave to travel from one site to the other, the wave speed is simply determined as $c=\Delta L/\Delta t$ (Milnor W.R. 1989). It is required a reference point on the waveform which is usually the foot of the pressure wave (**Figure 1.16**).

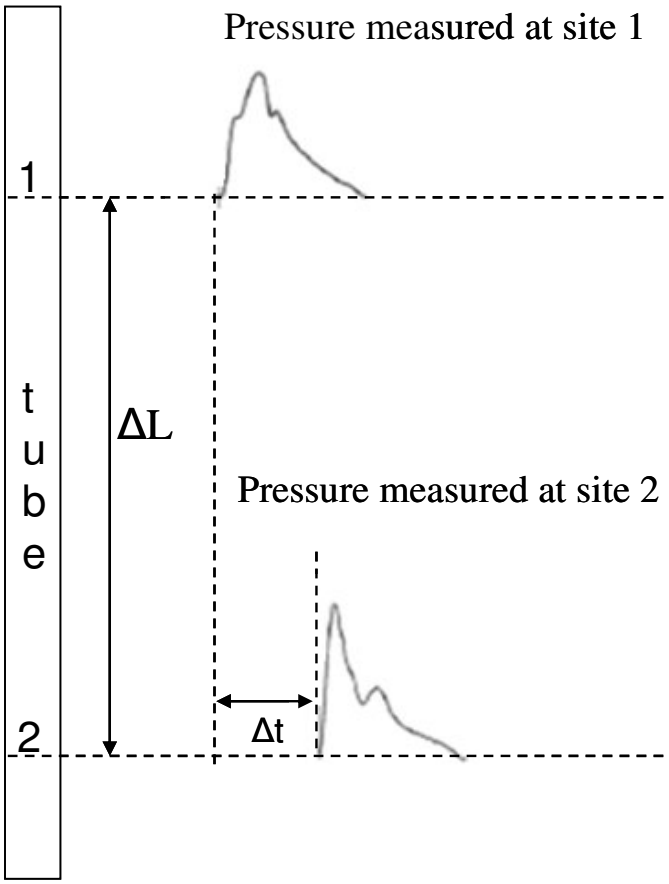

Figure 1.16 Foot-to-foot method: the wave speed (c) is determined from the distance (ΔL) between two points and the time interval (Δt) required by the wave to travel from one site to the other.

1.8.1.3 PU-loop

This method was introduced by Khir et al. (2001) and applied to pressure and velocity measurements in aorta. It is based on the Waterhammer equation and it requires the simultaneous measurement of pressure and velocity at a defined point. Plotting pressure against velocity the P-U loop is obtained. Considering the early part of the ejection from the heart, when only forward waves are present, the slope of the loop equals ρc

according to Waterhammer equation. Since the fluid density ρ is known the wave speed is easily determined.

1.8.1.4 Sum of squares technique

This technique is used in particular to derive the wave speed in coronaries where it is difficult to find a straight line for the PU loop application since the reflected waves appear early in the systole. It is therefore difficult to distinguish the slope and consequently to calculate the wave speed (Davies et al., 2006; Kolyva et al., 2008). In this case the sum of squares of dP and dU is considered over the whole cardiac cycle.

$$(\rho c)^2 = \frac{\sum dP^2}{\sum dU^2} \tag{1.5}$$

1.8.2 Sound wave propagation in flexible tubes

Despite the importance that wave speed can have in respiratory mechanics, the number of works related to wave propagation in airways and more in general in flexible tubes is very limited. According to Oruç and Çarpinlioğlu (2007) the study of flows in collapsible tubes has mostly been associated to liquid (blood and water) and there is a very limited number of publications related to airflow in flexible tubes. Propagation of sound waves in non rigid tubes can be very different from propagation phenomena in rigid tubes and the behaviour is strongly affected by the frequency of excitation (Guelke and Bunn, 1981; Suki et al., 1993) and the characteristic of the tube wall (Capper et al., 1991). The most complete work has been carried out by Guelke and Bunn in 1981. They started from the model valid for transmission line circuit of an element Δx of rigid tube with the assumptions of small radial dimensions of the tube respect to the wavelength. Based on this assumption the phase velocity (V_p) on rigid tubes reduces to

$$V_p = \frac{1}{\sqrt{(\rho / A)(A / p_0 \gamma)}} = \sqrt{\frac{p_0 \gamma}{\rho}} \tag{1.6}$$

In which A is the cross-sectional area, p_0 is the ambient pressure, γ the ratio of specific heats and ρ is the density of the fluid. By using the following values: p_0=1.0132*10^5Pa, γ=1.402 and ρ_{air}=1.2047Kg/m^3, Eq. (1.6) provides the speed of sound in free space (C_s=343m/s). Therefore the phase velocity in rigid tubes equals C_s. To account for the wall elasticity Guelke and Bunn added, to the rigid model, a wall model characterized by a wall resistance (R_w), wall inertance (I_w) and wall compliance (C_w), obtaining

expressions for the equivalent conductance (G_{eq}) and equivalent capacitance (C_{eq}) of the system. From these two values they were able to derive the values for attenuation (α) and phase factor (β) as function of frequency (f). In these new system: $V_p=2\pi f/\beta$.

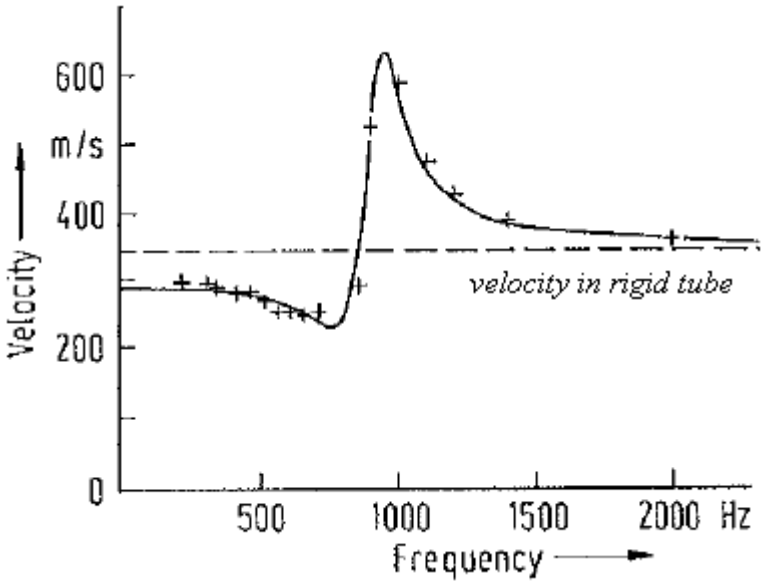

Figure 1.17: Measured (+ + +) and theoretical (-) phase velocity determined by Guelke and Bunn in elastic tubes perturbed at different frequencies by a loudspeaker (Reproduced from Guelke and Bunn, 1981)

Guelke and Bunn were able to validate the theory with experiments conducted in a rubber tube and excited canine trachea using an apparatus consisting of a loudspeaker and a probe microphone. According to both experimental and theoretical results (**Figure 1.17**) three frequency ranges were indentified (Guelke and Bunn, 1981). At low frequencies of system perturbation, the formula for phase velocity derived by Bramwell and Hill (Bramwell and Hill, 1922) gives a reasonable approximation:

$$V_p = \sqrt{\frac{VdP}{\rho dV}} = \sqrt{\frac{1}{\rho D_s}} \tag{1.7}$$

Where D_s=dV/VdP is the distensibility of the tube being V and P respectively the internal volume and the pressure. By increasing the frequency the resonance frequency (f_r) was found at:

$$f_r = \frac{1}{2\pi r}\sqrt{\frac{E}{\rho_w}} \tag{1.8}$$

where 'r' is the radius of the tube, 'E' is Young's modulus and ρ_w is the wall density. In correspondence of f_r the attenuation was found to reach the maximum with the phase velocity of the fluid reaching a speed value much higher than C_s. For frequency values higher than f_r the phase velocity asymptotically reaches the phase velocity in rigid tubes (Cs) as shown in **Figure 1.17**.

1.8.3 Influence of the wall properties and gas compressibility at low frequencies: original Korteweg's equation

Considering an incompressible fluid enclosed in an elastic thin walled tube, the wave speed can be calculated by using the well known Moens-Korteweg's equation (Korteweg, 1878; Moens, 1878)

$$c_1 = \sqrt{\frac{Eh}{\rho D}} \tag{1.9}$$

Where h is the wall thickness, E is the Young's modulus of tube wall and ρ is density of the fluid. Eq. (1.9) represents a limited case of a more general expression. Korteweg in fact derived Eq. (1.9) from a general study of the sound speed in fluids enclosed in elastic tubes. He discovered that sound speed is reduced in a fluid medium enclosed in an elastic tube. Under these conditions two cases were distinguished

- The first case is associated to the condition in which only the tube wall is elastic while the fluid is considered to be incompressible. Based on these assumptions Eq.(1.9) is valid.
- The second case is when only the fluid is elastic and the tube wall is considered rigid ($E = \infty$). In this case the pressure wave propagates with velocity

  $$c_2 = \sqrt{\frac{K}{\rho}} \tag{1.10}$$

  in which ρ and K are respectively the density and the bulk modulus of the fluid. This is also the common equation for the sound speed in free space (C_s), similarly to Eq. (1.6).

Korteweg indicated that when both the fluid and the tube wall are elastic the wave speed becomes a combination of the two cases

$$\frac{1}{c_k^{\,2}} = \frac{1}{c_1^{\,2}} + \frac{1}{c_2^{\,2}} \tag{1.11}$$

From Esq.s (1.9)-(1.11) the general expression can be derived

$$c_K = \left(\frac{\rho D}{hE} + \frac{\rho}{K} \right)^{-\frac{1}{2}} \tag{1.12}$$

The second term in Eq.(1.12), ρ/K, accounts for the effects of the fluid compressibility and in the case of blood in arteries has always been neglected since it is considered very small compared to ρD/Eh (Shalak, 1966).

1.8.4 Experimental measurements of wave speed in airways

David Rice has been one of the most important researchers working on the experimental evaluation of wave speed in respiratory system. Most of his work has been aimed to identify the parameters affecting the propagations of pressure waves in lungs and the preferential paths of propagation. Evidences about the influence of some important variables that may influence the propagation of sound were identified: gas motion, humidity, temperature, geometry in both static and dynamic conditions. In static conditions (no moving gas) Eq.(1.6) is valid. According to the respiratory gas concentration, at the body temperature (T=37 °C), it is possible to derive the sound speed for partially humified air (Cs=354 ms/s), satured inspiratory air (Cs=357 m/s) and expiratory air with a high content of CO_2 (Cs=352 m/s). These are the wave speeds in unconfined uniform gas. When the gas is moving at a speed 'v' the apparent sound velocity is given by 'Cs+v'. Rice (1980) confirmed experimentally that velocity of sound inside rigid tubes asymptotically equals the velocity of sound in free space almost independently from the area and the shape of the tube cross-section; consequently the main factors affecting the sound speed in rigid ducts as well as in free space are: the gas composition, temperature and the flow rate. In corrugated tubes the sound speed was found to decrease of 2-5%; considering this result, it was concluded that the corrugations introduced by cartilage ring in trachea may slow down the sound speed. In vivo experiments with measured sound speed in larger airways of dogs (c=349 m/s), at frequencies above 10Khz, provided experimental evidence that at high frequencies in trachea and more in general in larger airways the wall behaves as a rigid structure in which sound propagates as in the free space. The velocity of sound, moreover, was found to change according to the velocity of the fluid and to be insensitive to transpulmonary pressure, bronco constriction and lung volume. A velocity dependence in relation of the previous variables would have been expected with the airways wall interacting with sound propagation as it happens at low frequencies. At low frequencies (less than 100Hz) in fact the propagation of sound was believed to be affected by the elasticity of the airways walls due to reciprocal sound-wall interaction. According to Rice the properties of airway wall are not a determinant factor for high frequencies sound velocity but their effect becomes relevant at low frequencies. He suggested that measurement of wave propagation at low frequencies might be a very promising diagnostic indicator of respiratory pathologies (Rice, 1980).

Another important result for wave propagation and wall mechanics of respiratory system was obtained through experiments on calf trachea (Suki et al., 1993; Suki et al., 1993). Suki enhanced the presence of two different relative maxima in the phase velocity – frequency graph. These findings were in contrast with the single compartment model introduced by Guelke and Bunn with a single relative maximum at resonance frequency (**Figure 1.17**). Suki assumed that the two maxima in the phase velocity could be explained by means of a two wall compartment model each with a series of R_w, I_w, C_w. The two resonance frequencies were associated in fact to the main components of trachea: cartilage and soft tissue which may resonate at different frequencies. The results suggested that the measurement of V_p at high frequencies (above 200Hz) can provide important data about the mechanical properties of both tissues. For low frequencies between 64 and 200Hz, Vp was constant and lower compared to the sound speed in free space as predicted by the Guelke an Bunn's theory for these range of frequencies.

1.8.5 Central to peripheral sound propagation in excited lungs

The hypothesis that sounds generated artificially or naturally inside airways lumen, in order to reach pleural surface or the chest, must travel for a certain period in airways and for the remaining period through parenchyma and chest has been the main assumptions of many investigators. Different conclusions have been reached. In particular to check the preferential path of wave propagation in lungs, from central to peripheral airways and chest wall, many investigators have considered the effect of gas density on the acoustic transmission (Kraman, 1983; Mahagnah and Gavriely, 1995; Rice and Rice, 1987).

The speed of sound in free gas (or in rigid tubes) is inversely proportional to the square root of the density of the gas under consideration (Equations 1.6 and 1.10).

The parenchyma is a foam like structure (or two-phase porous medium) that with the hypothesises of not interconnected pores and wavelength much bigger than pores size can be assumed as an elastic continuum. With these assumptions of porous structure, the speed of a sound wave propagating through parenchyma is mostly influenced by tissue-gas volumetric ratio and not by the gas density.

According to these considerations a strong dependence of the wave speed upon the gas density can proof that the propagation is mainly inside the lumen of airways. On the contrary a wave speed independent from the gas density is usually associated to propagation through parenchyma.

Following this concept, Rice and Rice (1987) built a setup to check the time required to audible sounds to propagate from the trachea to the pleura surface in isolated horse and dog lungs, excited using a horn driver. The spectrum of excitation was not well defined due to the superimposition of incident and reflected sound waves. The speeds of audible sound were determined in earlier Rice's works for two respiratory structures: sound was found to propagate approximately at 60 m/s speed in parenchyma bulk (Rice, 1983) while at 350 m/s in larger airways (Rice, 1980). The time delay between the trachea and the specified point on the pleura was considered. Two paths were considered: straight line connecting the two points and along the airways. The observation of the time delays showed that the sound speed, calculated considering both paths, was always lower than 350 m/s and bigger than 60 m/s. On the other hand, the time delays changed with the gas composition. Since the only path mainly influenced by the gas composition is inside the airways lumen, it was suggested that the sound propagates mainly through airways (90% of the time of propagation) and the remaining time through parenchyma before reaching the external membrane (pleura). Opposite conclusions were expressed by Mahagnah (Mahagnah and Gavriely, 1995) and Kraman (Kraman, 1983) through in vivo experiments on human healthy patients. In both works the independence of the wave speed from gas density was proved suggesting, on the contrary of Rice's results, that wave propagation in respiratory system is dominated by propagation through the porous parenchyma. Mahagnah and Gavriely suggested that the difference in the results may be associated to methodological difference in considering in vivo and in vitro experiments.

1.8.6 Wave speed as mechanism for expiratory flow limitation

A very important clinical meaning of wave speed, associated to respiratory system, was introduced with the so called 'tube wave speed theory' applied to airways to explain the mechanism of expiratory flow limitation. It is well known in clinical practise that the flow measured at the mouth, during forced expiration, reaches a maximum at a given lung volume no matter the increase in pressure. In this situation the expiratory flow becomes an "effort independent mechanism" (Pedersen et al., 1997). Dawson and Elliott (Dawson and Elliott, 1977; Elliott and Dawson, 1977) suggested that the mechanism of expiratory flow limitation can be attributed to the wave speed of the pressure waves propagating in intrathoracic airways. They considered other works different from lung mechanics in which the flow limitation, occurring in elastic tubes, was associated to

the speed at which pressure waves travel inside the tube, the so called "wave speed theory". According to this theory, in an elastic tube the maximum of the flow is reached when the velocity of the fluid equals, in some point inside the tube, the wave speed; the point at which this happens has been called 'choke point'. In rigid tubes, the flow is found to limit when the fluid velocity equals the speed of sound (Shapiro, 1954). An intuitive physical explanation of this phenomenon can be understood considering that a disturbance downstream the choke point can not propagate upstream if the velocity of the fluid is higher than the tube wave speed; consequently changes in downstream can not affect the upstream flow rate. Elliott and Dawson considered equation Eq. (1.7) to calculate the wave speed in airways assuming that, analogously to the blood case, also in airways the term of air compressibility in Eq. (1.12) can be neglected (Elliott and Dawson, 1977). They proved experimentally the hypothesis of the wave speed theory on excited dog tracheas and rubber membrane. In their experiments, the pressure distance curves continued to change in the downstream section while remaining the same in the upstream section. This when, keeping fixed the upstream pressure, the down stream pressure was lowered below the value necessary to reach the maximum flow. From X-ray and Pitot tube measurements they were able to calculate the cross sectional area and the stiffness of the choke point and hence the wave speed from Eq.(1.7). The calculated wave speed was found to be close to the experimental maximum fluid velocity confirming the validity of the wave speed theory and equation Eq. (1.7) also for airways.

1.8.7 Serial distribution of airway structure

One of the first experimental attempts to associate particular features of airways to their distance from trachea using a time domain analysis was introduced by Jackson et al. in 1977. Using a system based on a spark source and a wave tube, the pressure wave was generated by the heat generated by the spark. Using the algorithm of Ware and Aki (Ware Ja and Aki k, 1969), Jackson was able to derive the change of characteristic impedances in correspondence of reflecting sites, by analyzing the amplitude of pressure incident (P_i) and reflected waves (P_r). The incident wave (P_i) travels until it encounters a discontinuity in impedance (for example from z_0 to z_1), where part of the wave will be reflected (P_r) and part transmitted (P_t). In correspondence of the reflective site: $P_i+P_r=P_t$ and $P_i/z_0-P_r/z_0=P_t/z_1$. From these relations the following relation can be obtained: $P_r/P_i=(z_1-z_0)/(z_1+z_0)$ (Jackson et al., 1977). Considering that the characteristic impedance is related to cross sectional area ($z=\rho c/A$), the determination of z together

with the analysis of time delays of the reflection (t=2x/c, where x is the distance) allowed the determination of an area-distance function. Jackson et al. (1997) applied this technique to determine the area distance function in excited dog lungs with the rigid wall assumption (c=Cs) and assuming moreover negligible losses and regular branching. The limitations of inference methods were analyzed by Fredberg and co-workers (Fredberg et al., 1980; Louis et al., 1994; Sidell and Fredberg, 1978) who identified the wall rigidity hypothesis and the assumption of symmetrical branching as the main factors affecting the correct area-distance determination. According to Fredberg, with compliant walls, the hypothesis of rigidity in the inference methods provokes a large overestimation of the cross sectional area of airways. The values of impedance in the two situations (Sidell and Fredberg, 1978) are given by:

$$Z_0 = \begin{cases} \dfrac{\rho c}{A} & rigid \\ \dfrac{\rho c}{A((B+K)/B)} & flexible \end{cases} \tag{1.13}$$

Therefore, with the hypothesis of rigid walls, the area was overestimated by a factor $(K+B)/B$ denoting respectively with B the specific elastance per unit length and K the bulk modulus of the gas. As solution, it was suggested, by the same authors, to increase the experiment range of excitation frequencies where the wall behaves more as rigid. Since the range of frequencies is limited by the gas wave speed (according to the area inference theory the assumptions of one dimensional wave front is valid only for $f<c/(2D_{max})$, where D_{max} is the maximum transversal dimension in airway), the increase of frequency was accomplished by a change in the gas composition.

1.9 Thesis motivation

This literature review has shown:

- The complexity of the respiratory tree as bifurcating asymmetrical network
- The existing morphological models in literature for the respiratory system
- Advantages and disadvantages of existing diagnostic techniques to assess the respiratory mechanics; features can be intuitively associated to time using time domain techniques
- Propagation of air pressure waves in elastic tubes: at low frequencies, wave speed is affected by the wall elasticity

According to these considerations, it would be very valuable to have a technique for the assessment of respiratory mechanics that, working in time domain, makes easier to associate features to time, allowing at the same time a certain freedom from the hypotheses of periodicity required by frequency domain. The possibility of using external pulses reduce the patient cooperation and, in the same time, if a low frequency pulse is used, the analysis of wave propagation might provide information about airway wall properties and change in the peripheral conditions as suggested by Rice (1980).

Most of the above requirements have been already satisfactorily investigated in arteries in both computational and experimental applications. The starting point of this work is therefore an existing 1-D formulation in space and time variables designed to model pulse propagation in cardiovascular system. The final aim of this thesis is to test the applicability of this 1-D modelling to describe air pulse propagation in flexible tubes and human airways through an experimental and computational study. Different respiratory pathologic conditions will be simulated computationally to investigate the possible diagnostic interest and applications that could derive from the application of the considered 1-D formulation to human lungs.

1.10 Thesis overview

The anatomical models of human airways and the literature related to wave propagation in flexible tubes and airways have been described in this chapter.

In Chapter 2, a detailed description of the mathematical model that will be used to simulate the propagation of air pulses in human central airways is presented. Wave Intensity Analysis (WIA) together with a detailed description of the experimental setup, used to validate the mathematical model, is also provided in Chapter 2.

In Chapter 3 the results of the experiments, carried out to validate the 1-D model, are presented: the capabilities of the 1-D formulation are tested and validated by comparing experimental data of air pulses propagating in flexible tubes with their computational equivalents. The applicability of the WIA to the air case is also tested in chapter 3.

In Chapter 4, computational results of air pulses propagating in simplified models of central airways are presented. Two models are considered: trachea and main bronchi (Bifurcation model) and a series of tubes (Multivessel model) with geometrical and mechanical properties defined according to the corresponding human airways.

In Chapter 5 more physiological features are introduced in the computational models accounting for the natural tree like structure and the characteristic asymmetry of the

human airway bifurcations. Two bifurcating models of central airways are considered: Weibel's symmetrical model and Horsfield's asymmetrical model. Results are presented based on different conditions of peripheral airways regarding both peripheral resistance and compliance variations.

A summary about the achievements of the thesis and suggestions for future work are presented in Chapter 6.

Chapter 2

Methodology

2.1 Introduction

In this chapter, the analogies between respiratory and cardiovascular system are introduced. The interest in reducing such complex 3-D problems to 1-D modelling, with related assumptions, is also presented. Next, the 1-D formulation is explained through the governing equations to study the propagation of pulse airwaves in idealised models of the human central airways. This formulation has been extensively applied to investigate the propagation of pulse waves in the arterial trees (Alastruey et al., 2008; Alastruey et al., 2009; Formaggia et al., 2006; Matthys et al., 2007a; Sherwin et al., 2003; Wan et al., 2002). According to these works, the shape of pulse waves changes as they propagate from central to peripheral arteries, influenced by geometries, mechanical properties and the boundary conditions of the arterial tree.

In order to validate the hypothesis that the 1-D formulation can be used, with certain assumptions, also to investigate the propagation of air pulses in flexible tubes, a series of experiments were conducted and they will be discussed in Chapter 3. The setup used for the experiments is also described in this chapter (Section 2.4) as well as the analytical principles of Wave intensity analysis (WIA) (Section 2.3).

2.2 Computational model

3-D models are ideal for a detailed description of airflow and velocity profiles in respiratory system; the main reason of using the 1-D formulation in this work is associated to the complexity of the system. As described in the previous chapter (Section 1.2) the bronchial tree contains a huge number of branches that make it even more intricate than the systemic circulation. For such systems, 3-D simulations appear too expensive computationally, limiting the analysis to few generations of bifurcations (de Rochefort et al., 2007; Liu et al., 2002; Liu et al., 2003; Luo and Liu, 2008); the choice of one-dimensional (1-D) modelling in time and space variables has been suggested as a good compromise between accuracy and computational cost (Matthys et al., 2007).

2.2.1 Assumption of 1-D computational model

- Each airway segment is modelled as a 1-D impermeable tube with a circular cross-sectional area (A) function of time, according to the wall deformability.
- The wave length is assumed to be large compared to the airways diameter so the

waves propagate mainly in the axial direction

- The airflow is considered only in the axial direction (x) with an average velocity (U) over the cross section. Experimental results in a human central airways models (Chang and Elmasry, 1982) have shown a relatively flat velocity profile (**Figure 2.1**) and in this thesis a nearly flat profile is assumed in all the 1-D segments. The presence of secondary flows in airways, particularly at airways bifurcations (Liu et al., 2002; Luo and Liu, 2008), are not taken into account and are neglected in this thesis.
- The airway wall diameter is a function of the internal pressure (P) which is assumed to be constant over the cross section. Wall deformation is considered only in the radial direction. The external pressure is assumed to be constant in space and time.
- In this thesis the peripheral airways that are not simulated by the 1-D model, are modelled by lumped parameter models (or 0-D models), coupled to the 1-D terminal segments (Section 2.2.5).

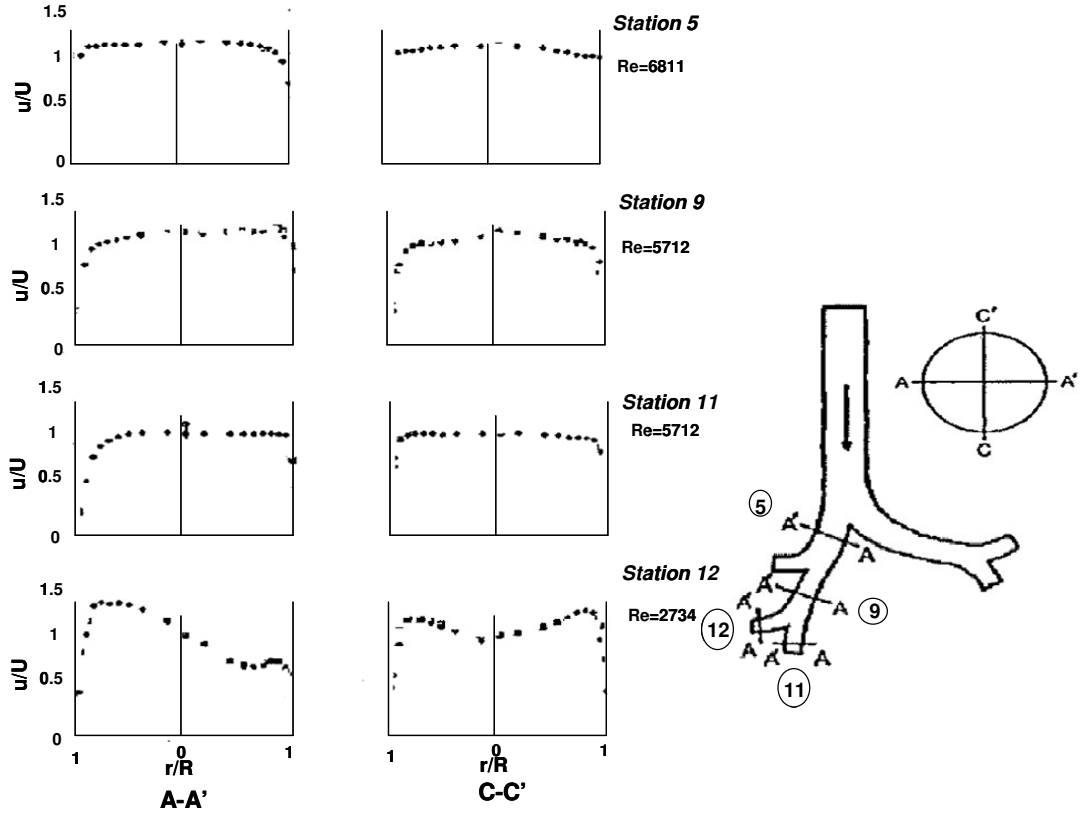

Figure 2.1 Measured axial velocity profiles in models of right main bronchus (station 5 and 9), in the right middle (station 12) and lower lobar bronchi (station 11) in frontal (A-A') and sagittal plane (C-C'). Re is the Reynolds number associated to the segment (Reproduced from Chang and Elmasry, 1982).

2.2.2 Air properties

Air is a mixture of dry air and water vapor. Dry air is a mixture of gases with the following percentage: 20.99% oxygen, 78.03% nitrogen, 0.94 % argon, 0.03% carbon dioxide and hydrogen. The molar mass of dry air is 28.9 Kg/kmol (Obert, 1960). Air (intended as mixture) can be considered as perfect gas for which the following equation can be used

$$P\upsilon = \frac{P}{\rho} = RT \tag{2.1}$$

In which P is the pressure, ν is the specific volume (inverse of the gas density ρ) and R is the gas constant of the particular gas, for air R= 287.058 J/(kg·K) and T is the absolute temperature (Shapiro, 1954). Neglecting the limited dependence of air viscosity on the temperature air can also be assumes as a Newtonian fluid. **Table 2.1** shows the values for air density, viscosity and sound speed in free air for three different values of temperature. Air density (ρ) is calculated using Eq. (2.1), with $P=p_0=1.0132\cdot10^5$Pa. Air viscosity (μ) is calculated using Sutherland's formula (Montgomery, 1947): $\mu = \mu_0 \frac{T_0 + C}{T + C}\left(\frac{T}{T_0}\right)^{3/2}$ where T is the input absolute temperature, μ_0 is the viscosity at reference temperature (T_0) and C is constant (C=120K for air). Sound speed in free air (C_s) is calculated using Eq. (1.6) ($C_s = \sqrt{\frac{p_0\gamma}{\rho}}$, γ=1.40). The temperature values are: 0°C, 20°C, 37°C). In particular 20°C has been chosen to represent the temperature of experiments; 37°C is the temperature inside lungs and 0°C has been chosen to show the margin of variation of the three quantities (ρ, μ, Cs). The values for ρ, μ and C_s, considered for the rest of this thesis are referred to experimental conditions (T=20 °C in **Table 2.1**) and are assumed constant.

ρ (Kg/m^3)	μ(Pa·s)	C_s(m/s)	T (°C)
1.29	$1.73\cdot10^{-5}$	331.56	0
1.20	$1.83\cdot10^{-5}$	343.48	20
1.14	$1.92\cdot10^{-5}$	353.30	37

Table 2.1 Air properties: density (ρ), viscosity (μ) and sound speed in free air (Cs) as function of the temperature (T)**.**

In this thesis, air is considered, to a first approximation, as an incompressible fluid (Kyriakou et al., 2007). According to Nguyen (2006), the Mach number (Ma) is a

measure of gas compressibility. It is defined as: $Ma = \frac{u}{C_s}$, where u is the fluid velocity and C_s is the sound speed, if Ma< 1 the flow is subsonic, while for Ma>1 the flow is supersonic. When Ma< 0.3 (if the wall is not heated locally or the tube is not too long) a flowing gas can be reasonably be assumed as incompressible so the density will not change while the gas is flowing through a system (Nguyen, 2006). In the respiratory system the maximum air speed is around 1-2 m/s while the sound speed is Cs~343m/s, the air flowing in lungs can be therefore reasonably assumed as incompressible fluid.

2.2.3 Theoretical analysis

In 1775, Euler derived the partial differential equations describing the conservation of mass and momentum for inviscid flow in arterial system. Euler's equations of motions are hyperbolic equations and were solved by Riemann (1860) after almost 100 years. Riemann introduced an analytical tool for the general solutions of the this type of equations widely known as the method of characteristics. Euler's equations were introduced for the specific application of blood and liquids, the main contribution of this work is to test their applicability to air in respiratory system.

2.2.3.1 Equations of mass and momentum conservation

Considering a vessel with a uniform circular cross sectional area along its length, it is possible to define the problem in one dimensional terms. The cross sectional area A(x,t) is a function of the axial coordinate (x) and the time (t). $P(x,t) = \frac{1}{R^2}\int_0^R 2rpdr$ and $U(x,t) = \frac{1}{R^2}\int_0^R 2rudr$ are respectively the average internal pressure and velocity over the cross –section, p and u denote the pressure and velocity values of each fluid particle in the cross-section A(x.t), r is the radial coordinate and R is the internal radius of the vessel. Euler's equations for a 1-D impermeable and elastic tubular control volume of Newtonian incompressible fluid can be expressed as (Sherwin et al., 2003)

$$\frac{\partial A}{\partial t} + \frac{\partial (AU)}{\partial x} = 0, \tag{2.2}$$

$$\frac{\partial U}{\partial t} + (2\alpha - 1)U\frac{\partial U}{\partial x} + (\alpha - 1)\frac{U^2}{A}\frac{\partial A}{\partial x} + \frac{1}{\rho}\frac{\partial p}{\partial x} = \frac{f}{\rho A}, \tag{2.3}$$

where ρ is the density of the air ($\rho = 1.204 kg/m^3$, **Table 2.1**), *f(x,t)* is the friction force per unit length and α(x, t) is a correction factor, non-dimensional defined as:

$$\alpha = \frac{1}{U^2 R^2} \int_0^R 2ru^2 dr \tag{2.4}$$

Equation (2.4) accounts for the non linearity of the radial velocity profile across each cross section A. In this thesis α is considered constant (it means that a constant velocity profile is assumed). The velocity profile is described by (Alastruey, 2006; Smith et al., 2002)

$$u = U \frac{\gamma + 2}{\gamma} \left[1 - \left(\frac{r}{R} \right)^{\gamma} \right] \tag{2.5}$$

Equation (2.5) describes an axial velocity profile characteristic of oscillatory flow, γ is a constant. The shape of the profile can be varied from a plug profile to fully developed parabolic profile (Smith et al., 2002). Using (2.5), the no-slip ($u\big|_{r=R} = 0$) and the axisymmetric flow condition are automatically satisfied. Substitution of (2.5) in (2.4) yields $\gamma = \frac{2-\alpha}{\alpha - 1}$, therefore

$$u = U \frac{\alpha}{2 - \alpha} \left[1 - \left(\frac{r}{R} \right)^{\frac{2-\alpha}{\alpha-1}} \right] \tag{2.6}$$

In this thesis the value γ=9 (corresponding to α=1.1) is always considered. This choice for airways can be justified by comparing the axial velocity profiles in **Figure 2.1** obtained experimentally by Chang and Elmasry (1982) with the ones shown in **Figure 2.2**: the velocity profiles, in most of the central airways, are closer to flat profile than to parabolic profile.

Equation (2.3) becomes simpler by neglecting the inertia convective terms ($2(\alpha - 1)U \frac{\partial U}{\partial x}$) and ($(\alpha - 1)\frac{U^2}{A}\frac{\partial A}{\partial x}$); these terms take into account that the velocity is not flat and are considered smaller compared to the other terms in the equation (Alastuey , 2006; Brooks et al., 1984). Equation (2.3) yields

$$\frac{\partial U}{\partial t} + U \frac{\partial U}{\partial x} + \frac{1}{\rho} \frac{\partial P}{\partial x} = \frac{f}{\rho A} \tag{2.7}$$

Considering (2.6), the expression for *f(x.t)* suggested by Smith et al., (2002), with γ=9, becomes

$$f = 2\mu \frac{A}{R}\left[\frac{\partial u}{\partial r}\right]_R = -2(\gamma+2)\mu\pi U = -22\mu\pi U \tag{2.8}$$

Where $\mu = 0.018$ mPa ·s is the viscosity of air (**Table 2.1**). Noting that $\gamma = 2$ corresponds to a parabolic profile and yields Poiseuille's flow resistance $f = -8\mu\pi U$.

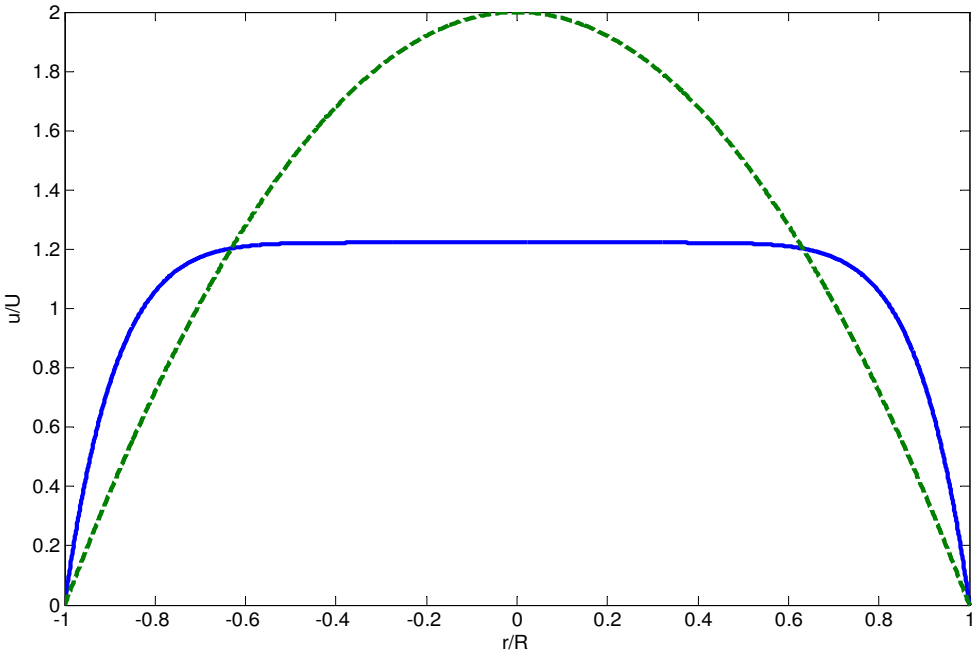

Figure 2.2 Velocity profile according to Equation (2.5) with γ=2 (dashed line) and γ=9 (solid line)

2.2.3.2 Tube law

Equations (2.2) and (2.7) provide three unknown values (P, U and A). One more equation is therefore required to close the system. The tube law used in this thesis is a pressure-area relationship determined using Laplace's law (assuming the wall to be thin, homogeneous and elastic) (Alastruey et al., 2008; Alastruey et al., 2009; Formaggia et al., 2003; Matthys et al., 2007a; Sherwin et al., 2003)

$$P = P_{ext} + \beta(\sqrt{A} - \sqrt{A_0}) \tag{2.9}$$

where β is a parameter associated with the mechanical properties of the tube wall.

$$\beta(x) = \frac{\sqrt{\pi} h_e E}{A_0(1-\nu^2)} \tag{2.10}$$

where E is the Young's modulus, P_{ext} is the external pressure and is assumed to be constantly zero (P_{ext}=0 Pa); ν is the Poisson's ratio (the vessel wall is considered to be incompressible, ν=0.5), A_0 is the sectional area at $P=P_{ext}$ and h_e is the wall thickness.

A_0 and β are assumed to be constant along each airways branch. Although the trachea and in general the airways behave as viscoelastic materials (Aljuri et al., 2006; Meyers et al., 1980), in this thesis the Young modulus of the wall is assumed to be constant in each airway independently from the internal pressure. The Young's modulus can be changed in the different airways to account for the cartilage decrease from central to peripheral airways (**Table 2.3** and **Table 2.4**). Defining the distensibility as $D_s = \frac{1}{A}\frac{dA}{dP}$ and differentiating (2.9) yields $D_s = \frac{2}{\beta\sqrt{A}}$.

2.2.3.3 Solution through the method of characteristics

Using the tube law described in equation (2.9), equations (2.2) and (2.7) can be written in the following matrix form (Alastruey 2006)

$$\frac{\partial \boldsymbol{\psi}}{\partial t} + \mathbf{H}\frac{\partial \boldsymbol{\psi}}{\partial x} = \mathbf{S} \tag{2.11}$$

Where

$$\boldsymbol{\psi} = \begin{pmatrix} A \\ U \end{pmatrix},\ \mathbf{H} = \begin{pmatrix} U & A \\ \frac{1}{\rho A}\frac{1}{D_s} & U \end{pmatrix},\ \mathbf{S} = \begin{pmatrix} 0 \\ \frac{1}{\rho}\left(\frac{f}{A} - \frac{\partial p}{\partial \beta}\frac{d\beta}{dx} - \frac{\partial p}{\partial A_0}\frac{dA_0}{dx}\right) \end{pmatrix}$$

The solutions of the characteristic polynomial $|\mathbf{H} - \lambda I| = 0$ are the eigenvalues of H, calculated by $\lambda_{\pm} = U \pm \sqrt{\frac{1}{\rho D_s}}$. The term under the square root has the dimensions of a velocity, it is the wave speed (c) of the system. In this thesis c is calculated as:

$$c = \sqrt{\frac{1}{\rho D_s}} = \sqrt{\frac{\beta}{2\rho}} A^{\frac{1}{4}} \tag{2.12}$$

The eigenvalues $\lambda_{\pm}$ refer to the speed of disturbance propagation (U+c and U-c respectively for forward and backward direction).

Riemann observed that, once defined the characteristic directions as

$$\frac{dx}{dt} = \lambda_{\pm} = U \pm c \tag{2.13}$$

along these directions the total derivative with respect to time is

$$\frac{d}{dt} = \frac{\partial}{\partial t} + \frac{dx}{dt}\frac{\partial}{\partial x} = \frac{\partial}{\partial t} + (U \pm c)\frac{\partial}{\partial x} \tag{2.14}$$

Along the characteristics the partial differential equations (PDE) can be reduced into ordinary differential equation (ODE). To achieve this, the matrix **H** can be formulated as

$$\mathbf{H} = \mathbf{L}^{-1}\mathbf{\Lambda}\mathbf{L} \tag{2.15}$$

Where $$\mathbf{L} = \zeta \begin{vmatrix} \frac{c}{A} & 1 \\ -\frac{c}{A} & 1 \end{vmatrix}, \ \mathbf{\Lambda} = \begin{vmatrix} \lambda_1 & 0 \\ 0 & \lambda_2 \end{vmatrix}$$

and ζ is a scaling factor (ζ=1 in this thesis). Inserting (2.15) in (2.11) and multiplying by **L** the following expression is obtained

$$\mathbf{L}\frac{\partial \boldsymbol{\psi}}{\partial t} + \mathbf{\Lambda}\mathbf{L}\frac{\partial \boldsymbol{\psi}}{\partial x} = \mathbf{LS} \tag{2.16}$$

Then, defining

$$\frac{\partial \mathbf{W}}{\partial \boldsymbol{\psi}} = \mathbf{L} \tag{2.17}$$

in which $\mathbf{W} = [W_1, W_2]^T$ is the vector of characteristic (or Riemann) variables, (2.16) becomes

$$\frac{\partial \mathbf{W}}{\partial t} + \mathbf{\Lambda}\frac{\partial \mathbf{W}}{\partial x} = \mathbf{LS} \tag{2.18}$$

Substituting Equation (2.14) into Equation (2.18) yields

$$\frac{d\mathbf{W}}{dt} = \mathbf{LS} \tag{2.19}$$

It is therefore possible to derive the solution W by solving ordinary differential equations along each characteristic direction. Integration of Eq. (2.17) (with $\frac{\partial^2 W_{\pm}}{\partial A \partial U} = \frac{\partial^2 W_{\pm}}{\partial U \partial A}$) allows the determination of the characteristic variables W_+ and W_- respectively in the forward and backward direction:

$$W_{\pm} = U - U_0 \pm \int_{A_0}^{A} \frac{c}{A} dA \tag{2.20}$$

Where (U_0, A_0) is the reference state. Changes in pressure and velocity propagates forward by W_+ and backward by W-. Inserting (2.12) in (2.20), an explicit form of **W** can be derived (Sherwin et al., 2003)

$$W_{\pm} = U - U_0 \pm 4(c - c_0) = u \pm 4\sqrt{\frac{\beta}{2\rho}}(A^{\frac{1}{4}} - A_0^{\frac{1}{4}}) \tag{2.21}$$

The Water hammer equation relates the change of P to change in U across a wavefront and can be easily derived from the method of characteristic described above.

Considering β and A_0 constant along x and according to the relation $c = \sqrt{\frac{1}{\rho D}} = \sqrt{\frac{A}{\rho}\frac{\partial P}{\partial A}}$, it is possible to derive $\frac{cdA}{A} = \frac{dP}{\rho c}$.

The change of variables introduced in Eq. (2.17) leads to d**W**=**L**d**ψ** and consequently

$$dW_+ = dU + \frac{c}{A}dA = dU + \frac{dP}{\rho c} = 0 \tag{2.22a}$$

$$dW_- = dU - \frac{c}{A}dA = dU - \frac{dP}{\rho c} = 0 \tag{2.22b}$$

The Water hammer equation can be therefore derived

$$dP_\pm = \pm \rho c dU_\pm \tag{2.23}$$

2.2.3.4 Wave speed and sound limit

As discussed in Section 1.8.6, Dawson and Elliott suggested that the term ρ/K related to air compressibility in Korteweg's equation (1.12) can be also neglected for the case of airflow in rubber tubes and in airways. Bramwell and Hill equation (Equation 1.7) was considered by Elliott, Dawson (Section 1.8.6) and Guelke (Section 1.8.2) to calculate the wave speed associated to airflow in elastic vessels. Also the expression for wave speed in Eq.(2.12) is derived from Bramwell and Hill equation but it can provide wave speed values that can be much bigger than sound speed in free air (C_s). Since the wave speed in rigid tubes equals *Cs* in free air (Cs=343 m/s) (except from frequencies close to the resonance frequency f_r) (Guelke and Bunn, 1981; Rice, 1980; Suki et al., 1993)**,** Cs is considered as the maximum value for wave speed in the whole computational part of this thesis. According to this assumption, a new wave speed c_β is introduced in this work. c_β=c (Equation 2.12) if c<Cs while for all the airways segments where c>Cs, *β* has been changed in Eq. (2.12) to obtain c=Cs by imposing

$$\beta = \frac{2\rho(C_S)^2}{A^{1/2}} \tag{2.24}$$

In this way the matching of wave speeds with the Cs value has been reached making the tube walls 'more compliant' for all the segments where c>Cs, the cross sectional area A does not change in this corrected formulation (the change of β is obtained by varying the product h_eE). The expression for c_β is therefore:

$$c_\beta = \begin{cases} c = \sqrt{\dfrac{1}{\rho D_s}} & if \;\; c < C_s \\ C_s & if \; c > C_s \end{cases} \tag{2.25}$$

2.2.3.5 Linearisation of the system equations

In this thesis, following the linear formulation suggested by Alastruey (2006), the linearisation of the governing system (2.11) is used for all the computational part, derived by perturbing a reference state *(A, P ,U)=(A_0, 0, 0)* with small amounts *Δa*, *Δp, Δu*, and ignoring quadratic terms. The resulting system of linear equations is

$$\frac{\partial \Delta \mathbf{U}}{\partial t} + \mathbf{H_0} \frac{\partial \Delta \mathbf{U}}{\partial x} = \mathbf{S_0} \;, \tag{2.26}$$

$$\Delta \mathbf{U} = \begin{bmatrix} \Delta a \\ \Delta u \end{bmatrix} \;;\; \mathbf{H_0} = \begin{bmatrix} 0 & A_0 \\ \dfrac{\beta}{2\rho A_0^{3/2}} & 0 \end{bmatrix} ;\; \mathbf{S_0} = \begin{bmatrix} 0 \\ \dfrac{1}{\rho}\left(\dfrac{f_0}{A_0} - \dfrac{\partial \Delta p}{\partial \beta} - \dfrac{d\beta}{dx} - \dfrac{\partial \Delta p}{\partial A_0}\dfrac{dA_0}{dx} \right) \end{bmatrix}.$$

The linear characteristic functions are calculated as $\Delta W_\pm = \Delta u + \frac{c_0}{A_0}\Delta A_0$ from the characteristic analysis applied to system (2.26).

2.2.3.6 Numerical discretisation

Sherwin et al. (2003) suggested a numerical method in order to proceed with the numerical solution of (2.11). The following conservative form was considered

$$\frac{\partial \boldsymbol{\psi}}{\partial t} + \frac{\partial \mathbf{F}}{\partial x} = \mathbf{S} \tag{2.27}$$

$$\boldsymbol{\psi} = \begin{bmatrix} A \\ U \end{bmatrix}, \quad \mathbf{F} = \begin{bmatrix} AU \\ \dfrac{U^2}{2} + \dfrac{P}{\rho} \end{bmatrix}, \; \mathbf{S} = \begin{pmatrix} 0 \\ \dfrac{1}{\rho}\left(\dfrac{f}{A} - \dfrac{\partial p}{\partial \beta}\dfrac{d\beta}{dx} - \dfrac{\partial p}{\partial A_0}\dfrac{dA_0}{dx} \right) \end{pmatrix}$$

It is worth noting that the vector **F** includes the volume flux and the energy per unit mass; **S** is a source term. The domain of each airway $\Omega = [0, l]$ is discretized into a mesh of N_{el} non overlapping elements $\Omega = \bigcup_{e=1}^{N_{el}} \Omega_e$ in which $\Omega_e = [x_e^L, x_e^R]$; the superscripts denote the left (L) and right (R) boundary of each element Ω_e, e=1…., N_{el} and $x_e^R = x_{e+1}^L$ for e=1,…, N_{el}-1.Multiplying (2.27) by a vector of test functions Φ, then integrating over the domain Ω, it is possible to obtain the weak form of (2.27). After

decomposing into the domain elements and integrating by part, Equation (2.27) becomes

$$\sum_{e=1}^{N_{el}}\left[\left(\frac{\partial \boldsymbol{\psi}}{\partial t},\boldsymbol{\Phi}\right)_{\Omega_e}-\left(\mathbf{F},\frac{d\boldsymbol{\Phi}}{dx}\right)_{\Omega_e}+\left[\mathbf{F}\cdot\boldsymbol{\Phi}\right]_{x_e^L}^{x_e^R}\right]=\sum_{e=1}^{N_{el}}\left(\mathbf{S},\boldsymbol{\Phi}\right)_{\Omega_e} \tag{2.28}$$

The solution $\boldsymbol{\psi}(x,t)$, as well $\boldsymbol{\Phi}$, is chosen to be in the finite space of $\mathbf{L}^2(\Omega)$ functions, polynomial of degree P on each element; the subscript δ denotes an element of such a space. Since $\boldsymbol{\psi}^{\delta}$ and $\boldsymbol{\Phi}^{\delta}$ may be discontinous at the interface of every elemental region, in order to obtain a global solution in the domain Ω, information must propagate between elemental regions Ω_e. This is reached by upwinding the boundary flux in the third term of (2.28). Denoting the upwinded flux as $\mathbf{F}^{u}$, the discrete weak formulation can be written

$$\sum_{e=1}^{N_{el}}\left[\left(\frac{\partial \boldsymbol{\psi}^{\delta}}{\partial t},\boldsymbol{\Phi}^{\delta}\right)_{\Omega_e}-\left(\mathbf{F}(\mathbf{U}^{\delta}),\frac{d\boldsymbol{\Phi}^{\delta}}{dx}\right)_{\Omega_e}+\left[\mathbf{F}^{u}\cdot\boldsymbol{\Phi}^{\delta}\right]_{x_e^L}^{x_e^R}\right]=\sum_{e=1}^{N_{el}}\left(\mathbf{S}(\mathbf{U}^{\delta},\boldsymbol{\Phi}^{\delta}\right)_{\Omega_e} \tag{2.29}$$

Equations (2.29) are solved using a discontinuous Galerkin scheme with a Legendre polynomial spectral/hp spatial discretisation, a second order Adams-Bashforth time-integration scheme, and the initial conditions *(P,U)=(0,0)* everywhere in the system. Polynomial order and quadrature order can be defined for each domain. A solver called Nectar was used for the numerical solution. (details about the numerical discretisation can be found in Alastruey (2006), Sherwin et al. (2003) and Karniadakis and S. J. Sherwin, (2003)).

2.2.3.7 Interfaces

The upwinded fluxed $\mathbf{F}^{u}$ in Eq. (2.29) in all the interfaces are calculated as the solution of a Riemann problem which neglects the characteristic information moving away from the boundary, accounting only for the characteristic information approaching the boundary (Alastruey 2006).

Inter element interfaces

Considering the interface which separate two elemental regions Ω_e (**Figure 2.3**), the Riemann problem is used to calculated the two upwind states (A_L^u, U_L^u) and (A_R^u, U_R^u) generated at time t+Δt on each side of the interface (respectively left and right) starting from the two constant states (A_L, U_L)$_t$ and (A_R, U_R)$_t$ at time t. Four equations are required to solve the system. Assuming inviscid flow between the two initial states, Eq.

(2.19) becomes $\frac{d\mathbf{W}}{dt} = 0$. Considering the characteristic information approaching both sides of the interface and neglecting the information moving away yields

$$W_+(A_L, U_L) = W_+(A_L{}^u, U_L{}^u) \tag{2.30}$$

$$W_-(A_R, U_R) = W_-(A_R{}^u, U_R{}^u) \tag{2.31}$$

Where $W_\pm$ are obtained from (2.21). The other two equations, required to solve the 4 unknowns at the interface, derive from the conservation of the mass and the continuity of the total pressure (Bernoulli's law)

$$A_L^u U_L^u = A_R^u U_R^u \tag{2.32}$$

$$\rho \frac{(U_L^u)^2}{2} + P(A_L^u) = \rho \frac{(U_R^u)^2}{2} + P(A_R^u) \tag{2.33}$$

Where $P(A)$ refer to the tube law (2.9). Equations (2.30)-(2.33) are solved using the iterative Newton-Raphson method to obtain ($A_L{}^u$, $U_L{}^u$) and ($A_R{}^u$, $U_R{}^u$) (Alastruey, 2006).

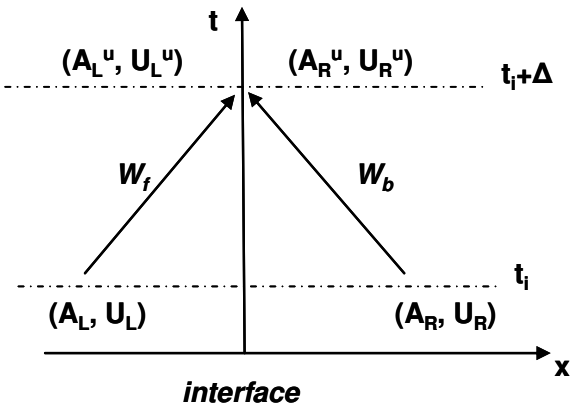

Figure 2.3 Schematic of Riemann problem at interface. From the initial states (A_L, U_L) and (A_R, U_R) at time t it is possible to calculate the corresponding upwind states at the interface at a later time (t+Δt) (Alastruey, 2006)

The characteristic information moving away from both sides of the interface does not change the solution if

$$\Delta t_{\max}(|U \pm c|) \le \frac{1}{2}\Delta x \tag{2.34}$$

where Δx is the distance between two subsequent quadrature points. With the condition (2.34) the characteristic information does not have enough time to interact with the characterisitic information coming from the adjacent quadrature points (Alastruey, 2006).

Inter junction interfaces

The one –dimensional model can be extended and applied to deal with bifurcating trees by defining suitable conditions at the interface of each domain. Two types of junction are considered: splitting flow and merging flow junction; the analytical procedures follow the steps described in "Inter element interfaces".

Splitting flows junctions

Considering a bifurcation in which the parent vessel is denoted as 1 and the two daughter vessels are 2 and 3 (**Figure 2.4**), the solution of the A and U variables in each vessel can be considered as solution of a Riemann problem. Six independent equations are required because of the six unknowns (A and U in all the three vessels at time t+Δt).

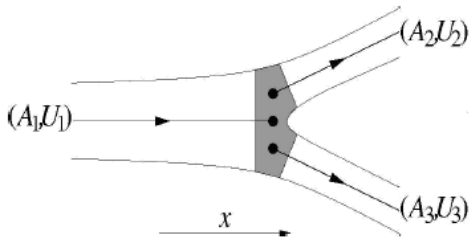

Figure 2.4 Notation for splitting flow junction. The arrows indicate the direction in which x is positive (Reproduced from Alastruey, 2006).

As it was done with the Equations (2.30) and (2.31), three conditions can be derived from the characteristic information in each vessel at a generic time t with the assumption of inviscid flow within the points adjacent to the junction (the subscript denote the vessel under consideration). From the conservation of characteristic variables approaching the bifurcation in each vessel

$$W_+(A_1^u, U_1^u) = W_+(A_1, U_1) \tag{2.35}$$

$$W_-(A_2^u, U_2^u) = W_-(A_2, U_2) \tag{2.36}$$

$$W_-(A_3^u, U_3^u) = W_-(A_3, U_3) \tag{2.37}$$

The remaining equations are derived from the conservation of mass

$$A_1^u U_1^u = A_2^u U_2^u + A_3^u U_3^u \tag{2.38}$$

and the Bernoulli's law

$$\rho\frac{(U_1^u)^2}{2}+P(A_1{}^u)=\rho\frac{(U_2^u)^2}{2}+P(A_2^u) \tag{2.39}$$

$$\rho\frac{(U_1^u)^2}{2}+P(A_1{}^u)=\rho\frac{(U_3^u)^2}{2}+P(A_3^u) \tag{2.40}$$

Merging flow junction

The merging flow junction is associated to the interface with the outlet of the two daughter vessels connected to the inlet of the parent vessel (**Figure 2.5**). The equations for the conservation of the characteristic variables approaching the junction are:

$$W_-(A_1{}^u,U_1{}^u)=W_-(A_1,U_1) \tag{2.41}$$

$$W_+(A_2{}^u,U_2{}^u)=W_+(A_2,U_2) \tag{2.42}$$

$$W_+(A_3{}^u,U_3{}^u)=W_+(A_3,U_3) \tag{2.43}$$

The expressions for conservation of mass and Bernoulli's law are analogous to equations (2.38)-(2.40).

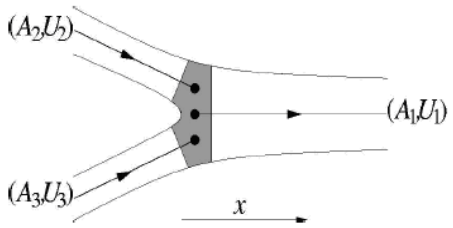

Figure 2.5 Notation for merging flow junction. The arrows indicate the direction in which x is positive (Reproduced from Alastruey, 2006).

2.2.3.8 Linear analysis of wave reflections

When an incident wave encounters a reflection site, there is a component of the wave that is reflected and another transmitted. A reflection coefficient (R_f) can be defined as $R_f=\delta p/\Delta p$, where δp is the magnitude of the reflected pressure and Δp is the magnitude of the incident wave. Different types of reflections can be generated according to the the R_f values (**Table 2.2**).

R_f	-1	1	0	-1<R_f<0	0<R_f<-1
Reflection site	Open end	Closed end	No reflections	Negative reflection	Positive reflecion

Table 2.2 Reflections associatet to R_f values

The type of reflected waves depends on two factors: the type of incident wave and the sign of the reflection sites. If the reflection site is positive, the type of reflected wave is the same as the incident wave: an incident compression wave generates, in this case, reflected compression wave while an incident expansion wave produces a reflected expansion wave. In contrast a negative reflection site has opposite effect (an incident compression wave produces a reflected expansion wave while an incident expansion wave generates a reflected compression wave).

In a bifurcation with the parent vessel denoted with the subscript P and the daughter vessels respectively with the subscripts D1 and D2 (**Figure 2.6**), there are three different reflection coefficients: one in the forward direction ($R_{f\,P}+$) and two in the backward directions ($R_{fD1}-$ and $R_{fD2}-$) with the following expressions

$$R_{f\,P}+=\frac{(A_P/c_P)-(A_{D1}/c_{D1})-(A_{D2}/c_{D2})}{(A_P/c_P)+(A_{D1}/c_{D1})+(A_{D2}/c_{D2})} \tag{2.44}$$

$$R_{f\,D1}-=\frac{(A_{D1}/c_{D1})-(A_P/c_P)-(A_{D2}/c_{D2})}{(A_P/c_P)+(A_{D1}/c_{D1})+(A_{D2}/c_{D2})} \tag{2.45}$$

$$R_{f\,D2}-=\frac{(A_{D2}/c_{D2})-(A_P/c_P)-(A_{D1}/c_{D1})}{(A_P/c_P)+(A_{D1}/c_{D1})+(A_{D2}/c_{D2})} \tag{2.46}$$

A reflection coefficient can also be calculated for a junction between two different tubes (tubes in series) by imposing $A_{D2}/c_{D2}=0$ in Eq. 2.44. The transmission coefficient is obtained as $T=1+R_f$.

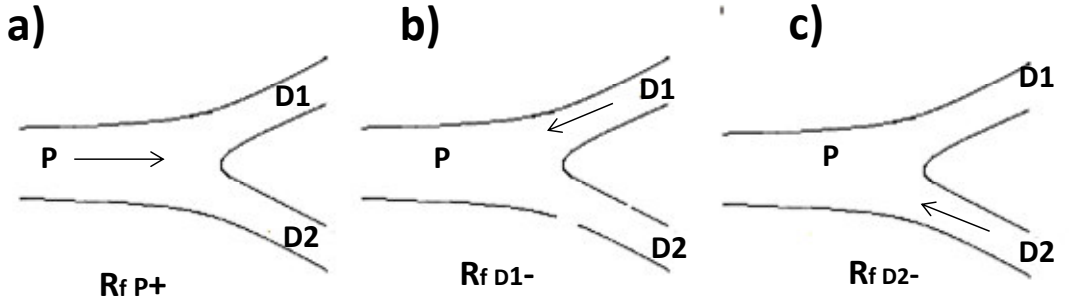

Figure 2.6 Schematic of a bifurcation and correspondence to reflection coefficients described in Section 2.2.3.8: reflection coefficients at bifurcation (a) in forward direction (Eq. 2.44) and in backward directions with the two waves from the daughter vessels approaching the bifurcation (b and c, Equations 2.45 and 2.46). The arrows indicate the direction of the incident wave.

2.2.4 Inlet boundary conditions

The 1-D model allows the prescription of the flow rate (Q_{in}) and velocity (U_{in}) at the inlet. Moreover the reflection coefficient of the inlet can be set to 1 or 0 after the inflow pulse. The condition is based on the solution of Riemann problem similarly to **Figure 2.3**. The state (A_R, U_R) corresponds, in this case to the solution at the beginning of the 1-D model, while (A_L, U_L) is a virtual state selected to satisfy the condition enforced by Q_{in} or U_{in}. Specific inlet boundary conditions as function of time will be defined in Chapter 3, 4 and 5 for each of the models under consideration.

2.2.5 Outlet boundary conditions

In Section 2.2 the 1-D formulation has been presented as a good solution for the trade off between accuracy and computational cost. However, even using the 1-D formulation, it appears too expensive computationally to model all the airways till alveoli because of the huge number of vessels (totally 2^{23} terminal airway segments according to Weibel's model). Furthermore the assumption of thin walled tube (Section 2.2.3.2), require by 1-D model, becomes less appropriate for airway with small calibre where the vessel radius becomes very close to the wall thickness.

For all these reasons, it necessary to truncate the 1-D modelling after a certain number of generations. Following Kobayashi et al. (1987), in this thesis the central airway resistance (R_c) is defined as the summation of the resistances from generation 0 (trachea) to generation 7, and the resistance of peripheral airways (R_p) as the sum of the resistances from Generation 8 to Generation 23 according to Weibel's model (Section 1.3.2.1). The 1-D modelling has been used for the central airways while the fluid dynamic conditions of peripheral airways have been modelled using lumped parameters model (or 0-D models). The pressure and flow at the outflow of each terminal 1-D segment are related therefore by ordinary differential equations. The parameters which characterize mainly the peripheral airways are the alveolar compliance (C) and the peripheral airway resistance (R) that are the most affected by the respiratory diseases (Section 1.2). Different models are used in this thesis to describe the fluid dynamic behaviour of peripheral airways with different combinations of the resistance and compliance. All the models are shown in **Figure 2.7**. The mathematical details are described in Section 2.2.5.1.

a)

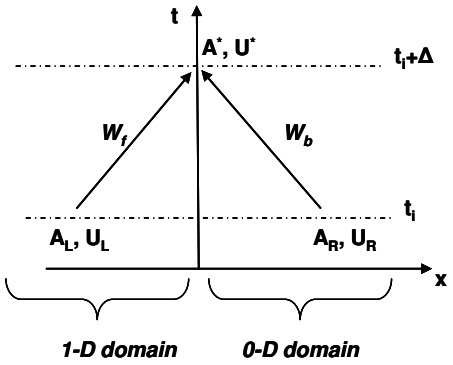

b)

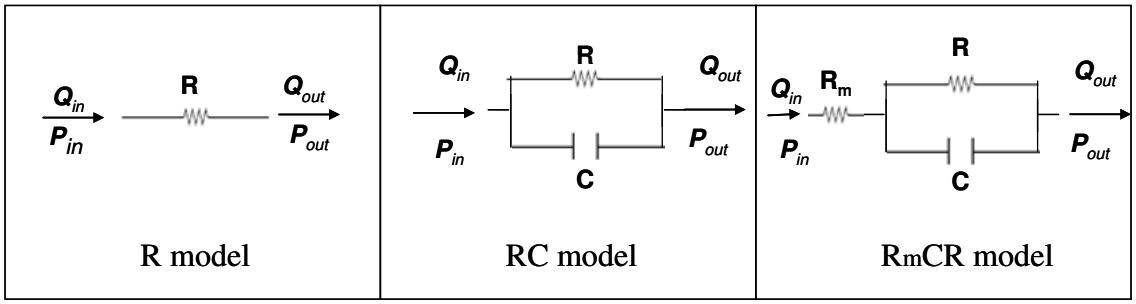

Figure 2.7 a) Riemann problem at the boundary between 1-D central airways model and 0-D peripheral model (modified after Alastruey et al., 2008). b) 0-D models for peripheral airways: terminal resistance (R model), two-element Windkessel model (RC model) and three-element Windkessel model (R_mCR model). For the notation of the variables refer to text.

2.2.5.1 Mathematical formulation

Considering Poiseuille's flow resistance (γ=2 in Equation 2.5) which is a better approximation for the peripheral airways (Pedley et al., 1970b) than the nearly flat profile assumed for the central airways and integrating (2.26) along the length of the domain, with $Q=AU$, leads to (Alastruey, 2006)

$$\begin{cases} C\dfrac{dP_{in}}{dt} + Q_{out} - Q_{in} = 0 \\ L\dfrac{dQ_{out}}{dt} + RQ_{out} + P_{out} - P_{in} = 0 \end{cases} \tag{2.47}$$

Where $Q_{in}=Q(0,t)$, $Q_{out}=Q(L,t)$, $P_{in}=P(0,t)$, $P_{out}=P(L,t)$ are the flow rates (Q) and pressures (P) respectively at the inlet and outlet. The equations in (2.47) are analogous to the equations of electric transmission line; in which flow and pressure correspond to electric current and potential, respectively. $R = \dfrac{8\pi\mu l}{(A_0)^2}$, $L = \dfrac{\rho l}{A_0}$ and $C = \dfrac{A_0 l}{\rho(c_0)^2}$ are the resistance to flow, air inertia and wall compliance, associated respectively to their zero dimensional (0-D) electric equivalent. In particular in this work R has been associated to peripheral airways resistance, C to the airway compliance (the compliance of airways is

assumed to be mostly concentrated in peripheral airways). The coupling between the 1-D model and 0-D models is based on the solution of a Riemann problem at the interface 1-D/0-D (**Figure 2.7a**). (A^*, U^*) is an intermediate state generated at time $t_i + \Delta t$ (Δt is the time step) from the time t_i of the states (A_L, U_L) and (A_R, U_R). (A_L, U_L) is the end point of the 1-D domain and (A_R, U_R) is a virtual state selected so that (A^*, U^*) satisfies (2.47).

The following models of peripheral airways are considered, derived from (2.47) (**Figure 2.7b**):

Terminal resistance (R model)

This model considers the only peripheral resistance (R) of airways. Imposing L=*0* and *C=0* in (2.47) leads to

$$Q_{out} = Q_{in} = Q = A^* U^* = \frac{P_{in} - P_{out}}{R} \quad . \tag{2.48}$$

In a system with a single resistance coupled to the outflow of a 1-D model terminal segment, the terminal reflection coefficient (R_t), can be expressed as

$$R_t = \frac{R - Z_0}{R + Z_0} \tag{2.49}$$

where Z_0, the characteristic impedance of the terminal segment of the 1-D model, is calculated as $Z_0 = \rho c / A_0$.

Two-element (RC) model

Two elements (RC) Windkessel model has been used as model for peripheral airways based on a recently proposed model which accounts for a separate peripheral compartment (extended RIC model, Section 1.4.2.3). This model assumes *L=0* and considers both peripheral resistance (R) and compliance (C) of lungs; Eq. 2.47 becomes

$$C \frac{dP_{in}}{dt} + \frac{P_{in} - P_{out}}{R} - Q_{in} = 0 \tag{2.50}$$

Three-element (R_mCR) model

This model accounts for an additive resistance (R_m) in RC model. R_m equals the characteristic impedance of the terminal segments of the 1-D model, it was introduced by Alastruey (2006) to avoid non physiological wave reflections in microcirculations.

In correspondence of R_m: $Q_{in} = \frac{P_{in} - P_C}{R_m}$, P_C denotes the pressure across the compliance *C*. For the RC block the following system is considered

$$\begin{cases} C\frac{dP_C}{dt} + Q_{out} - Q_{in} = 0 \\ RQ_{out} + P_{out} - P_C = 0 \end{cases} \quad (2.51)$$

2.2.6 Morphological and elastic properties for 1-D models

The 1-D models used in this thesis refer to Weibel and Horsfield's models (Section 1.4.2). **Figure 1.7** and **Figure 1.9** provide diameters and lengths of each generation/order. According to the mathematical 1-D formulation (Section 2.2.3) other information are required: wall thickness, Young's modulus and the airway size at the beginning of a normal inspiration (FRC) associated to each generation/order. All the data referred to symmetrical and asymmetrical model are shown respectively in **Table 2.3** and **Table 2.4**. The following sections describe how the data in the tables were derived; a summary about how all the data were derived is shown in **Figure 2.8**.

2.2.6.1 Wall thickness determination

Most of the morphometric models of human bronchial tree have focused so far on the bronchial lengths and internal diameter mainly obtained from direct measurements on cast. Due the methods used, it was not possible to provide information about bronchial wall thickness (Montaudon et al., 2007).

- ***Symmetrical model*:** the wall thickness associated to the Weibel's generations, used for the rest of this thesis, refers to the work of Montaudon et al. (2007). The authors provided in vivo wall thickness and lumen area values, assessed by multidetector computer tomography images in ten healthy subjects at full inspiration. The wall thickness values (h) for the Weibel's central airways are shown in **Table 2.3**.
- ***Asymmetrical model:*** the airways wall thickness for the asymmetrical model, similarly to symmetrical model, was derived from Mountadoun's measurements. Since the measurements are referred to Weibel's generations, the transformation matrix proposed by Wiggs et al. (1990) (which associates Weibel's generation to Horsfield's orders) is used in this thesis to derive the wall thickness for the asymmetrical model starting from the values referred to Weibel's generations (**Table 2.4**).

2.2.6.2 Airways Young Modulus determination

According to Habib et al. (1994) the airway walls can be simply assumed to be composed by two main kinds of tissue: cartilage and soft tissue. As described in Section 1.3, the largest content of cartilage in the airway walls is in trachea and decreases with increasing the airway generation (or decreasing airway order). Cartilage almost disappears in airway with diameters < 2mm. Sarma et al. (2003) showed that, due to different microstructural orientations of the muscle tissue fibres (the main component of soft tissue), smooth muscle exhibits anisotropic properties and consequently the elastic moduli appear different according to the directions. In this work both tissues (cartilage and soft tissue) are assumed to be linearly elastic, neglecting anisotropic and viscoelastic properties. The rule of mixtures, applied also for biological tissues by Rapoff et al. (1999), has been applied in this thesis to determine a total Young modulus (E) associated to the wall of each airway:

$$E = E_{cartilage} * \varphi + E_{softtissue} * (1 - \varphi) \tag{2.52}$$

Where φ is the content of cartilage in each airway and $E_{cartilage}$ and $E_{softtissue}$ are respectively the Young's modulus for cartilage and soft tissue. The two values for Young modulus considered are: $E_{cartilage}$=4.37 MPa taken from Lambert et al. (1991) and $E_{soft\ tissue}$=58kPa from Habib et al. (1994). Different approaches were used to estimate the cartilage content in the two models:

- ***Symmetrical model:*** in the symmetrical model, used in this thesis, the estimation of the cartilage content along the airways generation is based on the data provided by Wiggs et al. (1990). Wiggs and colleagues measured the proportion of muscle (PMC=1-φ) in the airway wall circumference respectively of trachea, main bronchi and lobar bronchi. The other airways were assumed to have PMC=1. **Table 2.3** shows the values for φ and the corresponding Young's modulus (E), calculated using Eq. (2.52).

- ***Asymmetrical model:*** the cartilage content associated to each order of the Horsfield's model in this thesis refers to Wiggs et al. (1990) for trachea, main bronchi and lobar bronchi same as for the symmetrical model. The cartilage content for the other orders has been determined using a quadratic expression relating φ to the airway diameter for each order (n). The expression was derived by Habib et al.(1994) from the data provided by Gunst and Stropp (1988):

$$\varphi(n) = -0.09D^2(n) + 0.25D(n) - 0.024 \quad (2.53)$$

Where D is the Horsfield's diameter according to **Figure 1.9**. **Table 2.4** shows the values for φ and the corresponding Young's modulus (E), calculated respectively using Eq.(2.53) and then Eq. (2.52).

2.2.6.3 Airway size at functional residual capacity

As suggested by Habib et al. (1994) and Wiggs et al. (1990) the Horsfield and Weibel's measurements were made in lungs inflated and subsequently fixed nearly at total lung capacity (TLC). Different scaling factors were introduced to derive the size of airways at functional residual capacity (FRC) from the Horsfield and Weibel's morphological measurements.

- ***Symmetrical model:*** the measurements of Weibel shown in **Figure 1.7** were made at approximately 75% of total lung capacity (TLC). Wiggs et al. (1990) derived a correction of the Weibel's diameters to estimate what could have been the diameters at FRC, using the equations developed by Lambert et al. (1982) to correlate pressure and area in airways:

$$F = 1 - (1 - \xi)(1 - P / P_0)^{-N} \quad (2.54)$$

Where F is the area intended as fraction of the TLC area, P_0 is the pressure at which Weibel's measurement were made (~8cmH_2O for 75%TLC), P is the pressure at which the geometry is desired (P ~5 cmH_2O for FRC), ξ and N are constants determined by Lambert et al. (1982) for each generation. The pressure at TLC is assumed to be 30 cmH_2O. Using Equation (2.54) a volume corrected diameter at FRC (D_{FRC}) was calculated by Wiggs from Weibel's diameters ($D_{75\%TLC}$) as:

$$D_{FRC} = La * D_{75\%TLC} \quad (2.55)$$

Where *La* is the Lambert's pressure –area correction derived for each generation. Airway lengths are assumed to be constant independently from the lung volumes.

In **Table 2.3**, the initial cross sectional area (A_0) has been calculated from Eq. (2.55) as $A_0 = \pi \frac{(D_{FRC})^2}{4}$.

- ***Asymmetrical model:*** in order to derive the airway lengths at FRC from Horsfield's measurements (supposed at TLC), Habib et al. (1994) used a single scaling factor $L_{FRC} = L_{fac} * L_{TLC}$ (the subscripts refer to the lung volumes) that scales all airway

lengths by the same relative amount. The mean value of L_{fac} (derived by fitting their model with the measured sub glottal impedance in nine humans) was found to be 1.07 ± 0.11 therefore not statistically different from the unity. According to this, the lengths of airway branches were not found to vary significantly with lung volume in airway orders as well as generations, as discussed in the previous paragraph. To account for the lung volume influence on airway diameter, Habib et al. used a sigmoidal curve, function of the Horsfield's diameter (D_{TLC}), to describe an order-dependent diameter scaling function D*fac*:

$$Dfac = \frac{a}{1 = [D_{TLC}(n)/d_p]^{-b}} \tag{2.56}$$

Where a and b are non dimensional constants and were found to be respectively 1.51± 0.28 and 0.422 ± 0.161, by fitting experimental data. d_p =0.2 cm is a constant representing the airway diameter at the transition between central and peripheral airways Habib et al. (1994). In order to obtain the diameter of airways at FRC (D_{FRC}) from the Horsfield's diameters (D_{TLC}) the following relation was considered

$$D_{FRC} = Dfac * D_{TLC} \tag{2.57}$$

In **Table 2.4,** the initial cross sectional area has been calculated as $A_0 = \pi \frac{(D_{FRC})^2}{4}$, with D_{FRC} determined using Eq. (2.57).

z	n	$A_0(m^2)$	φ	E (MPa)	h(m)	l(m)
0	1	$2.50\cdot10^{-4}$	0.67	2.950	$1.40\cdot10^{-3}$	$1.20\cdot10^{-1}$
1	2	$1.15\cdot10^{-4}$	0.67	2.950	$1.30\cdot10^{-3}$	$4.76\cdot10^{-2}$
2	4	$5.09\cdot10^{-5}$	0.33	1.482	$1.30\cdot10^{-3}$	$1.90\cdot10^{-2}$
3	8	$2.27\cdot10^{-5}$	0	0.058	$1.30\cdot10^{-3}$	$7.60\cdot10^{-3}$
4	16	$1.39\cdot10^{-5}$	0	0.058	$1.20\cdot10^{-3}$	$1.27\cdot10^{-2}$
5	32	$8.55\cdot10^{-6}$	0	0.058	$1.00\cdot10^{-3}$	$1.07\cdot10^{-2}$
6	64	$6.16\cdot10^{-6}$	0	0.058	$1.00\cdot10^{-3}$	$9.00\cdot10^{-3}$
7	128	$4.15\cdot10^{-6}$	0	0.058	$9.00\cdot10^{-3}$	$7.60\cdot10^{-3}$

Table 2.3 Symmetrical model: number of segments (n), length (l), initial cross sectional area (A_0) (Section 2.2.6.3), wall thickness (h) (Section 2.2.6.1), cartilage content (φ) and Young's modulus (E) (Section 2.2.6.2) according to the first eight Weibel's generations (z).

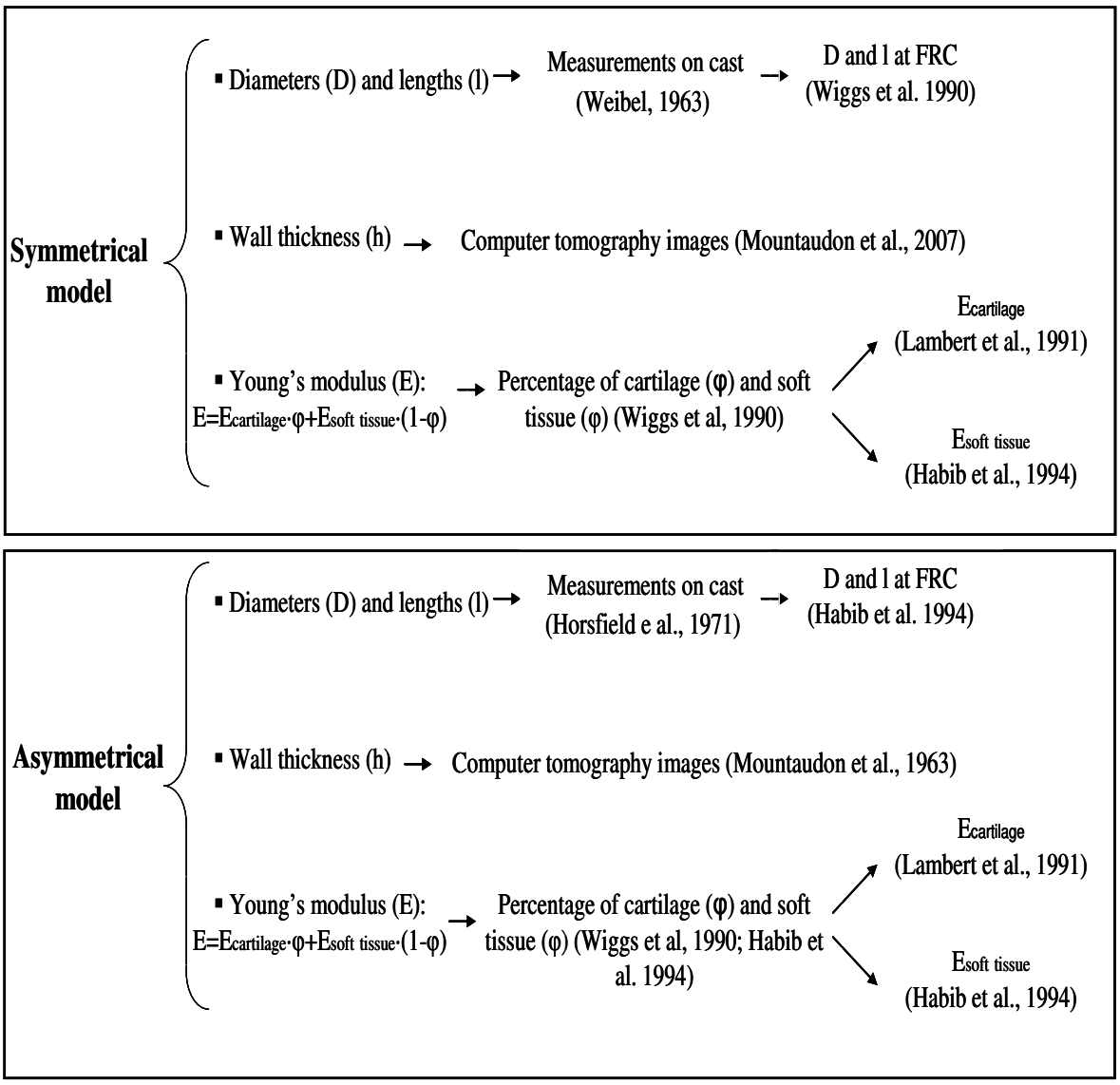

Figure 2.8 Morphological and elastic properties of human airways. The diagrams indicate for both models of central airways (Symmetrical and Asymmetrical) the references for diameters, lengths, wall thickness and Young's modulus used in this thesis.

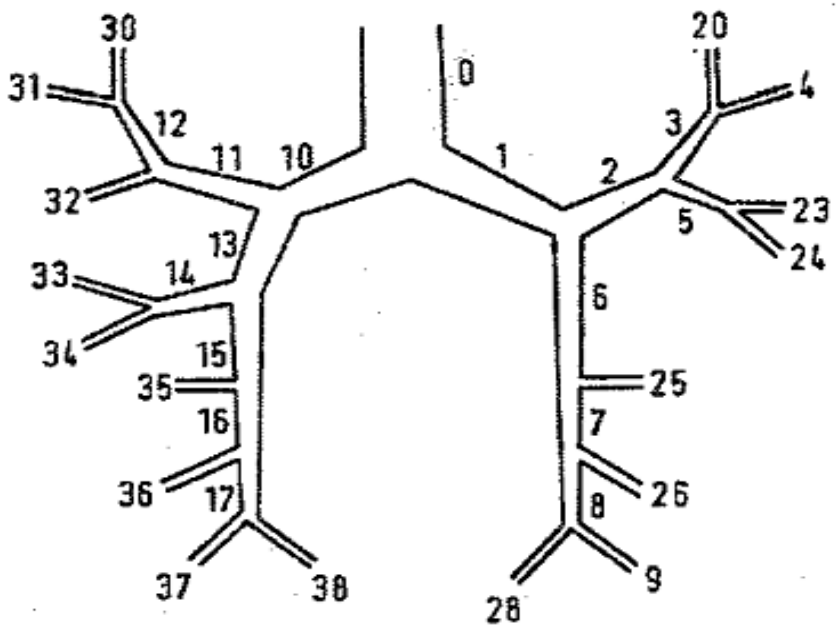

Figure 2.9 Asymmetrical model of human central airways (Reproduced from Horsfield et al., 1971).

Table 2.4 Asymmetrical model: branch number, orders, initial cross sectional area A_0 (Section 2.2.6.3), length (l), cartilage content (φ) and Young's modulus (E) (Section 2.2.6.2) , wall thickness (h) (Section 2.2.6.1), length (l) and number of end branches (T) supplied by each of the branch whose number is defined according to **Figure 2.9**.

branch number	order	$A_0(m^2)$	φ	E(MPa)	h(mm)	l(m)	(T)
0	31	$2.29\cdot10^{-4}$	0.67	2.95	1.4	$1.0\cdot10^{-1}$	216544
1	28	$1.19\cdot10^{-4}$	0.67	2.95	1.3	$5.0\cdot10^{-2}$	98432
2	27	$4.07\cdot10^{-5}$	0.33	1.48	1.3	$1.6\cdot10^{-2}$	44416
3	26	$3.83\cdot10^{-5}$	0.11	0.54	1.3	$1.0\cdot10^{-3}$	30592
4	25	$1.59\cdot10^{-5}$	0.08	0.40	1.2	$9.0\cdot10^{-3}$	13760
5	24	$1.98\cdot10^{-5}$	0.09	0.43	1.1	$1.1\cdot10^{-2}$	13824
6	27	$4.73\cdot10^{-5}$	0.33	1.48	1.3	$1.1\cdot10^{-2}$	54016
7	26	$2.93\cdot10^{-5}$	0.10	0.49	1.3	$1.8\cdot10^{-2}$	43840
8	25	$3.47\cdot10^{-5}$	0.11	0.52	1.2	$4.5\cdot10^{-3}$	27008
9	24	$1.98\cdot10^{-5}$	0.09	0.43	1.1	$7.5\cdot10^{-2}$	16832
10	30	$1.00\cdot10^{-5}$	0.67	2.95	1.3	$2.2\cdot10^{-2}$	118112
11	26	$3.83\cdot10^{-5}$	0.33	1.48	1.3	$1.6\cdot10^{-2}$	47008
12	25	$5.43\cdot10^{-5}$	0.12	0.59	1.2	$6.4\cdot10^{-3}$	23776
13	29	$6.04\cdot10^{-5}$	0.33	1.48	1.3	$2.6\cdot10^{-2}$	71104
14	25	$1.74\cdot10^{-5}$	0.08	0.41	1.2	$2.1\cdot10^{-2}$	20800
15	28	$2.82\cdot10^{-5}$	0.10	0.49	1.3	$8.0\cdot10^{-3}$	50304
16	27	$2.43\cdot10^{-5}$	0.09	0.46	1.3	$8.4\cdot10^{-3}$	35392
17	26	$2.62\cdot10^{-5}$	0.10	0.47	1.3	$1.5\cdot10^{-2}$	27520
20	24	$1.82\cdot10^{-5}$	0.08	0.42	1.1	$1.3\cdot10^{-2}$	16832
23	23	$6.85\cdot10^{-6}$	0.05	0.28	1.0	$1.1\cdot10^{-2}$	7872
24	22	$6.85\cdot10^{-6}$	0.05	0.28	1.1	$7.5\cdot10^{-3}$	5952
25	20	$1.98\cdot10^{-5}$	0.09	0.43	1	$8.5\cdot10^{-3}$	10176
26	24	$1.59\cdot10^{-5}$	0.08	0.40	1.1	$1.1\cdot10^{-2}$	16832
28	20	$1.59\cdot10^{-5}$	0.08	0.40	1.0	$8.5\cdot10^{-3}$	10176
30	24	$9.39\cdot10^{-6}$	0.06	0.32	1.1	$2.0\cdot10^{-3}$	16832
31	19	$9.39\cdot10^{-6}$	0.06	0.32	0.9	$1.3\cdot10^{-2}$	6944
32	25	$1.98\cdot10^{-5}$	0.09	0.43	1.2	$1.7\cdot10^{-2}$	23232
33	24	$9.39\cdot10^{-6}$	0.06	0.32	1.1	$1.0\cdot10^{-2}$	10400
34	24	$1.18\cdot10^{-5}$	0.07	0.35	1.1	$9.6\cdot10^{-3}$	10400
35	21	$1.18\cdot10^{-5}$	0.07	0.35	1.0	$6.2\cdot10^{-3}$	14912
36	23	$5.54\cdot10^{-6}$	0.05	0.26	1.0	$6.2\cdot10^{-3}$	7872
37	25	1.44E-05	0.08	0.38	1.2	$6.8\cdot10^{-3}$	13760
38	25	2.25E-05	0.09	0.45	1.2	$1.1\cdot10^{-2}$	13760

2.3 Wave intensity analysis

The analytical technique of Wave intensity analysis (WIA) is based on Riemann's method of characteristics. It was first introduced by Parker and Jones (1990) and applied to arteries. It is a time domain technique in which velocity and pressure waveforms are considered as successive wavefronts. Wave intensity (dI, in W/m^2) is defined as:

$$dI = dPdU \tag{2.58}$$

Where *dP* and *dU* are respectively the differentials of pressure and velocity measured simultaneously at the same site. The magnitude of *dI*, defined in (2.58), depends upon the sampling time; higher sampling rate cause lower amplitude waves and vice versa. In order to introduce a definition of wave intensity that does not depend on the sampling frequency, an alternative definition has been introduced (Ramsey and Sugawara, 1997):

$$dI' = \frac{dP}{dt} \cdot \frac{dU}{dt} \tag{2.59}$$

The units for *dI'* are W/m^2s^2. Researchers still use the *dI* formulation because of the physical meaning of the units, W/m^2, in fact is the flux of energy per unit area that is carried by the wave during its propagation.

Waves	dP	dU	dI	Flow direction
Compression	>0	>0	>0	FORWARD
Expansion	<0	<0	>0	
Compression	>0	<0	<0	BACKWARD
Expansion	<0	>0	<0	

Table 2.5 Wave classification: waves can be classified in four groups since compression and expansion waves can propagate in forward or backward direction with different effects on differential pressure (dP) and velocity (dU) and consequently on dI (Equation 2.58)

Waves can be classified in four groups since compression and expansion waves can propagate in forward or backward direction. As shown in **Table 2.5**, compression waves induce a pressure increase while expansion waves generate a pressure decrease in both forward and backward direction (Feng et al., 2007).

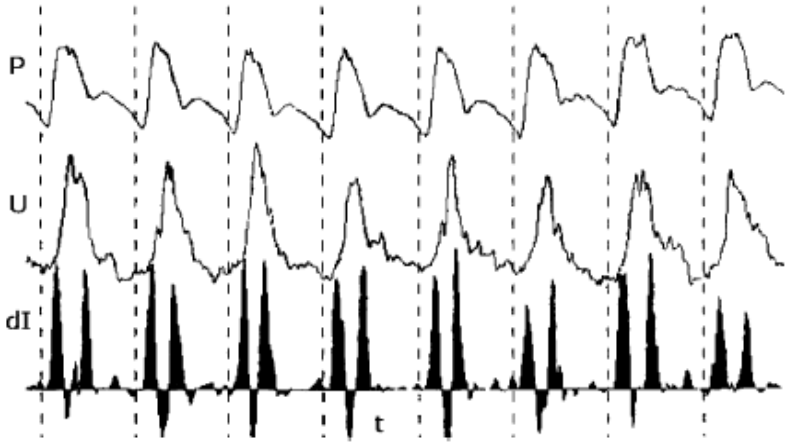

Figure 2.10 First measurement of wave intensity in the human ascending aorta (Reproduced from Parker, 2009): instaneous pressure (P) and velocity (U) (top two curves) and net wave intensity (dI) (bottom curve).

The velocity increases with compression forward waves and backward expansion waves; on the contrary, expansion forward and compression backward waves cause a decrease in velocity (**Table 2.5**). According to these considerations, the product *dI* of the pressure (*dP*) and velocity (*dU*) derivatives is positive for forward and negative for backward waves. The net wave intensity indicates therefore clearly if forward or backward waves are dominant at any given time. **Figure 2.10** shows the first example of WIA applied to human ascending aorta.

2.3.1 Wave separation

The net wave intensity does not require the knowledge of the wave speed, it can be simply calculated from the simultaneous measurements of pressure and velocity. The knowledge of wave speed is fundamental to separate the measured waveforms in their forward and backward component. Assuming that forward and backward waves add linearly when wave intersect, and defining with $dP_{\pm}$ and $dU_{\pm}$ respectively the changes in pressure and velocity in forward (+) and backward (-) directions, yields

$$dP = dP_+ + dP_- \tag{2.60}$$

$$dU = dU_+ + dU_- \tag{2.61}$$

Considering the Waterhammer equations for the forward and backward waves, the following relation can be derived

$$dP_\pm = \frac{1}{2}(dP \pm \rho c dU) \tag{2.62}$$

$$dU_\pm = \frac{1}{2}(dU \pm \frac{dP}{\rho c}) \tag{2.63}$$

Integrating (2.62) and (2.63) give the pressure and velocity in the forward (+) and backward (-) direction.

$$P_+ = P_0 + \sum_0^t dP_+ \qquad P_- = \sum_0^t dP_- \tag{2.64}$$

$$U_+ = U_0 + \sum_0^t dU_+ \qquad U_- = U_0 + \sum_0^t dU_- \tag{2.65}$$

Where t is the time and P_0 and U_0 are pressure and velocity at t = 0. Assuming that the forward and backward wave intensities are additive

$$dI = dI_+ + dI_- = dP_+ dU_+ + dP_- dU_- \tag{2.66}$$

the separated wave intensities can be derived

$$dI_\pm = dP_\pm dU_\pm = \pm \frac{1}{4\rho c}(dP + \rho c dU)^2 \tag{2.67}$$

2.4 Experimental setup

2.4.1 Introduction and general description

This section introduces the general features of the experimental setup with the description of the components, calibration and reproducibility. The experimental results will be presented in Chapter 3. The setup was mainly built to validate experimentally the 1-D modelling, described in Section 2.2, in simulating the propagation of air pulses in flexible tubes in both pressure and velocity waveforms. Moreover the setup was used for the comparisons of the computational wave speeds (Equation 2.25) with experimental wave speeds, determined using the foot to foot method (Section 1.8.1.2). The applicability of the Wave intensity and the principles of the wave separation (Section 2.3) to airflow will be also investigated and presented in Chapter 3 using the setup described in this chapter. A general schematic of the experimental setup is shown in **Figure 2.11**. Details about the specific setups will be separately described in Chapter 3 according to the specific experiments. The locations of the measurements in **Figure 2.11** are identified by 1 and 2. Pressure (P_1) and velocity (U) measurements are in the same site 1 (required by wave intensity analysis). Both measurement sites are at a certain distance from the inlet and outlets to reduce the effects of turbulence on the measurements. The two pressure transducers are inserted from the inlet (P_1) and from the outlet (P_2) through an Y-Junction and advanced inside the tubes till the desired position 1 and 2. The air pulse is generated by controlling the opening time of a solenoid valve connected to an air compressor. The distance between the two transducers (d) is used to calculate the wave speed according to the foot to foot method (Section 1.8.1.2). The velocity probe is inserted inside the tube through a T connector (**Figure 2.17**) which connects two parts of the same tube (flexible tube 1 and 2 in **Figure 2.11**). Flexible tubes were chosen approximately in the range of diameters, wall thicknesses and Young's modulus defined in **Table 2.3** and **Table 2.4**. According to **Figure 2.11**, four main components can be identified in the setup:

- Flexible tubes
- Pressure measuring equipment
- Velocity measuring equipment
- System for air pulse generation

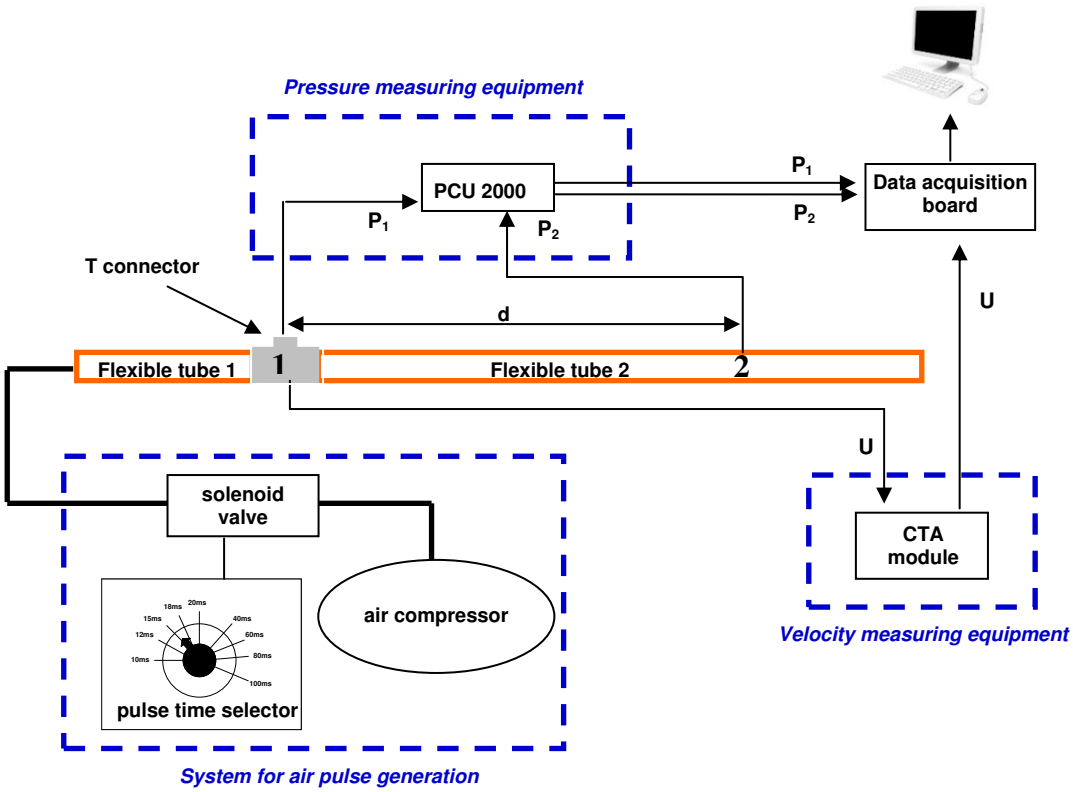

Figure 2.11 Schematic of the experimental setup used for the air wave propagation experiments in elastic tubes. Four main components can be identified in the setup: flexible tubes, pressure measuring equipment, Velocity measuring equipment, system for air pulse generation

2.4.2 Flexible tubes

Four different flexible tubes were considered during the experiments: latex tube (LXT), rubber tube (RT) and two silicon tubes defined respectively silicon 1 (ST1) and silicon 2 (ST2). **Table 2.6** shows the geometrical and mechanical properties of the tubes under consideration.

	D(mm)	h(mm)	E(MPa)	ρ_w(Kg/m^3)	Typology
LXT	32.1±0.7	0.33±0.02	0.68	1239	*collapsible*
RT	21.0±0.6	1.58±0.20	1.35	894	*non-collapsible*
ST1	17.3±0.1	2.59±0.06	1.76	1798	*non- collapsible*
ST2	29.7±0.4	1.63±0.11	1.81	1253	*non- collapsible*

Table 2.6 Geometrical and mechanical properties of the flexible tubes used for the experiments: diameter (D), wall thickness (h), Young's modulus (E) and density (ρ_w).

The tubes are assumed to be uniform along the whole length. Values of Young's modulus were measured through a tensile testing by considering, for each tube, the modulus in the range 0-10% of deformation (**Figure 2.12**). The tube densities (ρ_w) were calculated from the volume and weight of the specimens, diameter and wall thickness were measured through a digital caliper. All the considered tubes are flexible but not collapsible except from the latex tube (**Table 2.6**).

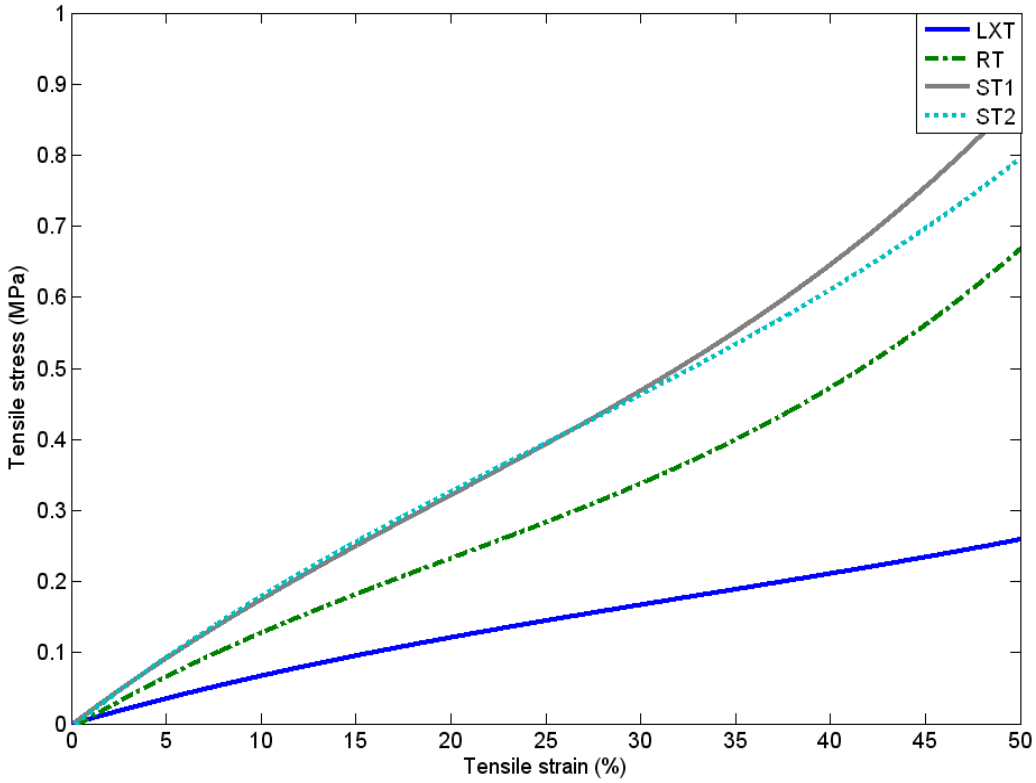

Figure 2.12 Stress–strain curve for latex (LXT), rubber (RT) and the two silicon tubes (ST1, ST2) considered during the experiments.

2.4.3 Pressure-measuring equipment

The pressure was measured with transducers-tipped sensors catheters. Different catheters were used during the experiments: 5F single sensor catheters (Gaeltec, Isle of Skye, UK) and 5F dual sensor catheter (model SPC-760 and SVPC-664D with PCU 2000 pressure control unit, Millar Instrument Inc, USA). As specified by the manufacturer of the Millar transducer, the frequency response of the dual sensor catheters is DC to 1000Hz (-3dB), minimum. The frequency response for the Gaeltec transducer is not clearly specified by the manufacturer. This kind of transducers are

usually applied and optimized for applications involving blood; since it is known that the dynamic response depends strongly on the transmission line under consideration (Clark, 1985), it is necessary, for the application of this thesis, to test the transducers response in a system filled with air. Therefore, before starting the pressure measurements in the experiments with the setup shown in **Figure 2.11**, a simple experiment was carried out to estimate the resonance frequency (f^*) of the considered pressure transducers in air. According to Clark (1985) if the risetime for a pressure step, applied to a transducer, is less than $1/f^*$, it is generally possible to excite resonance. The experiment to test f^* is shown in **Figure 2.13**. Free oscillations were induced by a balloon burst at one end of a glass tube with the testing transducers inside. The assumption is that the risetime of the pressure step caused by the balloon burst is much faster than $1/f^*$. **Figure 2.14** shows the resulting pressure waveforms for both pressure catheters.

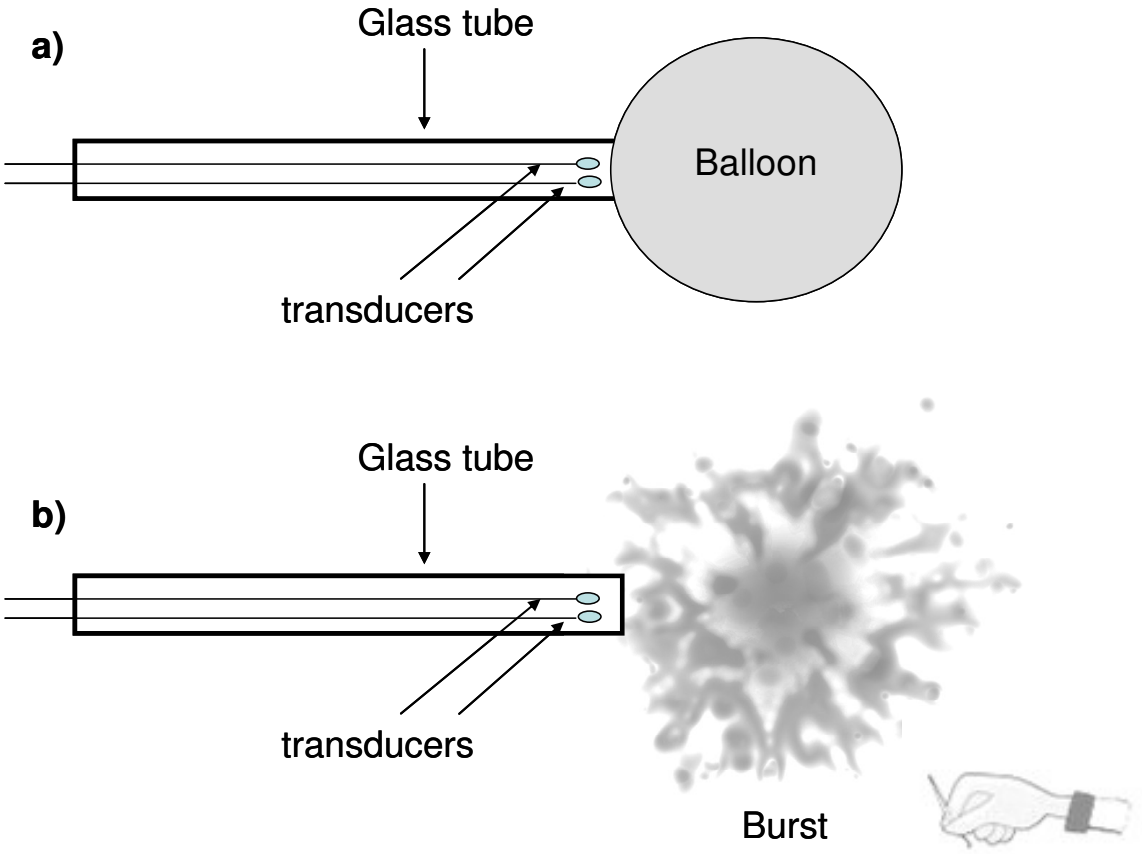

Figure 2.13 Experiment to test the resonance frequency of the pressure transducers in air: the pressure catheters (Millar and Gaeltec) are inserted in a rigid tube. a) A balloon is placed at one extreme of the rigid tube. b) The burst of the balloon generates a fast step in pressure that is used to excites the resonance of the transducer.

The experiment allows a comparison of the two transducers in terms of frequency response. According to the pressure waveform of the Gaeltec transducer, in **Figure 2.14**, the risetime (t_G) is 2.68 ms. The shape of the signal suggests that it is critically damped, therefore, it appears difficult to estimate a corresponding resonant frequency. However f^* will not be less than 1/(2·2.68 ms)=190Hz.

The rise time (t_M) of Millar catheter, in **Figure 2.14**, is about 0.85 ms (f= 1/(2·0.85ms)=588Hz) which is consistent with the frequency of the oscillations shown towards the end of the record of about $1/\lambda^*_M$=550 Hz. This experiment has provided an estimate of the frequency response of the transducers in air; the Gaeltec transducer appear to have a lower f* and a more dumped response compared to the Millar.

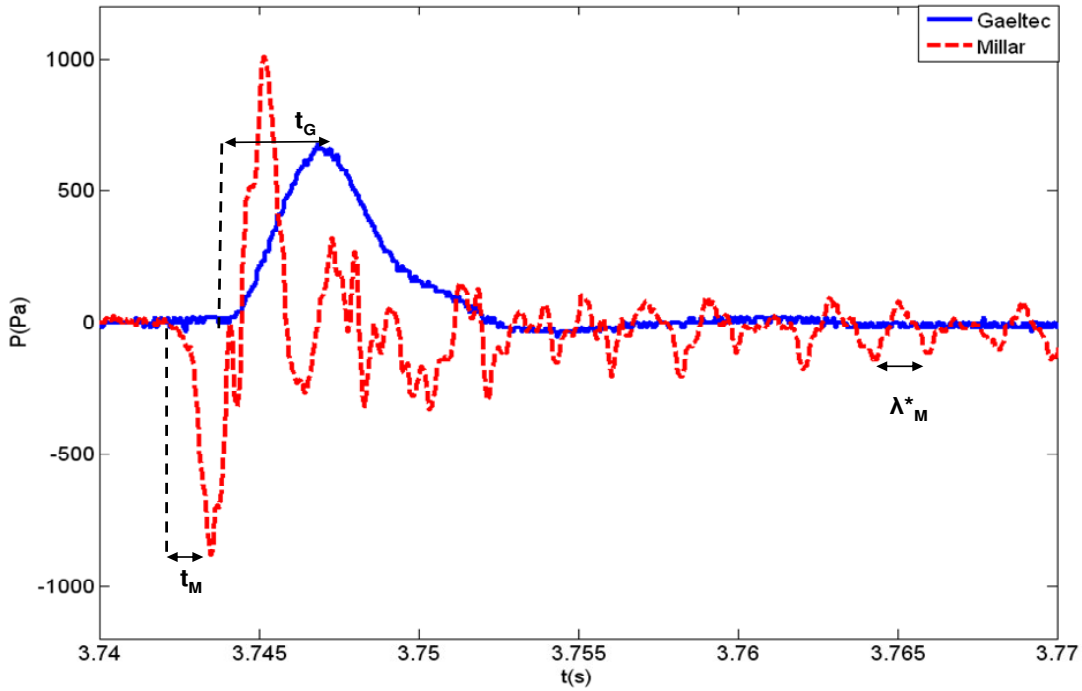

Figure 2.14 Pressure waveforms recorded during the experiment of balloon explosion (sampling rate=20KHz) to estimate the resonance frequency (f^*) of pressure transducer in air. Δt_1=0.85ms is the rising time, Δt_2=1.75ms is the oscillation period. t_M and t_G are the risetime respectively of Millar and Gaeltec transducer, λ^*_M is the period of oscillations in Millar transducer.

2.4.3.1 Pressure calibration

The calibrations of pressure transducer, repeated before each experiment, were performed using the method of column of water. This method consists in advancing the pressure sensor inside the water column from 0 up to a height of 50 cm in steps of 10

cm and recording the voltage in correspondence of each step. The voltages (V) and pressures (P) in correspondence of each pressure step were plotted and the regression line was obtained. An example of calibration curve for a pressure catheter is shown in **Figure 2.15**, the linearity of pressure- voltage function is clearly identified.

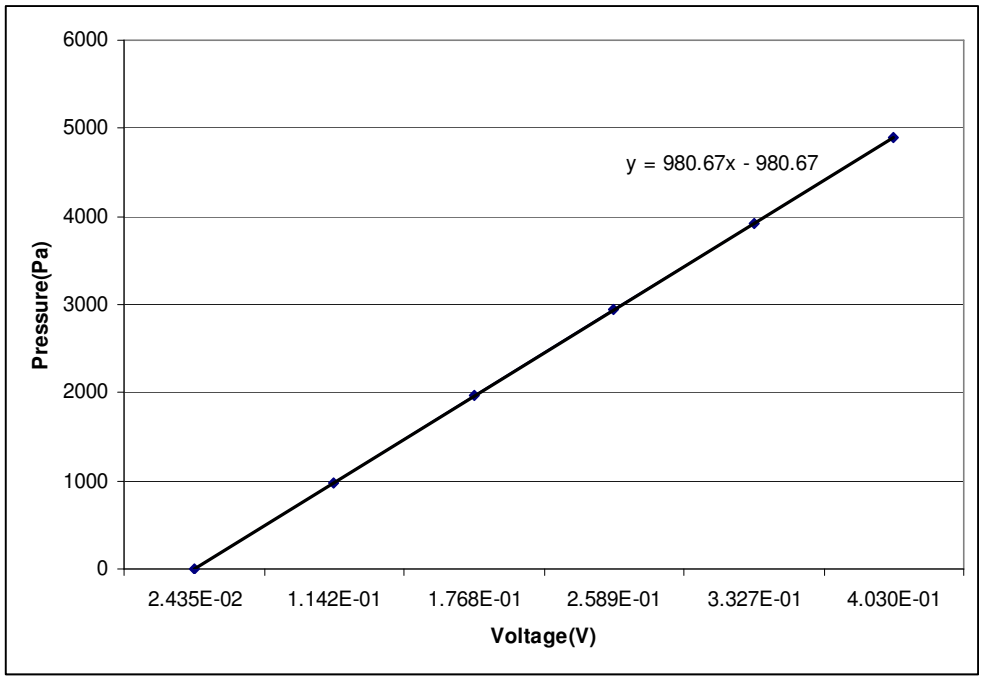

Figure 2.15 Pressure calibration for the Millar tip sensor: example of regression line used to convert voltages (V) in pressures (Pa).

2.4.4 Velocity-measuring equipment

The hot wire/film anemometry has been selected for measuring the velocity in the experiments of this thesis. This kind of anemometry is the most spread method for measuring instantaneous velocity; two working modalities are available: constant current (CC) mode and constant temperature mode (CT). The CT mode is the one used in this thesis. In 1914, King investigated the possibility of measuring the velocity, at a selected point in the flow, through a heated wire immersed in a fluid flow. The King's law (King, 1914) can be expressed as:

$$E^2 = A + BU^n \tag{2.68}$$

where U is the fluid velocity normal to the wire, E is the voltage across the wire and *A*, *B* and *n* are constants determined through the calibration process. The principle of a CT circuit is shown in **Figure 2.16**: the sensor resistance (R_w) is included in a Wheatstone bridge. As the flow conditions vary, if the flow is increased for example, the drop in the R_w, due to the cooling effect of the increased heat transfer, will change the error voltage

(e_1-e_2). The two voltages (e_1 and e_2) are the input of the operational amplifier (G) whose output voltage (E) will be increased to increase the current (i) through the sensor. The variation of the current is inversely proportional to the change of R_w in order to restore the balanced condition of the Wheatstone resistances. The output voltage (E) can be used therefore as indicator of the fluid velocity (Bruun, 1995).

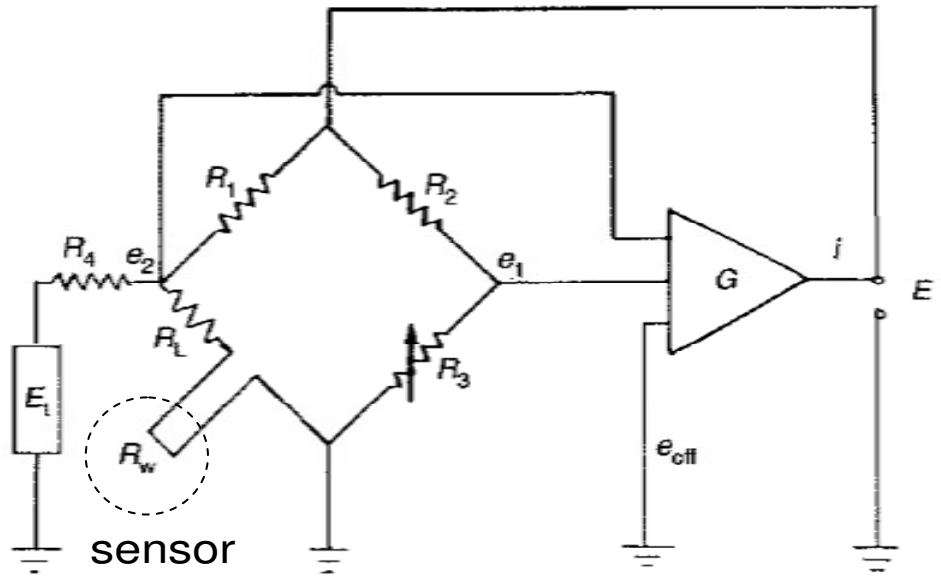

Figure 2.16 Constant temperature anemometer: the sensor is inserted in Wheatstone bridge. Measuring the output voltage of a feedback amplifier (E) it is possible to quantify the change in resistance R_W and consequently the fluid velocity (Bruun, 1995).

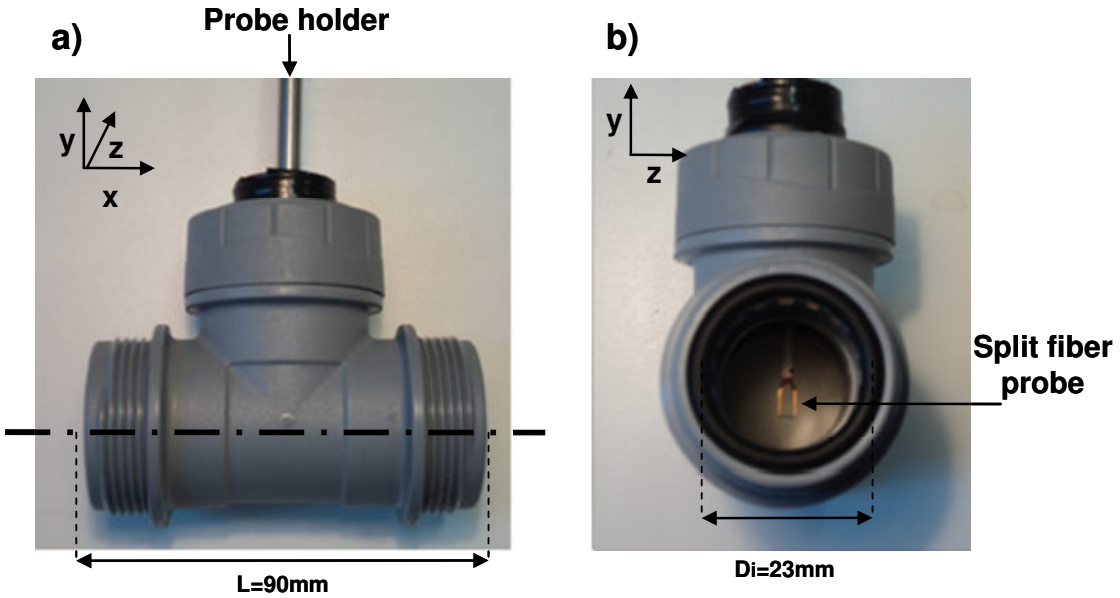

Figure 2.17 Picture of T connector for the access of the split fiber probe. a) lateral view. The x axis (dashed line) indicates the axis and the positive direction of the flow (forward direction). b) frontal view, particular of the probe measuring site. L and Di are respectively the length and the internal diameter of the T connector.

2.4.4.1 Split fiber probe

It is important for the velocity measurements during wave propagation experiments and subsequent wave intensity analysis that the velocity probe is sensitive to bidirectional flow. The probe used in the experiments is a Split-fiber straight probe (model 55R55; Dantec Dynamics, Denmark). The probe datasheet is shown in Appendix A. Split fiber probes are dual sensors probes which can be used for measuring one-dimensional bidirectional flow (Dantec website). The dual sensors split fiber probe consists of two parallel thin nickel films deposited on the same quartz fiber. Since there are two independent sensors, the value and the angle of the velocity can be both measured (Helle, 1993). **Figure 2.17b** shows the site at which the velocity probe is adjusted inside the T- connector.

2.4.4.2 Velocity measurement

The measurement of the absolute value of velocity, in split fiber probes, is based on a modification of Equation (2.68) (Helle, 1993)

$$E_1^2 + E_2^2 = A + B \cdot U^n \tag{2.69}$$

Where E_1 and E_2 are the voltages from the two sensors. A, B and n are constant determined with the calibration process (Section 2.4.4.4.2). According to Eq. (2.69) the square sum of the two voltages depends only on the velocity value and is independent from the flow direction.

2.4.4.3 Flow direction

In order to detect the forward flow fraction, different authors have suggested to place the split -fiber probe with the plane of splits perpendicular to the direction of the mean flow (Bruun, 1995; Kiya and Sasaki, 1983; Ra et al., 1990). The direction of the flow can be determined by comparing the voltages of the two sensors: E_1-E_2. Since the output from one anemometer is generally greater then the other accordingly to the flow direction, when the two signals are compared with each other, the flow direction can be easily detected (Ra et al., 1990). In this thesis the voltage comparison for each sampling time was made using a program written in Matlab (The MathWorks Inc., MA, USA). Considering the voltage difference at no flow, $(E1\text{-}E2)_{no\ flow}$=-0.284 V in Table 2.8, the program provides two coefficient (either 1 or -1) that are multiplied for the absolute velocity value U in Equation 2.69: respectively if E_1-E_2>$(E_1\text{-}E_2)_{no\ flow}$, the program gives

+1 and it is associated to the forward direction while if E_1-E_2<$(E_1$-$E_2)_{no\ flow}$ the program provides -1 as output which is associated to the backward direction.

2.4.4.4 Air velocity system calibration

The split fiber probe and the related probe support are connected through a BNC cable to a the BNC socket of 56C17 CTA bridge unit (**Figure 2.18**). The unit can be used either as a resistance measuring device, with the configuration shown in Appendix B or as a constant temperature anemometer (Appendix C). Internal switchers (**Figure 2.18a**) allow to set the length of the BNC cable (CABLE LENGTH) connected to the probe support, the gain (GAIN), the filtering (FILTER) and the sensor (SHAPE: flat, film or wire). Before starting a measurement through a constant temperature anemometer (CTA) system two steps need to be followed:

- Resistance measuring and balancing
- Calibration

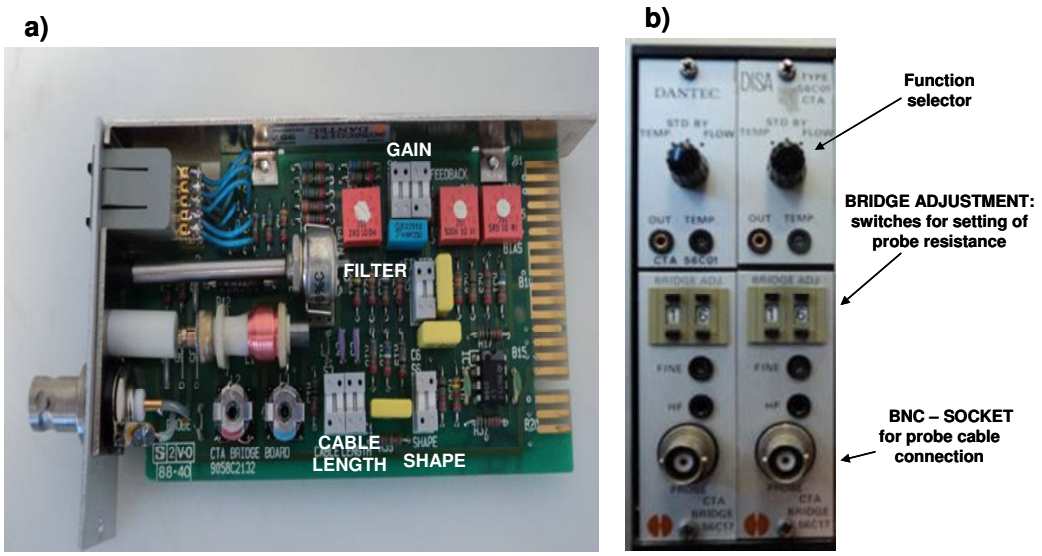

Figure 2.18 Constant temperature anemometer 56C17 unit a) lateral view , b) frontal view of two channels .

2.4.4.4.1 Resistance measuring and balancing

In all the devices for constant temperature anemometry it is necessary to balance the bridge of **Figure 2.16** with a specific setting of resistances, before starting any measurements and calibration. Firstly the initial electric resistance of the probe at ambient temperature is determined (*resistance measuring configuration)* and then, from this value, the heated resistance, in the *flow measuring configuration,* is derived. In the

resistance measuring configuration the probe is part of the circuit shown in Appendix B. This configuration allows the measurements of the total resistance (R_{tot}) and cable resistance at ambient temperature (Dantec, Instruction manual). The measured R_{tot} is the sum of three components

$$R_{tot} = R_0 + R_L + R_C \tag{2.70}$$

where R_0 is the probe resistance at ambient temperature, R_L is the probe lead resistance (R_L=0.5 according to the manufacturer) and R_C is the cable resistance, which is known. R_0 can be therefore determined from Eq. (2.70) as

$$R_0 = R_{tot} - (R_L + R_C) \tag{2.71}$$

The measured resistance values for the two sensors of the split fiber probe are shown in **Table 2.7**.

Sensor	R_0	R_L	R_C	$R_{tot(hot)}$
1	7.22	0.5	0.42	11.75
2	7.34	0.5	0.5	12.01

Table 2.7 Measured values (in Ohms) of probe resistance (R_0), cable resistance (R_C) and probe lead resistance (R_L) for the two sensors of the split fiber probe. $R_{tot(hot)}$ is determined through (2.73).

Once the *flow measuring configuration* (Appendix C) is activated the sensor resistance is heated. The overheating ratio (a) is defined as

$$a = \frac{R - R_0}{R_0} \tag{2.72}$$

Where R is the sensor heated resistance. The overheating ratio refers to the sensor sensitivity, a=0.5 for the split probe (according to manufacturer). Therefore the total heated resistance ($R_{tot(hot)}$) can be calculated as

$$R_{tot(hot)} = (1+a)R_0 + R_c + R_L \tag{2.73}$$

After determining the $R_{tot(hot)}$ using Eq. (2.73), the bridge of resistances can be balanced. Values for $R_{tot(hot)}$ are shown in **Table 2.7**.

2.4.4.4.2 Velocity calibration

In the configuration of *flow measuring configuration* (Appendix C) the probe gives an output voltage proportional to the airflow. The hot wire calibration system is shown in

Figure 2.19. It allows accurate probe calibrations in a wide range of velocities (from 0.02m/s to 300 m/s). The system in **Figure 2.19** generates air jets with known velocities that can be used as velocity references during calibrations to determine the constants *A*, *B* and *n* in Eq. (2.69). The probe to be calibrated is fixed at the jet exit and it can be rotated for calibration of directional sensitivity. For the calibration two nozzles creates the air jets according to the velocity ranges, nozzle 1 (range 0<U<0.5m/s) and nozzle 2 (U>0.5m/s). **Table 2.8** and **Table 2.9** show the voltages from both sensors (E_1 and E_2), the voltage difference (E_1-E_2, used to determine the flow direction) and the sum of square voltages (E_1^2-E_2^2) according to different set velocities (nozzle 1, **Table 2.8** and nozzle 2, **Table 2.9**) and in the two directions (forward, backward).

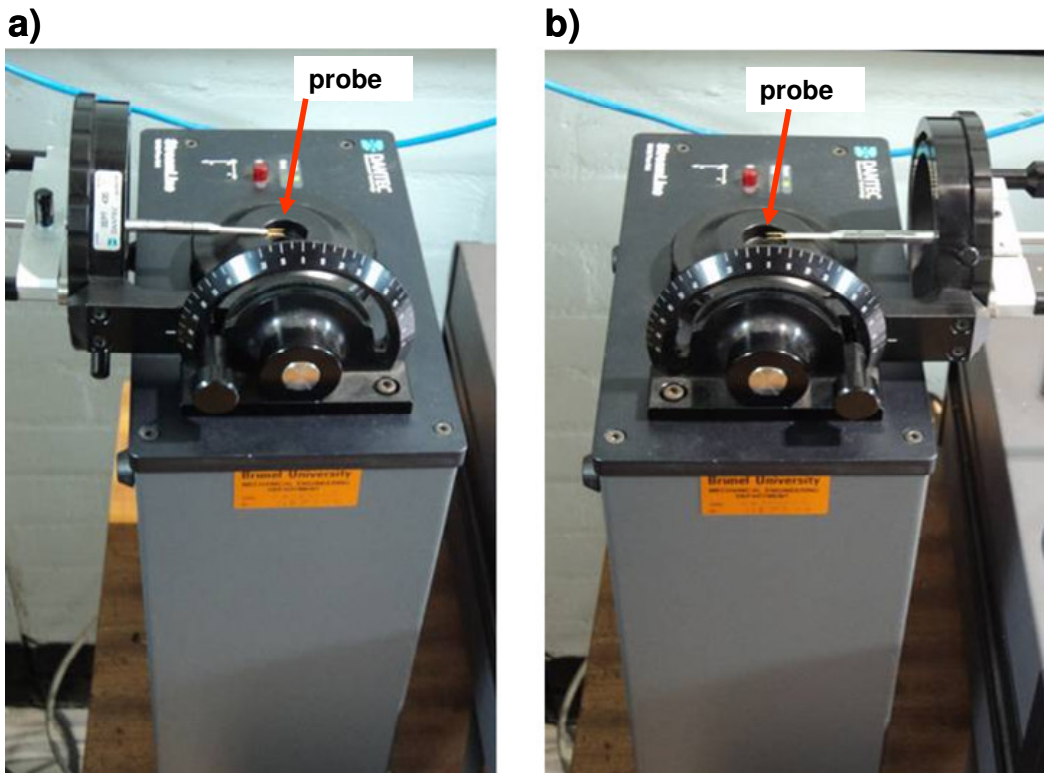

Figure 2.19 Streamline pro Automatic calibrator (Dantec Dynamics, Denmark). Two probe positions are considered during the calibration: a) -90 degree (forward direction), b) +90 degree (backward direction)

From **Table 2.8**, for nozzle 1 (velocity range 0-0.5m/s) the sum of square voltages does not change significantly with the increase of velocity, this range of velocity shows therefore an uncertainty of velocity measurement. According to the manufacturer, due

to the low velocity range for nozzle 1, the splif fiber probe insensitivity can be referred to the influence from natural convection (Dantec website).

On the contrary a significant increase of $E_1^2+E_2^2$ (in both directions) appear clear in the upper range of velocities (nozzle 2), according to velocity increases as shown in **Table 2.9**. The values shown in **Table 2.9** confirm the assumption that the sum of the square voltages does not dependent on the flow angle (Helle, 1993): $E_1^2+E_2^2$ provides very similar values in correspondence of the same U, independently from the direction of the flow.

Flow direction	Voltage operations	no flow	0.2 m/s	0.3 m/s	0.4 m/s	0.5 m/s
Forward	E_1	1.327	1.340	1.340	1.342	1.342
	E_2	1.611	1.611	1.613	1.613	1.612
	E_1-E_2	-0.284	-0.271	-0.273	-0.271	-0.270
	$E_1^2+E_2^2$	4.356	4.393	4.398	4.402	4.399
Backward	E_1	1.327	1.321	1.313	1.313	1.314
	E_2	1.611	1.624	1.623	1.629	1.629
	E_1. E_2	-0.284	-0.302	-0.310	-0.308	-0.314
	$E_1^2+E_2^2$	4.356	4.383	4.360	4.352	4.379

Table 2.8 Calibration nozzle 1: voltages from both sensors (E_1 and E_2), voltage difference (E_1-E_2) and the sum of square voltages (E_1^2-E_2^2) according to different set velocities in the lower range of velocities (0-0.5m/s) in forward/backward direction.

Flow direction	Voltage operations	0.5 m/s	0.8 m/s	1 m/s	1.5 m/s	2 m/s	2.5 m/s	3 m/s
Forward	E_1	1.678	1.796	1.859	1.984	2.079	2.160	2.222
	E_2	1.744	1.785	1.806	1.844	1.871	1.895	1.913
	E_1-E_2	-0.066	0.012	0.054	0.14	0.207	0.265	0.309
	$E_1^2+E_2^2$	5.859	6.415	6.717	7.339	7.825	8.257	8.598
Backward	E_1	1.463	1.515	1.535	1.574	1.603	1.626	1.647
	E_2	1.911	2.024	2.078	2.193	2.286	2.358	2.423
	E_1. E_2	-0.448	-0.508	-0.543	-0.618	-0.682	-0.732	-0.777
	$E_1^2+E_2^2$	5.792	6.392	6.675	7.287	7.797	8.202	8.584

Table 2.9 Calibration nozzle 2: voltages from both sensors (E_1 and E_2), voltage difference (E_1-E_2) and the sum of square voltages (E_1^2-E_2^2) according to different set velocities in the upper range of velocities (>0.5m/s) in forward/backward direction.

The $E_1^2+E_2^2$ values, shown in **Table 2.9**, were used to determine the three calibrations constant of Eq.(2.69). Following Helle (1993) the determinations of *A, B* and *n* is done by an iterating process automatically performed by a program written in Matlab (The MathWorks Inc., MA, USA). The program varies '*n*' from 0 to 1 with steps of 0.01; the constants *A* and *B* are calculated with the least-square method for each value of *n*. The optimum values for *n* (and related A and B values) is the one that provides the minimum square sum error with the measured voltage values. After the calibration procedure, Eq. (2.69) becomes

$$V_1^2 + V_2^2 = 2.6591 + 4.0407 \cdot U^{0.35} \tag{2.74}$$

2.4.4.4.3 Access of velocity probe: T connector

The access of the split-fiber probe to the internal space of the tube has to guarantee an easy and controllable access with the minimum disturbances on the flow and pressure measurements. A rigid T- connector was used (**Figure 2.17**) for this the purpose. **Figure 2.20** shows two configurations for the access of the probe according to the tube typology specified in **Table 2.6**. If the tube is collapsible, the T connector is placed between two tube segments which are sealed subsequently to the two extremes of the T-connector. In case of non collapsible tubes (with an external diameter lower than the internal diameter of T-connector) a hole has been created on the surface of the tube and the tube has been inserted and moved inside the T-connector till the hole reached the velocity probe access on the T-connector (**Figure 2.20**).

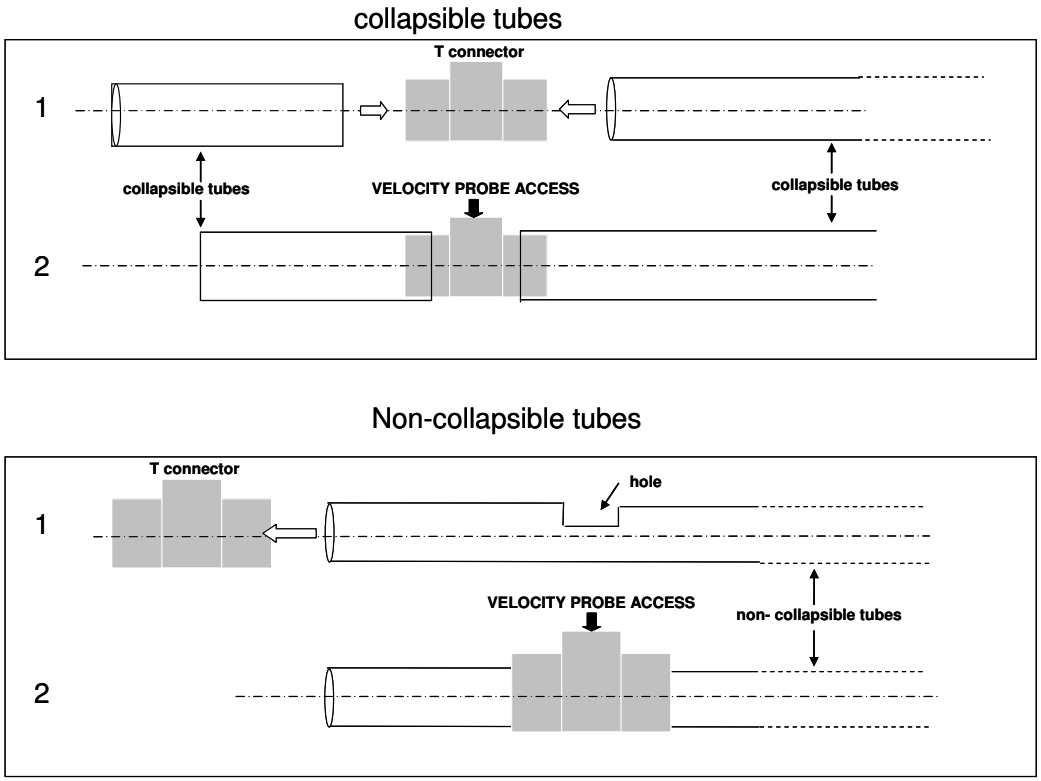

Figure 2.20 Velocity probe access for collapsible and non-collapsible tubes

2.4.5 System for pulse generation

One of the most critical points of setting up the experiments of air wave propagation regarded the possibility of generating an air pulse having a certain control on both duration and amplitude of the pulse. The aim was to reproduce a pulse that could have some physiological meaning. **Figure 2.21** shows an example of pulse used in clinical practise for impulse oscillometry system (IOS) (Smith et al., 2005) with approximately 40 ms duration and 0.3 l/s peak flow.

The solution was found using a solenoid valve connected to an air compressor: the duration of the pulse can be regulated by controlling the electric supply that drives the opening/closure time of the solenoid valve while the flow amplitude can be controlled, in first instance, by the pressure in the air compressor. Three components are included in the generation of the pulse:

- air compressor
- solenoid valve
- Selector of pulse duration

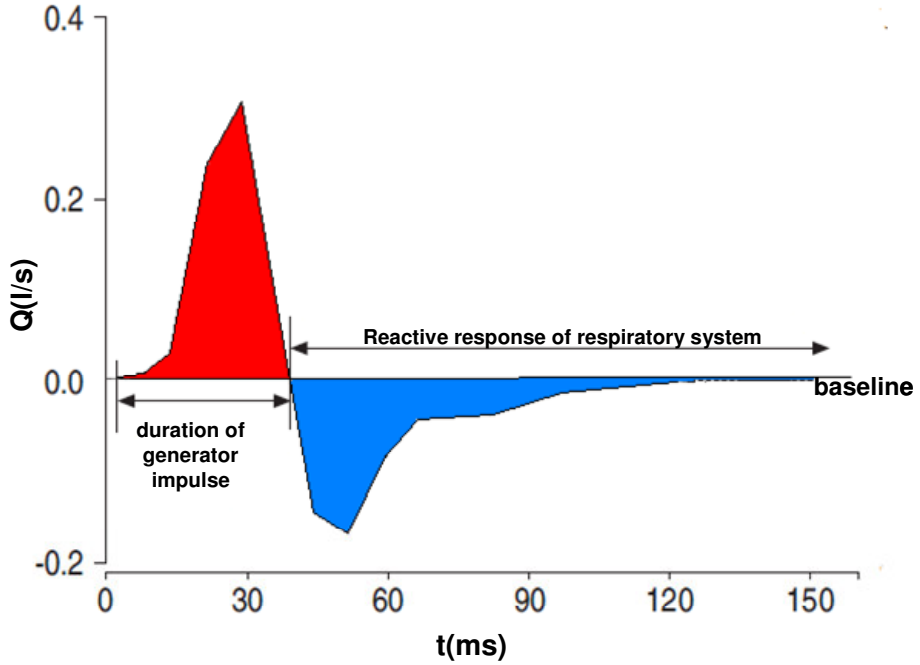

Figure 2.21 Example of flow pulse used in impulse oscillation system (IOS): (red) incident pulse $t \approx 40ms$, $Q_{peak} \approx 0.3l/s$, (blue) reactive response of respiratory system. Modified from (Smith et al., 2005).

2.4.5.1 Air compressor

The air compressor (model 4-4, JUN-AIR, Denmark) was always set to a pressure of 5 bar in all the experiments. This pressure inside the compressor was found, in the first instance, to generate pulses in a reasonable range of pressure and flows.

2.4.5.2 Solenoid valve

The solenoid valve used in this thesis is MHE3 FESTO solenoid valve (FESTO, Germany). It is a fast- switching valve, the technical specifications are shown in **Table 2.10.**

Voltage	Pressure range	Temp. range	Nominal flow rate	Nominal diameter	Switching time on/off
24V	-0.9…+8bar	-5…+60°C	200 l/min	3 mm	8 / 4.5 ms

Table 2.10 MHE3 Festo solenoid valve: technical specifications

Figure 2.22 shows the two configurations of the solenoid valve according to the voltage supplied. The valve is characterized by one input (input 1) connected to the air compressor, and two outputs (output 2 and 3). When no voltage is applied to the valve (**Figure 2.22a**), the air compressor is connected to output 2 (that is kept always blocked

with a plug). In **Figure 2.22b**, 24 Volts are provided by the power supply to the solenoid valve: input 1 switches to output 3 which is connected to the flexible tube of the setup. It is therefore possible to generate the pulse whose duration will depend on the duration of 24V signal provided by the power supply. In order to inject the air pulse into the flexible tube, the output 3 of solenoid valve is connected to the inlet of the flexible tube using the same Y-junction used for the pressure transducer (Section 2.4.1).

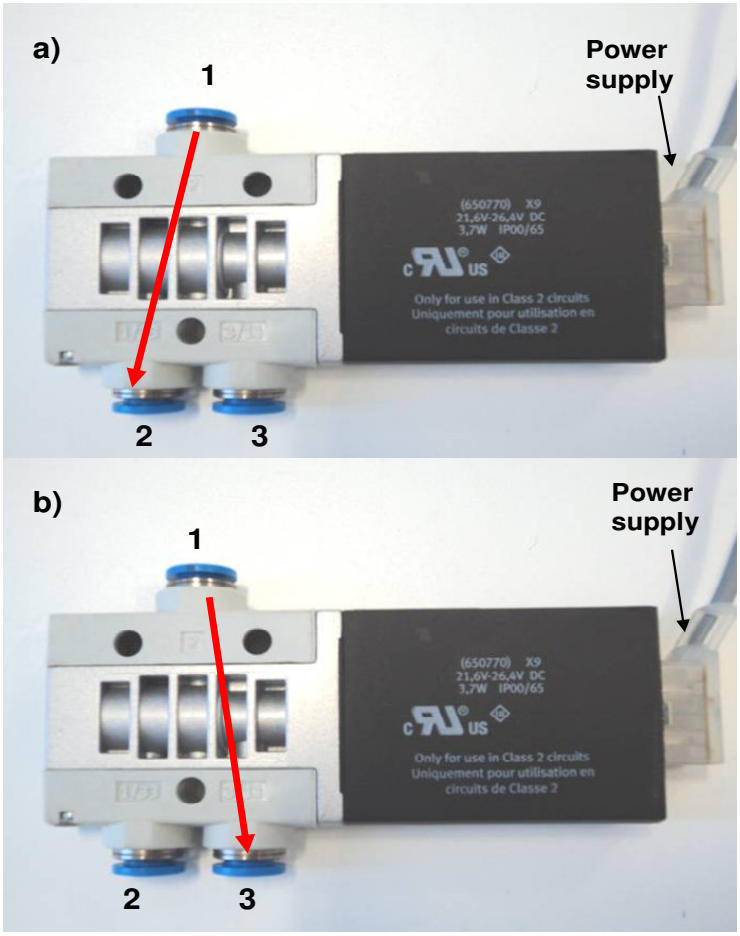

Figure 2.22 MHE3 FESTO solenoid valve, switch of the outputs: input 1 is connected to the air compressor, 2 is the blocked output, 3 is the output connected to the flexible tube of the setup. a) setting the power supply to 0V, input 1 is connected to output 2 b) setting the power supply is to 24V, input 1 is connected to output 3.

2.4.5.3 Selector of pulse duration

A picture of the device, designed to control the duration of the air pulse is shown in **Figure 2.23**. The power supply (24Volts) for the solenoid valve is activated by pressing the 'push button' that works as trigger for the 555 timer (see Appendix D). The pressing

of the push button generates a single electric signal of 24 Volts for a duration defined by the 'knob' indicator. As shown in **Figure 2.23** the following durations for the can be selected: 10-12-15-18-20-40-60-80-100-110 ms.

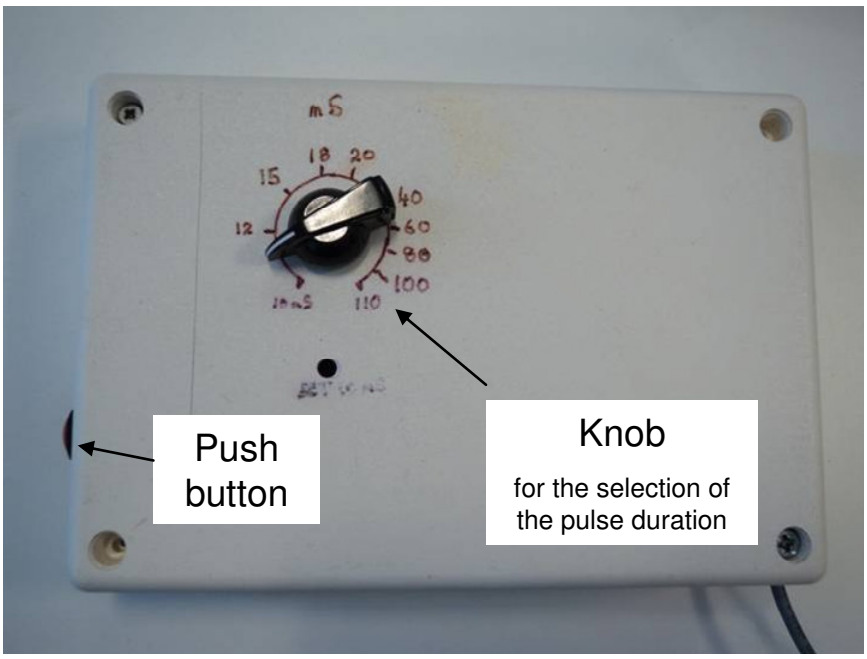

Figure 2.23 shows the selector of pulse duration, the device designed to generate the air pulse

2.4.6 Reproducibility

In order to assure that the pressure and velocity measurements are reproducible, three repetitions were conducted for each experiment. **Figure 2.24** shows, as an example, three pressure and velocity measurements (in site 1 of **Figure 2.11**) in the latex experiment that will be discussed with more details in the next chapter. The results appear reproducible for pressure as well as for velocity

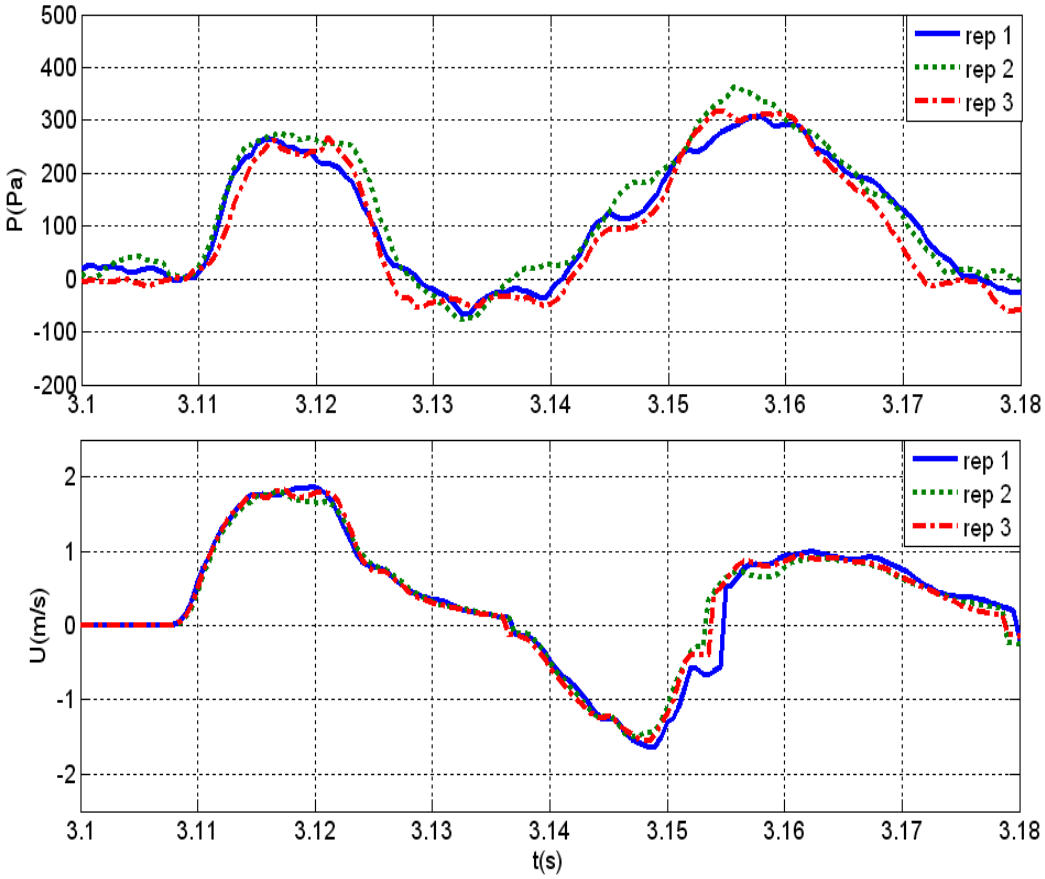

Figure 2.24 Comparison of three pressure (P) and velocity (U) measurements at site 1 of Figure 2.11. A pulse of 15ms has been enforced at the inlet of the latex tube (LXT).

.2.5 General discussions

In this chapter a detailed description of the mathematical 1-D modelling and the principles of Wave intensity analysis (WIA) have been presented. The model together with WIA, extensively applied to arteries, are for the first time applied, with this thesis, to air pulses propagating in flexible tubes and airways. The model will be validated in Chapter 3 with experiments of air wave propagation in flexible tubes. The experimental setup used for the validation has been also described in this chapter.

Chapter 3

Experimental results: propagation of air waves in flexible tubes

3.1 Introduction

The aim of this chapter is the validation of the 1-D formulation introduced in Section 2.2 (previously applied only to arteries) against well defined experimental models in which air pulses propagate in flexible tubes. Wave Intensity analysis, described in Section 2.3, will be used to classify the waves. A detailed description of the experimental setup, used during the experiments, was presented in Section 2.4.

Two experiments are considered, in this chapter, using the flexible tubes described in Section 2.4.2: 1) A single latex tube (*Latex experiment*) and 2) A series of three tubes (*Multivessel experiment*): two silicon tubes (ST1 and ST2 in **Table 2.6**) and the rubber Tube (RT). In **Figure 2.11** the general experimental setup was shown, schematics for each experiment showing the specific configuration of the elastic tubes with their lengths and locations of transducer will be provided in **Figure 3.2** and **Figure 3.9**. Two configurations are considered for the *Multivessel experiment*: open end with terminal reflection coefficient (R_t=-1) and closed end (R_t=1). The open end condition is simply achieved leaving the terminal end of the flexible tube open to the atmosphere; the closed end condition is obtained by blocking the terminal end with a stopper. Only the closed en condition is presented for the *Latex experiment* in inflated configuration since the open end condition implies many difficulties in keeping the circular cross section for the whole length of the tube, required by the 1-D formulation (Section 2.2.1).

3.2 Inlet boundary condition

In all the experiments the selector of pulse duration (Section 2.4.5) was always set to short pulses (10 or 15ms) to ensure that the arrival of reflected waves occurs after the end of the incident wave. Using these short pulses the waves, at least the first reflected waves, can be identified and classified.

In order to validate the 1-D formulation in space and time variables (Section 2.2) two computational 1-D models were designed with the same mechanical properties and geometries of the *Latex experiment* and *Multivessel experiment*. Since the setup is not connected to the air compressor when no power supply is provided to the solenoid valve (**Figure 2.22**), after the generation of the pulse the inlet is assumed to be a total reflective boundary with reflection coefficient R_f=1 (Section 2.2.4). The inlet boundary

condition for the computational models is an acceleration pulse defined by the following Gaussian expression (in m/s):

$$U(t) = A \cdot e^{-B \cdot (t-C)^2} \tag{3.1}$$

Where A, B and C are parameters that control respectively the height of the curve peak, the width of the 'bell' and the position of the peak on the *t* axis, as shown in **Figure 3.1**. The parameters in the Gaussian expression (3.1) were chosen, for each experiment, to match both duration and amplitude of the measured incident velocity pulse.

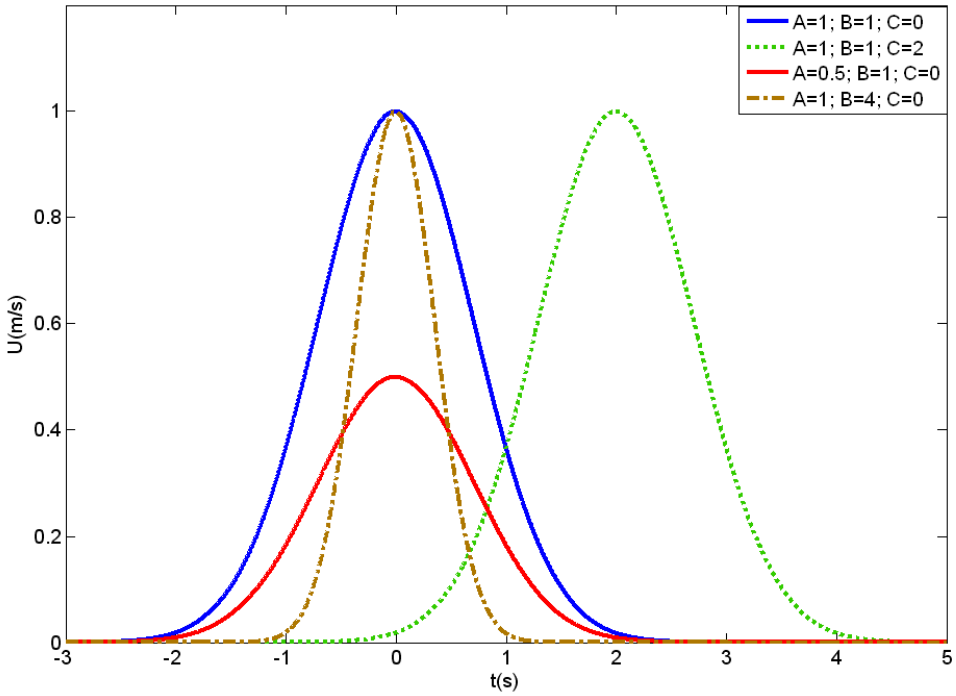

Figure 3.1 Example of different Gaussians according to change of A, B , C parameters in Eq. 3.1. The parameter *A* controls the height of the curve peak, *B* controls the width of the 'bell' while *C* defines the position of the peak on the *t* axis.

3.3 Wave paths and arrival time

This section explains a way of monitoring the waves propagating in elastic tubes. After giving the names to nodes in a system, each wave will have a history which is given by the sequence of nodes that has produced it. We define this sequence as wave path. For example in **Figure 3.9** considering X_1 as the measurement point, the wave path IX_1 denotes the incident wave that after entering the tube through I, has reached point X_1 propagating forward. In the same manner the wave path IX_1AX_1 denotes a wave that

after entering the tube, through I, propagates forward till the point A, where it is reflected, and then it moves backward to X_1. IX_1AX_1 is the notation for the wave that, after entering the tube, moves forward till point A where it is reflected backward to the inlet I and then from the inlet is again reflected forward to X_1.

By considering that a certain wave has travelled along N tubes (wave path), once the wave speed and length are known for each tube, it is possible to estimate the theoretical arrival time (t) of the reflected wave at the measuring site X_1 :

$$t_{theor} = t_{foot} + \Delta t_{theor} = t_{foot} + \sum_{i=1}^{N} \frac{l_i}{c_i} \tag{3.2}$$

Where t_{foot} is the time of the pressure foot of the incident wave at the observation point; Δt_{theor} is the theoretical time delay between the t_{foot} and the onset of the considered reflected wave at the observation point. Δt_{theor} is calculated from l_i and c_i that are respectively the length and wave speed of each tube; i is the number of the segments in which the wave has travelled.

3.4 Latex experiment

Tube: Latex (LTX) (mechanical and geometrical properties shown in **Table 2.6**)
Pressure Transducer: Gaeltec
Sampling frequency: 2KHz
Configurations: inflated tube with closed end
Pulse duration: 15ms

A schematic of the setup for the *Latex experiment* with the lengths of the tube segments is shown in **Figure 3.2**. A set of four experiments were conducted to determine the wave speed (c_{foot}) in the latex tube through the foot to foot method (Section 1.8.1.2). The foot to foot method provides: $c_{foot}=L_1/\Delta t=102\pm8$ m/s, where L_1 is the distance between the pressure transducers (X_2 annd X_1) and Δt is the time required for the wave to travel from position X_1 to position X_2 (**Figure 3.2**). Once determined the c_{foot} , the theoretical arrival times at the measurement point (X_1) (**Figure 3.2**) can be calculated from Eq. 3.2 according to the wave path, as shown in **Table 3.1**.

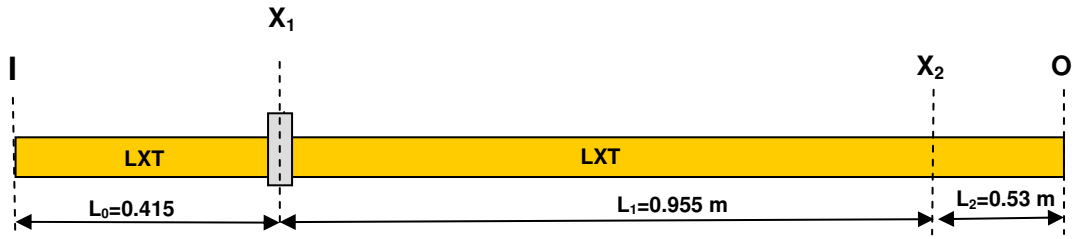

Figure 3.2 Schematic of the Latex (LXT) tube experiment. X_1 and X_2 refer to the pressure transducers location (for wave speed determination through the foot to foot method), I and O are respectively the inlet and outlet of the tube. L defines the lengths of each tube segment.

In all the figures, for this experiment, the solid arrow indicates the calculated arrival time (t=3.1366 s) for the first backward wave (wave O in **Table 3.1**) while the dashed arrow refers to the arrival time (t=3.1447s) of the forward wave, re-reflected from the inlet (wave O', in **Table 3.1**)

Wave path	**wave**	**Δt_{theor}(s)**	**t_{theor} (s)**
IX_1 incident wave	-	-	3.1075
IX_1OX_1	O	0.0291	3.1366
$IX_1OX_1I\ X_1$	O'	0.0372	3.1447

Table 3.1 Theoretical arrival time (t_{theor}) of waves at X_1 position (**Figure 3.2**) according to Eq.3.2: $t_{theor}=t_{foot\ incident\ wave}+\Delta t_{theor}$. The theoretical time delays (Δt_{theor}) of the onset of the reflected waves, starting from the foot of the incident wave (t=3.1075s), are determined according to the total lengths (L_{tot}) in which the wave has travelled (defined by the wave path) and the c_{foot}=102m/s.

3.4.1 Pressure and velocity waveforms

The experimental pressure (P_{exp}) and velocity (U_{exp}) waveforms, for the Latex experiment, are obtained using the equipments described in sections 2.4.3 and 2.4.4 with a sampling frequency $f_{sampling}$=2KHz. The subscript 'exp' is always used to indicate all the quantities that are directly derived from P_{exp} and U_{exp} while the subscript 'comput' refers to quantities derived from computational pressure (P_{comput}) and velocity (U_{comput}). The experimental signals were filtered in Matlab (Mathworks Inc., MA, USA) with the Savitzky-Golay filtering, a third polynomial order and a window size of 15 samples were selected for the filtering. The latex tube was inflated with an initial constant pressure (P_i=800Pa) before the experiment; during the data analysis P_i was

subtractet from the measured pressure to start at atmospheric pressure. The panel 'a' of **Figure 3.3** and **Figure 3.4** shows the waveforms of P_{exp} and U_{exp}. In the panel 'b' of the figures, P_{exp} and U_{exp} are separated into their forward (+) and backward (-) components using Esq.s 2.64 and 2.65 (Wave intensity analysis), c_{foot}=102 m/s is used as the wave speed for the separation.

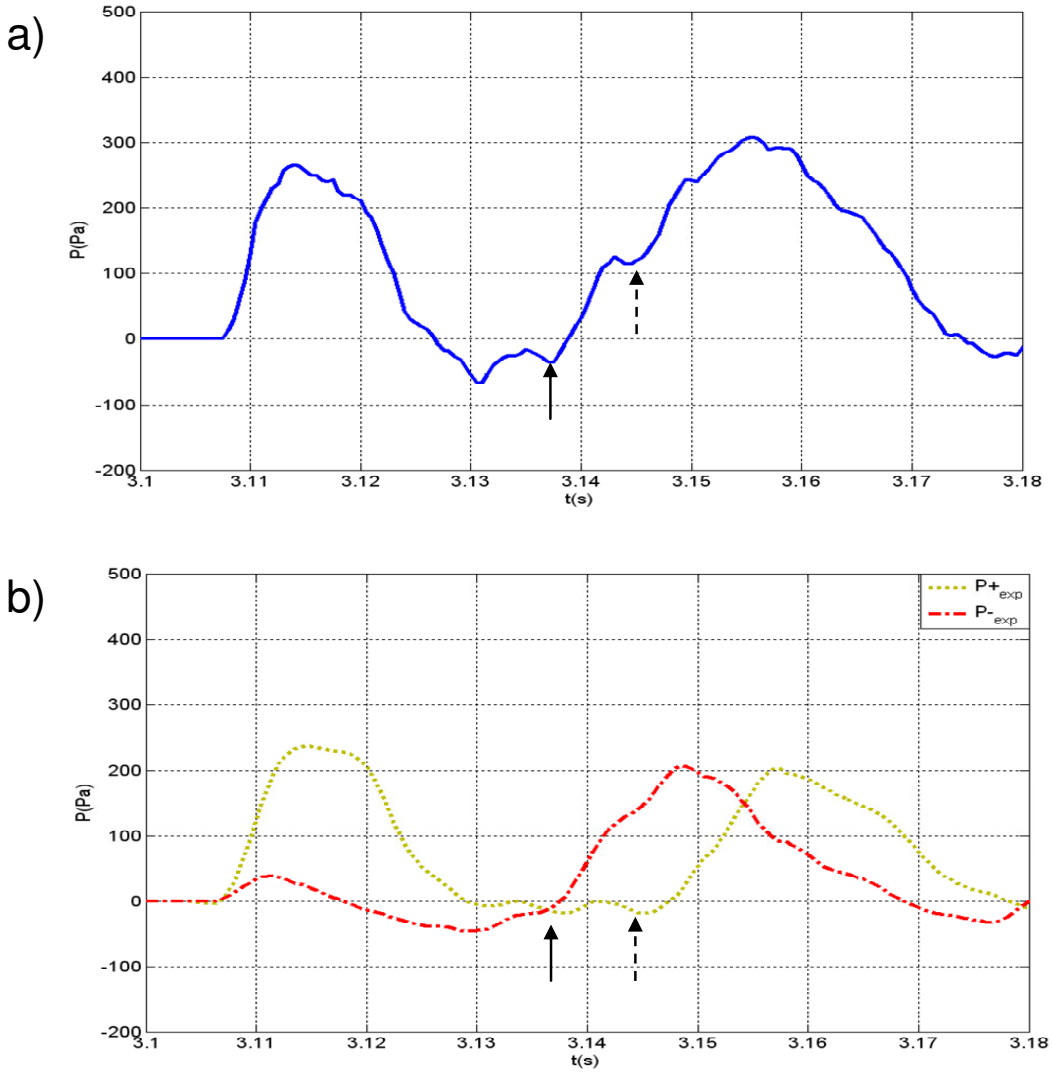

Figure 3.3 a) Experimental pressure waveforms (P_{exp}) in Latex tube measured at site X_1 in closed end configuration (R_t=1), P_{exp} is separated in b) into its forward ($P+_{exp}$) and backward ($P-_{exp}$) components using Wave intensity analysis, as described in Section 2.3.1. The solid arrow indicates the theoretical arrival time of the wave reflected backward from the tube outlet (wave O in **Table 3.1**). The dashed arrow indicates the theoretical arrival time of the wave re-reflected forward from the inlet (R_t=1) (wave O' in **Table 3.1**).

As shown in **Figure 3.3** and **Figure 3.4**, changes in the slope of pressure and velocity appear, within a certain approximation, according to the theoretical arrival times

indicated by the arrows. The backward compression wave (produced by the reflection from the closed end), whose theoretical arrival time is indicated by the solid arrow, generates an increase in pressure and a decrease in velocity. Once the same wave gets re- reflected from the inlet in the forward direction, it generates increase in pressure and increase in velocity with its arrival to the measurement site, indicated by the dashed arrow (**Figure 3.3** and **Figure 3.4**) in line with the theoretical expectation of Table 2.5.

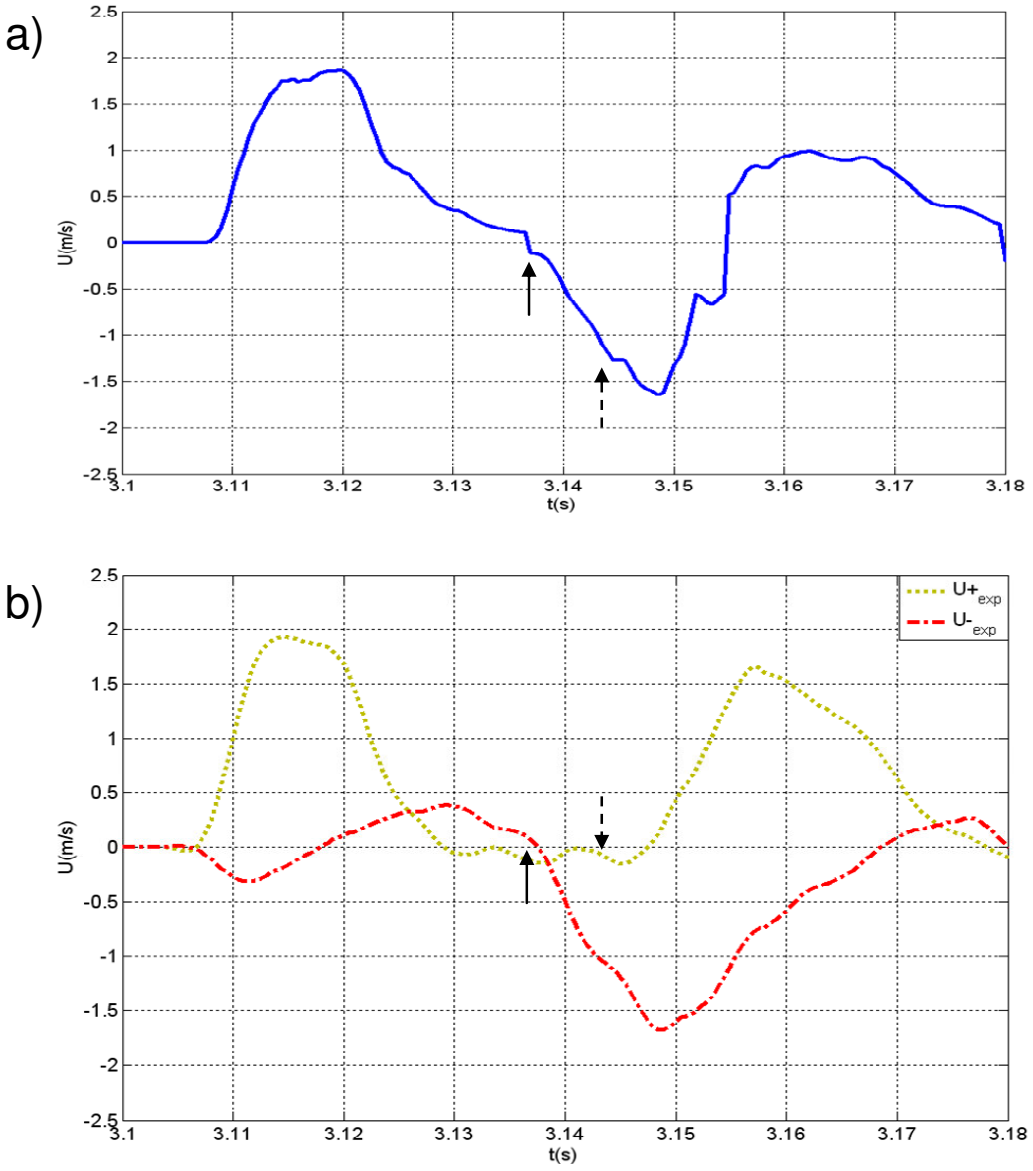

Figure 3.4 a) Experimental velocity waveforms (U_{exp}) in Latex tube measured at site X_1 in closed end configuration (R_t=1), U_{exp} is separated in b) into its forward ($U+_{exp}$) and backward ($U-_{exp}$) components using the analytical wave separation described in section 2.3.1. The solid arrow indicates the theoretical arrival time of the wave reflected backward from the tube outlet (wave O in **Table 3.1**). The dashed arrow indicates the theoretical arrival time of the wave re-reflected forward from the inlet (R_t=1) (wave O' in **Table 3.1**).

3.4.2 Wave intensity analysis

Figure 3.5 shows the wave intensity (dI_{exp}) waveforms derived from P_{exp} and U_{exp} and the decomposition into their forward ($dI+_{exp}$) and backward ($dI-_{exp}$) components according to the wave intensity analysis, described in Section 2.3.1.

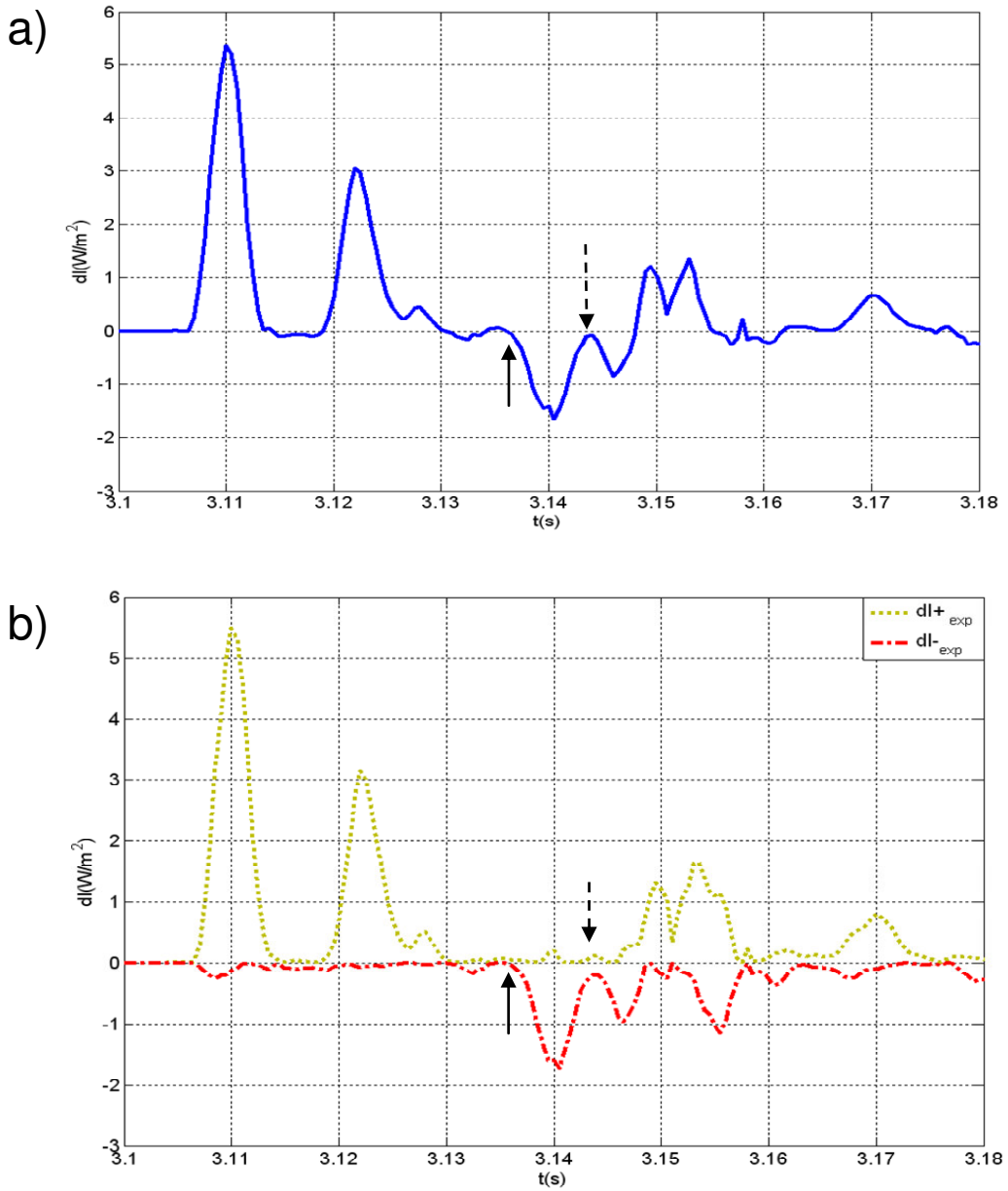

Figure 3.5 a) Wave intensity (dI_{exp}) derived from experimental pressure and velocity b) dI_{exp} is separated into its forward ($dI+_{exp}$) and backward ($dI-_{exp}$) components using the wave intensity analysis described in section 2.3.1. The solid arrow indicates the theoretical arrival time of the wave reflected backward from the tube outlet (wave O in **Table 3.1**). The dashed arrow indicates the theoretical arrival time of the wave re-reflected forward from the inlet (R_t=1) (wave O' in **Table 3.1**).

Also for the Wave intensity the theoretical arrival times indicates, within a certain approximation, changes in the slope of the dI waveforms. therefore. The solid arrow is in correspondence of the onset of a negative peak of dI_{exp} and $dI-_{exp}$ while the dashed arrow is close to a foot of $dI+_{exp}$. The experimental onset of the waves is in good agreement with the theoretical predictions.

3.4.3 Validation of the computational 1-D model

A computational 1-D model of the latex tube experiment shown in **Figure 3.2** was developed according to the 1-D formulation described in Section 2.2. In order to give more relevance to the comparison, the wave speed of the computational model was changed to match the c_{foot}=102m/s by changing β in Eq. 2.12. The cross sectional area (A) of the model refers to the internal diameter of the latex tube according to **Table 2.6**. The inflow boundary condition for the model was defined according to Eq. 3.1 which was adjusted to match the incident velocity wave (amplitude and duration) of the experiment. The alignment for computational and experimental waveforms was based on the alignment of velocity peaks of the incident wave as shown from the peaks of incident waves in **Figure 3.7a**. The T connector for the access of the velocity probe is neglected in the computational model.

A comparison between computational (P_{comp}) and experimental (P_{exp}) pressure waveforms is shown in **Figure 3.6**; separation into forward and backward components for both experimental and computational pressures are also shown. **Figure 3.7** shows the comparison (experimental / computational) for the velocity waveforms while in **Figure 3.8** forward and backward component of wave intensities (dI) from experimental data are compared with the computational dI waveforms. All the experimental waveforms show a pattern very similar, in terms of timing and amplitude, to the computational waveforms. A quantitative analysis of the phase difference between the measured and computational results is shown in **Table 3.7** (Section 3.6), the timing of the onset of the refected wave in the experiments is compared with the computational time by considering the foot of the corresponding wave in **Figure 3.8**

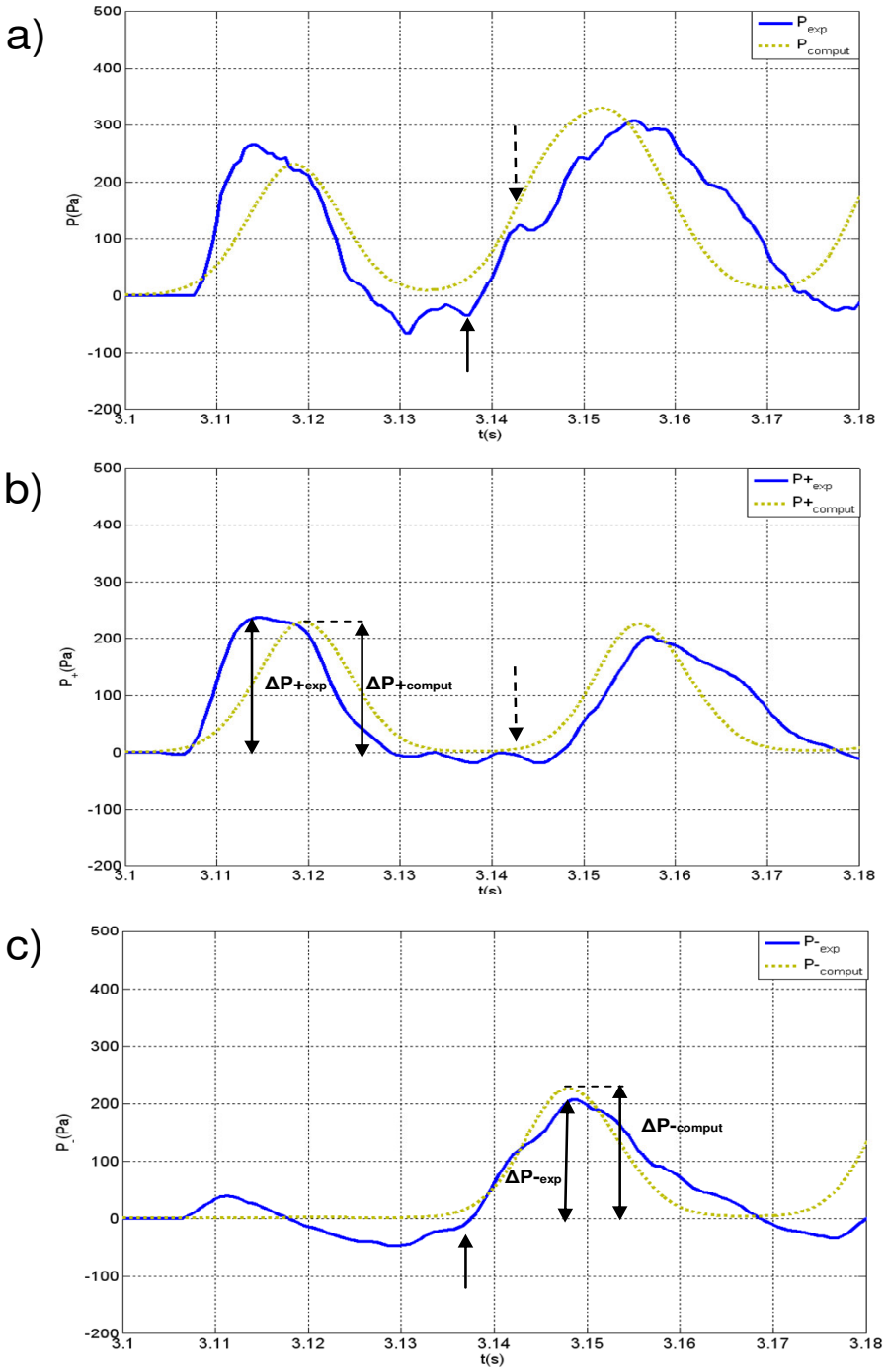

Figure 3.6 Comparison between experimental and computational (time step=10^{-7}s) pressure waveforms, the wave speed of the model was set to c_{foot}=102m/s. a) Experimental (subscript 'exp') and computational (subscript 'comput') pressure waveforms (P) are separated in b) into their forward ($P+_{exp}$ and $P+_{comput}$) and in c) into their backward ($P-_{exp}$ and $P-_{comput}$) components using the analytical wave separation described in Section 2.3.1. The double arrows indicate the amplitude of the incident wave (ΔP_+) and the first reflected wave (ΔP_-). The solid arrow indicates the theoretical arrival time of the wave reflected backward from the tube outlet (wave O in **Table 3.1**). The dashed arrow indicates the theoretical arrival time of the wave re-reflected forward from the inlet (R_t=1) (wave O' in **Table 3.1**).

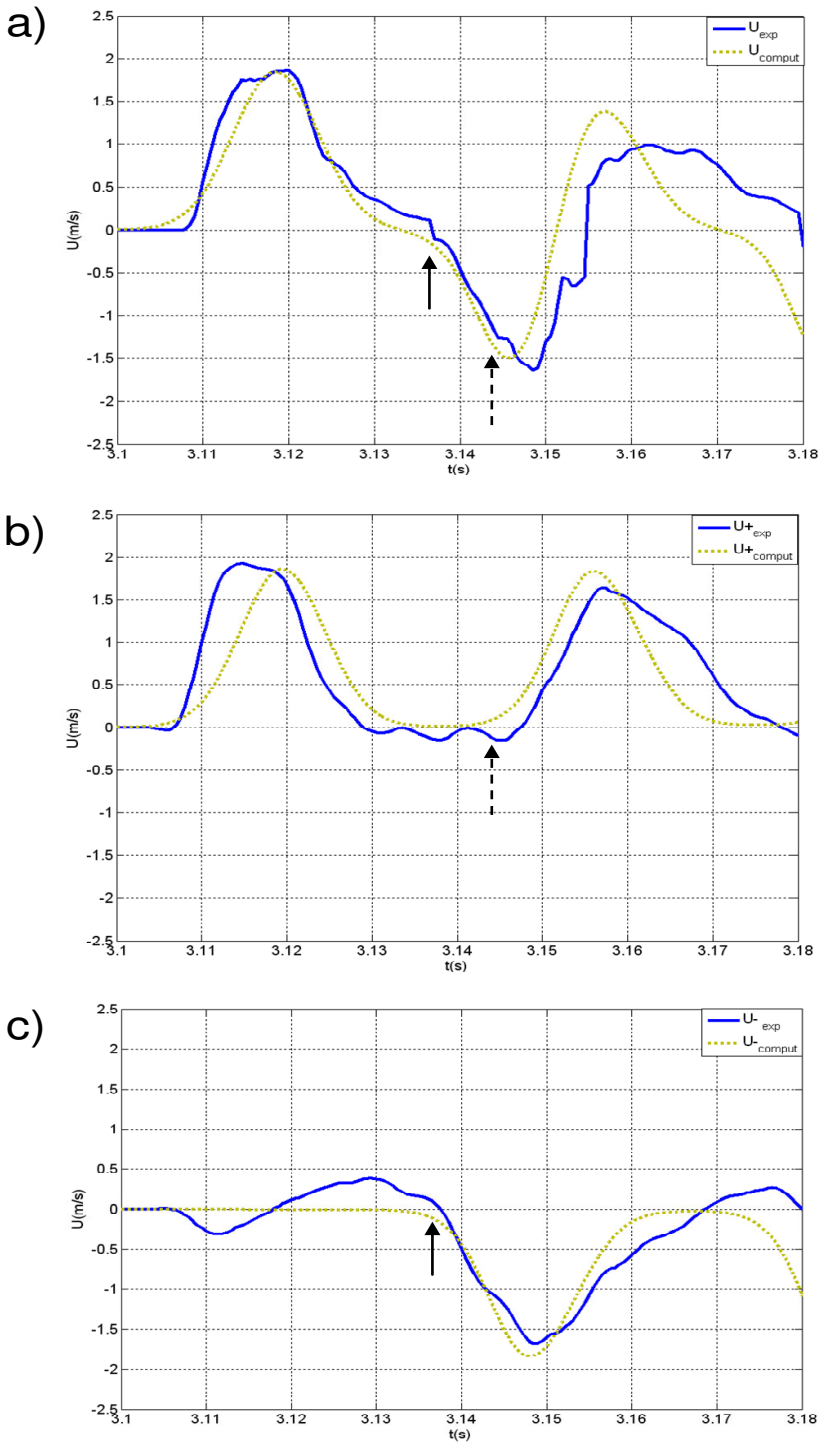

Figure 3.7 Comparison between experimental and computational (time step=10^{-7}s) velocity waveforms, the wave speed of the model was set to c_{foot}=102m/s. a) Experimental (U_{exp}) and computational (U_{comput}) pressure waveforms are separated in b) into their forward ($U+_{exp}$ and $U+_{comput}$) and in c) into their backward ($U-_{exp}$ and $U-_{comput}$) components using the analytical wave separation described in Section 2.3.1. The solid arrow indicates the theoretical arrival time of the wave reflected backward from the tube outlet (wave O in **Table 3.1**). The dashed arrow indicates the theoretical arrival time of the wave re-reflected forward from the inlet (R_t=1) (wave O' in **Table 3.1**).

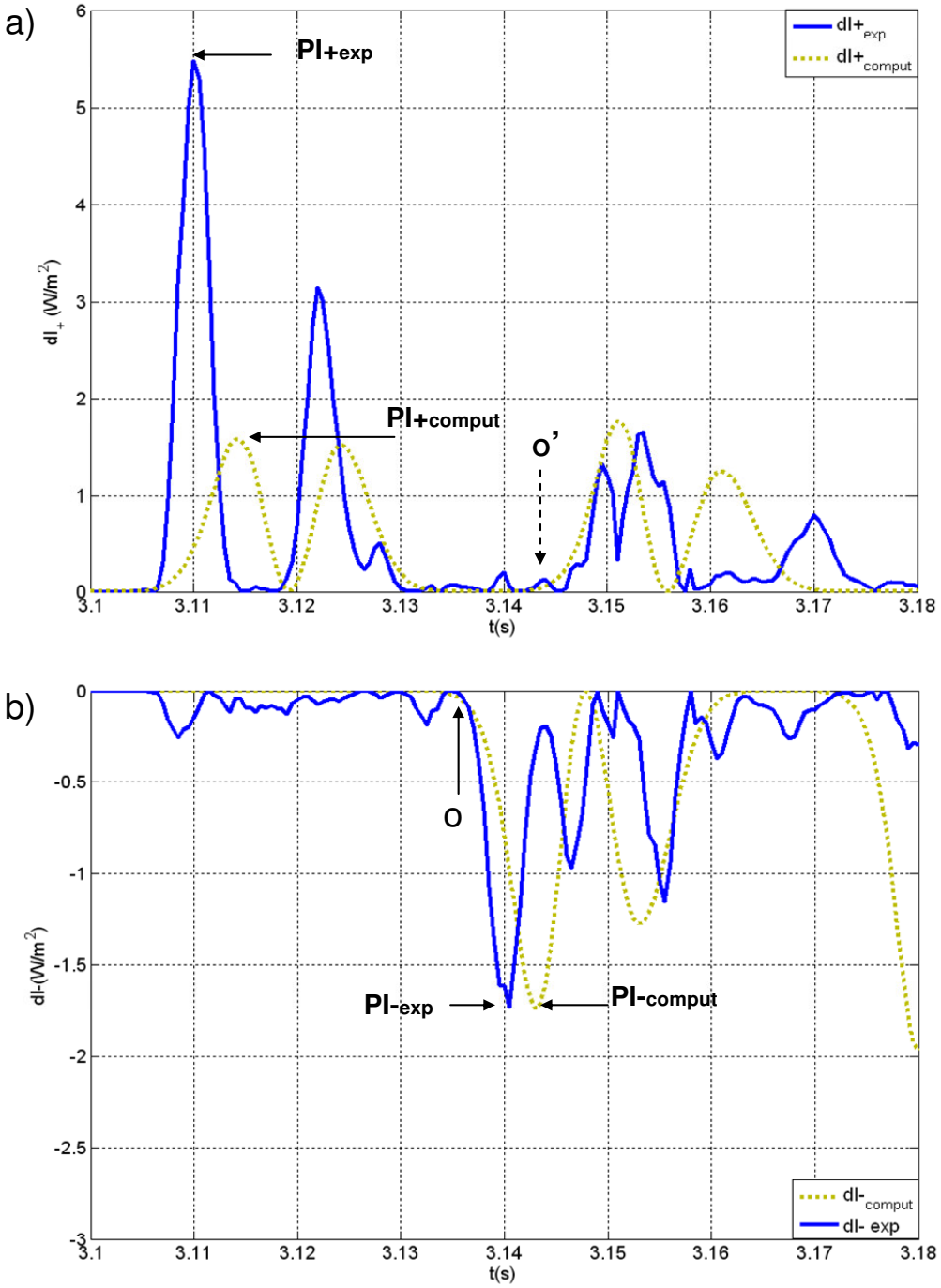

Figure 3.8 Comparison between experimental and computational wave intensities in forward and backward direction. The wave speed of the model was set to c_{foot}=102m/s. a) forward component of wave intensity: experimental ($dI+_{exp}$) and computational ($dI+_{exp}$). b) backward component of wave intensity: experimental ($dI-_{exp}$) and computational ($dI-_{exp}$). $PI+_{exp}$ and $PI+_{comput}$ refer to peak intensities of forward waves respectively for experimental and computational data while $PI-_{exp}$ and $PI-_{comput}$ are the peak intensities of the first backward waves. O indicates the calculated arrival time of the wave reflected backward from the tube outlet (wave path IX_1OX_1 in **Table 3.1**). O' indicates the calculated arrival time of the wave re-reflected forward from the inlet (R_t=1) (wave path $IX_1OX_1IX_1$ in **Table 3.1**).

3.5 Multivessel experiment

Series of Tubes: ST1-ST2-RT (mechanical and geometrical properties of the tubes are shown in **Table 2.6**).

Pressure Transducer: Millar

Sampling frequency: 20KHz

Configurations: open and closed end

Pulse duration: 10ms

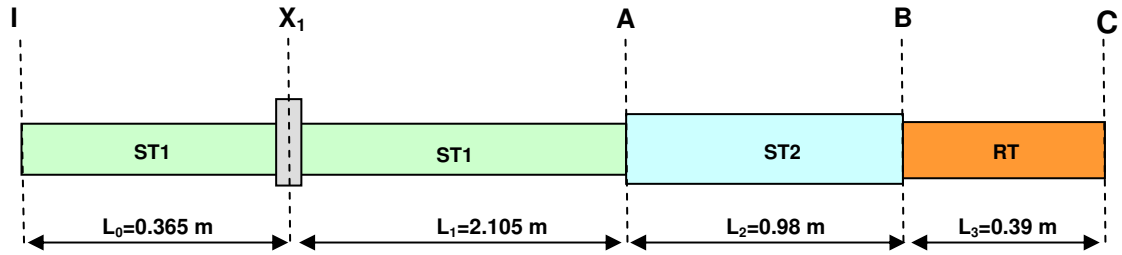

Figure 3.9 Schematic of the Multivessel experiment. X_1 refer to the location where pressure and velocity measurements take place. I and C are respectively the inlet and outlet of the tube, A and B denotes the tube junction. L defines the lengths of each tube segment.

A schematic of the setup for the *Multivessel experiment* together with the lengths of the tube segments is shown in **Figure 3.9**. Two silicon tubes (ST1 and ST2) and one rubber tube (RT) are considered in this experiment (mechanical and geometrical properties of the tubes are shown in **Table 2.6**); **Figure 3.9** shows also the sequence of the tubes: ST1-ST2-RT. A set of four experiments (considering the single tubes) were carried out to determine the wave speed (c_{foot}), using the foot to foot method (Section 1.8.1.2), for each of the considered tubes. The resulting wave speeds are shown in **Table 3.2**.

	ST1	**ST2**	**RT**
c_{foot} (m/s)	328±3	282±19	277±5

Table 3.2 Wave speeds determined with foot to foot method (C_{foot}) for the tubes used in the Multivessel experiment: rubber tube (RT) and two different silicon tubes (ST1, ST2).

The reflection coefficients at the reflective sites (A, B, C) of **Figure 3.9** are shown in **Table 3.3**, calculated using Eq. (2.44) using the wave speeds of **Table 3.2** and cross sectional area (A) from **Table 2.6**. Two configurations are considered for the

Multivessel experiment; open end and closed end condition associated in **Table 3.3** respectively to a reflection coefficient -1 and +1 in the position C of **Figure 3.9**.

	A	B	C	
$\mathbf{R_f}$	-0.55	0.33	*Closed end*	*Open end*
			+1	-1

Table 3.3 Reflection coefficients (R_{f+}) at the reflective sites (A, B, C) of **Figure 3.9** calculated using Eq. 2.44 from the c_{foot} in **Table 3.2** and cross sectional area (A) from **Table 2.6.** Since two configurations (open and closed end) are considered for the Multivessel experiment, the reflection coefficient in C is either -1 (open end) or +1 (closed end).

Once determined the c_{foot}, the theoretical arrival times at the site of measurement (X_1) (**Figure 2.11**) can be calculated from Eq. (3.2) according to the wave path, as shown in **Table 3.4**.

Wave path		Wave	Δt_{theor}(s)	t_{theor} (s)
IX1 - incident wave		-	-	2.38345
Backw	**$IX_1A\ X_1$**	A	0.01283	2.39628
	$IX_1A\ BAX_1$	B	0.01978	2.40323
	$IX_1A\ BCBAX_1$	C	0.02260	2.40607
Forw	**$IX_1A\ X_1I\ X_1$**	A’	0.01506	2.39851
	$IX_1A\ BAX_1I\ X_1$	B’	0.02201	2.40490
	$IX_1A\ BCBAX_1I\ X_1$	C’	0.02482	2.40827

Table 3.4 Theoretical arrival time (t_{theor}) of waves at X_1 position (**Figure 3.9**) according to Eq. 3.2 $t_{theor}=t_{foot\ incident\ wave}+\Delta t_{theor}$. The theoretical time delays (Δt_{theor}), starting from the foot of the incident wave (t=2.38345), are determined according to the lengths and c_{foot} (**Table 3.2**) of the tubes in which the wave has travelled (defined by the wave path). According to the wave path the waves can be classified in forward (Forw.) or backward (Back.) waves. Each wave path is associated to a wave (A, B, C, A’, B’,C’).

3.5.1 Pressure and velocity waveforms

The experimental pressure (P) and velocity (U) waveforms in the Multivessel experiment, were obtained using the equipments described in Sections 2.4.3 and 2.4.4 for the two configurations: open end ($P_{exp\ oe}$ and $U_{exp\ oe}$) and closed end condition ($P_{exp\ ce}$ and $U_{exp\ ce}$). Since the c_{foot} for this experiment (**Table 3.2**) are much higher then the c_{foot} in the latex experiment (c_{foot}=102m/s), to catch all the potential waves, the sampling frequency was increased to 20KHz and the Millar pressure transducer, that in

Section 2.4.3 has been shown to have higher frequency response, was used. The signals were filtered in Matlab (Mathworks Inc., MA, USA) with the Savitzky-Golay filtering, a third polynomial order and a window size of 55 samples were selected for the filtering. **Figure 3.10a** shows a comparison between the waveforms of $P_{exp\ ce}$ with $P_{exp\ oe}$ while in **Figure 3.11a** the velocity waveforms of open and closed configuration are compared ($U_{exp\ oe}$ and $U_{exp\ oe}$). Since the two configurations are the same apart from the outlet (point C in **Figure 3.9**) that has a different reflection coefficients (R_f=1 for closed end and R_f=-1 for open end, **Table 3.3**) the pressure and velocity waveforms are supposed to be the same until the theoretical arrival time of the waves reflected from the outlet. Since the pulse enforced at the inlet is always a forward compression wave, the nature of the backward reflected waves depend just on the type of reflection sites (Section 2.2.3.8). In open end configuration the wave reflected backward from the outlet is an expansion wave while in the closed end a backward compression wave is generated. **Figure 3.10a** shows that a separation of the two pressure waveforms appears exactly at the theoretical arrival time of the C wave and it is reinforced by the re-reflection C' with the dP increasing for the closed end condition and the dP reduced for the open end condition. In **Figure 3.11a** the velocity waveforms of the two configurations, similarly to the pressure waveforms, separate distinctly at the theoretical arrival time of the reflection from the outlet (wave C) with the velocity increasing in the open end condition and decreasing (inverting the direction of the flow) in closed end condition in line with the theoretical expectation shown in **Table 2.5**. According to **Table 3.3** the other two reflective sites A and B have respectively a negative and positive reflection coefficient. This causes a decrease in pressure and increase in velocity at the arrival of wave A (**Figure 3.10** and **Figure 3.11**) while increase in pressure and decrease in velocity are shown at the arrival of wave B. This appears more evident analysing the separated waves, both pressure and velocity, in their forward and backward components (**Figure 3.10b** and **Figure 3.11b**).

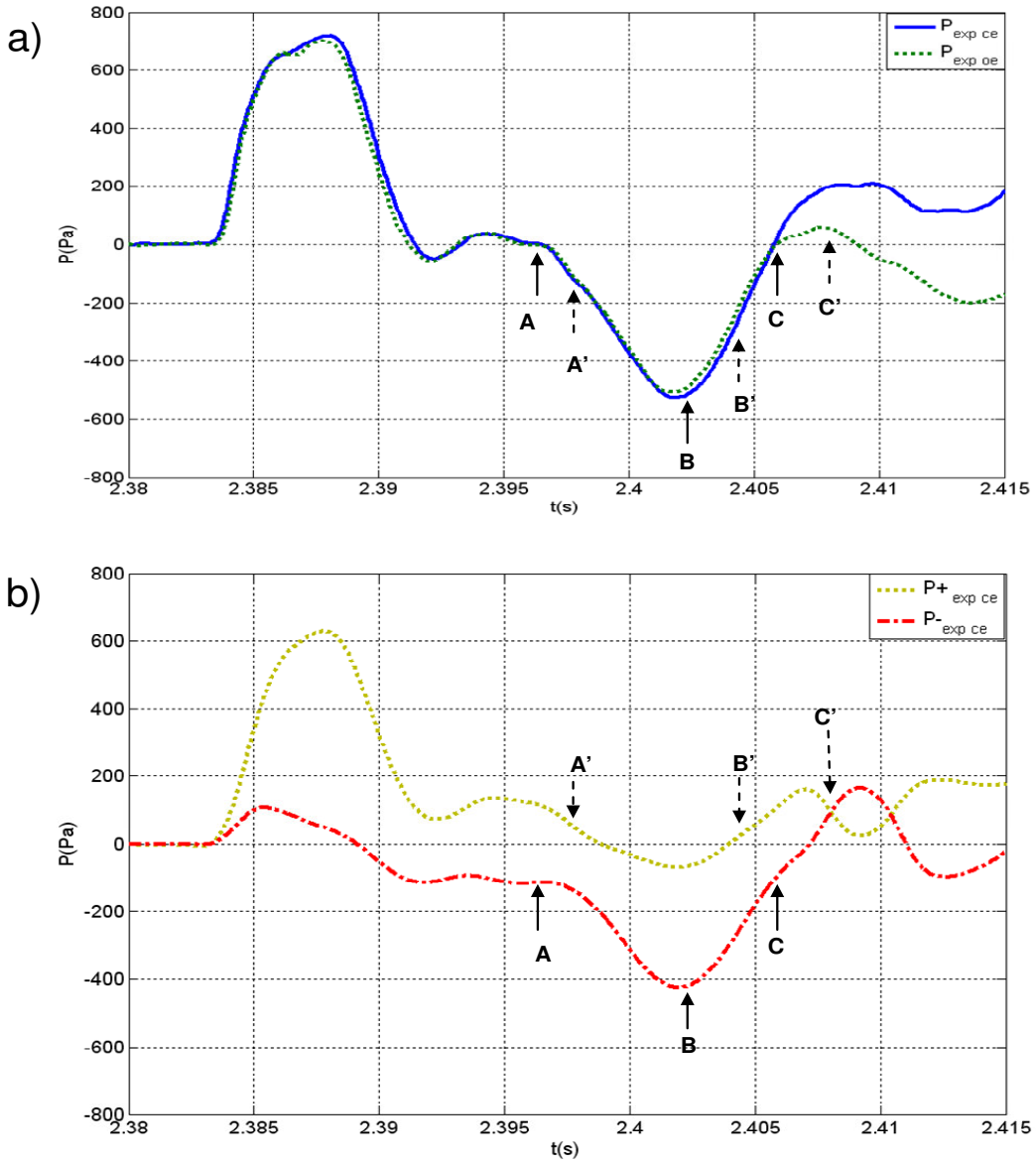

Figure 3.10 a) Experimental pressure waveforms at site X_1 in closed end ($P_{exp\ ce}$) and open end configuration ($P_{exp\ oe}$). b) $P_{exp\ ce}$ is separated into its forward ($P+_{exp\ ce}$) and backward ($P-_{exp\ ce}$) components using the analytical wave separation described in section 2.3.1. The solid arrows indicate the theoretical arrival time of the wave backward reflected from the reflective sites (A, B, C) of **Figure 3.9** according to the timing and notation of **Table 3.4**. The dashed arrows indicate the calculated arrival time of the wave re-reflected forward from the inlet.

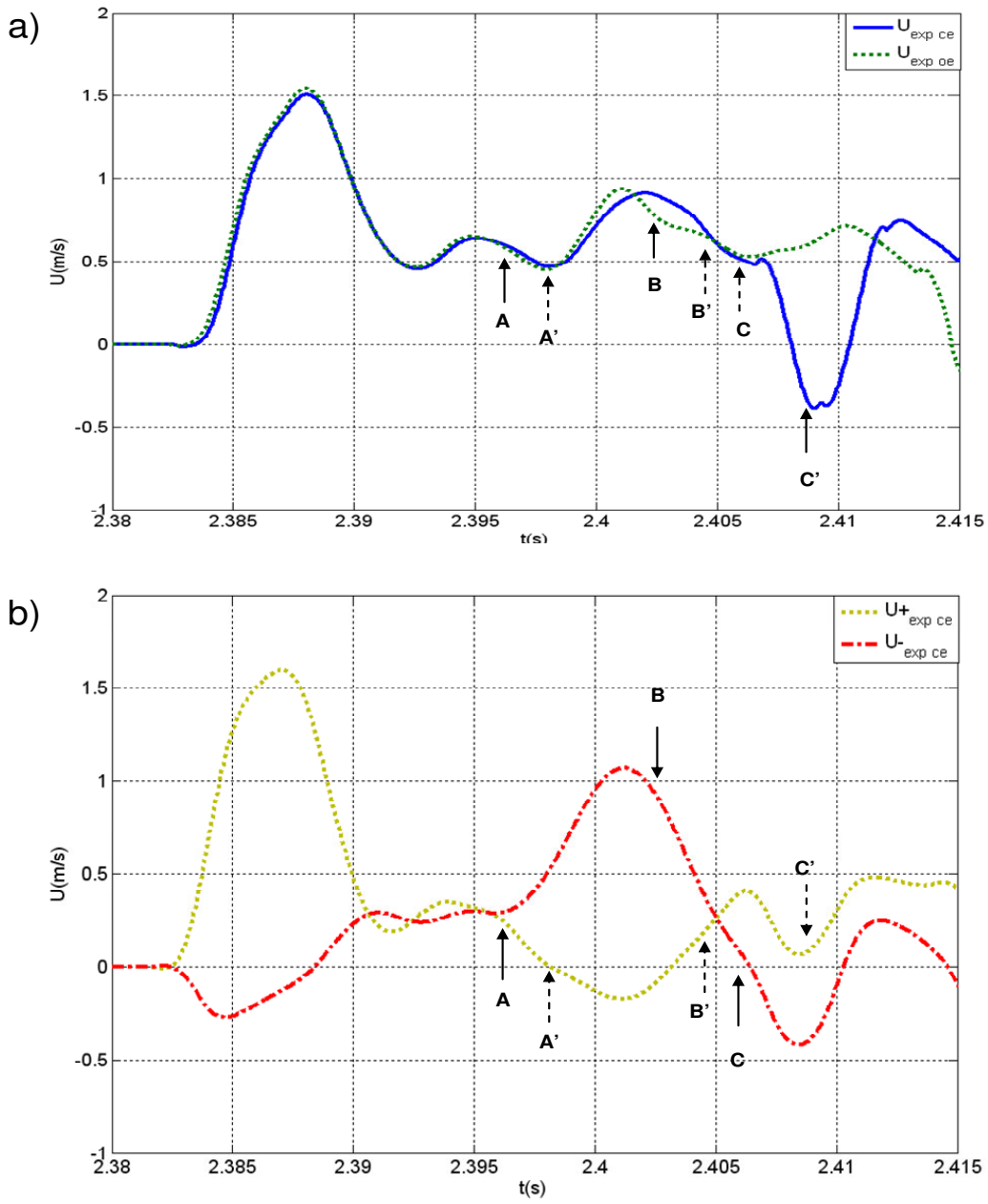

Figure 3.11 a) Experimental velocity waveforms at site X_1 in closed end ($U_{exp\ ce}$) and open end configuration ($U_{exp\ oe}$) . b) $U_{exp\ ce}$ is separated into its forward ($U+_{exp\ ce}$) and backward ($U-_{exp\ ce}$) components using the analytical wave separation described in section 2.3.1. The solid arrows indicate the theoretical arrival time of the wave reflected backward from the reflective sites (A, B, C) of **Figure 3.9** according to the timing and notation of **Table 3.4**. The dashed arrows indicate the calculated arrival time of the wave re-reflected forward from the inlet.

3.5.2 Wave intensity analysis

Figure 3.12 shows the wave intensity waveform associated to the closed end condition ($dI_{exp\ ce}$) and the decomposition into its forward ($dI+_{exp\ ce}$) and backward ($dI-_{exp\ ce}$) components according to Wave intensity analysis (Section 2.3.1). Also for the Wave intensity, the theoretical arrival times indicate, within a certain approximation, change in the slope of the $dI_{exp\ ce}$. This appears evident in the waveform of $dI-_{exp\ ce}$ where the theoretical times (**Table 3.4**), indicated by the arrows, are very close to the onsets of the $dI-_{exp\ ce}$ negative peaks.

3.5.3 Validation of the computational 1-D model

A computational 1-D analogous to the Multivessel experiment shown in **Figure 3.9** was developed according to the 1-D formulation described in Section 2.2. In order to give more relevance to the comparison, the wave speeds of the computational model were changed to match the c_{foot} of **Table 3.2** by changing β in Eq.2.12. The cross sectional area (A) of the model for all the tubes refers to their internal diameters according to **Table 2.6**, in this way the model has the same reflections coefficient of **Table 3.3**, having the same wave speeds and cross sectional area of the experiment. The inflow boundary condition for the 1-D model was defined according to Eq. (3.1), adjusted to match the incident velocity wave (amplitude and duration) of the experiment. The alignment for computational and experimental waveforms was based on the alignment of velocity peaks of the incident wave as shown from the peaks of the incident waves in **Figure 3.14a**. The T connector for the access of the velocity probe is neglected in the computational model.

Figure 3.13 and **Figure 3.14** show the comparison between computational (P_{comp} and U_{comp}) and experimental ($P_{exp\ ce}$ and $U_{exp\ ce}$) pressure and velocity waveforms; separation into forward and backward components for both experimental and computational are also shown. Relevant similarities, between experimental and computational data, can be indentified in the backward components for both pressure and velocity waveforms in terms of amplitude and timing (**Figure 3.13c** and **Figure 3.14c**); the forward pressure and velocity appear in general quite different. In **Figure 3.15**, the forward and backward components of wave intensities (dI) from experimental data are compared with the computationaldI waveforms ($dI\pm_{comput}$). Also for the wave intensities the analogy

between experimental and computational curve is more evident in the backward components in terms of wave amplitudes and timing.

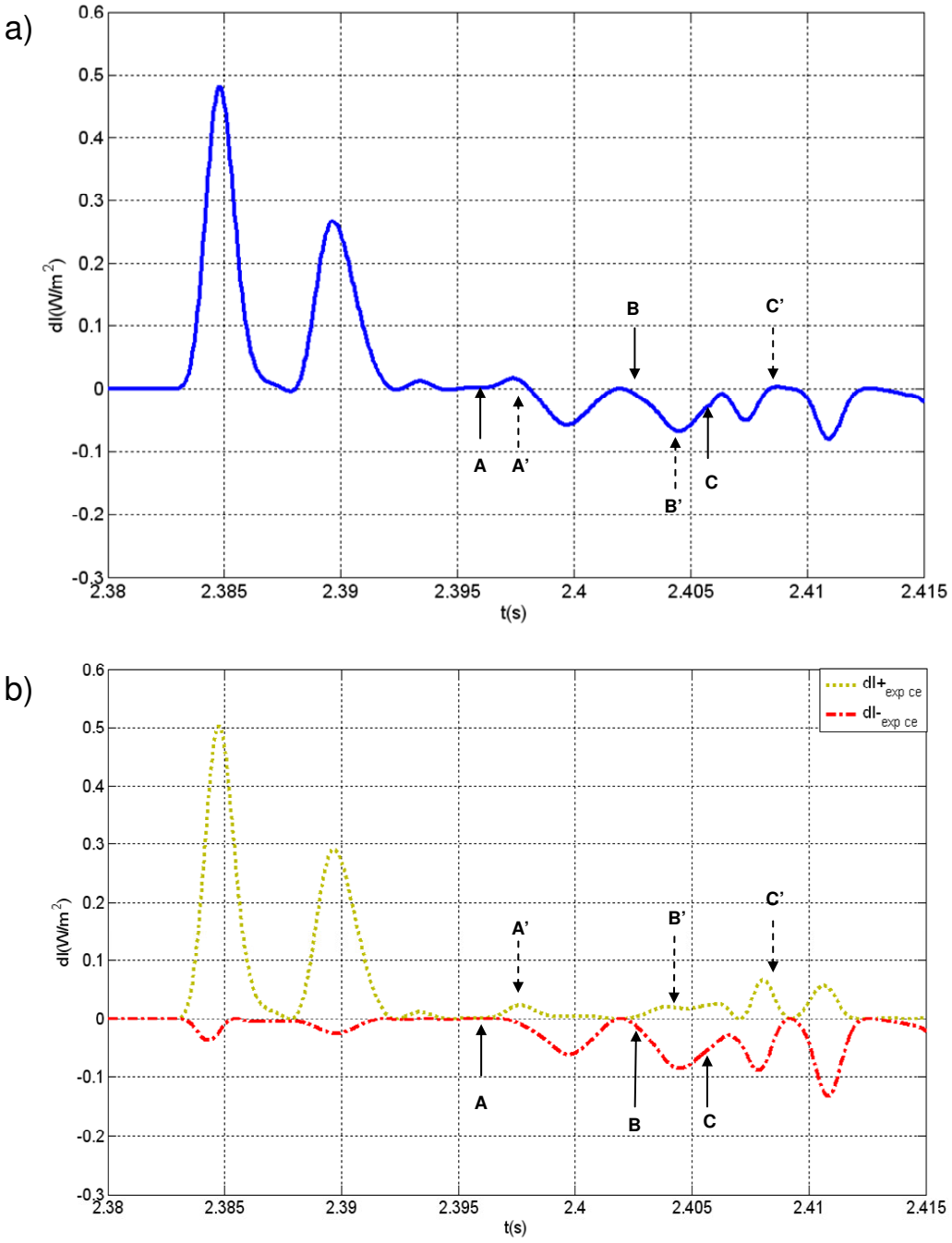

Figure 3.12 a) Wave intensity for the closed end configuration ($dI_{exp\ ce}$) derived from experimental pressure and velocity b) $dI_{exp\ ce}$ is separated into its forward ($dI+_{exp\ ce}$) and backward ($dI-_{exp}$ ce) components using the analytical wave separation described in section 2.3.1. The solid arrows indicate the theoretical arrival time of the wave reflected backward from the reflective sites (A, B, C) of **Figure 3.9** according to the timing and notation of **Table 3.4**. The dashed arrows indicate the theoretical arrival time of the wave re-reflected forward from the inlet.

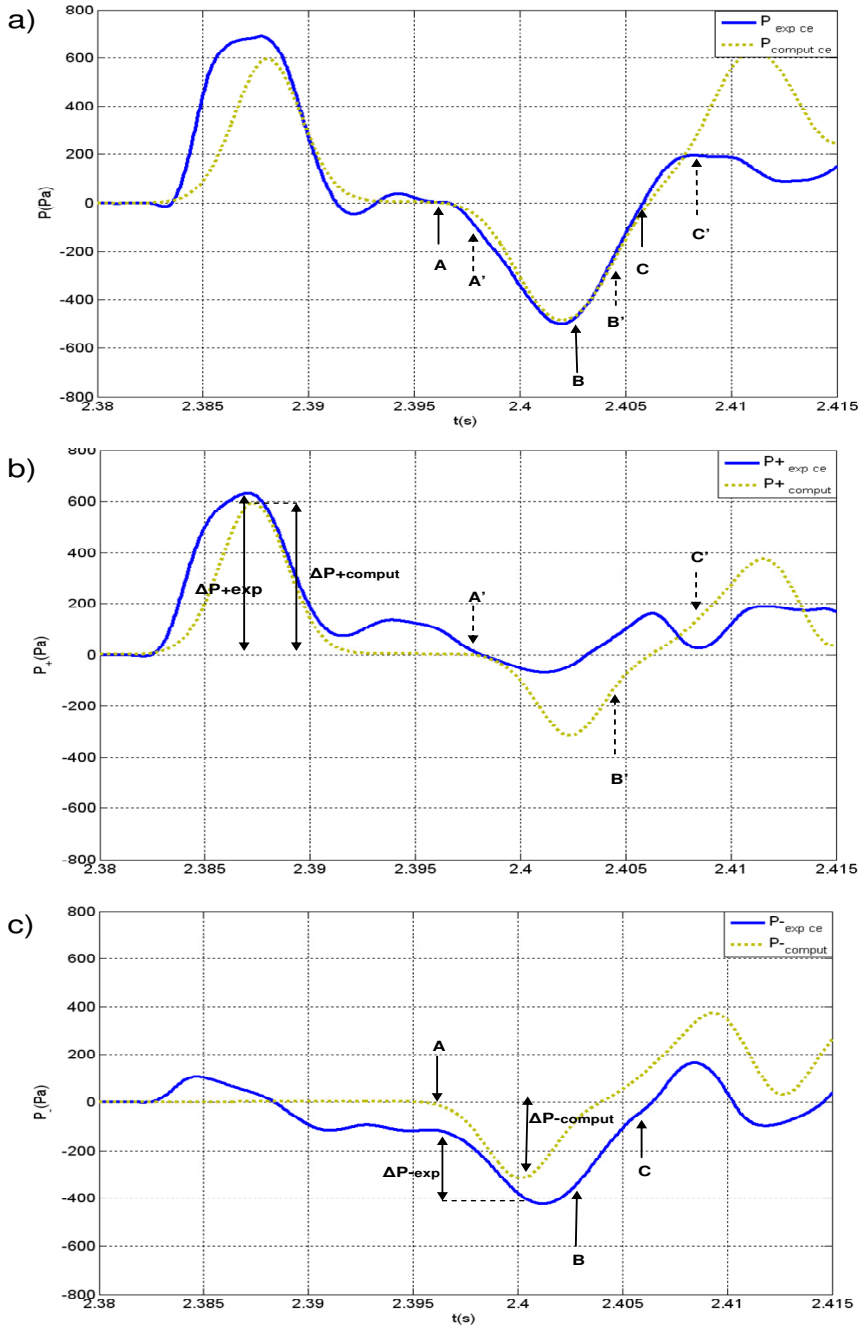

Figure 3.13 Comparison between experimental and computational (time step=10^{-7}s) pressure waveforms for the closed end configuration, the wave speeds of the model were set according to c_{foot} of **Table 3.2**. a) Experimental (subscript 'exp') and computational (subscript 'comput') pressure waveforms are separated into their b) forward ($P+_{exp\ ce}$ and $P+_{comput}$) and c) backward ($P-_{exp}$ ce and $P-_{comput}$) components using the analytical wave separation described in Section 2.3.1. The double arrows indicate the amplitude of the incident wave (ΔP_+) and the first reflected wave (ΔP_+). The solid arrows indicate the theoretical arrival time of the wave reflected backward from the reflective sites (A, B, C) of **Figure 3.9** according to the timing and notation of **Table 3.4**. The dashed arrows indicate the theoretical arrival time of the wave re-reflected forward (A', B', C') from the inlet.

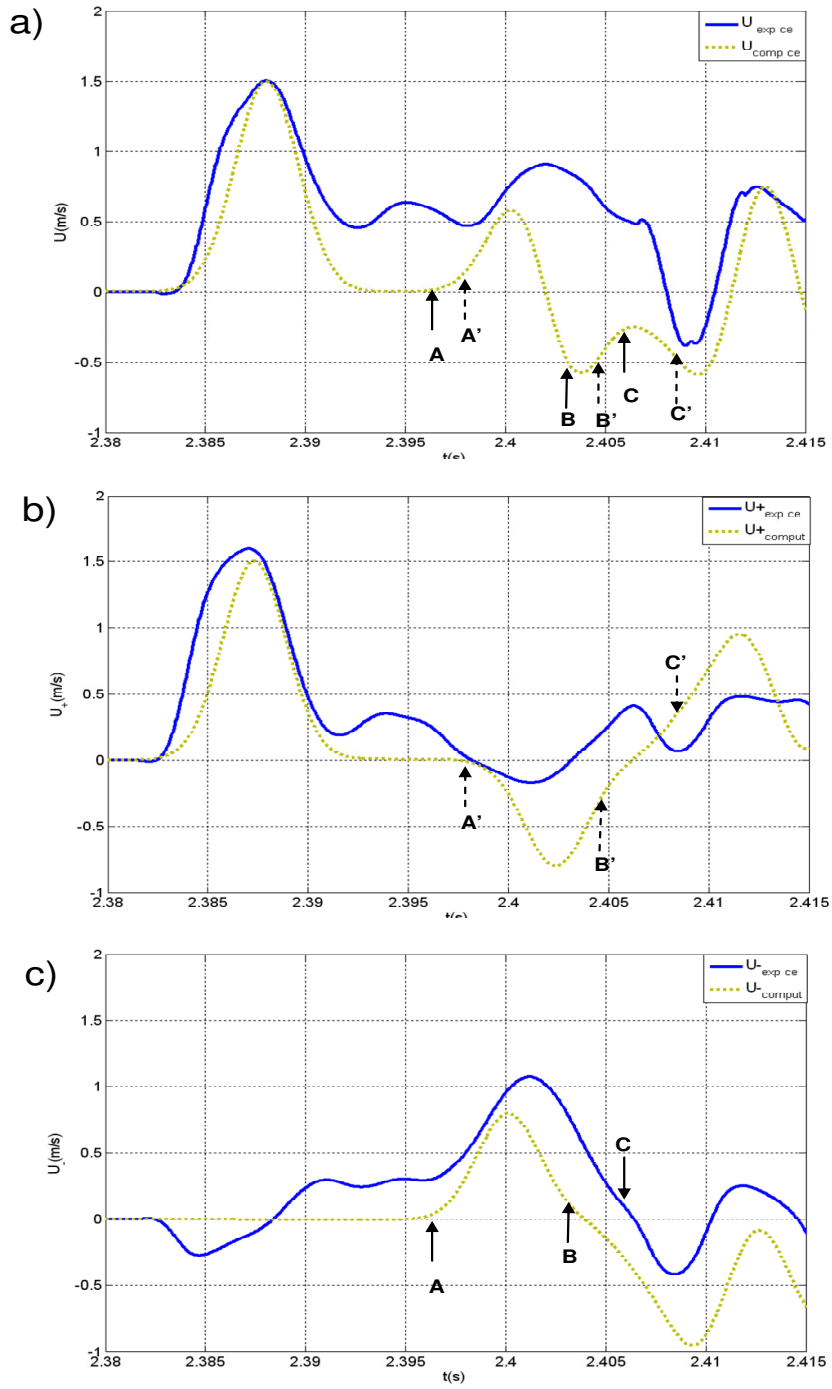

Figure 3.14 Comparison between experimental and computational (time step=10^{-7}s) velocity waveforms for the closed end configuration, the wave speeds of the model were set according to c_{foot} values of **Table 3.2**. a) Experimental ($U_{exp\ ce}$) and computational (U_{comput}) pressure waveforms are separated into their b) forward ($U+_{exp\ ce}$ and $U+_{comput}$) and c) backward ($U-_{exp}$ ce and $U-_{comput}$) components using the analytical wave separation described in Section 2.3.1. The solid arrows indicate the theoretical arrival time of the wave reflected backward from the reflective sites (A, B, C) of **Figure 3.10** according to the timing and notation of **Table 3.4**. The dashed arrows indicate the theoretical arrival time of the wave re-reflected forward from the inlet.

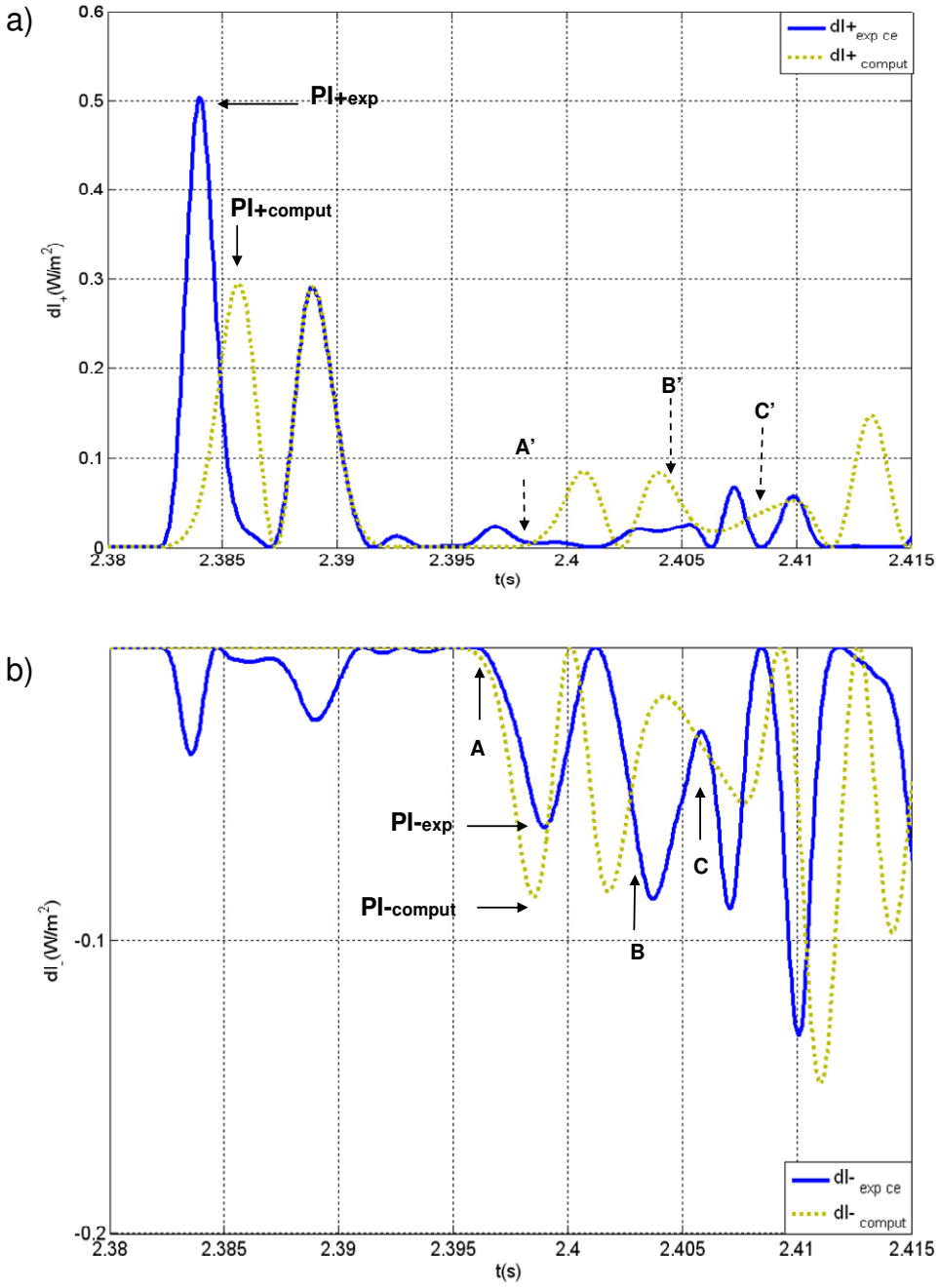

Figure 3.15 Comparison between experimental and computational wave intensities in forward and backward direction. The wave speeds of the model were set according to c_{foot} of **Table 3.2**. a) forward component of wave intensity: experimental ($dI+_{exp}$) and computational ($dI+_{comput}$). b) backward component of wave intensity: experimental ($dI-_{exp}$) and computational ($dI-_{comput}$). $PI+_{exp}$ and $PI+_{comput}$ refer to peak intensities of forward waves respectively for experimental and computational data while $PI-_{exp}$ and $PI-_{comput}$ are the peak intensities of backward waves. The solid arrows indicate the calculated arrival time of the wave reflected backward from the reflective sites (A, B, C) of **Figure 3.10** according to the timing and notation of **Table 3.4**. The dashed arrows indicate the calculated arrival time of the wave re-reflected forward from the inlet.

3.6 Discussions

In Section 1.8.2, it was pointed out that in an elastic tube filled with air, if the frequency of excitation is lower than the resonance frequency (f_r) of the tube wall, the wave speed is lower than the sound speed in free air (C_s) (Guelke and Bunn, 1981). Since the calculated resonance frequencies (f_r) for the tubes, used in the experiments of this thesis (**Table 3.5**), are much higher than the maximum frequency of excitation in the experiments (~1/10ms=100Hz), the c_{foot} associated to all the tubes (**Table 3.6**) are lower than C_s=343 m/s. This is in line with Guelke and Bunn's theory.

	LXT	**RT**	**ST1**	**ST2**
f_r **(Hz)**	232	587	576	407

Table 3.5 Resonance frequencies (f_r) calculated for the considered tubes using Eq. (1.6) ($f_r = \frac{1}{2D}\sqrt{\frac{E}{\rho_w}}$) and the tube properties shown in **Table 2.6**.

Direct derivation of the wave speeds using the foot to foot method (c_{foot}) is not always possible. A formulation for wave speed that, based on the geometrical and mechanical properties of the considered tubes, could provide a good estimation of c_{foot}, appears therefore highly desirable. In Section 1.8.3 (Eq. 1.12) the general Korteweg's equation (c_K), which considers also the fluid compressibility has been introduced, while in Section 2.2.3.4 a new formulation (Eq. 2.25) for wave speed (c_β) has been introduced as variation of the existing c (Eq. 2.12). **Table 3.6** shows the values for c_K and c_β calculated from the tubes properties of **Table 2.6**; percentage errors (% e_{ck} and % $e_{c\beta}$) in comparison with c_{foot} are also provided. The percentage errors of **Table 3.6** show that c_β appears in general to provide a better approximation of c_{foot} in all the considered tubes with an average error of 14% compared to 21.3% of c_k.

In order to compare the influences of the different wave speeds on the pressure waveforms, comparisons between experimental pressure waveforms (P_{exp}) with the computational pressures are shown in **Figure 3.16** and **Figure 3.17**. P(c_K) is the computational pressure obtained using the Korteweg's equation, P(c_β) and P(c_{foot}) are the pressure obtained using as wave speed respectively c_β and c_{foot}. The waveforms were aligned according to the time of the velocity peaks. The Korteweg's formulation tends in general to underestimate the wave speed values as shown for all the tubes in

Table 3.6 and in the waveforms of **Figure 3.16** and **Figure 3.17** where the $P(c_K)$ appears delayed compared to $P(c_\beta)$ and $P(c_{foot})$.

TUBES	c_{foot}	c_K	c_β	% e_{ck}	% $e_{c\beta}$
LXT	102	74	88	27.4	13.7
RT	277	221	335	20.2	20.5
ST1	328	276	**540** →343	15.8	4.6
ST2	282	220	331	22.0	17.4
Average % error				**21.3%**	**14.0**

Table 3.6 Wave speeds (m/s) determined with Korteweg's equation c_K (Eq. 1.12) and c_β (Eq. 2.66) are compared with the c_{foot} for all the tubes considered in the experiments. Percentage errors and the average errors are shown: $\%e_{C_K} = \frac{c_K - c_{foot}}{c_{foot}} \cdot 100$ and $\%e_{C'_\beta} = \frac{c_\beta - c_{foot}}{c_{foot}} \cdot 100$.For ST1 since $c>C_s$ (c =540 m/s), c_β has been enforced to equal Cs (Section 2.2.3.4).

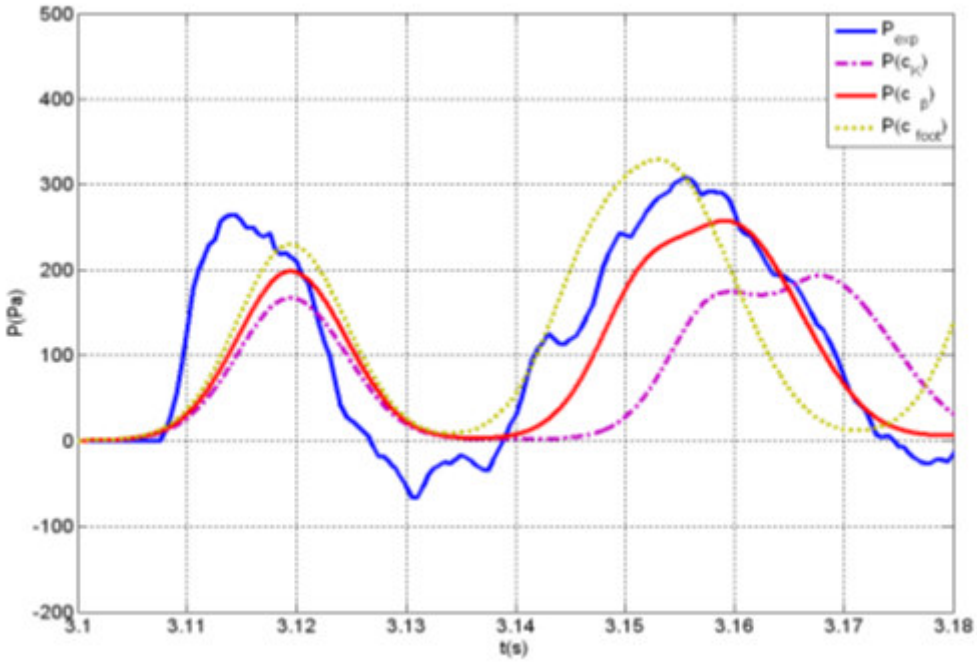

Figure 3.16 Latex experiment: comparison between the experimental pressure (P_{exp}) and computational pressure waveforms using waves speed determined with the foot to foot $P(c_{foot})$, Korteweg's equation $P(c_K)$ and the corrected wave speed $P(c_\beta)$.

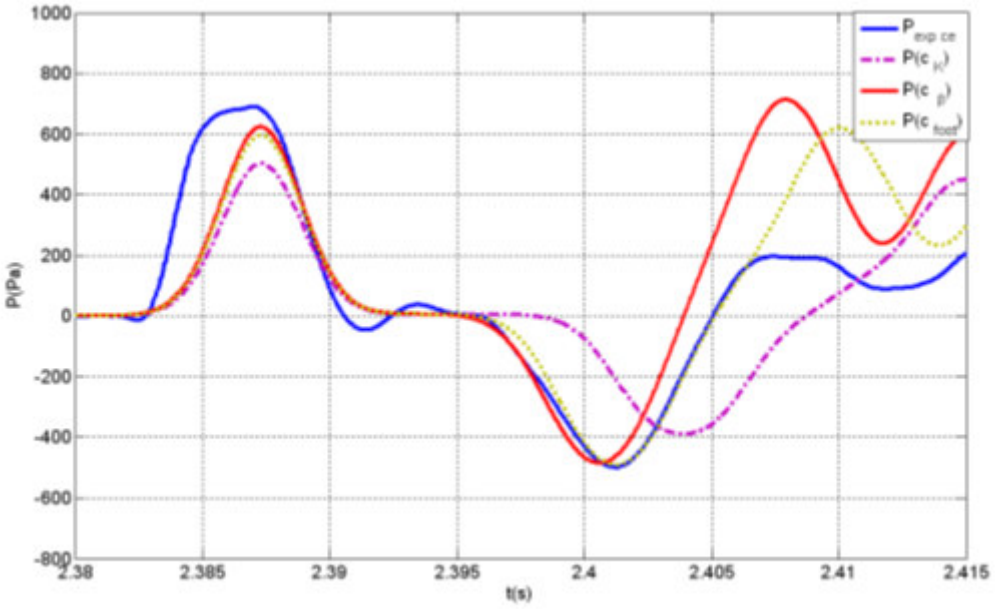

Figure 3.17 Multivessel experiment: comparison between the experimental pressure (P_{exp}) in closed end configuration and computational pressure waveforms according to the waves speed determined with the foot to foot $P(c_{foot})$, Korteweg's equation $P(c_K)$ and the corrected wave speed $P(c_\beta)$.

According to Feng and Khir (2008) an incident pressure waveform (before any reflection) can be interpreted as a sequence of two semi sinusoidal waves: the first half of the waveform is a compression wave (FCW) since the pressure increases, the second half is an expansion wave (FEW) that starts when the pressure starts to decrease. The presence of these two forward waves appears clear with the two initial positive peaks of dI in the wave intensity waveforms (**Figure 3.5** and **Figure 3.12**). The backward components of wave intensity (dI-) in **Figure 3.8** and **Figure 3.15** were used to identify the time of the onsets of the reflected waves in experimental and computational waveforms. The experimental (Δt_{exp}) and computational (Δt_{comput}) delays of the arrival of the reflected waves, were compared with the theoretical ones (Δt_{theor}) defined in **Table 3.1** and **Table 3.4**, results are shown in **Table 3.7**. The comparison is not available in **Table 3.7** for the wave B in Multivessel model since it was not possible to identify any possible onset of reflected wave in the dI- waveforms (probably hidden by the arrival of the FEW reflected in A). The average errors of both computational and experimental delays are close to 2% and, particularly for the computational delays errors can be associated to alignment problems (since the values refer to c_{foot}).

The calculation of the local reflection coefficient (R_f) is used to quantify the amount of wave reflection from a given reflection sites (Greenwald et al., 1990; Khir and Parker,

2002; Latham et al., 1985). As explained by Mynard et al. (2008), three approaches have been used in literature for calculating R_f from Wave intensity analysis and are considered in this thesis as comparison (for both experimental and computational R_f) with the theoretical reflection coefficients.

Wave		Δt_{theor}	Δt_{exp}	Δt_{comput}	% e(Δt_{exp})	% e (Δt_{comput})
LATEX	**O**	0.0291	0.0290	0.0285	0.3	2.0
	O'	0.0372	0.0390	0.0360	4.8	3.2
MULTIVESSEL	**A**	0.01283	0.01395	0.0137	2.8	0.9
	B	0.01978	-	-	-	-
	C	0.02260	0.02285	0.022	1.1	2.6
Average % error					**2.25**	**2.17**

Table 3.7 Theoretical time delays Δt_{theor} of the onset of the reflected waves starting from the foot of the incident wave for Latex (values from **Table 3.1**) and Multivessel experiment (values from **Table 3.4**), are compared with the delays determined experimentally (Δt_{exp}) and computationally (Δt_{comput}) from the onset of reflected waves of dI- waveforms in **Figure 3.8** and Figure 3.15. % errors are calculated as $\%e(\Delta t_{exp}) = \frac{\Delta t_{exp} - \Delta t_{theor}}{\Delta t_{theor}} \cdot 100$ and $\%e(\Delta t_{comput}) = \frac{\Delta t_{comput} - \Delta t_{theor}}{\Delta t_{theor}} \cdot 100$.

In the first approach the reflection coefficient is calculated from the ratio between the change in amplitude of the backward (ΔP_-) and forward (ΔP_+) pressure (Khir and Parker, 2002)

$$R_{f\Delta P} = \frac{\Delta P_-}{\Delta P_+} \tag{3.3}$$

The second approach uses the ratio of cumulative intensities (CI), or wave area, of backward (CI_-) and forward (CI_+) waves (Hollander et al., 2001; Smolich et al., 2008)

$$R_{fCI} = \pm\sqrt{\frac{|CI_-|}{CI_+}} \tag{3.4}$$

In the third approach, the reflection coefficient is calculated from the ratio of the peaks

of the wave intensities of forward (PI_+) and backward (PI-) waves (Bleasdale et al., 2003; Mynard et al., 2008)

$$R_{fPI} = \pm\sqrt{\frac{|PI_-|}{PI_+}} \tag{3.5}$$

Comparison of the three approaches (**Table 3.8**) shows that among the reflection coefficients, calculated from the experimental data, Eq. (3.3) ($R_{\Delta P}$) provides the best match with the theoretical values (Average error=12.3%). These results are in line with the results of other investigators. According to Mynard et al. (2008), $R_{\Delta P}$ is unaffected by the degree of elastic non linearity and appears more accurate than R_{fCI} and R_{fPI}. Vessel wall elastic non-linearities cause attenuation of expansion waves and amplification of compression waves in their propagation, causing increasing errors with the distance particularly for R_{fCI} and R_{fPI}. The small deviations (error 1.8% in **Table 3.8**) from theoretical data associated to the reflection coefficients derived from computational data can be associated to the friction force per unit length accounted in Eq. 2.8 (γ=9 is always considered in this thesis providing $f = -2(\gamma+2)\mu\pi U = -22\mu\pi U$). Comparisons of computational pressure waveforms (for both Latex and Multivessel 1-D models) are shown **Figure 3.18**, where the two values for the velocity profile (γ=9 and γ=2) are compared against the inviscid condition (μ=0 in Eq. (2.8)).

Experiment	Theoretical	Experimental			Computational		
	R_f	$R_{f\Delta P}$	R_{fPI}	R_{fCI}	$R_{f\Delta P}$	R_{fPI}	R_{fCI}
Latex	1	0.88	0.56	0.54	1	1	1
Multivessel	-0.55	-0.48	-0.35	-0.38	-0.53	-0.53	-0.53
Average % error		**12.3**	**40.0**	**38.4**	**1.8**	**1.8**	**1.8**

Table 3.8 Reflection coefficients of the first reflection site in the two experiments from the analysis of the first reflected wave (O for Latex and A for Multivessel model). Theoretical values (R_f=1 for latex tube due to the closed end and R_f=-0.55 in the Multivessel model from **Table 3.3**) are compared with computational and experimental R_f (Eq.s (3.3)-(3.5)): $R_{f\Delta P}$(experimental)=$\Delta P\text{-}_{exp}/\Delta P+_{exp}$ and $R_{f\,\Delta P}$(computational)=$\Delta P\text{-}_{comput}/\ \Delta P+_{comput}$ according to the amplitudes of **Figure 3.6** and **Figure 3.13**; $R_{fPI}(\exp erimental) = \pm\sqrt{\frac{|PI_{-\exp}|}{PI_{+\exp}}}$ and $R_{fPI}(computational) = \pm\sqrt{\frac{|PI_{-comput}|}{PI_{+comput}}}$ are determined according to the peak values of **Figure 3.8** and **Figure 3.15**. The values for R_{fCI} are calculated using Eq. 3.4 with the area of the waves indicated by the peaks in **Figure 3.8** and **Figure 3.15** (CI- is the area of the waves whose peaks are $PI\text{-}_{exp}$ ad $PI\text{-}_{comput}$, CI_+ is the area of the waves whose peaks are $PI+_{exp}$ ad $PI+_{comput}$).

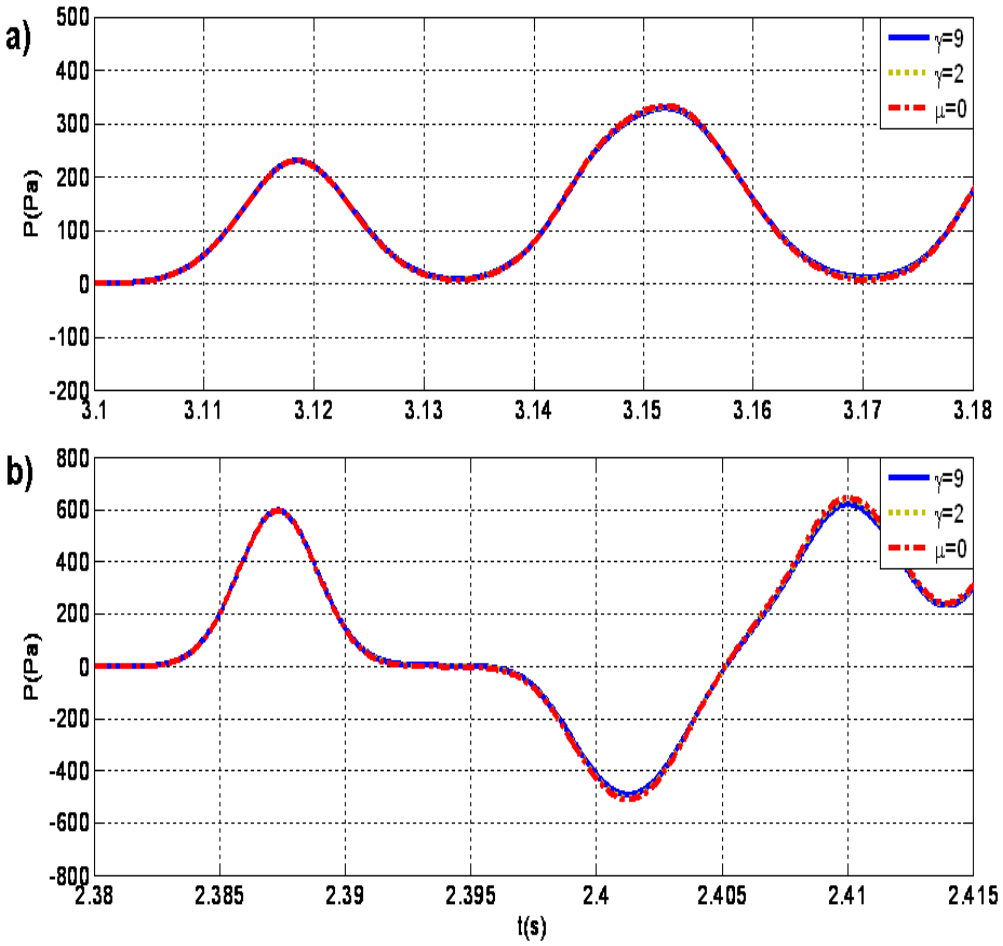

Figure 3.18 Influence of the velocity profile: computational pressure waveforms obtained with the 1-D model considering the two velocity profiles defined in Figure 2.2: nearly flat (γ=9) and parabolic profile (γ=9) are compared with the inviscid formulation (μ=0). a) Latex model, b) Multivessel model.

3.6.1 Limitations

Different waves, in the experimental data and other sources of noise, can not be matched with the theory. These need to be investigated. As an example all the negative peaks of wave intensity in the backward direction ($dI-_{exp}$) that appear before the arrival of the first reflected wave (**Figure 3.5** and **Figure 3.12**) can be associated to setup limitations. The following limitations can be identified:

1. In this thesis the effect due to the discontinuity introduced by the T-connector are neglected. This might not be exactly true since the site for measurement for both pressure and velocity are in correspondence of this discontinuity. In fact,

apart from the increased rigidity (introduced with the T-connector), the site where the flow probe is inserted introduces also a local increase of cross sectional area (**Figure 2.17**) which might encourage the formation of vortex (not considered in the 1-D theory).

2. The split fiber probe provides a value for the velocity which refers to the specific position inside the tube. It changes according to the radial position; this value for simplicity was assumed to be the average velocity to be compared with the computational data (in which nearly flat velocity profile (γ=9) was assumed, Equation 2.5). According to **Figure 2.2** and Equation 2.5, the radial position for the average velocity in a circular tube is $r/R = 1/\sqrt{2} = 0.7$ for parabolic profile and $r/R = \left(\frac{2}{11}\right)^{1/9} = 0.83$ for the nearly flat velocity profiles. The position of the probe was fixed approximately in the range defined by these two positions during each experiment to provide a reasonable value for average velocity. The effect of the radial position on velocity have been neglected in this thesis.
3. Concentrated dissipation at the tube junctions are neglected and dissipations along the tube need to be better investigated.
4. Insensitivity of the velocity probe to flow velocities lower than 0.5 m/s, as discussed in Section 2.4.4.4.1, are also not considered
5. The opening/closure time of the solenoid valve is not instantaneous (Section 2.4.5.2), the process might affect the rising time of both pressure and velocity of the incident wave.

3.7 Conclusions

The experiments discussed in this chapter have shown the possibility of studying propagation of air waves in flexible tubes following the 1-D modelling in time and space variables which has been extensively applied to investigate the propagation of waves in arterial trees (Alastruey et al., 2008; Alastruey et al., 2009; Matthys et al., 2007a; Sherwin et al., 2003). The modelling, introduced in Section 2.2, has been experimentally validated in terms of wave speed, timing and amplitude. The results have shown that, once the wave speed is known, it is possible to map the distance of the reflective sites based on the time delays of the reflected waves. Computational pressure and velocity waveforms have been calculated for each setup according to three different expressions for wave speed: the first wave speed is directly determined from the foot to

foot method (c_{foot}) while the other two are calculated from the mechanical and geometrical properties of the tubes respectively using the Korteweg' s expression (c_k) and the corrected wave speed introduced in Section 2.2.3.4 (c_β). The c_β expression has shown to provide values which are closer to the measured c_{foot} values with an average percentage error of 14%. The comparison between computational and experimental pressure waveforms have confirmed that c_β expression provides pressure curves that follow more faithfully the experimental results compared to c_K.

According to the theoretical expectations (Table 2.5) the experiments have shown, in general, that also for air pulses the arrival of backward compression waves generate an increase of P and decrease of U while expansion backward waves produce a decrease of P and increase of U. According to these principles, wave intensity analysis (WIA) has been calculated from the measured pressure and velocity waveforms. WIA is a time domain technique which allows the separation of pressure and velocity waves travelling in the forward and backward directions from the measured pressure and velocity waveforms. WIA has shown negative and positive peaks, within a certain allowance, in correspondence of the arrival time of waves propagating respectively in backward and forward direction as theoretically expected. The error in determining the arrival time of the considered waves was around 2% while the minimum error for reflection coefficient estimation from experimental data was found to be around 12%, compared to theoretical values. On the basis of these experimental findings and the validation of the 1-D model, discussed in this chapter, the following chapters will extend the study firstly to simplified model (Chapter 4) and then to bifurcating tree model of human central airways.

Chapter 4

Computational results: models of central airways

4.1 Introduction

In Chapter 3 the 1-D modelling in space and time variables has been validated, within a certain approximation, using experimental results referred to a single tubes and series of tubes with an air pulse enforced at the inlet. Experimental results have shown that the c_β formulation (Section 2.2.3.4) of the wave speed has provided the best match with the measured c_{foot} (comparing to the c_K) therefore c_β has been suggested as the wave speed formulation used in the computational models in this chapter and in chapter 5. To identify and classify the waves, the tubes used in the experiments were long enough ensuring that the incident wave was not affected by the arrival of reflected waves. One of the main advantages of the computational models, once validated, is the possibility to study systems that are difficult to set up experimentally.

In Chapter 2 the principles of the 1-D modelling have been introduced (Section 2.2) and the geometrical and mechanical properties of airways have been provided for both symmetrical and asymmetrical model (**Table 2.3** and **Table 2.4**). This chapter aims to apply the 1-D formulation to two simplified 1-D models of central airways according to Weibel's model: 1) A bifurcation model; the trachea and main bronchi, 2) A multivessel model; a series of eight tubes each with the properties of the corresponding physiological airways generation. Different lumped parameters (0-D) models have been coupled to the terminal segment of each 1-D model to simulate airflow in peripheral airways (Section 2.2.5). This chapter introduces the importance that the study of wave propagation and reflection in lungs may have on the diagnosis of respiratory diseases in simple geometries; the study will be expanded in Chapter 5 where more complex and physiological features of human bronchial tree will be discussed.

4.2 Methodology

4.2.1 Inflow boundary condition

Two compression waves are enforced at the inlet of trachea in both models. The inlet is assumed to behave as an absorbing site ($R_f=0$) after the generation of the pulse. The following pulses have been considered:

Short pulse: An acceleration pulse has been enforced using the Gaussian function (in m^3/s)

$$q(t) = 10^{-4} e^{-10^{9.7}(t-0.01)^2} \tag{4.1}$$

which generates an incident wave of approximately 0.06 ms with a peak value at 0.01s. Due to the high wave speed in air, this short pulse is necessary to ensure that the arrival of reflected waves to the measurement site occurs after the end of the incident wave (Clavica et al., 2009).

Impulse oscillometry pulse: To test the sensitivity of the code to changes in the peripheral parameters, the following longer pulse has been considered (in m^3/s)

$$q(t) = 0.15 \times 10^{-3} e^{-10^{4.8}(t-0.03)^2} \tag{4.2}$$

which generates a 40 ms pulse, similar to the air pulse (**Figure 2.21**) used for clinical diagnosis in impulse oscillometry system (IOS).

4.2.2 Outlet boundary conditions

As described in Section 2.2.5, the parameters which characterise mainly the peripheral airways are the alveolar compliance (C) and the peripheral airway resistance (R) that are the most affected during the chronic pulmonary diseases either obstructive or restrictive (Section 1.2). In Section 4.2.2.1 the numerical values for C and R will be provide based on normal and pathologic conditions.

The 0-D models of flow in the periphery, introduced in Section 2.2.5, that are considered in this thesis are: resistance (R) model, two-element (RC) and three-element (R_mCR) Windkessel models. The assumption is that all peripheral segments have the same value of compliance and resistance and are in parallel.

4.2.2.1 Peripheral Resistance and compliance

The minimum (R_1) and the maximum (R_3) value of total peripheral airway resistance that are considered in this thesis and coupled to all the models of central airways are based on Hogg's measurements (Hogg et al., 1968) referring respectively to normal and emphysematous lungs. The measurements by Hogg et al. were taken using the retrograde catheter technique (Section 1.7.1).

The third resistance considered in this thesis is the average of the two previous ones to simulate a progressive increase of resistances from R_1 to R_3: $R_2 = (R_1+R_3)/2$. **Table 4.1** shows the values for peripheral airways resistance that are considered in this thesis.

R_1	R_2	R_3
$17 \cdot 10^3$	$154 \cdot 10^3$	$291 \cdot 10^3$

Table 4.1: Total peripheral resistance values in Pa·s/m^3 for normal (R_1) and emphysematous lungs (R_3). $R_2 = \frac{R_1 + R_3}{2}$

The minimum value for total alveolar compliance C_1 is derived from Tiddens's (1999) *in vitro* measurements in a single peripheral airway ($C_{s.aw}$) (Section 1.7.3). Considering 2^7=128 terminal segments in parallel, the total compliance is derived as $C_1=128 \cdot C_{s.aw}$. The value C_1 corresponds to the average value of dynamic compliance of small airways from lungs of smokers with different degrees of chronic obstructive pulmonary disease (COPD). The maximum value for total compliance (C_3) is taken from Kobayashi et al. (1987) and represents the compliance in healthy subjects. C_2 has been chosen to have an intermediate value between C_1 and C_3; a value of the same order (C=8·10^{-6} m^3/Pa) has been suggested also by Diong et al. (2007) as the alveolar compliance in his extended RIC model (Section 1.4.2)**.** The alveolar compliances values, considered in this thesis, are shown in **Table 4.2**.

C_1	C_2	C_3
$1.9 \cdot 10^{-9}$	$5 \cdot 10^{-8}$	$1.9 \cdot 10^{-6}$

Table 4.2: Total peripheral compliances values in m^3/Pa for normal (C_3) and lungs with chronic obstructive pulmonary disease (C_1). C_2 has a an intermediate value between C_1 and C_3

4.2.3 One-dimensional models

The models under consideration are simplifications of Weibel's model (Weibel, 1963). Since geometrical and mechanical properties of the models refer to human airways, these models are able to describe propagation of air pulses in simple systems of flexible tubes, as in the previous chapter, but with a more physiological relevance.

4.2.3.1 Bifurcation model

Bifurcation model (**Figure 4.1a**) is a 1-D model of the first bifurcation of respiratory system: the segment of generation zero (trachea) bifurcates in two segments of

Generation 1 (left and right main bronchi). The values for the morphological and elastic parameters, shown in **Table 4.3** are derived from **Table 2.3** referring to generation 0 and 1. Since the main bronchi are assumed to be segments in parallel, the total peripheral resistance, coupled to each terminal segment, is doubled and the compliance is halved as shown in **Table 4.3** in correspondence of R and C.

z	**n**	**A_0** (m^2)	**E** (MPa)	**h** (mm)	**l** (m)	**R** ($Pa \cdot s/m^3$)	**C** (m^3/Pa)
0	1	$2.50 \cdot 10^{-4}$	2.95	1.4	0.12	-	-
1	2	$1.16 \cdot 10^{-4}$	2.95	1.3	0.047	$2R_1$ $2R_2$ $2R_3$	$C_1/2$ $C_2/2$ $C_3/2$

Table 4.3: Bifurcation model (trachea and main bronchi), number of segments (n), initial cross sectional area (A_0), Young's modulus (E), wall thickness (h), length (l), values for peripheral resistance (R) and compliance (C) (**Table 4.2**), coupled to each terminal 1-D segment, according to Weibel's generations (z).

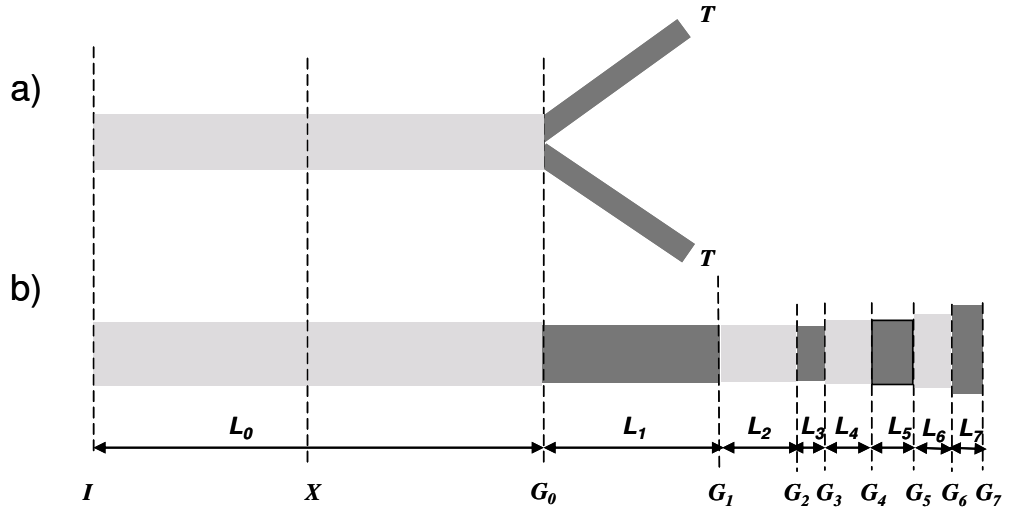

Figure 4.1 Schematic representation of a) Bifurcation model with trachea and main bronchi and b) Multivessel model. G indicates the reflection sites whose subscripts denote Weibel's generation of the corresponding tube, L is the lengths, I is the input and T is the terminal point of the main bronchi in Bifurcation model. The site selected as observation poin pressure (X), for calculations, is at midpoint of the trachea (60mm from the inlet).

4.2.3.2 Multivessel model

Multivessel model (**Figure 4.1b**) consists of a sequence of eight one-dimensional tubes modelling the central airways. Each tube corresponds to one of the eight generations of Weibel's model (from 0 to the 7^{th}), the values for E, h, l are the same of **Table 2.3**, the total cross sectional area is calculated as $A_t=A_0 \cdot n$ (n is the number of segments). The distinctive values for the Multivessel model are shown in **Table 4.4**.

z	**A_t** (m^2) x10^{-4}	**E** (MPa)	**h** (m)	**l** (m)	**R** (Pa·s/m^3)	**C** (m^3/Pa)
0	2.50	2.95	1.4	0.12	-	-
1	2.30	2.95	1.3	0.0476	-	-
2	2.03	1.48	1.3	0.019	-	-
3	1.81	0.058	1.3	0.0076	-	-
4	2.22	0.058	1.2	0.012	-	-
5	2.73	0.058	1	0.0107	-	-
6	3.94	0.058	1	0.009	-	-
7	5.31	0.058	0.9	0.0076	R_1 R_2 R_3	C_1 C_2 C_3

Table 4.4: total cross section area (A_t), Young's modulus (E), wall thickness (h), length (l) and peripheral resistance (R) and compliance (C) (from **Table 4.1** and **Table 4.2**) according to Weibel's generations (z).

4.3 Results

4.3.1 Wave speed correction

The wave speed values in each domain of the considered models, calculated using Eq.(2.12), are shown in form of histogram, in **Figure 4.2**. Since the calculated wave speeds of the three segments of the Bifurcation model and the first three segments of the Multivessel model are above the sound speed in free air (*Cs*), for all these segments the parameter β has been changed in order to match *Cs* according to Equation 2.25. **Table 4.5** shows the reflection coefficient (R_f) and the characteristic impedance of the terminal segment associated with the 1-D models (Bifurcation and Multivessel) after the wave speed correction.

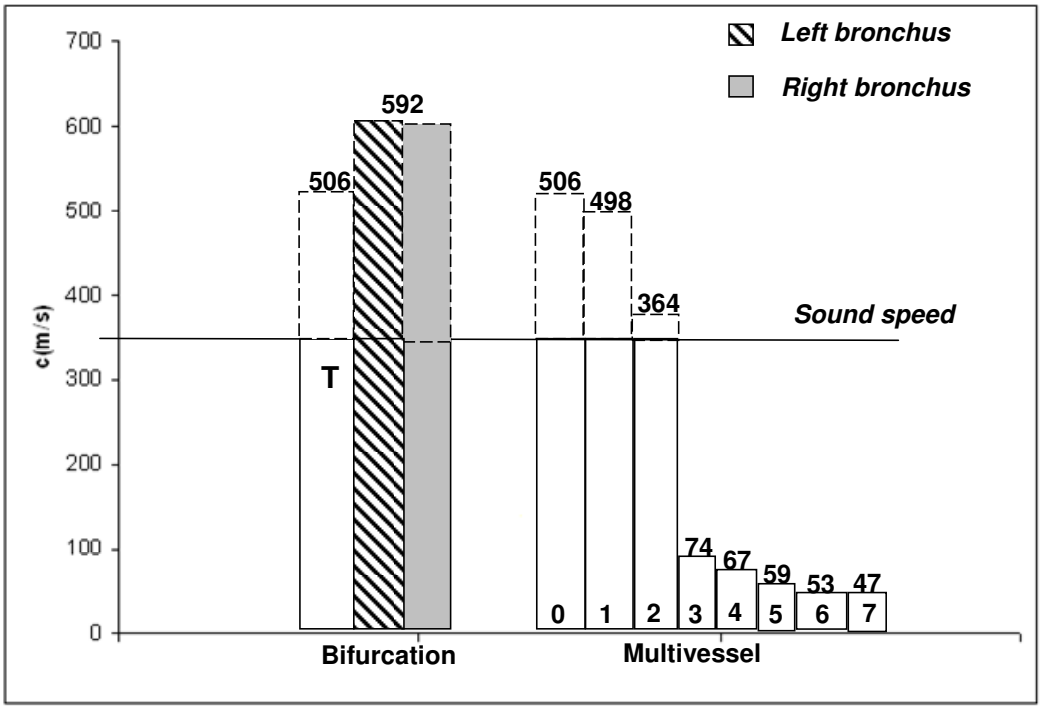

Figure 4.2: Wave speed in each segment of the two models under consideration (the value for wave speed in m/s is shown on the top of each rectangle). The horizontal line denotes the value for the speed of sound in free air (C_s=343m/s), T denotes the tracheal segment.

	Bifurcation			**Multivessel**								
	G_0	R_1	R_3	G_0	G_1	G_2	G_3	G_4	G_5	G_6	R_1	R_3
R_f	0.04	-0.98	-0.72	0.04	0.06	-0.61	-0.15	-0.17	-0.22	-0.21	-0.71	0.46
$\mathbf{Z_0\ (Pa{\cdot}s/m^3)}$ x10^4	358			10.6								

Table 4.5 Reflection coefficients (R_f) associated to the interfaces (G_i) shown in **Figure 4.1** and to the peripheral resistances R_1 and R_3. Z_0 is the characteristic impedance of the terminal segment for each of the models under consideration ($Z_0 = \rho c / A_e$). The values are calculated after the wave speed correction.

4.3.2 Short pulse

Computational pressure waves at the midpoint of the trachea, obtained with the short pulse enforced at the inlet of the two 1-D models, are shown in **Figure 4.3**. The outlet conditions refer to peripheral resistance for normal (R_1) and emphysematous lungs (R_3). **Table 4.6** and **Table 4.7** provide the wave paths, theoretical arrival times (defined in Section 3.3) and the theoretical amplitude for the waves associated respectively to Bifurcation and Multivessel model. The theoretical amplitude are calculated accordingly to the theory of linear analysis of wave reflection (Section 2.2.3.8), considering the reflection coefficients shown in **Table 4.5**.

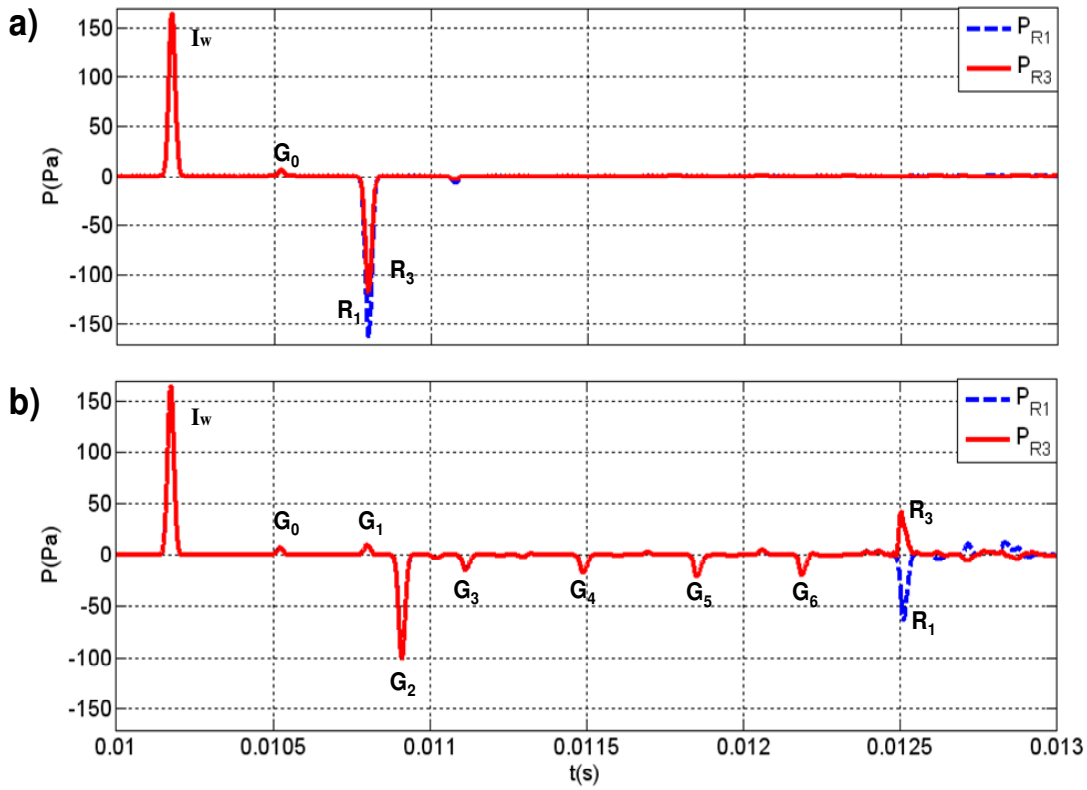

Figure 4.3 Computational pressure waveforms at the mid-point of the trachea (60mm from its inlet) when the short pulse propagates in a) Bifurcation, and b) Multivessel model. I_w indicates the incident wave. The waves are identified through their time of arrival calculated from the length (l) and wave speed (c) in each segment according to **Table 4.6** and **Table 4.7** . The peaks are the reflected waves from the boundaries shown in **Figure 4.1** and from the different terminal resistances (R_1 and R_3, respectively the peripheral resistance associated to normal and emphysematous lung).

Wave	Wave path	t(s)	Theoretical amplitude(Pa)
I_w	IX	0.01018	165
G_0	IXG_0X	0.01052	6.6
R_1	IXG_0TG_0X	0.01080	-162
R_2			-119

Table 4.6 Bifurcation model: wave paths and associated wave with theoretical arrival time of peaks (Eq. 3.2) at the middle point of the mother tube (point X). I_w indicates the incident wave The numbering refers to **Figure 4.1**, wave path is defined according to Section 3.3. The theoretical amplitudes are calculated based on the amplitude according to the linear analysis of wave refection (Section 2.2.3.8).

The waves shown in **Figure 4.3** are associated to the corresponding paths accordingly to the arrival times of waves shown in **Table 4.6** and **Table 4.7**. The peaks are the reflected waves from the boundaries (G_i) shown in **Figure 4.1** and from the different terminal resistances (R_1 and R_3, respectively the peripheral resistance associated to normal and emphysematous lung). The computational peaks of the first reflections, in **Figure 4.3**, appear exactly at the time defined in **Table 4.6** and **Table 4.7** with the same amplitude as specify by the tables.

Wave	Wave path	t(s)	Amplitude(Pa)
I_w	IX	0.01018	165
G_0	IXG_0X	0.01052	6.8
G_1	$IXG_0G_1G_0X$	0.01080	9.9
G_2	$IXG_0G_1G_2G_1G_0X$	0.01091	-100
G_3	$IXG_0G_1G_2G_3G_2G_1G_0X$	0.01112	-15.4
G_4	$IXG_0G_1G_2G_3G_4G_3G_2G_1G_0X$	0.01149	-17.1
G_5	$IXG_0G_1G_2G_3G_4G_5G_4G_3G_2G_1G_0X$	0.01185	-21.6
G_6	$IXG_0G_1G_2G_3G_4G_5G_6G_5G_4G_3G_2G_1G_0X$	0.01219	-19.5
R_1	$IXG_0G_1G_2G_3G_4G_5G_6G_7G_6G_5G_4G_3G_2G_1G_0X$	0.01251	-63.7
R_2			41.3

Table 4.7 Multivessel model: wave paths with theoretical arrival time (Eq.3.2) of the peaks at the middle point of the mother tube (point X). I_w indicates the incident wave. The numbering of path refers to **Figure 4.1**, wave path is defined according to Section 3.3. The amplitudes refer to the calculated amplitude using the linear analysis of wave reflection (Section 2.2.3.8).

4.3.3 Impulse oscillometry system (IOS) pulse

The effects due to a decrease of compliance in RC models, coupled to the 1-D models of **Figure 4.1**, on the computational pressure waveforms with the IOS pulse enforced at the inlet (Eq. 4.2) are shown in **Figure 4.4**: R_2 is maintained constant while the compliance is varied from C_1 to C_3. Pressure waveforms are also shown for the single resistance (R_2) and single compliance model (C_3).

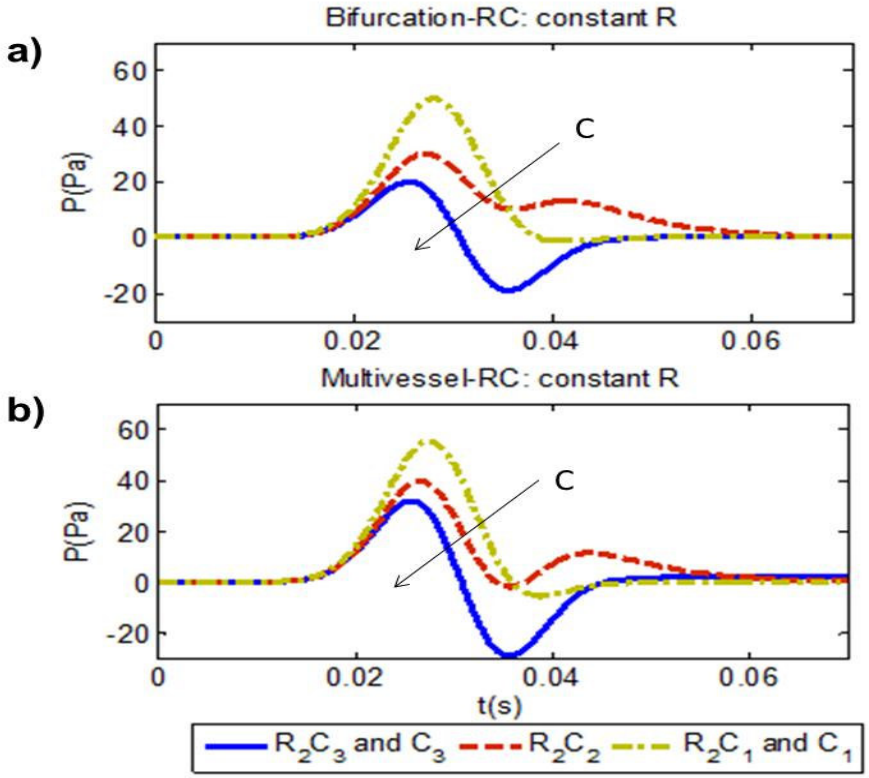

Figure 4.4 Pressure waveforms at the mid-point of the trachea generated by the IOS pulse (Eq. 4.2) in a the 1-D models under consideration. A 0-D two element Windkessel model (RC), for peripheral airways, is coupled respectively with Bifurcation (a) and Multivessel model (b). In order to simulate the effects of a decrease in compliance, R has been kept constant at an average resistance value (R_2) and C has been varied from healthy (C_3) to pathologic compliance (C_1). The arrows indicate the direction of increase for C. Figures on the left show also results for only resistance (R_2) and only compliance (C_3) models.

Using the same models (RC coupled to 1-D models of **Figure 4.1**), **Figure 4.5** shows the effects on computational pressure waveforms when the resistance increases from healthy (R_1) to pathologic values (R_3), with the compliance value set to C_2. **Figure 4.6** is analogous to **Figure 4.4** and **Figure 4.5** together, but with R_mCR models, instead of RC, coupled to terminal segments of the 1-D models (**Figure 4.1**); R_m is the

characteristic impedance of the terminal segment of the 1-D model (defined in Section 2.2.5). The results only differ in the boundary conditions enforced at peripheral airways. On the left of **Figure 4.6** R_2 is maintained constant, but the compliance is varied from C_1 to C_3. Pressure waveforms are also shown for the single resistance (R_2) and single compliance model (C_3). On the right of **Figure 4.6** C_2 is maintained constant and the three values for resistance are considered (R_1, R_2, R_3). In general P increases with increasing R and decreases with increasing C in both RC and R_mCR models.

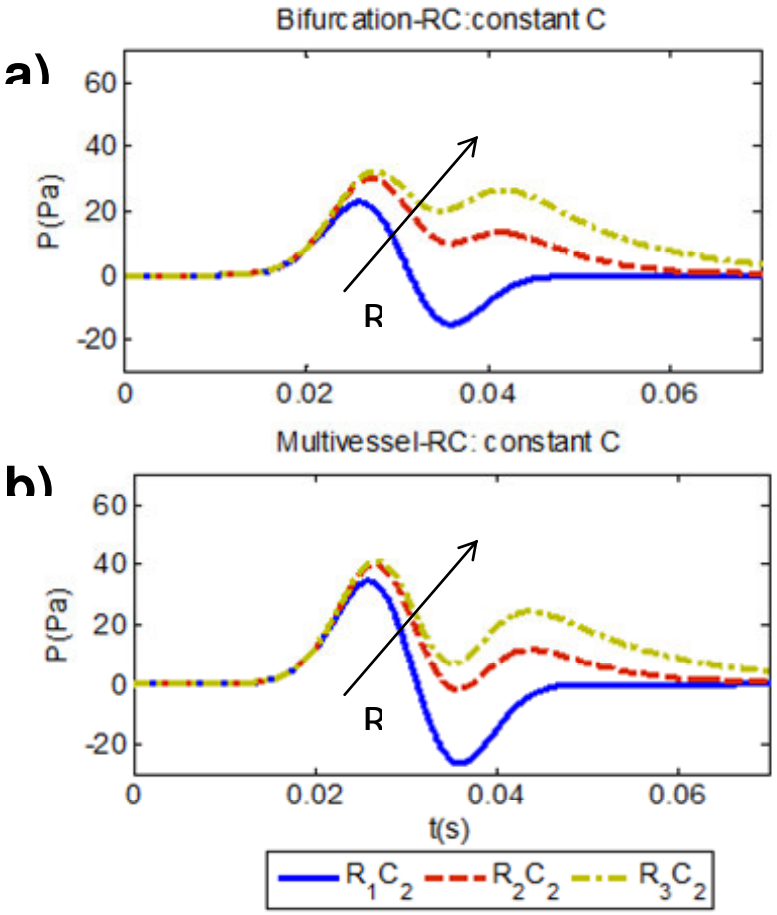

Figure 4.5 Pressure waveforms at the mid-point of the trachea generated by the IOS pulse (Eq. 4.2) in a the 1-D models under consideration. A 0-D two element Windkessel model (RC), for peripheral airways, is coupled respectively with Bifurcation (a) and Multivessel model (b). In order to simulate the effects of an increase of peripheral airway resistance, C has been kept constant at an average resistance value (C_2) and R has been varied from healthy (R_1) to pathologic resistance (R_3). The arrows indicate the direction of increase for R.

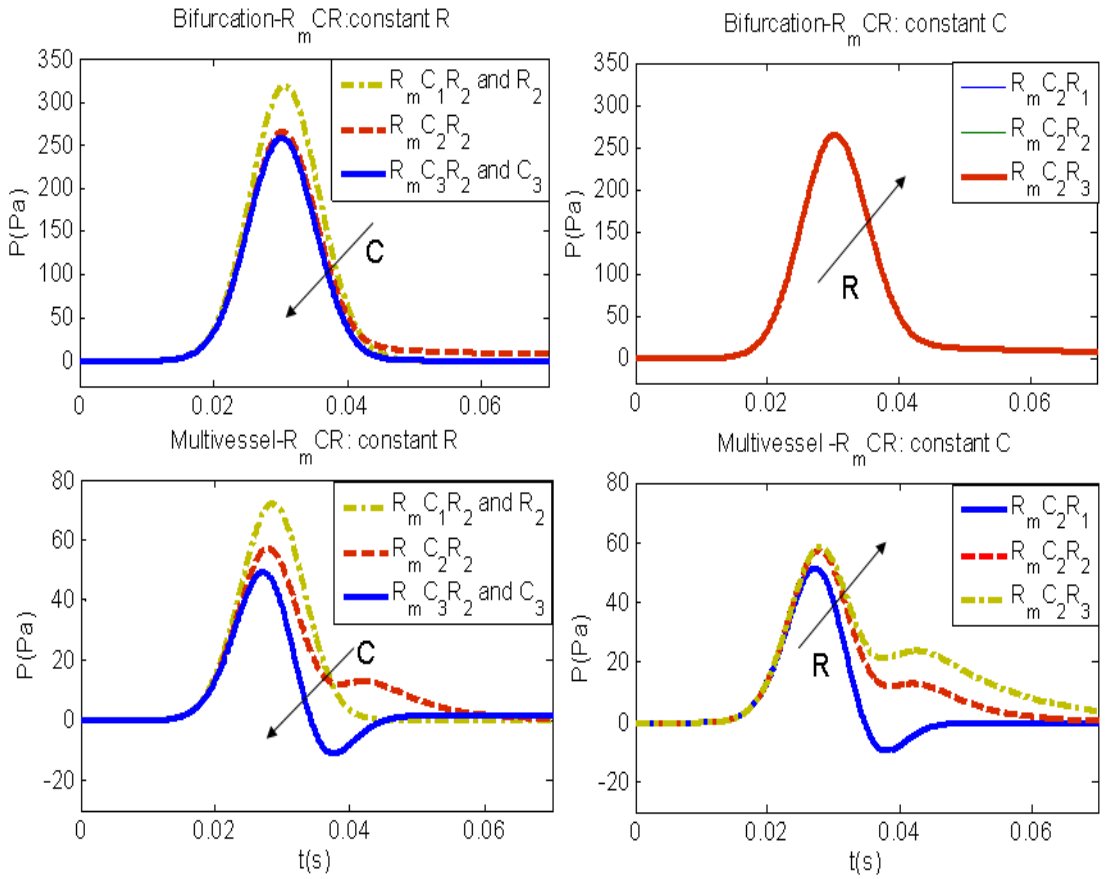

Figure 4.6 Pressure waveforms at the mid-point of the trachea generated by the IOS pulse in all the three 1-D models under consideration. Windkessel three parameters model (R_mCR) is coupled respectively with Bifurcation and Multivessel model. R_m is the characteristic impedance of the terminal segment of the 1-D model (Section 2.2.5). Two different groups of simulations are considered: in the first group (left figures) R has been kept constant at an average resistance value (R_2) and C has been varied from healthy (C_3) to pathologic compliance (C_1). In the second group (right figures) constant average compliance (C_2) has been considered, and R has been varied from healthy (R_1) to pathologic resistance (R_3). The arrows indicate the direction of increase for both R or C.

4.4 Discussions

In this study two pulses have been generated at the inlet of the computational simplified models of human central airways and the pressure waveforms have been calculated at a point close to the inlet. The relative accuracy of the model in determining the correct amplitudes and arrival times of the reflected waves has been demonstrated by comparing the values in **Table 4.6** and **Table 4.7**, determined with the theoretical linear analysis of wave reflections (Section 2.2.3.8), with the computational pressure

waveforms in **Figure 4.3** when the short pulse is enforced. According to Feng and Khir (2008) it is possible to classify a wave according to its effect on pressure: a compression wave induces an increase while a expansion (or decompression) wave induces a decrease in pressure. All the reflection sites with negative values of R_f (**Table 4.5**) generate, in **Figure 4.3,** backward decompression waves while the positive ones generated backward compression waves, which is in line with theoretical expectations. The two resistances coupled at each 1-D model and associated to normal (R_1) and emphysematous (R_3) peripheral airways generate different terminal reflection coefficient (**Table 4.5**) and, consequently, different amplitude of the reflected waves from the periphery. In particular in the Multivessel model the reflected wave from the periphery (**Figure 4.3**) changes from being a backward decompression wave (with normal peripheral resistance associated to R_f = -0.71) to backward compression wave (emphysematous peripheral resistance, R_f= 0.46).

The second pulse has a duration of approximately 40ms, similar to the one commonly used in impulse oscillometry (Smith et al., 2005). Several 0-D peripheral models have been presented according to this input. In this work the two-element (RC) Windkessel model has been used as a model for peripheral airways based on a recently proposed model for airways which accounts for a separate peripheral compartment (extended RIC model) (Diong et al., 2007); R stands for peripheral resistance of airways and C is the compliance of the alveolar region. In **Figure 4.4** the waveforms referring to R_2 and C_3 models are not visible because they are completely identical respectively to R_2C_1 and R_2C_3. Therefore, once the peripheral resistance has been kept constant in RC models the pressure waveform, calculated at a position close to the inlet, varies passing from a single resistance model (R_2) (in correspondence of low alveolar compliance, R_2C_1) to single compliance model (C_2) (in correspondence of high alveolar compliance, R_2C_3) by increasing the compliance value.

Figure 4.5 shows that the pressure waveforms at the inlet of each system are sensitive also to changes in resistance values once the compliance has been kept constant (C_2). Since the values of resistance and compliance have been selected to reproduce normal and pathological airway conditions, the results appear of physiological interest. In the 1-D model of central airways coupled with 0-D R_mCR models of periphery (**Figure 4.6**) presented in this work, relevant changes in pressure waveforms can be observed only in the Multivessel model in relation with changes of peripheral resistance or compliance. These can be explained by comparing the values of the peripheral resistance with the characteristic impedance values in **Table 4.5**: while in the Bifurcation model $Z_0 >> R_1$

and $Z_0 >> R_3$, in Multivessel model the values are almost of the same order. These considerations reveal that using R_mCR models, significant differences of pressure waveforms can be identified only if the characteristic impedance of the terminal 1-D segment has a value comparable with the peripheral resistances under consideration.

4.5 Conclusions

In this chapter the time-domain 1-D model has been shown to be suitable for studying the propagation of air waves in flexible tubes, with mechanical and geometrical properties close to the physiologic airways, with different outlet boundary conditions. The results indicate that the model is able to accurately predict the wave timing and amplitude compared to a theoretical linear analysis of wave reflections. Calculated pressures waveforms at a site close to the inlet are shown to change accordingly to both peripheral resistance and compliance variations, suggesting a possible non invasive assessment of peripheral conditions. The 1-D modelling, after being successfully applied to simplified airways model in this chapter, will be used, in the next chapter, to describe more physiological and complex structures enhancing the characteristic asymmetrical and bifurcating tree nature of the human airways.

Chapter 5

Computational results: physiological models of human central airways

5.1 Introduction

Most of the morphometric data regarding the respiratory tree derived from measurements on cast and, due to their amount, these data have been organized in form of models; in Section 1.3.2 Weibel and Horsfield's model were presented for central airways. These two models are the most widely used in literature; the Weibel's model is simpler in terms of information required to describe a single bifurcation: "for a given parent diameter and length, a symmetrical bifurcation may be specified by fixing a diameter, a length and an angle for the daughters" (Phillips and Kaye, 1997). The real branching structure of airways is significantly asymmetrical in human and it is even more marked in other species such as dogs and rats. Although Horsfield's model provides an asymmetrical structure for human bronchial tree, closer to the physiological structure than the symmetrical model, comparisons between these two models are still very limited in literature. This chapter is organized to present firstly the results according to the symmetrical model and then the study will be expanded to the more complex asymmetrical structure. Pulses are generated in the respiratory tree either naturally, during normal respiration, or artificially using artificial ventilation or forced oscillation technique (FOT) and impulse oscillometry (IOS). Two compression waves (short pulse and IOS pulse) were considered in the previous chapter (Section 4.2.1) according to geometries similar to the experimental setups of Chapter 3. This chapter aims to expand the study of air wave propagation to 'more physiological' 1-D models of central airways and 'more physiological' inflow conditions: a new inflow boundary condition is introduced in this chapter to simulate the normal inspiration phase of the breathing.

5.2 Inflow boundary condition

Three different pulses are considered as inflow boundary conditions in this chapter: two forward compression waves (enforced at the inlet of trachea) which run from trachea to periphery and one backward expansion waves which runs from periphery to trachea to reproduce one single inspiration process.

5.2.1 Forward Compression waves

The inlet of trachea is assumed to behave as an absorbing site ($R_f=0$) after the generation of the pulse. The two compression forward waves pulses enforced at the inlet of the trachea, in both symmetrical and asymmetrical models (in m^3/s), are the same as defined by Eq. (4.1) and (4.2) respectively for Short pulse and Impulse oscillometry system (IOS) pulse.

Short pulse:

$$q(t) = 10^{-4} \cdot e^{-10^{9.7}\cdot(t-0.01)^2} \tag{5.1}$$

Impulse oscillometry system (IOS) pulse:

$$q(t) = 0.15\times10^{-3} e^{-10^{4.8}(t-0.03)^2} \tag{5.2}$$

5.2.2 Backward expansion waves (inspiration phase)

The inspiratory airflow waveforms is commonly assumed as a sine function of time (Mead, 1963; Otis et al., 1950). Lafortuna et al. (1984) measured the inspiratory flow pattern (in m^3/s) at rest in the mouth (q_m) of six healthy adult males providing the following function of time t:

$$q_m(t) = 0.644\cdot10^{-3}\times\sin\frac{2\pi t}{T_i} \tag{5.3}$$

Where T_i is the inspiratory time. During a normal inspiration as the diaphragm and intercostal muscles move to increase the size of the thorax, the pressure within alveoli decreases below atmospheric pressure and air moves into the lungs. The inspiration can be therefore interpreted as expansion waves propagating from the alveoli to the mouth. Equation 5.3 is used to derive an estimation of the flow in a generic terminal segment (q_i) of the 1-D symmetrical and asymmetrical models using the following expression

$$q_i(t) = \begin{cases} q_m(t)\times K & t < T_i \\ 0 & t > T_i \end{cases} \tag{5.4}$$

Where K is a coefficient that describes the flow in the terminal segments as percentage of the flow in the trachea as suggested by Horsfield et al. (1971). In the symmetrical model with 7 generations and 2^7=128 terminal segments, K=1/128 while for the asymmetrical model K will be define in Section 5.4.2**.**

5.3 Outlet boundary conditions

The 0-D models of flow in the periphery, described in Section 4.2.2, are used also in this chapter: R model, two-element (RC) and three-element (R_mCR) Windkessel models. The three values for total peripheral resistance and total alveolar compliance according to normal and pathological conditions were defined in **Table 4.1** and **Table 4.2**; their values are summarized in **Table 5.1**.

Perypheral Airways properties	**Minimum values R_1, C_1**	**Average values R_2, C_2**	**Maximum values R_3, C_3**
R (Pa·s/m^3)	$17 \cdot 10^3$	$154 \cdot 10^3$	$291 \cdot 10^3$
C (m^3/Pa)	$1.9 \cdot 10^{-9}$	$5 \cdot 10^{-8}$	$1.9 \cdot 10^{-6}$

Table 5.1 Total peripheral resistances (Section 4.2.2). for normal (R_1) and emphysematous lungs (R_3). $R_2 = \frac{R_1 + R_3}{2}$ and total peripheral compliances values for normal (C_3) and lungs with chronic obstructive pulmonary disease (C_1). C_2 has been chosed to have an intermediate value between C_1 and C_3.

5.4 Bifurcating tree models

Since the 1-D modelling has been validated and applied in simplified models described in chapter 3 and chapter 4, more complex geometries are considered in this chapter following the more physiological features of bifurcating tree structure typical of the respiratory system.

5.4.1 Weibel's model of central airways

Following Kobayashi et al. (1987) the central airway resistance (R_c), in this thesis, are defined as the summation of the resistance from generation 0 (trachea) to Generation 7, and the resistance of peripheral airways (R_p) as the sum of the resistances from Generation 8 to Generation 23.

z	n	A_0 (m^2) $\cdot 10^{-4}$	E (MPa)	h (m) $\cdot 10^{-3}$	l (m)	R (Pa·s/m^3)	C (m^3/Pa)
0	1	2.4969	2.95	1.4	0.12	-	-
1	2	1.1499	2.95	1.3	0.0476	-	-
2	4	0.5090	1.48	1.3	0.019	-	-
3	8	0.2273	0.058	1.3	0.0076	-	-
4	16	0.1392	0.058	1.2	0.012	-	-
5	32	0.0085	0.058	1	0.0107	-	-
6	64	0.0061	0.058	1	0.009	-	-
7	128	0.0041	0.058	0.9	0.0076	$128 \cdot R_1$ $128 \cdot R_2$ $128 \cdot R_3$	$C_1/128$ $C_2/128$ $C_3/128$

Table 5.2: number of segments (n), cross sectional area (A_0), Young modulus (E), wall thickness (h), length (l) and peripheral resistance (R) and compliance (C) (values R_1, R_2, R_3 and C_1, C_2, C_3 refer to **Table 5.1**) according to Weibel's generations (z).

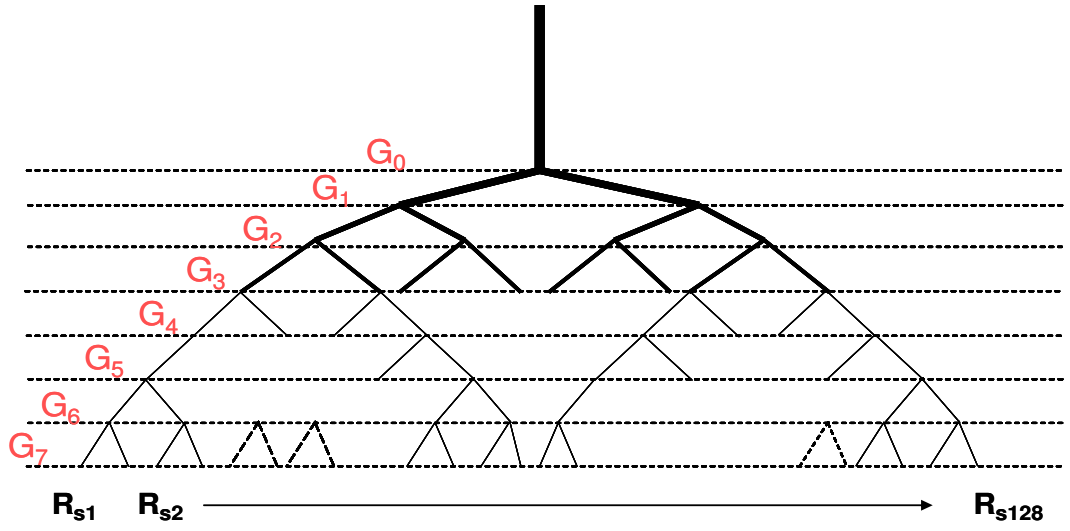

Figure 5.1 Symmetrical model: model of central airways (from generation 0 to generation 7). G describes a bifurcation whose subscript denotes the generation of the corresponding parent vessel.

In this thesis 1-D modelling has been used for the central airways while the fluid dynamic conditions of peripheral airways have been modelled using lumped parameters (Section 2.2.5). **Figure 5.1** shows a schematic representation of the 1-D model of seven generations. The values shown in **Table 5.2** are taken from **Table 2.3**. All the peripheral airways (2^7=128 terminal segments) are assumed to be in parallel therefore the values for R and C (shown in **Table 5.1**), coupled to each terminal segment, are respectively multiplied and divided by 128 as shown in **Table 5.2**.

5.4.2 Horsfield's complete model of central airways

The central airways considered for the 1-D asymmetrical model are totally 33 (with 17 terminal segments) and follow the numbering (N) given by Horsfield et al. (1971) as shown in **Figure 5.2**. Details about the model were provided in **Table 2.4**. Because of the asymmetry of the model, the assignation of peripheral resistance and compliance to each 1-D terminal segment is more complex than the Weibel's symmetrical model. For this reason the attribution of R and C is based on the proportion of the number of end branches that each terminal central airways supplies. The qualitative assumption is that the more are the alveoli available at the considered terminal segment, the more compliant and less resistive that peripheral region would be. In **Table 2.4**, T denote the number of "end branches" supplied by each airway. For example, the number of distal branches supplied by trachea (T_0) equals 216544. The parameter K defines the ratio of the end branches number supplied by the considered airway (i) over the total supplied by trachea ($K_i = T_i/T_0$). It is therefore reasonable to consider K for approximating the peripheral asymmetrical distribution of R and C, as previously used to determine the flow in Eq. 5.4. Assuming the end branches as segments in parallel, the estimated value of resistance (R_s) and compliance (C_s) assigned to each terminal central airway (i) in **Figure 5.2** is calculated as

$$R_{si}=R/K_i \tag{5.5}$$

$$C_{si}=C\cdot K_i \tag{5.6}$$

where R and C are the total resistance and compliance values for peripheral airways (**Table 5.1**). **Table 5.3** shows all the values for R and C and all the properties (mechanical and geometrical) associated to the central airway segments of the asymmetrical model.

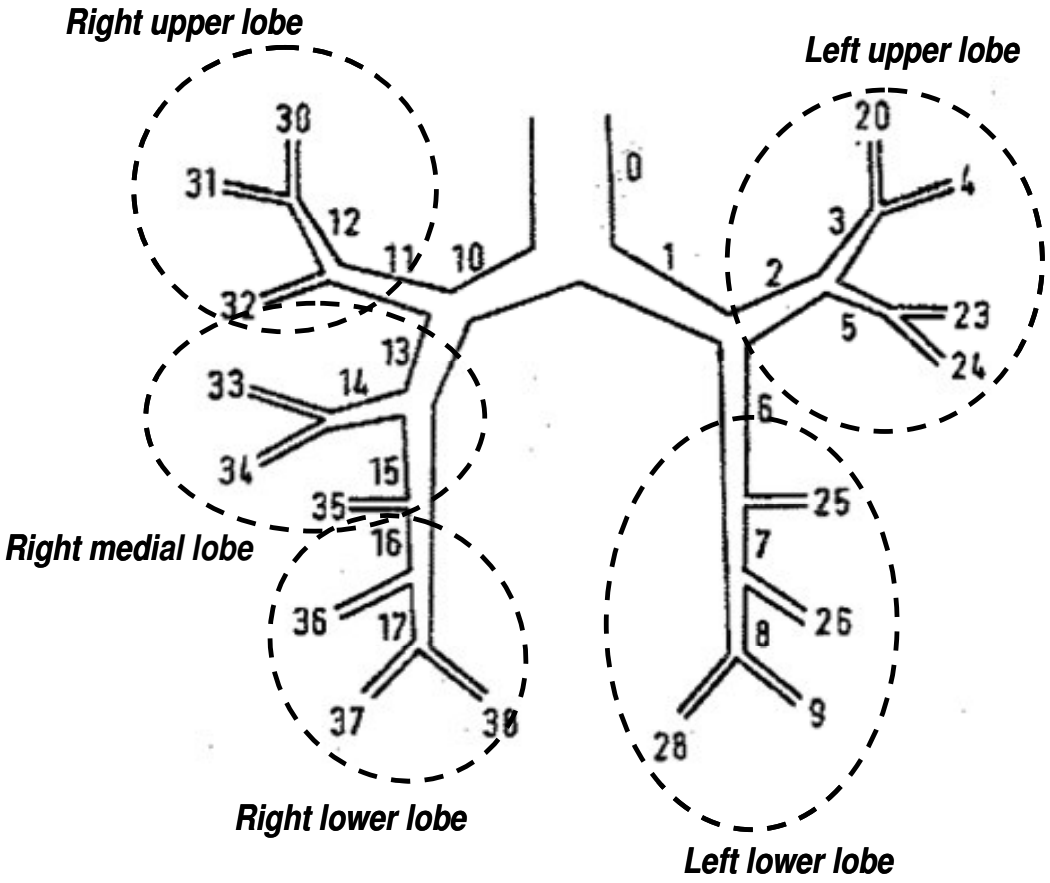

Figure 5.2 Asymmetrical model of human central airways (Modified from Horsfield et al., 1971), all the terminal segments are classified by lobes.

Table 5.3 Initial cross sectional area (A_0), Young modulus (E), wall thickness (h), length (l) and peripheral resistance (R) and compliance (C) (values R_{1s}, R_{2s}, R_{3s} and C_{1s}, C_{2s}, C_{3s} are calculated using Eq.s 5.5 and 5.6) according to each branch number (branch number) of Horsfield's model (**Figure 5.2**). K defines the ratio of the number of end branches supplied by the considered airway (i) over the total supplied by trachea.

branch number	A_0 (m^2)	E (MPa)	h (mm)	l (m)	K	R_{1s} ($Pa \cdot s/m^3$)	R_{2s} ($Pa \cdot s/m^3$)	R_{3s} ($Pa \cdot s/m^3$)	C_{1s} (m^3/Pa)	C_{2s} (m^3/Pa)	C_{3s} (m^3/Pa)
0	$2.29 \cdot 10^{-4}$	2.95	1.4	0.1	1.000	-	-	-	-	-	-
1	$1.19 \cdot 10^{-4}$	2.95	1.3	0.05	0.455	-	-	-	-	-	-
2	$4.07 \cdot 10^{-4}$	1.48	1.3	0.016	0.205	-	-	-	-	-	-
3	$3.83 \cdot 10^{-4}$	0.53	1.3	0.001	0.141	-	-	-	-	-	-
4	$1.59 \cdot 10^{-4}$	0.39	1.2	0.009	0.064	277761	2432980	4588829	1.19E-10	3.18E-09	1.26E-07
5	$1.98 \cdot 10^{-4}$	0.43	1.1	0.011	0.064	-	-	-	-	-	-
6	$4.73 \cdot 10^{-4}$	1.48	1.3	0.011	0.249	-	-	-	-	-	-
7	$2.93 \cdot 10^{-4}$	0.49	1.3	0.018	0.202	-	-	-	-	-	-
8	$3.47 \cdot 10^{-4}$	0.51	1.2	0.0045	0.125	-	-	-	-	-	-
9	$1.98 \cdot 10^{-5}$	0.43	1.1	0.0075	0.078	227067	1988938	3751324	1.46E-10	3.89E-09	1.55E-07
10	$1.00 \cdot 10^{-4}$	2.95	1.3	0.022	0.545	-	-	-	-	-	-
11	$3.83 \cdot 10^{-5}$	1.48	1.3	0.0156	0.217	-	-	-	-	-	-
12	$5.43 \cdot 10^{-5}$	0.59	1.2	0.0064	0.110	-	-	-	-	-	-
13	$6.04 \cdot 10^{-5}$	1.48	1.3	0.026	0.328	-	-	-	-	-	-
14	$1.74 \cdot 10^{-5}$	0.41	1.2	0.021	0.096	-	-	-	-	-	-
15	$2.82 \cdot 10^{-5}$	0.48	1.3	0.008	0.232	-	-	-	-	-	-
16	$2.43 \cdot 10^{-5}$	0.46	1.3	0.0084	0.163	-	-	-	-	-	-
17	$2.62 \cdot 10^{-5}$	0.47	1.3	0.0148	0.127	-	-	-	-	-	-
20	$1.82 \cdot 10^{-5}$	0.41	1.1	0.0135	0.078	227067	1988938	3751324	$1.46 \cdot 10^{-10}$	$3.89 \cdot 10^{-9}$	$1.55 \cdot 10^{-7}$
23	$6.85 \cdot 10^{-6}$	0.28	1	0.0115	0.036	48551	4252771	8021123	$6.83 \cdot 10^{-11}$	$1.82 \cdot 10^{-9}$	$7.23 \cdot 10^{-8}$
24	$6.85 \cdot 10^{-6}$	0.28	1.1	0.0075	0.027	642137	5624632	10608582	$5.17 \cdot 10^{-11}$	$1.37 \cdot 10^{-9}$	$5.46 \cdot 10^{-8}$
25	$1.98 \cdot 10^{-5}$	0.43	1	0.0085	0.047	375589	3289879	6205020	$8.83 \cdot 10^{-11}$	$2.35 \cdot 10^{-9}$	$9.34 \cdot 10^{-8}$
26	$1.59 \cdot 10^{-5}$	0.39	1.1	0.0115	0.078	227067	1988938	3751324	$1.46 \cdot 10^{-10}$	$3.89 \cdot 10^{-9}$	$1.55 \cdot 10^{-7}$
28	$1.59 \cdot 10^{-5}$	0.39	1	0.0085	0.047	375589	3289879	6205020	$8.83 \cdot 10^{-10}$	$2.35 \cdot 10^{-9}$	$9.34 \cdot 10^{-8}$
30	$9.39 \cdot 10^{-6}$	0.32	1.1	0.002	0.078	227067	1988938	3751324	$1.46 \cdot 10^{-10}$	$3.89 \cdot 10^{-9}$	$1.55 \cdot 10^{-7}$
31	$9.39 \cdot 10^{-6}$	0.32	0.9	0.0134	0.032	550403	4821113	9093070	$6.03 \cdot 10^{-11}$	$1.6 \cdot 10^{-9}$	$6.37 \cdot 10^{-8}$
32	$1.98 \cdot 10^{-5}$	0.43	1.2	0.017	0.107	164514	1441021	2717901	$2.02 \cdot 10^{-10}$	$5.36 \cdot 10^{-9}$	$2.13 \cdot 10^{-7}$
33	$9.39 \cdot 10^{-6}$	0.32	1.1	0.01	0.048	367500	3219020	6071373	$9.03 \cdot 10^{-11}$	$2.4 \cdot 10^{-9}$	$9.55 \cdot 10^{-8}$
34	$1.18 \cdot 10^{-5}$	0.35	1.1	0.0096	0.048	367500	3219020	6071373	$9.03 \cdot 10^{-11}$	$2.4 \cdot 10^{-9}$	$9.55 \cdot 10^{-8}$
35	$1.18 \cdot 10^{-5}$	0.35	1	0.0062	0.069	256303	2245025	4234327	$1.29 \cdot 10^{-10}$	$3.44 \cdot 10^{-9}$	$1.37 \cdot 10^{-7}$
36	$5.54 \cdot 10^{-6}$	0.25	1	0.0062	0.036	485518	4252771	8021123	$6.83 \cdot 10^{-11}$	$1.82 \cdot 10^{-9}$	$7.23 \cdot 10^{-8}$
37	$1.44 \cdot 10^{-5}$	0.38	1.2	0.0068	0.064	277761	2432980	4588829	$1.19 \cdot 10^{-10}$	$3.18 \cdot 10^{-9}$	$1.26 \cdot 10^{-7}$
38	$2.25 \cdot 10^{-5}$	0.44	1.2	0.0106	0.064	277761	2432980	4588829	$1.19 \cdot 10^{-10}$	$3.18 \cdot 10^{-9}$	$1.26 \cdot 10^{-7}$

5.5 Results and discussions

5.5.1 Weibel's symmetrical model

5.5.1.1 Wave speeds and characteristic impedances

The values for wave speed, determined using Eq. 2.25, and the characteristic impedance for each of the eight generations of the symmetrical model are shown in **Table 5.4**. Since the first three generations (0-1-2) have a wave speed higher than the sound speed in free air (C_s=343 m/s) (bold values in **Table 5.4**), Cs has been enforced to be the wave speed for these segments (Section 2.2.3.4).

z	**0**	**1**	**2**	**3**	**4**	**5**	**6**	**7**
c (m/s)	**506**→343	**592**→343	**514**→343	125	135	140	157	166
Z (Pa·s/m^3)	1.6x10^6	3.6x10^6	8.1x10^6	6.6x10^6	1.17x10^7	1.9x10^7	3.1x10^7	4.80x10^7

Table 5.4 Symmetrical model: wave speeds (c) and characteristic impedance (Z=ρc/A) for the seven central airways generation (z) of Weibel's model. The values in bold are corrected wave speeds according to Eq. (2.25).

5.5.1.2 Reflection coefficients and short pulse waveforms

Table 5.5 shows the reflection coefficients in correspondence of the bifurcations (G_i) indicated in **Figure 5.1** in the forward (+) and backward (-) direction (Section 2.2.3.8). **Figure 5.3** shows the pressure and velocity waveforms when the the short pulse is enforced at the inlet of the trachea in the symmetrical model of central airways. Apart from the first two bifurcations (G_0 with R_{f+}=0.04 and G_1 with R_{f+}=0.06) which generate backward compression waves in **Figure 5.3**, reflection coefficients for all the other bifurcations are negative and consequenty backward expansion waves are generated (**Figure 5.3**). The system appears in general well matched in the forward direction (low reflections); the appearance of the high reflection coefficient in G_2 is due to the big discontinuity of the wave speed passing from the segments of second generation (c=343 m/s) to the segments of the third generation (c=125m/s) as shown in **Table 5.4**. This discontinuity is mainly due to a significant decrease of the wall Young modulus (from 1.48 MPa to 0.058 MPa MPa; **Table 5.2**) associated to a reduction of the cartilage content, the stiffer component of airway wall.

		$R_{f\,P+}$	$R_{f\,D1}$ -	$R_{f\,D2}$ -
G_0		0.04	-0.52	-0.52
G_1		0.06	-0.53	-0.53
G_2		-0.42	-0.29	-0.29
G_3		-0.06	-0.47	-0.47
G_4		-0.09	-0.46	-0.46
G_5		-0.14	-0.43	-0.43
G_6		-0.13	-0.44	-0.44
G_7	R_1	-0.90	-	-
	R_3	-0.10		

Table 5.5 Reflection coefficients in the forward (+) and backward (-) directions (equations 2.44-2.46) associated to the bifurcations (G_i) shown in Figure 5.1and according to the two terminal reflections (Eq. 2.49) with normal (R_1) and emphysematous (R_3) lung resistance. The values are calculated after the wave speed correction (Table 5.4).

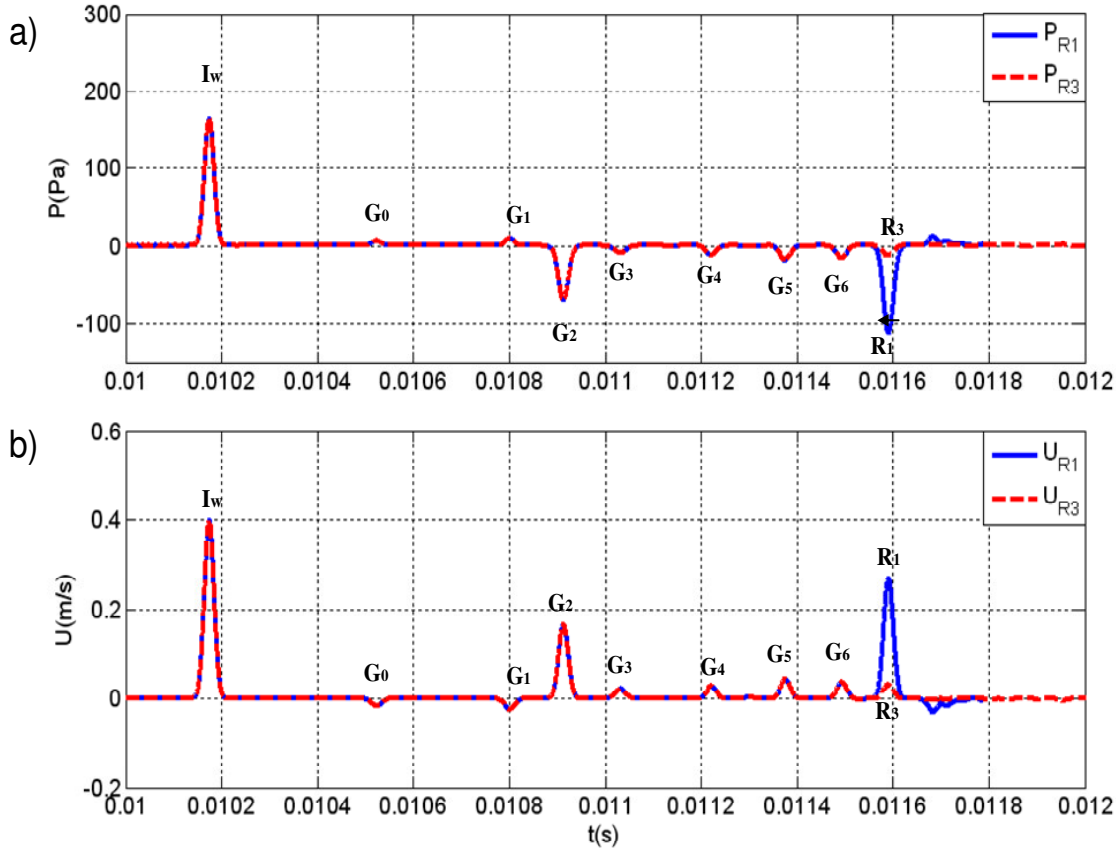

Figure 5.3: Computational pressure (a) and velocity (b) waveforms at the mid-point of the trachea (60mm from its inlet) when the short pulse (Section 5.2.1) propagates in the Symmetrical model of central airways. I_w denotes the incident wave. The waves are identified through their arrival time calculated from the length (l) and wave speed (c) in each segment. The peaks are the reflected waves from the boundaries shown in **Figure 5.1** and from the different terminal resistances (R_1 and R_3, respectively the peripheral resistance associated to normal and emphysematous lung).

The terminal reflection coefficients, associated to single resistance models with normal (R_1) and emphysematous (R_3) peripheral airways resistance values, change from being almost an open end condition (R_f+=-0.9) to an almost absorbing condition (R_f+=-0.1). This appears particularly clear comparing the pressure and velocity waveforms in the two cases (R_1 and R_3) of **Figure 5.3**.

5.5.1.3 Impulse oscillometry system (IOS) pulse

Similarly to the IOS pulse applied to the simplified models of central airways described in Section 4.3.3, **Figure 5.4** and **Figure 5.5** show the pressure waveforms for the symmetrical model when the IOS pulse is enforced at the inlet of trachea. The results only differ in the boundary conditions enforced at the peripheral airways. In **Figure 5.4** two element Windkessel model (RC) is considered for peripheral airways, while in **Figure 5.5** three Windkessel model (R_mCR) is used as lumped parameter model for periphery. On the left of the figures (panels 'a' of **Figure 5.4** and **Figure 5.5**) R_2 is maintained constant while the compliance is varied from C_3 to C_1 to reproduce the effects of the change in compliance, characteristic of restrictive pulmonary diseases (values from **Table 5.1)**. On the contrary, on the right of the Figures (panels b **Figure 5.4** and **Figure 5.5**) C_2 is kept constant and the three values for resistance are considered (R_1, R_2, R_3) reproducing the effects of increased resistance of obstructive pulmonary diseases (values from **Table 5.1)**. In **Figure 5.4,** starting from the RC models with constant R (panel 'a'), pressure waveforms are also shown for the single resistance (R_2) and single compliance model (C_3), they are not visible since they are completely identical respectively to R_2C_1 and R_2C_3. Analogously to the Bifurcation and Multivessel models (**Figure 4.4**), also for the Symmetrical model changes in compliance (simulating the restrictive pulmonary disease) affects the pressure waveforms in trachea. Once the peripheral resistance has been kept constant in RC models, the pressure waveforms vary passing from a single compliance model (C_3) (in correspondence of high alveolar compliance, R_2C_3) to a single resistance model (R_2) (in correspondence of low alveolar compliance, R_2C_1) by decreasing the compliance values. In panel 'b' of **Figure 5.4**, pressure waveforms in trachea are affected also by changes in resistance values (from R_1 to R_3 to reproduce a progression of an obstructive pulmonary disease) once the compliance has been fixed to C_2 value.

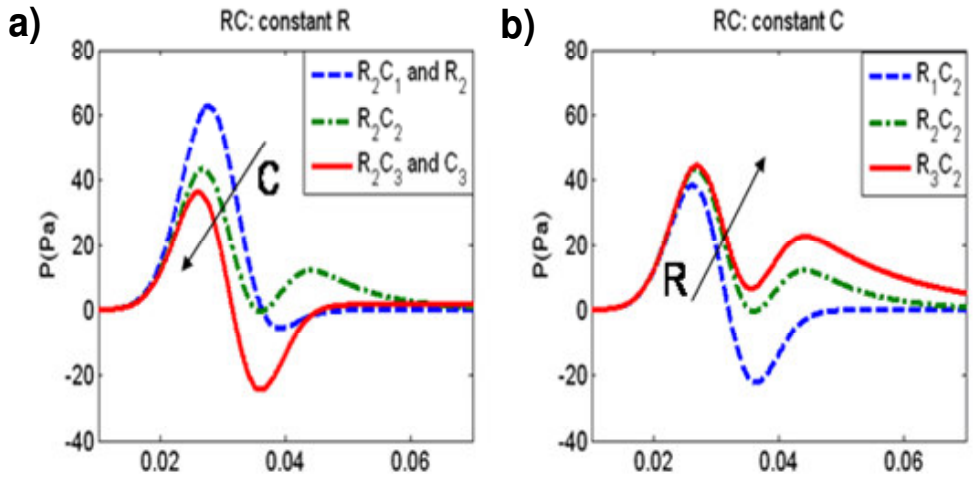

Figure 5.4 Pressure waveforms generated by the IOS pulse enforced at the inlet of trachea in the Symmetrical model. 0-D two element Windkessel models (RC) are coupled with the 128 terminal segments of the Symmetrical model. Two different groups of simulations are considered: in the first group (a) R has been kept constant at an average resistance value (R_2) and C has been varied from healthy (C_3) to pathologic compliance (C_1). In the second group (b) constant average C_2 has been considered, and R has been varied from healthy (R_1) to pathologic resistance (R_3). The arrows indicate the direction of increase for both R or C. Panel 'a' shows also results for only resistance (R_2) and only compliance (C_3) peripheral models.

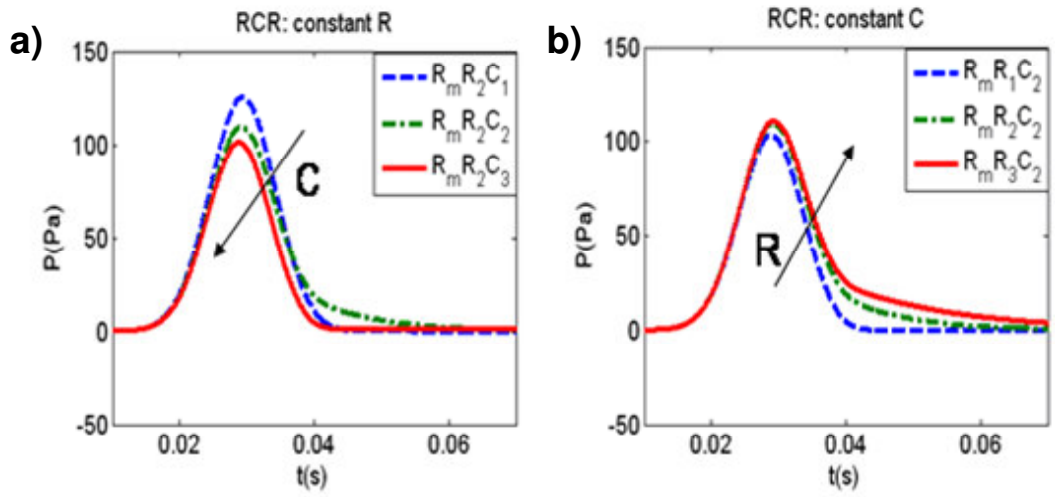

Figure 5.5 Pressure waveforms generated by the IOS pulse enforced at the inlet of trachea in the Symmetrical model. 0-D three element Windkessel models (R_mRC) are coupled with the 128 terminal segments of the Symmetrical model. R_m is the characteristic impedance of the terminal segments of the 1-D model (Section 2.2.5).Two different groups of simulations are considered: in the first group (a) R has been kept constant at an average resistance value (R_2) and C has been varied from healthy (C_3) to pathologic compliance (C_1). In the second group (b) constant average C_2 has been considered, and R has been varied from healthy (R_1) to pathologic resistance (R_3).

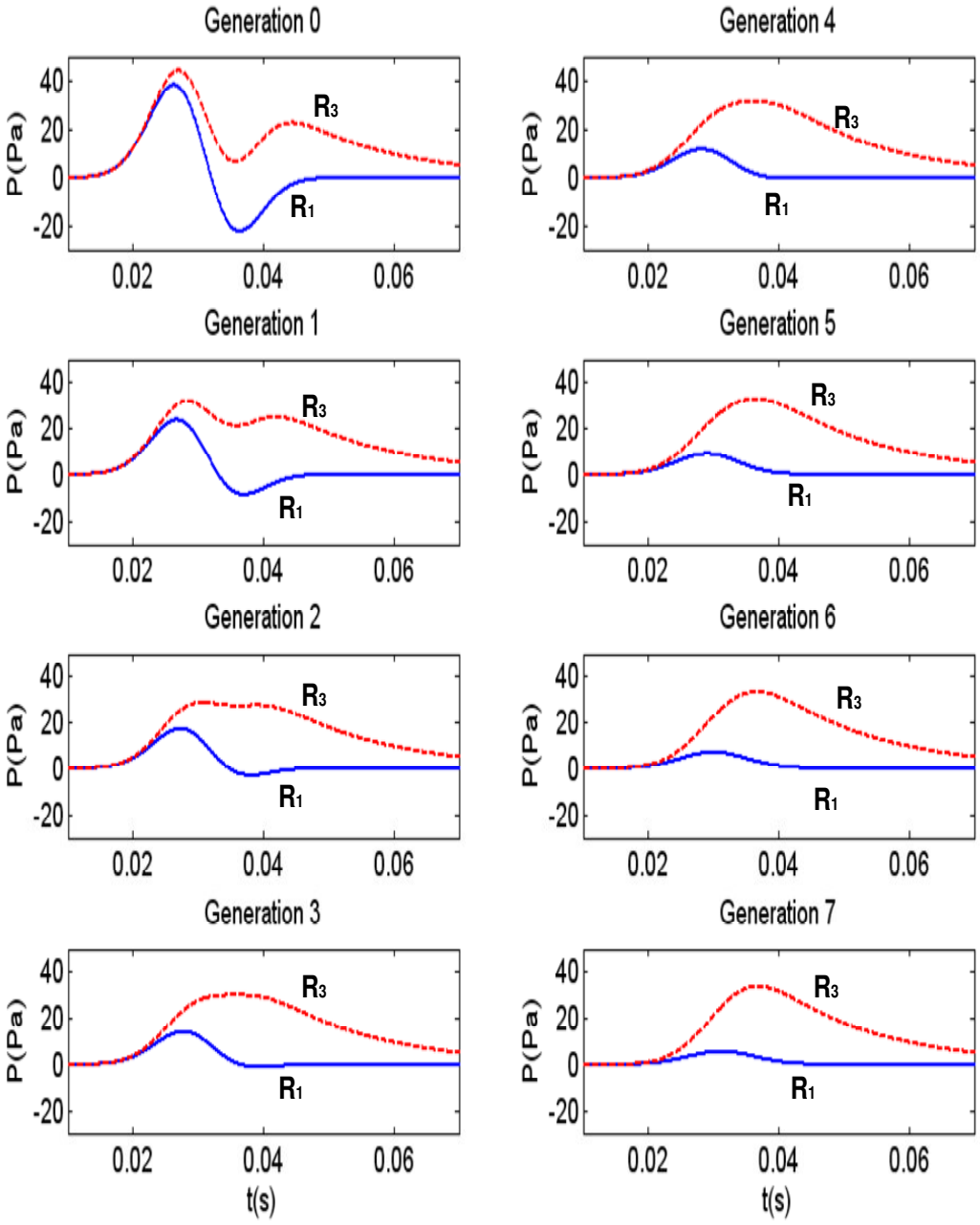

Figure 5.6 Pressure waveforms generated by the IOS pulse enforced at the inlet of trachea in all the eight generations of central airways described by the Symmetrical model. Two element Windkessel models (RC) is considered for periphery (only as an example of the 1-D modelling capability in calculating pressure waveforms difference in all the generations), the values for total peripheral resistance are R_1=17.6x10^3 Pa·s/m^3 (solid line, associated to normal values) and R_3= 291x10^3 Pa·s/m^3 (dashed line, associated to enmphysema); C_2 is the value for compliance (**Table 5.1**).

For the R_mCR Windkessel model (**Figure 5.5**), as described in Section 4.3.3 (**Figure 4.6**), since the characteristic impedance of the terminal 1-D segment of symmetrical model (generation 7 in **Table 5.4**) has a value comparable with the range of resistances

between $R_1 \cdot 128$ and $R_3 \cdot 128$, relevant changes in pressure waveforms can be also observed in this case in relation with changes of peripheral resistance or compliance. The 1-D modelling allows for the calculation of the pressure waveforms in all the generations of the considered model. As an example of this capability, **Figure 5.6** shows how the pressure profiles evolve from trachea to generation 7 of airways referring to both normal and pathologic values of resistances (R_1 and R_3). The purpose of the results shwon in **Figure 5.6** is only an example to show the 1-D modelling ability in detecting pressure waveforms changes in all the generation segments. The choice of RC model instead of RCR is therefore only due to a visual purpose, since RC models are more affected by changes in R and C (from **Figure 5.4**). It is worth noting that pressure waveforms change from generation 0 to generation 3 while from generation 3 till generation 7, pressure waveforms remain almost constant.

5.5.1.4 Backward expansion waves (inspiration phase)

The pulses, considered untill now, are compression waves enforced at the inlet of the respiratory system models. Since the process requires an external pulse generator and it is far from the natural process of respiration, this section aims to study the pressure and velocity waveforms generated during a natural inspiration, when decompression waves created at the level of alveoli are likely to be responsible of the airflow at the mouth. Equation 5.4 is therefore the boundary condition for the terminal segments in both Symmetrical (the present section) and Asymmetrical model (Section 5.5.2.4), according to the K parameter. In this section the possible effects of unven ventilation are interpreted in terms of interacting waves propagating originally from peryphery to central airways in symmetrical model and that are reflected and rereflected throughout the respiratory tree.

Uneven ventilation: many studies have shown that ventilation in lungs is uneven as consequence of regional differences in pleural pressure due to posture, age, body weight and mechanical properties of various lung units and obstructions (Demedts, 1980; Engel et al., 1974; Krieg et al., 2007; Milic-Emili et al., 1966;). Because of this phenomenon the gas mixing is not the same in all the alveoli with some alveoli expanding more than others. In these terms, as an example, this sections aims to show the 1-D modelling capability in interpreting possible uneven air distribution in lungs, comparisons between normal ventilation and an example of uneven ventilation are presented.

Two examples for the Symmetrical model are shown in **Figure 5.7** to account for normal and uneven ventilation distribution. In this work normal ventilation refers, as an example, to the condition where Eq. 5.4 is applied to all the 128 terminal segments (**Figure 5.7a**). The uneven ventilation example is associated to the condition in which Eq. 5.4 is applied only to a part of the terminal segments (right lung) while the remaining terminal segments do not expand because of some obstruction (left lung): the left lung in this case is modelled using an RC model considering a value of resistance (R_3) typical of obructive pulmonary disease (**Figure 5.7b**).

A comparison between pressure and velocity waveforms at trachea, in the two configurations described in **Figure 5.7**, is shown in **Figure 5.8**. Since the "working part" is halved in the uneven ventilation, pressure and velocity are approximately 50% of the normal ventilation (**Figure 5.8**).

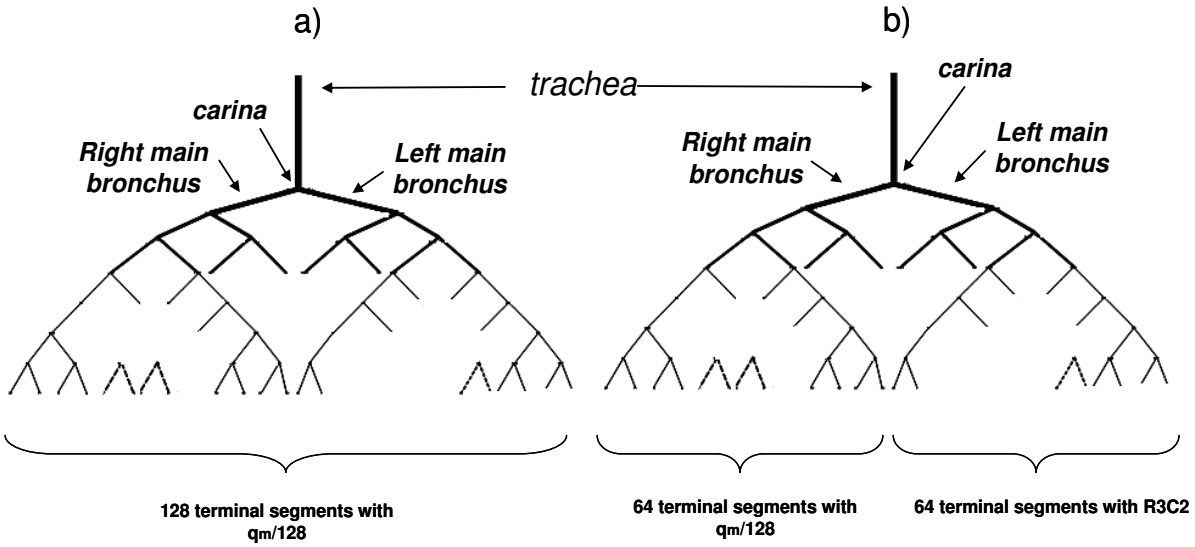

Figure 5.7 two configurations are considered for the symmetrical model a) normal ventilation: with 128 sinusoidal expansion waves (Eq. 5.4) enforced at each terminal segment in both right and left lung b) uneven ventilation: expansion waves are enforced only in the right lung while for the terminal segments of the left lung 2 elements Windkessel models (R_3C_2). The choice of R_3C_2 for the left lung is just an example aimed to show the effects of an obstruction (R_3 is the resistance associated to obstructive pulmonary disease, **Table 5.1**) in the left lung which prevents the expansion of this part.

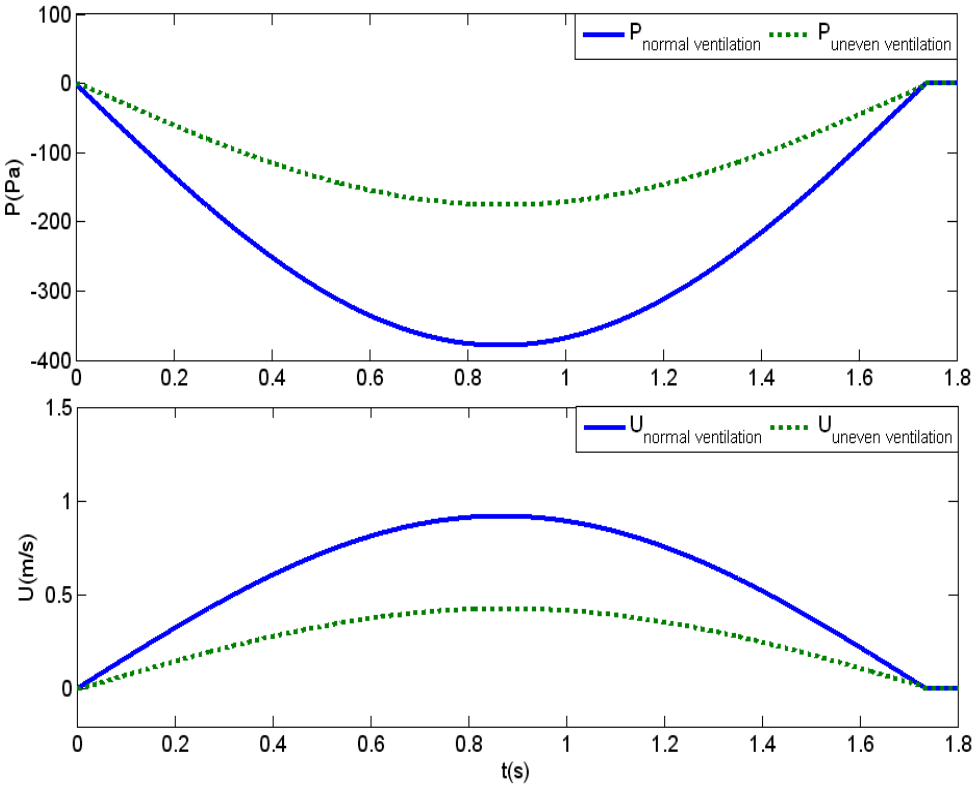

Figure 5.8 Symmetrical model: Pressure and velocity waveforms calculated at midpoint of the trachea in normal and uneven ventilation conditions as specified in **Figure 5.7**.

Comparisons of pressure and velocity waveforms, for right and left bronchus according to the uneven ventilation condition of **Figure 5.7b**, are shown respectively in **Figure 5.9** and **Figure 5.10**. Total pressure (P) and velocity (U) (**Figure 5.9** and **Figure 5.10**, panel 'a') are decomposed into their forward (panel 'b') and backward (panel 'c') components using Wave intensity analysis (WIA). Forward (+) direction (and consequently positive direction of the flow) is when the wave is propagating from trachea to alveoli, backward direction (-) is from alveoli to trachea. The total pressures (sum of forward and backward components) shown in **Figure 5.9a** are approximately the same in the two bronchi; on the contrary the total velocities (**Figure 5.10a**) are of opposite signs. In particular, while in the right bronchus the air flows towards the alveoli (since $U_{\text{right bronchus}}$ is positive), in the left bronchus the direction of the flow is towards the carina ($U_{\text{left bronchus}}$ is negative). According to these results, this creates a kind of recirculation of air from left to the right bronchus. The decomposition into forward and backward components for both pressure and velocity can be used, in this case, to better understand the reflection phenomena that are applied to this specific example of uneven ventilation for which a possible explanation is provided.

In the right bronchus the reflection of expansion backward travelling waves at carina produces a forward compression wave. This can be observed considering that the backward wave (subscript '–' in the P and U legends of **Figure 5.9**c and **Figure 5.10c**) derives from a combination of flows defined by Eq. (5.4) at peripheral airways. It is therefore a backward expansion wave **(Table 2.5)** since it is associated to a negative pressure wave ($P_{-\text{right bronchus}}$, **Figure 5.9c**) and positive velocity ($U_{-\text{right bronchus}}$, **Figure 5.10c**).

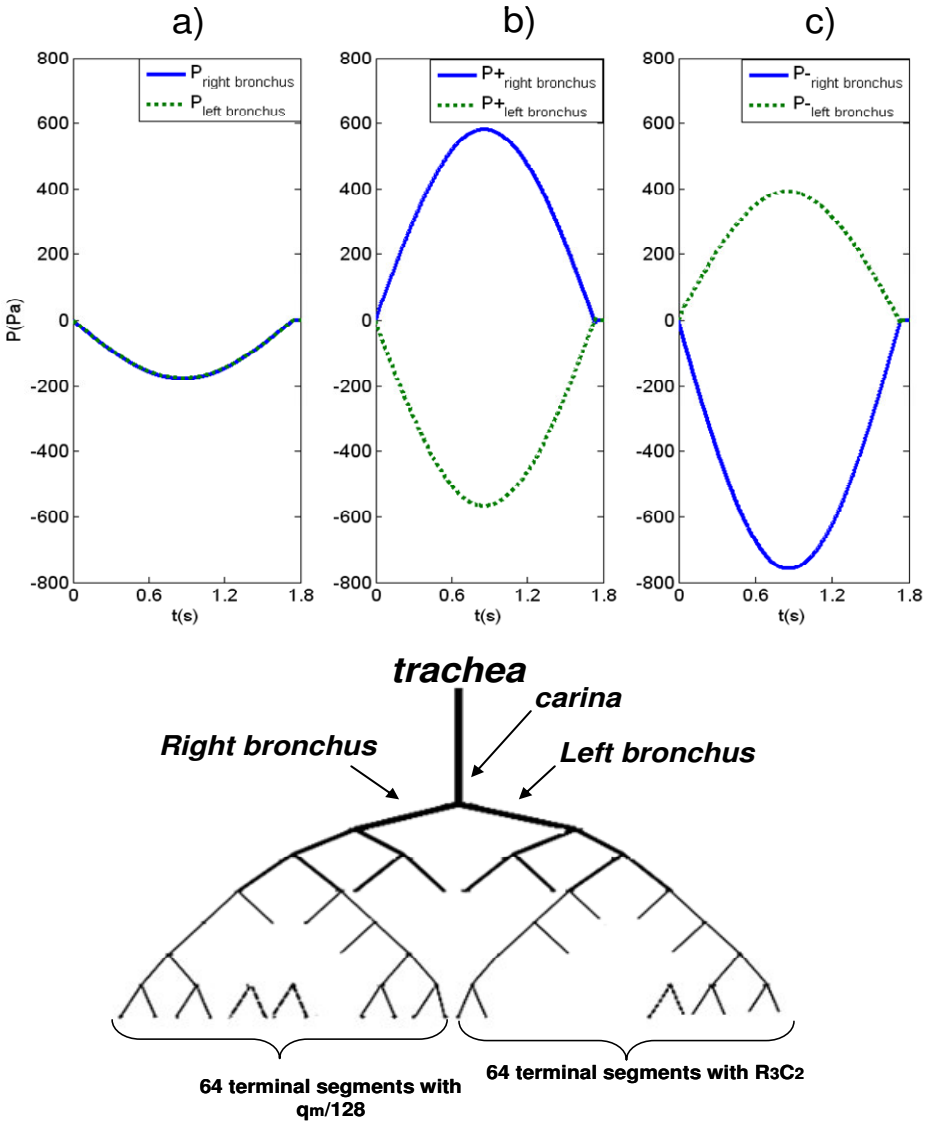

Figure 5.9 Symmetrical model: a) comparison between total pressure waveforms calculated at right and left bronchus ($P_{\text{right bronchus}}$ and $P_{\text{left bronchus}}$) during the uneven ventilation described in Figure 5.7b. The pressure waves for the two bronchi are separated in (b) into their forward (+) and in (c) into their backward (-) components.

The forward wave in the right bronchus ($P+_{\text{right bronchus}}$, **Figure 5.9b**) derives mostly from the reflection of $P-_{\text{right bronchus}}$ at carina (R_{f1}-=-0.55,**Table 5.5**). Due to the negative reflection coefficient of the carina, the forward pressure $P+_{\text{right bronchus}}$ at the right

bronchus is inverted from negative to positive. It is therefore a forward compression wave which causes the air ($U+_{right\ bronchus}$) to flow in the positive direction (**Figure 5.10b**).

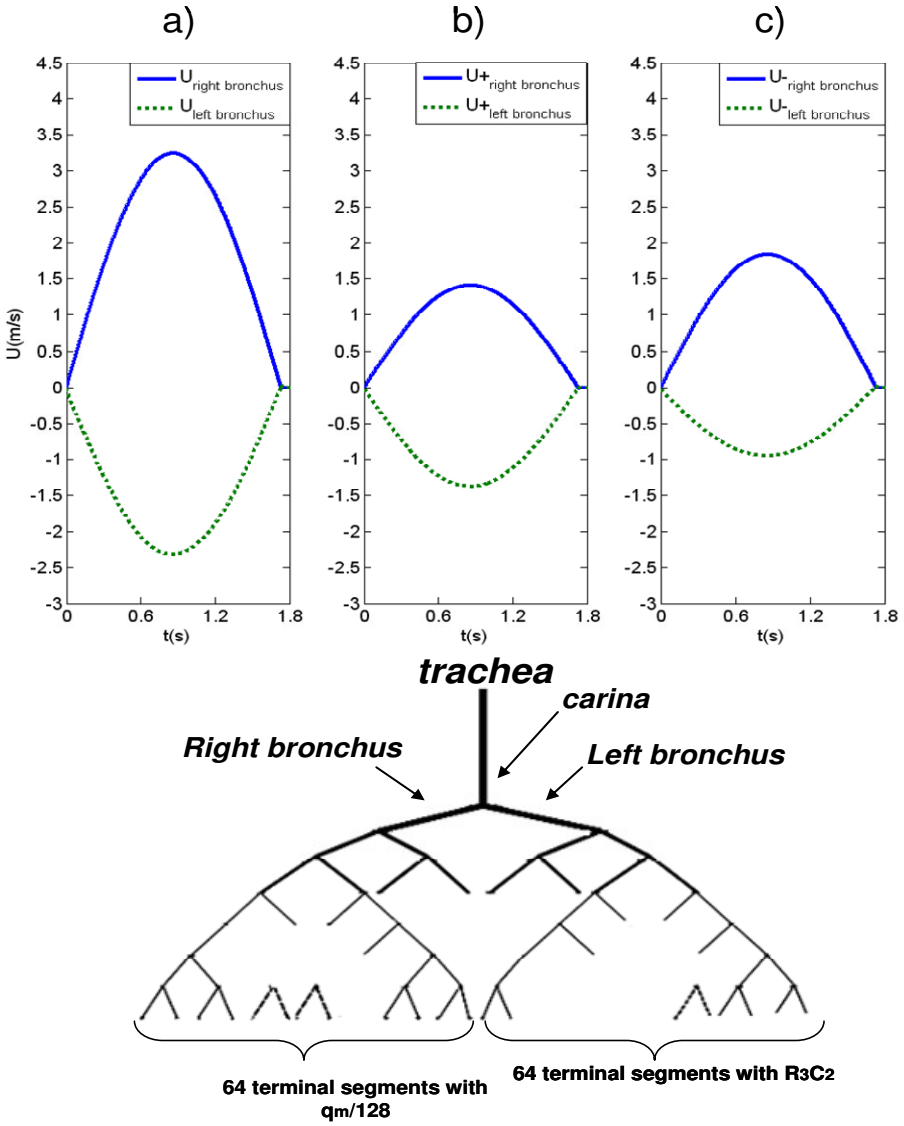

Figure 5.10 Symmetrical model: a) comparison between total velocity waveforms calculated at right and left bronchus ($U_{right\ bronchus}$ and $U_{left\ bronchus}$) during the uneven ventilation condition described in Figure 5.7b. The velocity waves for the two bronchi are separated in (b) into their forward (+) and in (c) into their backward (-) components.

On the contrary, for the left bronchus the reflection of a forward expansion wave produces a backward compression wave: the forward pressure waves for the left bronchus in **Figure 5.9b** ($P_{left\ bronchus}$ +) (no flows enforced at the terminal segments) is an expansion wave which derives mostly from $P-_{right\ bronchus}$ transmitted through the carina into the left bronchus. Being an expansion forward wave the associated velocity $U+_{left\ bronchus}$ is negative in **Figure 5.10b** (**Table 2.5**). The global effect of the reflections

from the RC model of periphery of left bronchus and from all the bifurcations (of left bronchus) on $P+_{\text{left bronchus}}$ is a negative reflection since the backward pressure wave $P-_{\text{left bronchus}}$ is a compression wave; it is the pressure wave generated from the reflection of $P+_{\text{left bronchus}}$ with all the bifurcations and RC models (**Figure 5.9c**). This backward compression wave is associated (**Table 2.5**) to a negative velocity ($U-_{\text{left bronchus}}$ in **Figure 5.10c**).

5.5.2 Horsfield's asymmetrical model

After discussing the results associated to the symmetrical model, in section 5.5.1, this section aims to investigate the effects of the pulses (defined in Section 5.2) in the Horsfield's model, focusing on the natural asymmetry of the respiratory system. On the contrary of the symmetrical model in which the definition of the properties of each generation refers to all the segments belonging to that generation, the asymmetrical model of central airways appears much more complex since it is necessary to specify the properties for each branch and bifurcation.

5.5.2.1 Wave speeds and characteristic impedances

The wave speeds and the characteristic impedances for all the central airway segments of the asymmetrical model (**Figure 5.2**) are shown in **Table 5.6** with the sound speed limitation (bold values), according to Eq. (2.25). All the values for the wave speed are close to the sound speed in free space, therefore the central airways in the asymmetrical model behaves similarly to a network of rigid tubes.

5.5.2.2 Reflection coefficients and short pulse waveforms

In **Table 5.7** each bifurcation is identified by the number of the parent vessel and the two daughter vessels, according to the numbering of **Figure 5.2**; reflection coefficients in the forward and backward directions, as defined in Section 2.2.3.8, are provided for each bifurcation (**Table 5.7**). Based on the reflection coefficients values, also the asymmetrical model appears well matched in the forward direction, having only two bifurcations with $R_f+>0.3$. The values for terminal reflection coefficients (R_t) in correspondence of normal condition (R_1) and emphysema (R_3) are presented in **Table 5.8**. The terminal segments are classified by lobes according to their branch number as defined in **Figure 5.2**. Similarly to the Symmetrical model the R_t values are close to the open end condition in correspondence of R_1 and they become less negative in

correspondence of R_3, in the range -0.99 and -0.58. The complexity of the reflections for the Asymmetrical model is shown in **Figure 5.11** where the pressure and velocity waveforms are shown as a result of the short pulse enforced at the inlet of trachea when the two different resistance values (R_1 and R_3, **Table 5.3**) are coupled to each of the terminal segments. Apart from the reflection from carina (R_f+=0.02) it is difficult to identify clearly the origin of the reflected waves as it was possible with the symmetrical model. It is worth noting that to identify the onset of the reflections from peripheral airways, the point where the two curves (pressure and velocity for R_1 and R_3) separate from each other can be considered (**Figure 5.11**).

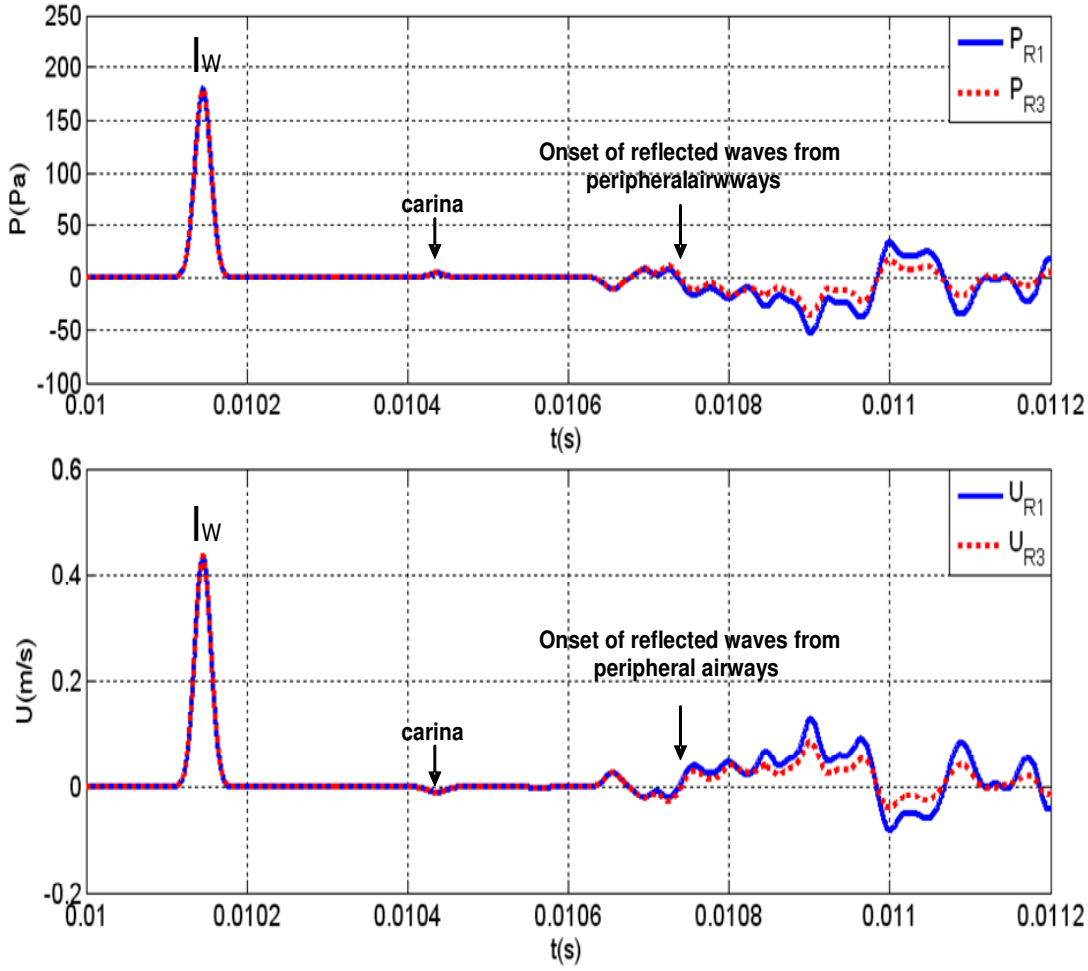

Figure 5.11 Computational pressure (a) and velocity (b) waveforms at the mid-point of the trachea when the short pulse propagates in the 1-D Asymmetrical model of central airways. I The arrows indicate the arrival time of the reflection from carina and peripheral airways (R_1 and R_3, respectively the peripheral resistance associated to normal and emphysematous lungs, **Table 5.3**).

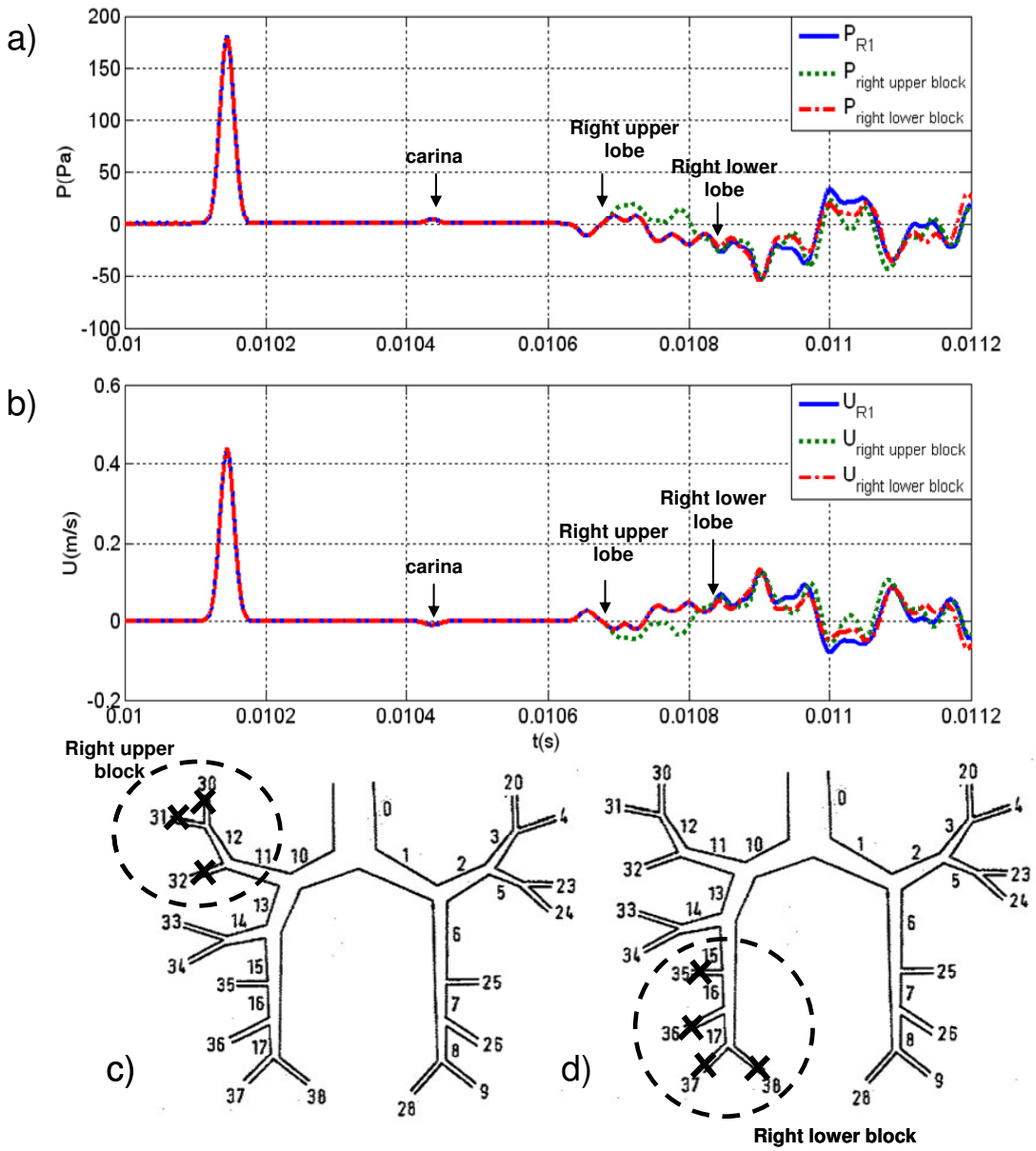

Figure 5.12 Computational pressure (a) and velocity (b) waveforms at the mid-point of the trachea when the short pulse is enforced at the inlet of the Asymmetrical model of central airways. Three conditions are analyzed (see text for details): normal condition (P_{R1} and U_{R1}) and two different peripheral blocks (R_t=1) in correspondence respectively of c) right upper ($P_{\text{right upper lobe}}$ and $U_{\text{right upper lobe}}$) and d) right lower lobe ($P_{\text{right lower lobe}}$ and $U_{\text{right lower lobe}}$) blocks.

The short pulse can be used also to associate, based on the time delay, the onset of reflected waves to specific lobe blockage, as shown in **Figure 5.12**. Three conditions are analyzed in **Figure 5.12**: the first (P_{R1} and U_{R1}) is the control condition where all the terminal segments of the Asymmetrical model are coupled with the normal values for peripheral resistance (R_1) according to **Table 5.3**. The other two conditions simulate two different peripheral blocks (R_t=1) in correspondence respectively of right upper

(branch number: 30, 31, 32) and right lower lobe (branch number: 36, 37, 38) with the remaining peripheral resistance set to R_1 values. The arrival times of the reflected waves from the blocked lobes can be easily indentified by the points where P and U waveforms separate from P_{R1} and U_{R1}. As indicated by the arrows in **Figure 5.12**, the reflected waves from the right upper lobe reach the midpoint of trachea before the ones reflected from the right lower lobes. According to the time delays is therefore possible to obtain an estimation of the locations of the reflective sites also for the asymmetrical model.

Branch number	**0**	**1**	**2**	**3**	**4**	**5**	**6**	**7**	**8**	**9**	**10**
c (m/s)	**518** 343	**587** 343	**544** 343	332	343	323	**525** 343	341	322	323	**613** 343
Z ($Pa \cdot s/m^3$)	$2.7x10^6$	$6x10^6$	$1.6x10^7$	10^7	$2.6x10^7$	$2x10^7$	$1.3x10^7$	$1.4x10^7$	$1.1x10^7$	$1.9x10^7$	$7.4x10^6$
Branch number	**11**	**12**	**13**	**14**	**15**	**16**	**17**	**20**	**23**	**24**	**25**
c (m/s)	**553** 343	307	**493** 343	340	342	**346** 343	**344** 343	325	327	343	308
Z ($Pa \cdot s/m^3$)	$1.7x10^7$	$6.8x10^6$	$9.8x10^6$	$2.4x10^7$	$1.5x10^7$	$1.7x10^7$	$1.6x10^7$	$2.1x10^7$	$5.7x10^7$	$6x10^7$	$1.9x10^7$
Branch number	**26**	**28**	**30**	**31**	**32**	**33**	**34**	**35**	**36**	**37**	**38**
c (m/s)	328	313	338	306	337	338	334	318	329	**345** 343	334
Z ($Pa \cdot s/m^3$)	$2.5x10^7$	$2.4x10^6$	$4.3x10^6$	$3.9x10^7$	$2x10^7$	$4.3x10^7$	$3.4x10^7$	$3.2x10^7$	$7.2x10^7$	$2.9x10^7$	$1.8x10^7$

Table 5.6 Asymmetrical model: wave speeds (c) determined from Eq. (2.12) and characteristic impedances ($Z=\rho c/A$) for the central airways of Horsfield's model. The branches are indicated using their branch number defined in Figure 5.2. The c values in bold are the wave speeds that, since they overcome the sound speed in free space (Cs), are corrected according to Eq. (2.25).

Parent	Daughter 1	Daugter 2	$R_{fP}+$	$R_{fD1}-$	$R_{fD2}-$
0	10	1	0.02	-0.55	-0.47
1	2	6	0.15	-0.61	-0.54
2	3	5	-0.20	-0.22	-0.58
3	20	4	0.06	-0.49	-0.57
5	23	23	0.20	-0.59	-0.61
6	7	25	-0.04	-0.40	-0.55
7	8	26	-0.29	-0.11	-0.6
8	9	28	-0.02	-0.44	-0.54
10	11	13	0.01	-0.61	-0.39
11	12	32	-0.36	0.02	-0.66
12	30	31	0.50	-0.76	-0.74
13	14	15	0.14	-0.67	-0.47
14	33	34	-0.11	-0.51	-0.38
15	15	35	-0.13	-0.26	-0.61
16	17	36	-0.14	-0.07	-0.79
17	37	38	-0.18	-0.55	-0.27

Table 5.7 Reflection coefficients in forward (+) and backward (-) directions (Eq 2.44-2.46) of all the bifurcations of the asymmetrical model. Bifurcations are identified by the branch number of the parent vessel Parent P) and the two daughter vessels (Daughter1 and Daughter 2). The values are calculated after the wave speed correction (**Table 5.6**).

	Left upper lobe Branch number				**Left lower lobe Branch number**				**Right upper lobe Branch number**			**Right medial lobe Branch number**			**Right lower lobe Branch number**		
	4	**20**	**23**	**24**	**9**	**25**	**26**	**28**	**30**	**31**	**32**	**33**	**34**	**35**	**36**	**37**	**38**
R_1	-0.98	-0.98	-0.98	-0.98	-0.98	-0.96	-0.98	-0.97	-0.99	-0.97	-0.98	-0.98	-0.98	-0.98	-0.99	-0.98	-0.96
R_3	-0.70	-0.70	-0.75	-0.70	-0.68	-0.50	-0.74	-0.58	-0.84	-0.62	-0.76	-0.75	-0.69	-0.77	-0.79	-0.72	-0.59

Table 5.8 Terminal reflection coefficients (Eq. 2.44) associated to the terminal segments of **Figure 5.2** (classified by lobes and indentified by their branch number) according to normal (R_1) and emphysematous (R_3) lung resistance.

5.5.2.3 Impulse oscillometry pulse (IOS)

Similarly to the symmetrical model (**Figure 5.4** and **Figure 5.5**), in order to test the sensitivity of the tracheal pressure of the asymmetrical model to peripheral variations, various simulations (**Figure 5.13** and **Figure 5.14**) were considered according to the 40ms IOS pulse (Eq. 5.2). Changes of peripheral compliance (C) (panel a of **Figure 5.13** and **Figure 5.14**) and peripheral resistance (R) (panel b of **Figure 5.13** and **Figure 5.14**) are considered for both RC and R_mCR Windkessel models of peripheral airways.

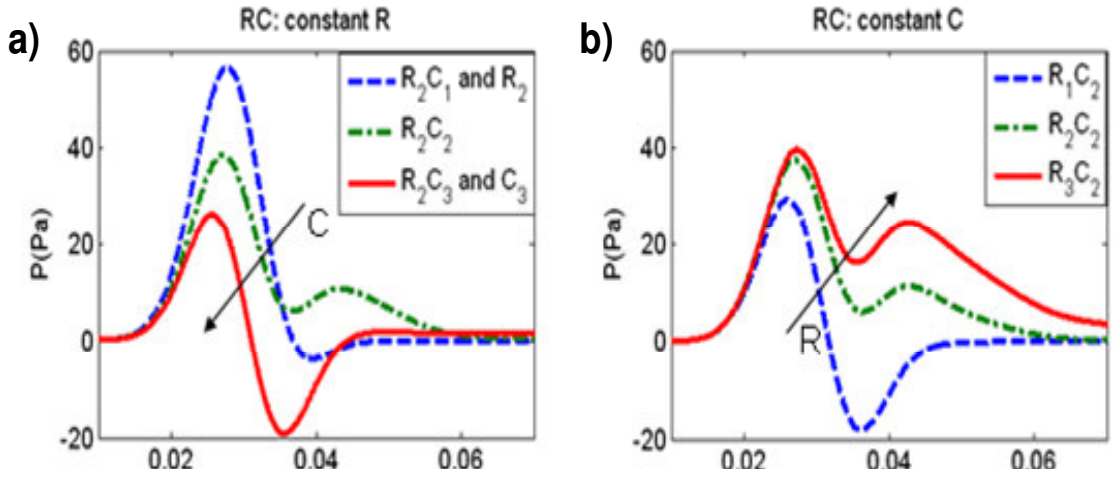

Figure 5.13 Pressure waveforms generated by the IOS pulse enforced at the inlet of trachea in the Asymmetrical model. 0-D two element Windkessel models (RC) are coupled with each of the terminal segments of the Asymmetrical model according to resistance and compliance distribution defined in **Table 5.3**. Two different groups of simulations are considered: in the first group (a) R has been kept constant at an average resistance value (R_2) and C has been varied from healthy (C_3) to pathologic compliance (C_1). In the second group (b) constant average C_2 has been considered, and R has been varied from healthy (R_1) to pathologic resistance (R_3). The arrows indicate the direction of increase for both R or C. Panel 'a' shows also results for only resistance (R_2) and only compliance (C_3) peripheral models

The simulations were aimed to model respectively the effects of restrictive and obstructive pulmonary diseases on the tracheal pressure of the asymmetrical model. The values and numbering of R and C refers to **Table 5.3**. In general P increases with increasing R and decreases with increasing C particularly for the RC model. In R_mCR model since the characteristic impedance of the terminal segments (**Table 5.6**) is much higher than the values of resistances in **Table 5.3**, the effects on pressure waveforms are less evident than in the symmetrical model (Section 5.5.1.3).

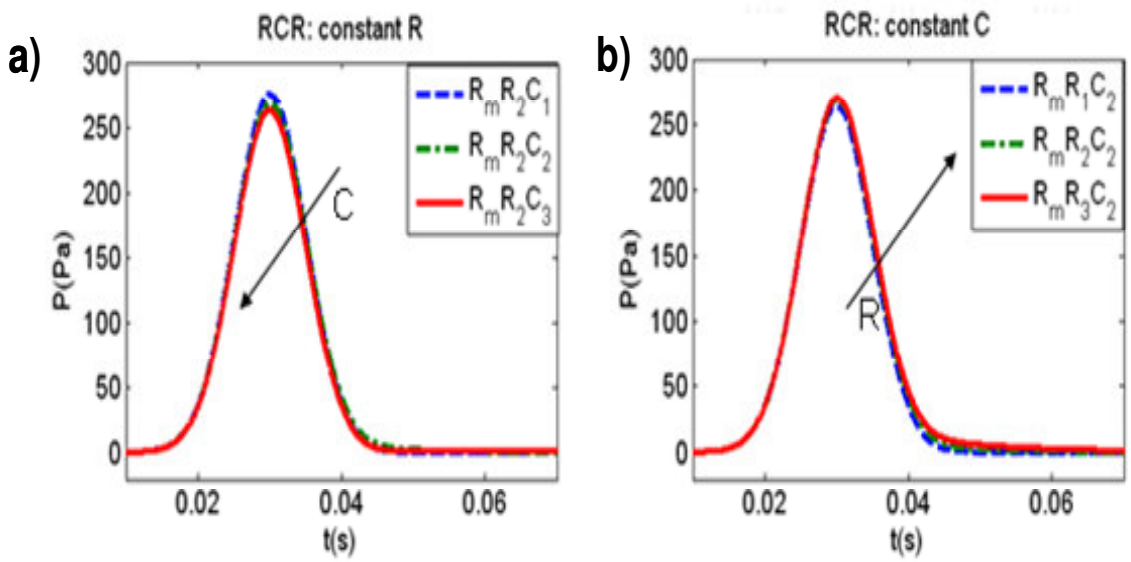

Figure 5.14 Pressure waveforms generated by the IOS pulse enforced at the inlet of trachea in the Asymmetrical model. 0-D three element Windkessel models (R_mCR) are coupled with each of the terminal segments of the Asymmetrical model according to resistance and compliance distribution defined in Table 5.3. R_m is the characteristic impedance of the terminal segments of the 1-D model (Section 2.2.5). Two different groups of simulations are considered: in the first group (a) R has been kept constant at an average resistance value (R_2) and C has been varied from healthy (C_3) to pathologic compliance (C_1). In the second group (b) constant average C_2 has been considered, and R has been varied from healthy (R_1) to pathologic resistance (R_3). The arrows indicate the direction of increase for both R or C.

5.5.2.4 Backward expansion waves (inspiration phase)

This section aims to investigate the effect of backward expansion wave on pressure waveforms in trachea. The results are also used to investigate the possible effects of eneven ventilation also in the Asymmetrical model (uneven ventilation in symmetrical model was discussed in Section 5.5.1.4). As an example, referring to asymmetrical model, the normal ventilation is associated to the condition of Eq. (5.4) enforced to all the terminal segments (Figure 5.15a). The uneven ventilation for the asymmetrical model, as an example of flow disomogenities in this thesis, is associated to the condition in which Eq. (5.4) is enforced to all the terminal segments apart from the left upper lobe (dashed circle in Figure 5.15b). The choice of R_3C_2 model for the left upper lobe is just an example aimed to show the effects of an obstruction (R_3 is the resistance associated to obstructive pulmonary disease, Table 5.1) in the lobe which prevents the expansion of this part.

Figure 5.16 shows a comparison between pressure (P) and velocity (U) waveforms at trachea in the two configurations described in **Figure 5.15** (normal and uneven ventilation): the values of both waveforms (P and U) are lower in the uneven ventilation because of the less number of terminal segments contributing to the flow. **Figure 5.17** and **Figure 5.18** show respectively the pressure and velocity waveforms for the case of uneven ventilation (as defined in **Figure 5.15b**) at midpoint of segment 2 (the parent vessel for the left upper lobe) and segment 6 of **Figure 5.15**. The waveforms are separated into their forward and backward components according to the theory of wave intensity analysis (section 2.3.1). Similarly to the uneven ventilation in the Symmetrical model, discussed in Section 5.5.1.4, while the total pressure waveforms are approximately the same (**Figure 5.17a**), big differences can be distinguished in forward and backward components (**Figure 5.17**, panel b and c). The total (or net) velocities have opposite signs (**Figure 5.18a**), positive for segment 6 and negative for segment 2. Therefore, according to **Figure 5.18** while during the inspiration in most of the lobes of the model the air flows from trachea down to alveoli, in the left upper lobe there might be some air moving in the opposite direction.

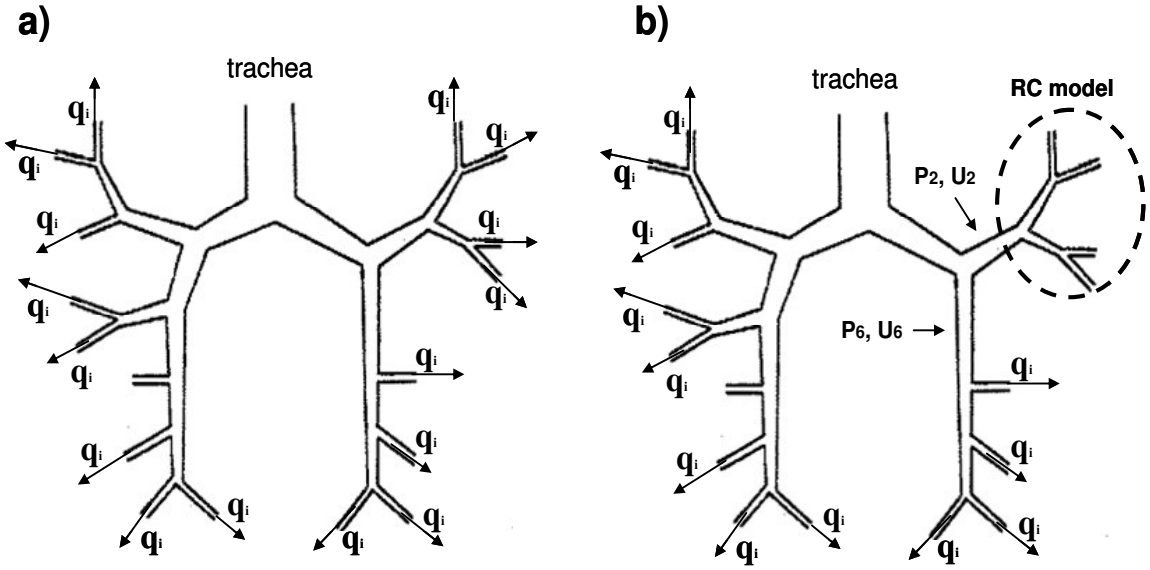

Figure 5.15 Example of uneven ventilation in Asymmetrical model. Two configurations are considered: a) normal ventilation, flows (Eq. 5.4) are enforced in all the terminal segments and are indicated by the arrows; b) uneven ventilation in upper left lobe (dashed circle): 2 elements Windkessel model (R_3C_2) is considered for left upper lobe while Eq. 5.4 is enforced to all the other lobes. P_6, U_6 and P_2 and U_2 are the pressures and velocities of segment 6 and 2 (**Figure 5.2**), indicated by the arrows.

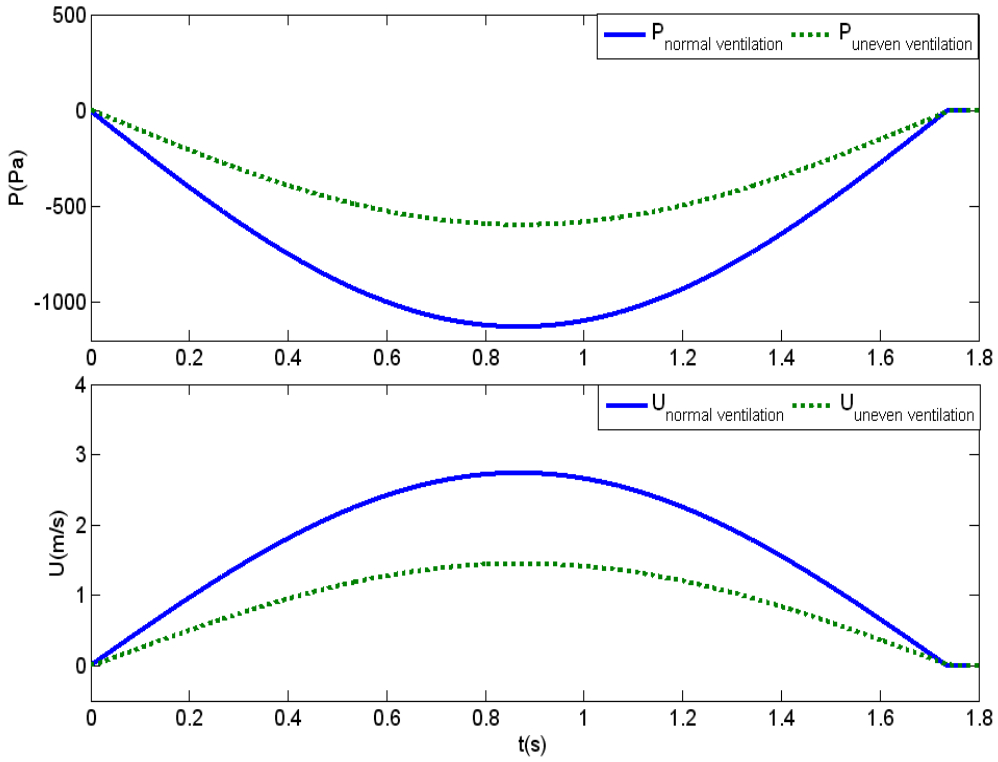

Figure 5.16 Asymmetrical model: calculated pressure (P) and velocity (U) waveforms at trachea in the examples for normal and uneven ventilation condition shown in Figure 5.15.

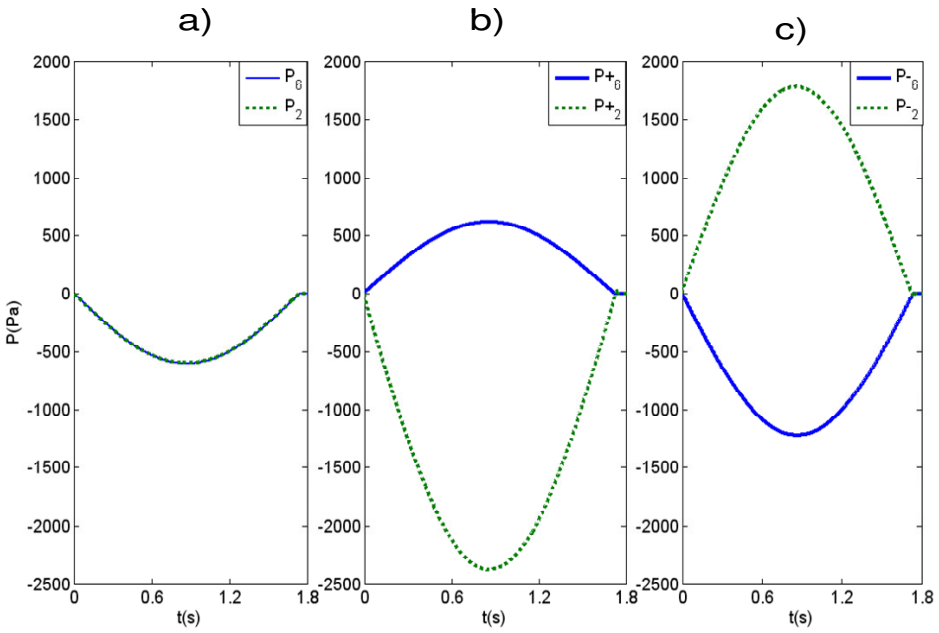

Figure 5.17 Asymmetrical model: a) computational pressure waveforms comparison between segment 2 and segment 6 (P_2 and P_6) in the uneven ventilation condition (**Figure 5.15b**). P_2 and P_6 are separated in b) into their forward (+) and in c) into their backward (-) components (section 2.3.1)

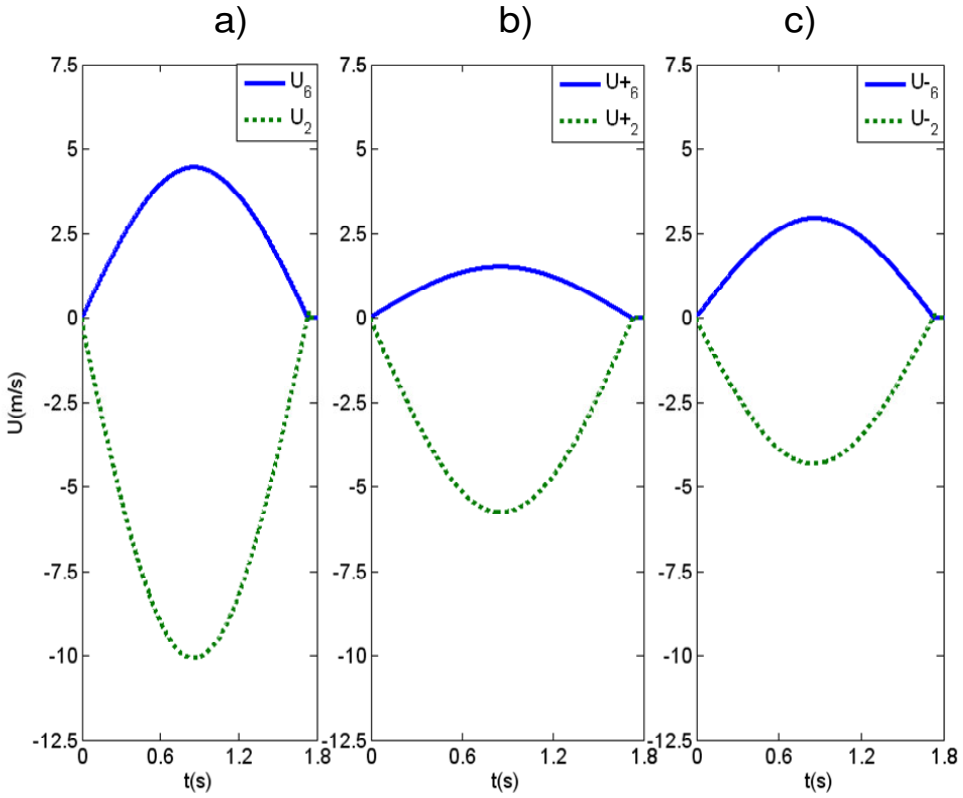

Figure 5.18 Asymmetrical model: a) computational velocity waveforms comparison between segment 2 and segment 6 (U_2 and U_6) in the uneven ventilation condition (**Figure 5.15**). U_2 and U_6 are separated in b) into their forward (+) and in c) into their backward (-) components (section 2.3.1).

5.6 General discussions and conclusions

The 1-D modelling in time and space variables (described in Section 2.2) has been shown, in this chapter, to be suitable for studying the propagation of air waves in models of central airways. Starting from the more idealised Weibel's symmetrical model, three different flow boundary condition have been investigated with different models for peripheral airways. The 1-D model has been then extended to introduce the asymmetry of the bifurcations, characteristic of the human airways, according to the Horsfield's model. Winter and Pimmel (1980) analysed and compared the effects that reflections may have on apparent phase velocity measurements in trachea (cross correlation was used to determine the apparent velocities) according to a symmetrical and an asymmetrical model. Their results showed that the effects of reflections were particularly marked in the symmetrical model while they were much smoother in the asymmetrical model. This was attributed to the destructive interference due the phase difference caused by the random nature of diameters of the asymmetrical model. The

same concept can be applied to the pressure waveforms shown in **Figure 5.3** and **Figure 5.12**; for the symmetrical model the onset of reflected waves is clearly identified since the waves reflected by analogous locations are in phase and sum each other. This does not happen in the asymmetrical model due to the phase difference of reflected waves. The models have shown in general to respond sensibly to variation of the peripheral boundaries of both resistance and compliance through variations in pressure waveforms calculated in trachea when the IOS pulse is enforced at the inlet (**Figure 5.4** and **Figure 5.13**). The aim of these simulations was to reproduce the effects of the increase of peripheral resistance (characteristic of the obstructive pulmonary diseases) and the reduction of peripheral compliance (characteristic of the restrictive pulmonary diseases). Since the peripheral airways have been described as the 'silent zone', due to their small contribution to the total airways resistance (Bates and Suki, 2008), the results shown in **Figure 5.4** and **Figure 5.13** (panel 'a' and 'b') appear relevant even if they seem influenced by 0-D model adopted for the periphery. For example in the R_mCR model coupled to the asymmetrical model (**Figure 5.13**, panel 'c' and 'd'), the variations of tracheal pressure are not significant.

Pressure and velocity waveforms can be investigated in all the segments with the 1-D modelling, as shown in the example of **Figure 5.6,** and their forward and backward components can be separated using Wave intensity analysis (Section 2.3.1). **Figure 5.19** shows a qualitative comparison between a clinical acquisition of pressure and flow, measured at the mouth of a man using an impulse oscillometry system, and the computational pressure and flow. Computational waveforms were obtained enforcing the IOS pulse at the inlet of the Symmetrical model and adopting an R_mCR model for the periphery with C_2 and R_1 values from **Table 5.1**.

The IOS pulse, defined in Eq. 5.2, was derived based on the pulse shown in **Figure 2.21**, it represents an example of pulse used in Impulse oscillometry system (Smith et al., 2005). The amplitude difference between measured and computational values, in both pressure and flow (**Figure 5.19),** may be due either to the pulse (that could be different according to the manufacturer) or to a difference in the respiratory impedance or to a combination of both. Assuming that the amplitude difference depends just on the pulse amplitude, **Figure 5.20** shows the computational pressure and flow obtained when a bigger pulse is enforced at trachea (three times bigger in amplitude than Eq. 5.2). Although the 1-D model does not take into account the upper respiratory tract (mouth/ nose, pharynx, larynx), the similarities of the overall pattern of the waveforms (**Figure 5.19a** and **Figure 5.20**) highlight the interest in investigating more deeply the time

domain 1-D formulation also for airways. Once pressure and velocity waveforms are obtained, it is possible to separate them in their forward (+) and backward (-) components using wave intensity analysis, as shown in **Figure 5.21**. It is worth noting that the the incident pressure wave ($P+_{b.p.}$) is a forward compression wave and that the global reflection coefficient, due to all the bifurcations and the RmCR models, has a negative nature since a backward expansion wave is generated ($P-_{b.p.}$).

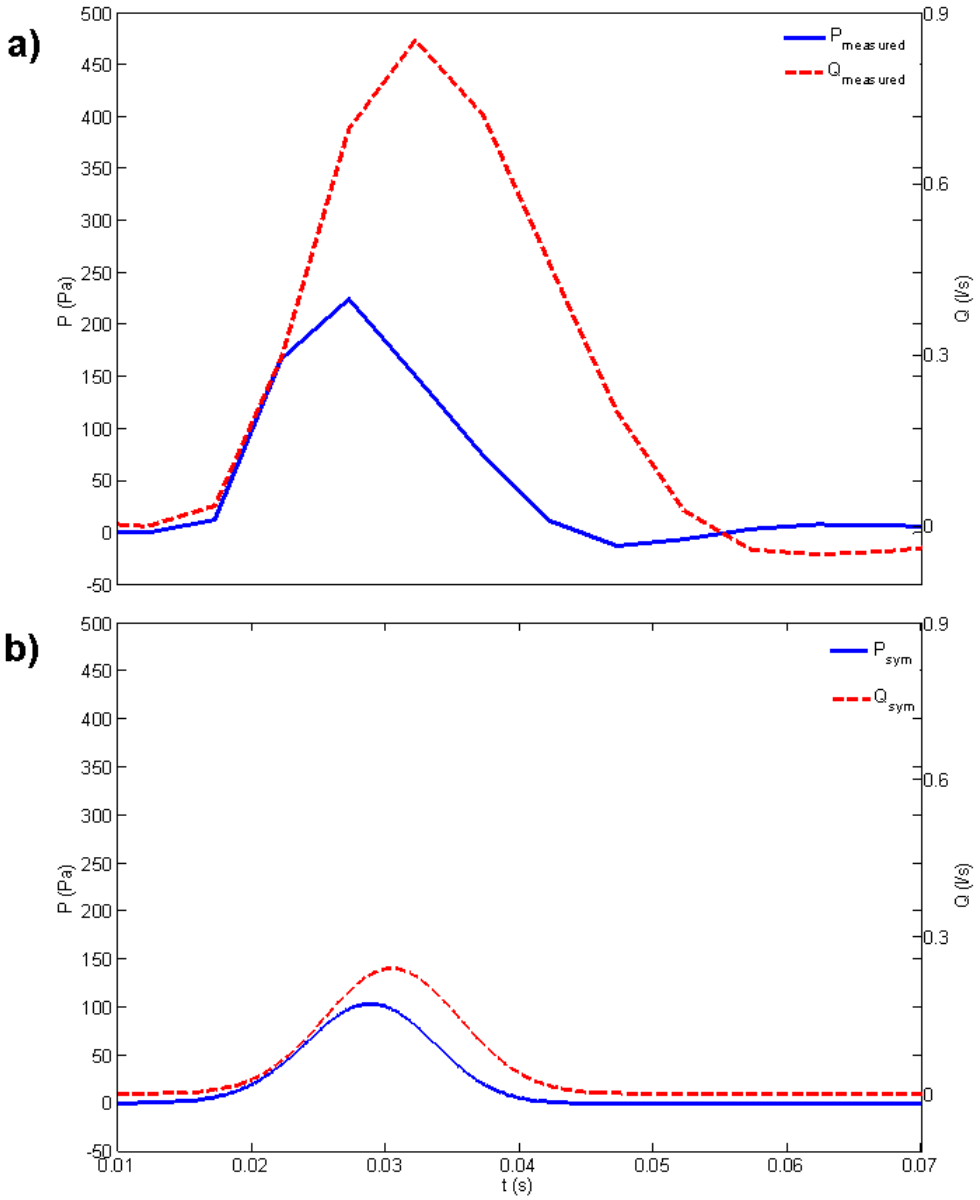

Figure 5.19 Pressure (solid line) and flow (dashed line) waveforms (a) measured using impulse oscillometry IOS (measurement site: mouth; subject information – sex: male - age: 57 respiratory diseases: none) and (b) obtained using the Symmetrical 1-D model with IOS pulse enforced at the inlet.

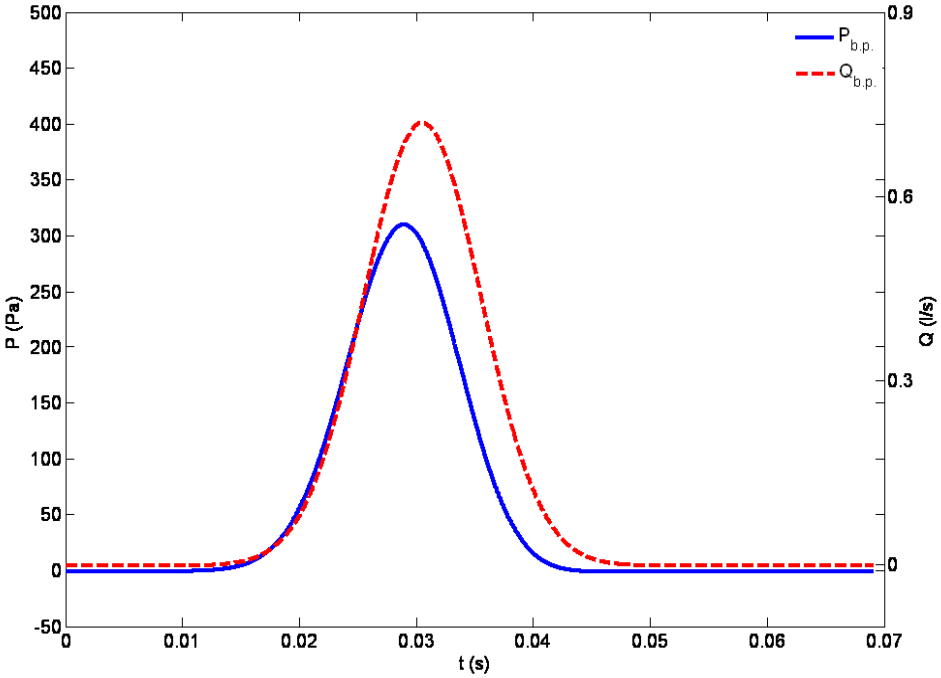

Figure 5.20 Pressure (solid line) and flow (dashed line) waveforms calculated with the bigger pulse (b.p.) enforced at the inlet of the Symmetrical 1-D model. The amplitude of the bigger pulse is three times bigger than the pulse defined in Eq. 5.2, with the same duration.

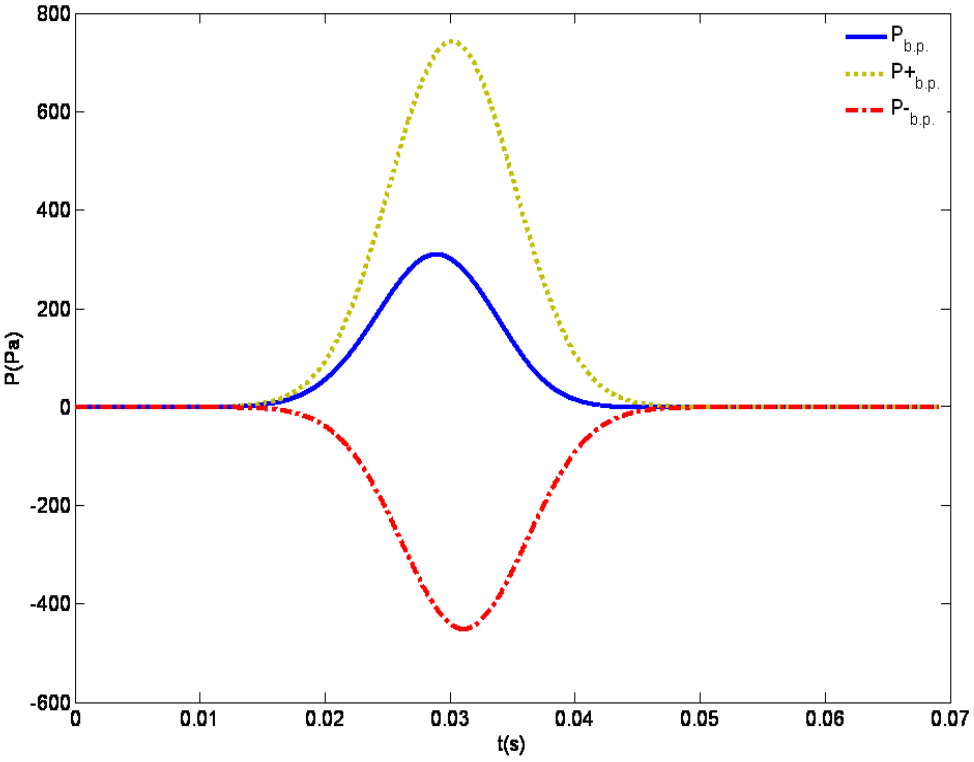

Figure 5.21 Computational pressure waveforms, associated to the bigger pulse enforced at trachea of symmetrical model (**Figure 5.20**), are separated into their forward (+) and backward (-) components using wave intensity analysis.

Separation of waves in + and - components has been also used to investigate some example of uneven ventilation in both symmetrical (**Figure 5.9** and **Figure 5.10**) and asymmetrical model (**Figure 5.17** and **Figure 5.18**). The results have shown that even if total pressure could appear similar in different regions of the respiratory system, the separation in forward and backward components can provide information of clinical interest to understand the dynamic of reflections in lungs.

Chapter 6

Conclusions and future developments

6.1 Conclusions

The one-dimensional modelling in space and time variables (described in Chapter 2), extensively applied to simulate blood pressure and flow in the cardiovascular system, has been applied for the first time in this thesis, to the knowledge of the author, to study the propagation of air pulses in the human bronchial tree and distensible tubes in general.

Information on the morphology and functionality of the cardiovascular and respiratory systems can be derived by analyzing pulse waveforms in arteries (Alastruey et al., 2008; Alastruey et al., 2009) and airways (Clavica et al., 2009; Clavica et al., 2010), respectively. According to the 1-D formulation, arterial and respiratory pulse waves change continuously their shapes propagating from central to peripheral arteries and airways respectively: pulse waveforms are influenced by geometry and boundary conditions. Understanding the underlying mechanisms of pulse wave propagation in normal conditions and the impact of disease and anatomical variation on the patterns of propagation is therefore relevant to improve prevention, diagnosis and treatment of diseases.

The applicability of the 1-D modelling and Wave intensity Analysis (WIA), both described in Chapter 2, in studying air waves propagating in flexible vessels has been experimentally tested and validated in Chapter 3. Using the theory of linear analysis of wave reflections the experiments have shown that also for air pulses forward compression waves produces an increase of pressure (P) and velocity (U) while forward expansion waves generate a decrease of both P and U. Furthermore reflected backward compression waves generate an increase of P and decrease of U while backward expansion waves produce a decrease of P and an increase of U. WIA has shown in general negative and positive peaks in correspondence of the arrival time of waves propagating respectively in backward and forward direction as theoretically expected. Experimental arrival times of reflected waves, at the measurement point, and the reflection coefficients have been compared with the theoretical values from the linear analysis of wave reflections; the results were encouraging and suggest further developments of the setup. Moreover experimental values for wave speed in different tubes has been obtained using the foot to foot method. Based on the experimental results

for wave speed, a correction of the computational wave speed, previously used only to study blood flows in arteries, has been introduced to limit its value to the sound speed (C_s) in free space. This was also based on the fact, described in literature, that C_s is the speed at which pressure disturbances travel in rigid tubes (Chapter 1) and it is therefore considered the maximum value. Comparisons were made between the new corrected formulation (c_β) and the original Korteweg's equation (considering the compressibility of the fluid); the results showed that c_β can provide values closer to the experimental wave speeds.

In the computational part of this thesis c_β was applied as the wave speed firstly in 1-D simplified models of airways (Chapter 4), simple geometries similar to the ones used for experiments, and then to symmetrical and asymmetrical bifurcating systems (Chapter 5), which produced more accurate morphological structure of the respiratory systems in humans. Weibel's symmetrical and Horsfield's asymmetrical models of central airways were used, being the most complete models in terms of geometrical and mechanical data available in literature. The results of both Chapter 4 and 5 indicate the possibility of a non invasive mapping of the reflective sites once a short pulse is enforced at the inlet of each model. Considering the arrival time and amplitude of reflected waves, information respectively about the distance and the nature of the reflective site can be derived. In the symmetrical model the onset of reflected waves is clearly identified since the waves, reflected by analogous locations, are in phase and sum each other. In the asymmetrical model the identification of the reflective sites appear more complex due to the phase difference of reflected waves. Calculated pressures waveforms at a site close to the inlet of trachea showed to change with variations of peripheral resistance and compliance according to normal and pathologic values (**Figure 5.4-5** and **Figure 5.13-14**). Since changes in peripheral resistance and compliance are characteristic respectively of obstructive and restrictive pulmonary diseases the results appear of physiological interest. A favourable comparison with typical pressure and flow waveforms from impulse oscillometry (Chapter 5), which has recently been introduced as a clinical diagnostic technique, was also shown (**Figure 5.21**). Furthermore, in Chapter 5, a pulse reproducing a single inspiration of the breathing was obtained as combination of several expansion sinusoidal waves moving from the peripheral airways to trachea. The results were used to interpret the possible effects of uneven ventilation (Fig. 5.12-18) showing the possible air recirculation among the lobes.

The possibility of investigating pressure (P) and velocity (U) in each segment of the bronchial tree (using the 1-D modelling) and the separation of P and U in their forward and backward components, using wave intensity analysis, has revealed to be an important tool for the understanding of the wave reflections phenomena in lungs, particularly when the analysis of total pressure and velocity does not provide relevant results.

In general, the results provided by this work, in both computational and experimental aspects, suggest the time-domain 1-D modelling as a potential tool of clinical importance. It can be used to study and understand the effects of pathological and anatomical variations on the pattern of pressure and velocity waveforms in each airway segment.

6.2 Limitations and future developments

The objectives, set out in Section 1.9, were successfully achieved with this thesis. Being the 1-D modelling in space and time variables together with the wave intensity analysis applied to respiratory tree for the first time in this work, many limitations need to be identified for further improvements of the present study.

6.2.1 Computational model

- Most of the limitations of the modelling presented in this work are based on the difficulties in accounting for the in vivo complex airways structure:
  - Upper respiratory tract and the influence of surrounding tissues have been neglected. One of the main reasons was associated to the difficulties in obtaining the geometrical and mechanical properties of segments like pharynx and larynx. It would be valuable to include, in a future development of the 1-D model, also this tract to have a more complete model of the whole system. In this sense it would be interesting to include, in the mathematical model, the Venturi effect, characteristic of supralaryngeal airways (Jaeger and Matthys, 1968; Schroter and Sudlow, 1969).
  - The extraluminal pressure (P_{ext}) or pleural pressure has been assumed constant throughout the thesis. This assumption can be considered valid for the compression waves defined in Section 5.2.1, enforced at the inlet of trachea but it is not physically valid during the respiration when changes of pleural

pressure drive the air flow to and from the alveoli. Further improvement of the mathematical model may consider this effect by allowing variation of the extraluminal pressure in Eq. (2.9).

- The trachea together with other airways, with a certain cartilage content, introduces complex structures and consequently complex mechanical properties and behaviour. In Chapter 2 they were considered and simplified as homogeneous tubes with mechanical properties averaged between soft tissue and cartilage. The model could be modified to account for the discontinuities introduced by the cartilage rings. For example the model could be constructed as short cylinders alternating cartilage and soft tissue mechanical properties. This could help to understand and quantify the effects of tissue discontinuities on the pressure and flow waveforms.

- The presence of secondary flows and turbulences in airways, particularly at airways bifurcation, can not be taken into account when using the 1-D formulation. For this reason they were neglected in this thesis even if they may have strong influence on the velocity profiles, particularly at high Reynolds (Re) number (Liu et al., 2002; Luo and Liu, 2008; Olson et al., 1973; Schroter and Sudlow, 1969). Energy losses at junctions can be accounted, in future development of the mathematical model, by adding a loss coefficient into the Bernoulli's law (Eq. 2.39-2.40) which should depend on Re according to the experiments and calculations by Schroter and Pedley (Pedley et al., 1970a; Pedley et al., 1970b; Schroter and Sudlow, 1969).
- The wave speed was assumed in the current model to be unaffected by the frequency of excitation. This might not be physically correct particularly when the short pulse (Eq. 5.1) is considered. In future developments, the wave speed limitation to the Cs value could be applied also for frequencies higher than the resonance frequency based on **Figure 1.17**.

6.2.2 Experimental setup

- For the experimental part of this thesis, only single tubes and series of tubes were considered and a qualitative classification of the wave was conducted according to the timing and change of slopes in both P and U waveforms. It was not possible to investigate more quantitatively the amplitude of the reflections, after the first one, due to the limitations described in Section 3.6.1. Future

developments of the experimental work could study also the effect of bifurcations on the propagation of air waves. More attention could be dedicated to amplitudes and the related distributed and concentrated dissipations in airflow.

- Since the velocities measured by the split fiber probe are referred to a specific radial position, a more rigourous definition of the radial measurement position is required to evaluate the velocity profiles in the tubes used in the experiments. An experimental function relating velocity and radial position would help also to define a computational velocity profile (Eq. 2.6) closer to the experimental data.
- A very interesting part for future work would be to test the applicability of the P-U loop method (described in Section 1.8.1.3) to obtain wave speed values also for air waves by pressure and velocity measurements in one location. This will require a less invasive measurement site than the rigid T connector used in this thesis.

6.2.3 Further comparisons with clinical data

The comparison shown in **Figure 5.19** represents the first attempt of interpreting clinical data using the 1-D modelling. It gives only a qualitative comparison of the computational pressure and flow waveforms with real clinical data from impulse oscillometry. The comparison was aimed to enhance the clinical potentialy that the 1-D modelling may have if applied to relate particular features of pressure and flow waveforms to specific pathologies. The favourable comparison encourages future studies of air wave propagation to focus more on the clinical data. This could be used for example to test that the curves shown in **Figure 5.4-5** and **Figure 5.13-14** are compatible with pressure waveforms associated to patients with different obstructive and restricive diseases.

Appendix A: Split fiber probe datasheet

Technical Datasheet for split fiber probe). The asterix indicates the influence from natural convection up to approx. 0.20 m/s. (Dantec Dynamics website)

Technical data for split-fiber sensors	
Thickness of quartz coating	0.5 µm
Medium	Air
Sensor material	Nickel
Sensor dimensions	200 µm dia, 1.25 mm long
Sensor resistance R20 (approx.)	6 Ω
Temperature coefficient of resistance (TCR) $\alpha 20$ (approx.)	0.40%/°C
Max. sensor temperature	300°C
Max. ambient temperature	150°C
Min. velocity	0.05 m/s *
Max. velocity	350 m/s
Frequency limit fmax (CTA mode)	175 kHz

Appendix B:

56C01/c17 unit as resistance measuring device

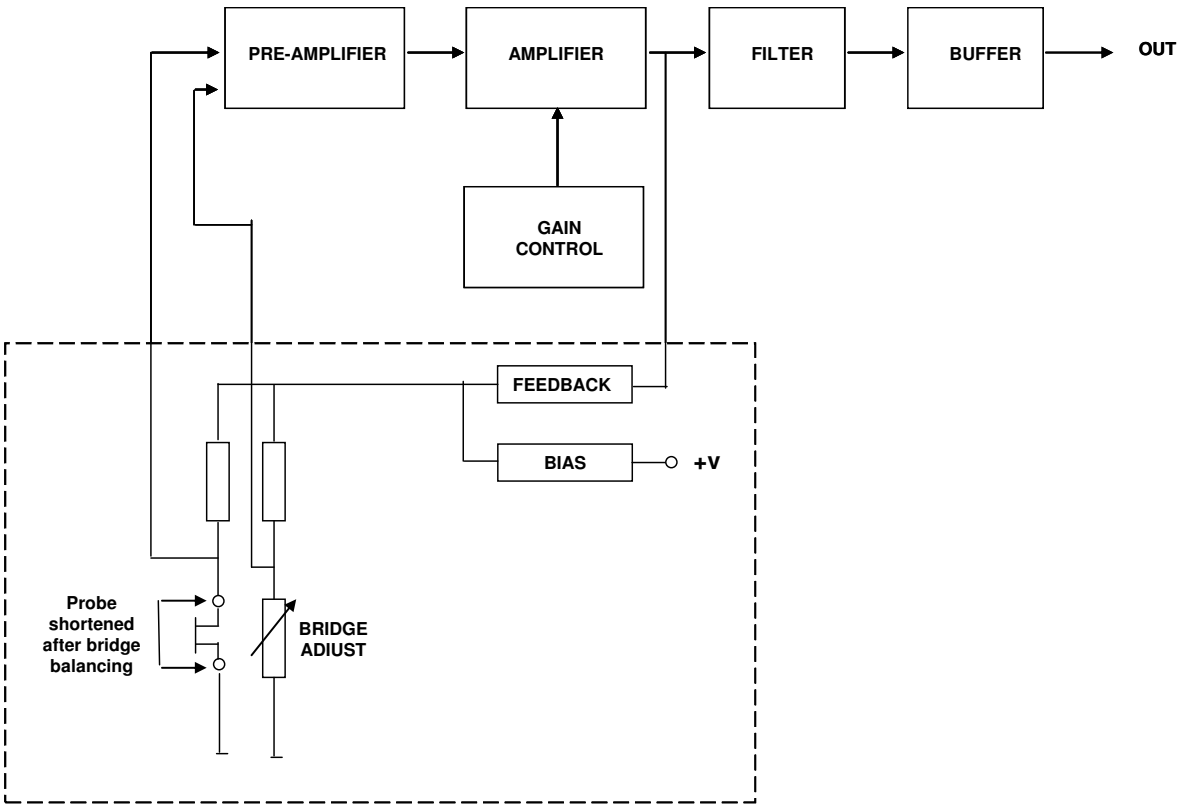

Appendix C:

56C01/c17 unit as constant temperature anemometer (CTA)

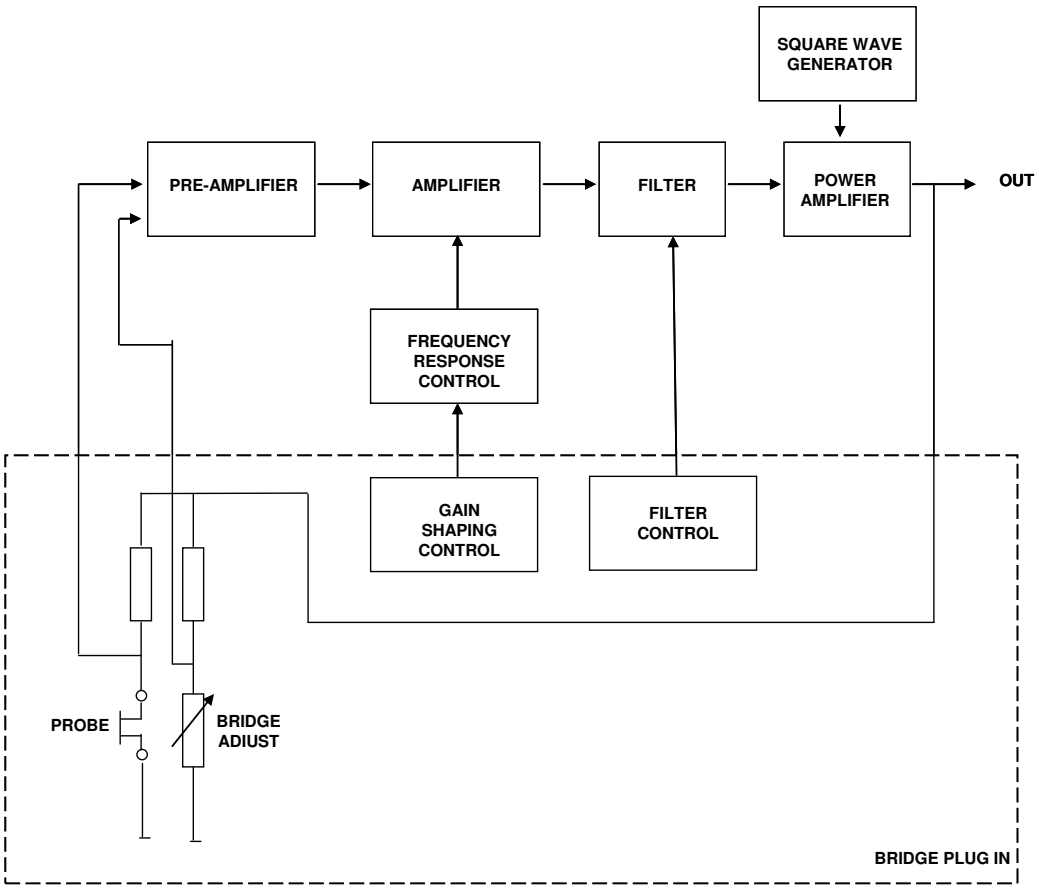

Appendix D:

Electric circuit controlling the solenoid valve

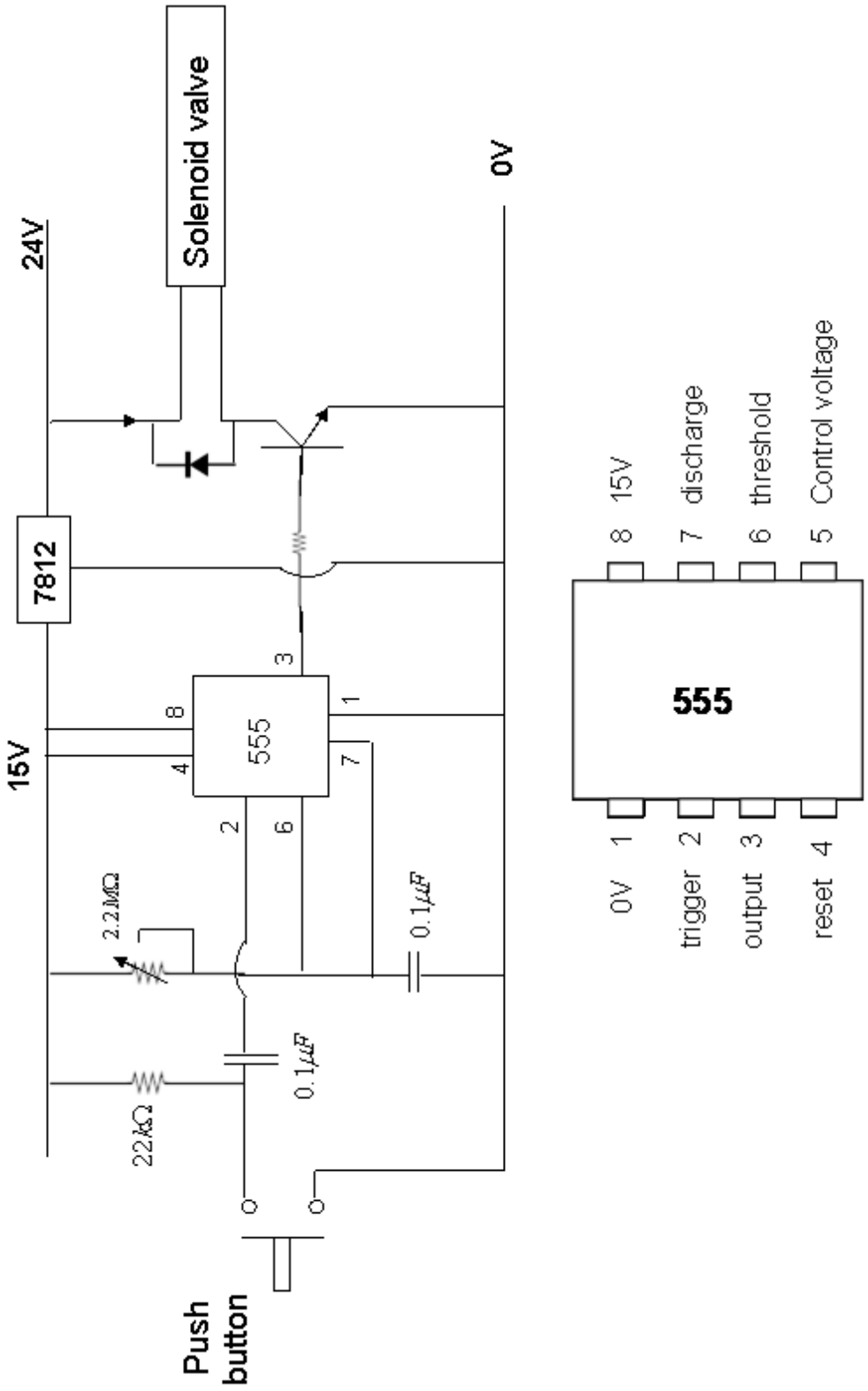

Appendix E:

List of publications

Conferences

Clavica, F., Alastruey, J., Sherwin, S. J., Khir, A. W., 2009. One-dimensional modelling of pulse wave propagation in human airway bifurcations in space-time variables. (Talk) Conf Proc IEEE Eng Med Biol Soc 1, 5482-5.

Clavica, F., Alastruey, A., Sherwin, S. J., Khir, A. W., 2010. One-dimensional modelling of pulse wave propagation in a mdel of human airways. (Talk) European Society of Biomechanics Conference (ESB2010).

Clavica, F., Alastruey, J., Borlotti, A., Sherwin, S. J., Khir, A. W., 2010. One-dimensional computational model of pulse wave propagation in the human bronchial tree. (Poster) Conf Proc IEEE Eng Med Biol Soc 1, 2473-6.

Clavica, F., Alastruey, A., Sherwin, S. J., Khir, A. W., 2011. One-dimensional computational model of air in asymmetrical human bronchial trees. (Poster) Physiological fluid Mechanics Conference.

REFERENCES

Adler, A., Cowley, E. A., Bates, J. H., Eidelman, D. H., 1998. Airway-parenchymal interdependence after airway contraction in rat lung explants. Journal of Applied Physiology 85, 231-237.

Alastruey J. 2006. Numerical modelling of pulse wave propagation in the cardiovascular system: development, validation and clinical applications. Ph.D. thesis, Imperial College London, University of London.

Alastruey, J., Parker, K. H., Peiró, J., Sherwin, S. J., 2009. Analysing the pattern of pulse waves in arterial networks: A time-domain study. Journal of Engineering Mathematics 64, 331-351.

Alastruey, J., Parker, K. H., Peiró, J., Sherwin, S. J., 2008. Lumped parameter outflow models for 1-D blood flow simulations: Effect on pulse waves and parameter estimation. Communications in Computational Physics 4, 317-336.

Aljuri, N., Venegas, J. G., Freitag, L., 2006. Viscoelasticity of the trachea and its effects on flow limitation. Journal of Applied Physiology 100, 384-389.

Arets, H. G. M., van der Ent, C. K., 2004. Measurements of airway mechanics in spontaneously breathing young children. Paediatric Respiratory Reviews 5, 77-84.

Bates, J. H. T., Decramer, M., Zin, W. A., 1986. Respiratory resistance with histamine challenge by single-breath and forced oscillation methods. Journal of Applied Physiology 61, 873-880.

Bates, J. H. T., Mishima, M., Balassy, Z., 1995. Measuring the mechanical properties of the lung in vivo with spatial resolution at the acinar level. Physiological Measurement 16, 151-159.

Bates, J. H. T., Suki, B., 2008. Assessment of peripheral lung mechanics. Respiratory Physiology and Neurobiology 163, 54-63.

Bergner, A., Sanderson, M. J., 2003. Airway hyperresponsiveness: From molecules to bedside - Selected contribution: Airway contractility and smooth muscle Ca2+ signaling in lung slices from different mouse strains. Journal of Applied Physiology 95, 1325-1332.

Bleasdale, R. A., Mumford, C. E., Campbell, R. I., Fraser, A. G., Jones, C. J. H., Frenneaux, M. P., 2003. Wave intensity analysis from the common carotid artery: A new noninvasive index of cerebral vasomotor tone. Heart and Vessels 18, 202-206.

Bokulic, R. E., 1992. The lung: Scientific foundations. By Ronald G. Crystal and John D. West. New York: Raven Press, Ltd., 1991, 2 volumes, 2,224 pp. Pediatric Pulmonology 12, 194-195.

Bramwell, J.C., Hill, A. V. 1922. The velocity of pulse wave in a man. Proc. Roy. Soc. B 93, 298.

Brooks, L. J., Castile, R. G., Glass, G. M., 1984. Reproducibility and accuracy of airway area by acoustic reflection. Journal of Applied Physiology Respiratory Environmental and Exercise Physiology 57, 777-787.

Bruun, H. H., 1995. Hot-wire anemometry : principles and signal analysis. Oxford University Press, Oxford, pp. 507.

Capper, W. L., Guelke, R. W., Bunn, A. E., 1991. The estimation of tube wall compliance using acoustic input impedance. IEEE Transactions on Biomedical Engineering 38, 544-550.

Chang, H. K., Elmasry, O. A., 1982. A Model Study of Flow Dynamics in Human Central Airways .1. Axial Velocity Profiles. Respiration Physiology 49, 75-95.

Clark, C., 1985. A differential pressure transducer for the measurement of high-frequency fluctuations in liquids. Journal of Physics E: Scientific Instruments 18, 297-302.

Clavica, F., Alastruey, J., Sherwin, S. J., Khir, A. W., 2009. One-dimensional modelling of pulse wave propagation in human airway bifurcations in space-time variables. Conf Proc IEEE Eng Med Biol Soc 1, 5482-5.

Clavica, F., Alastruey, J., Borlotti, A., Sherwin, S. J., Khir, A. W., 2010. One-dimensional computational model of pulse wave propagation in the human bronchial tree. Conf Proc IEEE Eng Med Biol Soc 1, 2473-6.

Davies, J. E., Whinnett, Z. I., Francis, D. P., Willson, K., Foale, R. A., Malik, I. S., Hughes, A. D., Parker, K. H., Mayet, J., 2006. Use of simultaneous pressure and velocity measurements to estimate arterial wave speed at a single site in humans. American Journal of Physiology-Heart and Circulatory Physiology 290, H878-H885.

Dawson, S. V., Elliott, E. A., 1977. Wave-Speed Limitation on Expiratory Flow - Unifying Concept. Journal of Applied Physiology 43, 498-515.

de Rochefort, L., Vial, L., Fodil, R., Maitre, X., Louis, B., Isabey, D., Caillibotte, G., Thiriet, M., Bittoun, J., Durand, E., Sbirlea-Apiou, G., 2007. In vitro validation of computational fluid dynamic simulation in human proximal airways with hyperpolarized He-3 magnetic resonance phase-contrast velocimetry. Journal of Applied Physiology 102, 2012-2023.

Demedts, M., 1980. Regional distribution of lung volumes and of gas inspired at residual volume: influence of age, body weight and posture. Clinical Respiratory Physiology 16, 271-285.

Diong, B., Nazeran, H., Nava, P., Goldman, M., 2007. Modeling human respiratory impedance. IEEE Engineering in Medicine and Biology Magazine 26, 48-55.

Don, h. f., robson, j. g., 1965. The mechanics of the respiratory system during anesthesia. the effects of atropine and carbon dioxide. Anesthesiology 26, 168-178.

Dubois, A. B., Brody, A. W., Lewis, D. H., Burgess, B. F., 1956. Oscillation Mechanics of Lungs and Chest in Man. Journal of Applied Physiology 8, 587-594.

Elliott, E. A., Dawson, S. V., 1977. Test of wave speed theory of flow limitation in elastic tubes. Journal of Applied Physiology Respiratory Environmental and Exercise Physiology 43, 516-522.

Engel, L. A., Utz, G., Wood, L. D. H., Macklem, P. T., 1974. Ventilation distribution in anatomical lung units. Journal of Applied Physiology 37, 194-200.

Euler L., 1755 Principia pro motu sanguinis per arterias determinando. *Opera posthuma mathematica et physica anno 1844 detecta*, 2 (1775) 814–823. ediderunt PH Fuss et N Fuss Petropoli; Apund Eggers et Socios.

Feng, J., Khir, A. W., 2008. The compression and expansion waves of the forward and backward flows: An in-vitro arterial model. Proceedings of the Institution of Mechanical Engineers, Part H: Journal of Engineering in Medicine 222, 531-542.

Feng, J., Long, Q., Khir, A. W., 2007. Wave dissipation in flexible tubes in the time domain: In vitro model of arterial waves. Journal of Biomechanics 40, 2130-2138.

Formaggia, L., Lamponi, D., Quarteroni, A., 2003. One-dimensional models for blood flow in arteries. Journal of Engineering Mathematics 47, 251-276.

Formaggia, L., Lamponi, D., Tuveri, M., Veneziani, A., 2006. Numerical modeling of 1D arterial networks coupled with a lumped parameters description of the heart. Computer Methods in Biomechanics and Biomedical Engineering 9, 273-288.

Fredberg, J. J., Hoenig, A., 1978. MECHANICAL RESPONSE OF THE LUNGS AT HIGH FREQUENCIES. Journal of Biomechanical Engineering 100, 57-66.

Fredberg, J. J., Keefe, D. H., Glass, G. M., 1984. Alveolar pressure nonhomogeneity during small-amplitude high-frequency oscillation. Journal of Applied Physiology Respiratory Environmental and Exercise Physiology 57, 788-800.

Fredberg, J. J., Wohl, M. E. B., Glass, G. M., Dorkin, H. L., 1980. Airway Area by Acoustic Reflections Measured at the Mouth. Journal of Applied Physiology 48, 749-758.

Greenwald, S. E., Carter, A. C., Berry, C. L., 1990. Effect of age on the in vitro reflection coefficient of the aortoiliac bifurcation in humans. Circulation 82, 114-123.

Guelke, R. W., Bunn, A. E., 1981. Transmission-Line Theory Applied to Sound-Wave Propagation in Tubes with Compliant Walls. Acustica 48, 101-106.

Guerin, C., Richard, J. -., 2007. Measurement of respiratory system resistance during mechanical ventilation. Intensive Care Medicine 33, 1046-1049.

Gunst, S. J., Stropp, J. Q., 1988. Pressure-volume and length-stress relationships in canine bronchi in vitro. Journal of Applied Physiology 64, 2522-2531.

Habib, R. H., Chalker, R. B., Suki, B., Jackson, A. C., 1994. Airway geometry and wall mechanical properties estimated from subglottal input impedance in humans. Journal of Applied Physiology 77, 441-451.

Helle L. 1993. The use of a split-fiber probe for aerodynamic research. Dantec Infromation No. 12 February.

Hicks, G. H., 2000. Cardiopulmonary anatomy and physiology. W.B. Saunders, Philadelphia ; London, pp. 523.

Hogg, J. C., Macklem, P. T., Thurlbeck, W. M., 1968. Site and nature of airway obstruction in chronic obstructive lung disease. New England Journal of Medicine 278, 1355-1360.

Hollander, E. H., Wang Jr., J., Dobson, G. M., Parker, K. H., Tyberg, J. V., 2001. Negative wave reflections in pulmonary arteries. American Journal of Physiology - Heart and Circulatory Physiology 281, H895-H902.

Horsfield, K., 1990. Diameters, generations, and orders of branches in the bronchial tree. Journal of Applied Physiology 68, 457-461.

Horsfield, K., Cumming, G., 1968a. Functional consequences of airway morphology. Journal of Applied Physiology 24, 384-390.

Horsfield, K., Cumming, G., 1968b. Morphology of the bronchial tree in man. Journal of Applied Physiology 24, 373-383.

Horsfield, K., Cumming, G., 1967. Angles of branching and diameters of branches in the human bronchial tree. The Bulletin of Mathematical Biophysics 29, 245-259.

Horsfield, K., Dart, G., Olson, D. E., Filley, G. F., Cumming, G., 1971. Models of the human bronchial tree. Journal of Applied Physiology 31, 207-217.

Horsfield, K., Thurlbeck, A., 1981. Relation between diameter and flow in branches of the bronchial tree. Bulletin of Mathematical Biology 43, 681-691.

Jackson, A. C., Butler, J. P., Millet, E. J., 1977. Airway geometry by analysis of acoustic pulse response measurements. Journal of Applied Physiology Respiratory Environmental and Exercise Physiology 43, 523-536.

Jaeger, M. J., Matthys, H., 1968. The pattern of flow in the upper human airways. Respiration Physiology 6, 113-127.

Karniadakis and S.J. Sherwin. Spectral /hp element methods for CFD. Oxford University Press, 2003.

Khir, A. W., Henein, M. Y., Koh, T., Das, S. K., Parker, K. H., Gibson, D. G., 2001. Arterial waves in humans during peripheral vascular surgery. Clinical Science 101, 749-757.

Khir, A. W., Parker, K. H., 2002. Measurements of wave speed and reflected waves in elastic tubes and bifurcations. Journal of Biomechanics 35, 775-783.

King, L. V., 1914. On the Convection of Heat from Small Cylinders in a Stream of Fluid: Determination of the Convection Constants of Small Platinum Wires, with Applications to Hot-Wire Anemometry. Proceedings of the Royal Society of London.Series A, Containing Papers of a Mathematical and Physical Character 90, pp. 563-570.

Kiya, M., Sasaki, K., 1983. Structure of a turbulent separation bubble. Journal of Fluid Mechanics 137, 83-113.

Kobayashi, H., Abe, T., Kawashiro, T., Tanabe, K., Yokoyama, T., 1987. Estimation of the distribution profile of airway resistance in the lungs. Computers and Biomedical Research 20, 507-525.

Kolyva, C., Spaan, J. A. E., Piek, J. J., Siebes, M., 2008. Windkesselness of coronary arteries hampers assessment of human coronary wave speed by single-point technique. American Journal of Physiology-Heart and Circulatory Physiology 295, H482-H490.

Korteweg, D. J. 1878. Uber die Fortflanzungsgeschwindigkeit des Schalles in elastischem Rohern. Ann. Phys, Chem. (NS) 5, 525-542.

Kraman, S. S., 1983. Speed of low-frequency sound through lungs of normal men. Journal of Applied Physiology Respiratory Environmental and Exercise Physiology 55, 1862-1867.

Krieg, S., Alison, J. A., McCarren, B., Cowell, S., 2007. Position affects distribution of ventilation in the lungs of older people: An experimental study. Australian Journal of Physiotherapy 53, 179-184.

Kyriakou, E., McKenzie, D. R., Suchowerska, N., Fulton, R. R., 2007. Breathing as a low frequency wave propagation in nonlinear elastic permeable medium. Physica B: Condensed Matter 394, 311-314.

Lambert, R. K., Baile, E. M., Moreno, R., Bert, J., Pare, P. D., 1991. A method for estimating the Young's modulus of complete tracheal cartilage rings. Journal of Applied Physiology 70, 1152-1159.

Lambert, R. K., Wilson, T. A., Hyatt, R. E., Rodarte, J. R., 1982. A computational model for expiratory flow. Journal of Applied Physiology Respiratory Environmental and Exercise Physiology 52, 44-56.

Latham, R. D., Rubal, B. J., Westerhof, N., Sipkema, P., Walsh, R. A., 1987. Nonhuman primate model for regional wave travel and reflections along aortas. American Journal of Physiology - Heart and Circulatory Physiology 253.

Latham, R. D., Westerhof, N., Sipkema, P., 1985. Regional wave travel and reflections along the human aorta: A study with six simultaneous micromanometric pressures. Circulation 72, 1257-1269.

Liu, Y., So, R. M. C., Zhang, C. H., 2003. Modeling the bifurcating flow in an asymmetric human lung airway. Journal of Biomechanics 36, 951-959.

Liu, Y., So, R. M. C., Zhang, C. H., 2002. Modeling the bifurcating flow in a human lung airway. Journal of Biomechanics 35, 465-473.

Louis, B., Glass, G. M., Fredberg, J. J., 1994. Pulmonary airway area by the two-microphone acoustic reflection method. Journal of Applied Physiology 76, 2234-2240.

Lucangelo, U., Bernabé, F., Blanch, L., 2005. Respiratory mechanics derived from signals in the ventilator circuit. Respiratory Care 50, 55-65.

Lumb, A. B., Nunn, J. F., 2005. Nunn's applied respiratory physiology. Elsevier Butterworth-Heinemann, Oxford, pp. 501.

Luo, H. Y., Liu, Y., 2008. Modeling the bifurcating flow in a CT-scanned human lung airway. Journal of Biomechanics 41, 2681-2688.

Lutchen, K. R., Costa, K. D., 1990. Physiological interpretations based on lumped element models fit to respiratory impedance data: Use of forward-inverse modeling. IEEE Transactions on Biomedical Engineering 37, 1076-1086.

Macklem, P. T., Mead, J., 1967. Resistance of central and peripheral airways measured by a retrograde catheter. Journal of Applied Physiology 22, 395-401.

Mahagnah, M., Gavriely, N., 1995. Gas density does not affect pulmonary acoustic transmission in normal men. Journal of Applied Physiology 78, 928-937.

Matthys, K. S., Alastruey, J., Peiró, J., Khir, A. W., Segers, P., Verdonck, P. R., Parker, K. H., Sherwin, S. J., 2007a. Pulse wave propagation in a model human arterial network: Assessment of 1-D numerical simulations against in vitro measurements. Journal of Biomechanics 40, 3476-3486.

Matthys, K. S., Alastruey, J., Peiró, J., Khir, A. W., Segers, P., Verdonck, P. R., Parker, K. H., Sherwin, S. J., 2007b. Pulse wave propagation in a model human arterial network: Assessment of 1-D numerical simulations against in vitro measurements. Journal of Biomechanics 40, 3476-3486.

Mead, J., 1963. The control of respiratory frequency. Annals of the New York Academy of Sciences 109, 724-9.

Mead, J., 1961. Mechanical Properties of Lungs. Physiological Reviews 41, 281-&.

Meyers, A. D., Bishop, H. E., Peters, S., 1980. Biomechanical characteristics of the human trachea. Otolaryngology - Head and Neck Surgery 88, 409-411.

Milic-Emili, J., Henderson, J. A., Dolovich, M. B., Trop, D., Kaneko, K., 1966. Regional distribution of inspired gas in the lung. Journal of Applied Physiology 21, 749-759.

Moens, A.I. 1877 Over de voortplantingssneheild von des pols (on the speed of propagation of the pulse). Technical report, Leiden 814-823.

Montaudon, M., Desbarats, P., Berger, P., de Dietrich, G., Marthan, R., Laurent, F., 2007. Assessment of bronchial wall thickness and lumen diameter in human adults using multi-detector computed tomography: Comparison with theoretical models. Journal of Anatomy 211, 579-588.

Mynard, J., Penny, D. J., Smolich, J. J., 2008. Wave intensity amplification and attenuation in non-linear flow: Implications for the calculation of local reflection coefficients. Journal of Biomechanics 41, 3314-3321.

Nguyen, N., 2006. Fundamentals and applications of microfluidics. Artech House, Boston, Mass. ; London, pp. 497.

Obert, E. F., 1960. Concepts of thermodynamics. McGraw-Hill, New York ; London, .

Olson, D. E., Sudlow, M. F., Horsfield, K., Filley, G. F., 1973. Convective patterns of flow during inspiration. Archives of Internal Medicine 131, 51-57.

Oostveen, E., MacLeod, D., Lorino, H., Farre, R., Hantos, Z., Desager, K., Marchal, F., ERS Task Force Resp Impedan, 2003. The forced oscillation technique in clinical practice: methodology, recommendations and future developments. European Respiratory Journal 22, 1026-1041.

Oruç, V., Çarpinlioğlu, M. Ö., 2007. A test rig for the investigation of airflow through collapsible tubes. Proceedings of the Institution of Mechanical Engineers, Part C: Journal of Mechanical Engineering Science 221, 275-280.

Otis, A. B., Fenn, W. O., Rahn, H., 1950. Mechanics of Breathing in Man. Journal of Applied Physiology 2, 592-607.

Parker, K. H., 2009. An introduction to wave intensity analysis. Medical and Biological Engineering and Computing 47, 175-188.

Parker, K. H., Jones, C. J. H., 1990. Forward and backward running waves in the arteries: Analysis using the method of characteristics. Journal of Biomechanical Engineering 112, 322-326.

Pedersen, O. F., Brackel, H. J. L., Bogaard, J. M., Kerrebijn, K. F., 1997. Wave-speed-determined flow limitation at peak flow in normal and asthmatic subjects. Journal of Applied Physiology 83, 1721-1732.

Pedley, T. J., Schroter, R. C., Sudlow, M. F., 1970a. Energy losses and pressure drop in models of human airways. Respiration Physiology 9, 371-386.

Pedley, T. J., Schroter, R. C., Sudlow, M. F., 1970b. The prediction of pressure drop and variation of resistance within the human bronchial airways. Respiration Physiology 9, 387-405.

Phillips, C. G., Kaye, S. R., 1997. On the asymmetry of bifurcations in the bronchial tree. Respiration Physiology 107, 85-98.

Phillips, C. G., Kaye, S. R., Schroter, R. C., 1994a. A diameter-based reconstruction of the branching pattern of the human bronchial tree. Part I. Description and application. Respiration Physiology 98, 193-217.

Phillips, C. G., Kaye, S. R., Schroter, R. C., 1994b. A diameter-based reconstruction of the branching pattern of the human bronchial tree. Part II. Mathematical formulation. Respiration Physiology 98, 219-226.

Ra, S. H., Chang, P. K., Park, S. O., 1990. Measurement of the forward-flow fraction using a split film sensor. Experiments in Fluids 10, 57-59.

Raabe, O. G., Yeh, H.C., Schum, G. M., Phalen, R. F. 1976 Tracheobronchial Geometry: Human, Dog, Rat, Hamster. LF-53. Albuquerque, NM: Lovelace Foundations for Medical Education and Research

Ramsey, M. W., Sugawara, M., 1997. Arterial wave intensity and ventriculoarterial interaction. Heart and Vessels 12, 128-134.

Rapoff, A. J., Heisey, D. M., Vanderby Jr., R., 1999. A probabilistic rule of mixtures for elastic moduli. Journal of Biomechanics 32, 189-193.

Rice, D. A., 1983. Sound speed in pulmonary parenchyma. Journal of Applied Physiology Respiratory Environmental and Exercise Physiology 54, 304-308.

Rice, D. A., 1980. Sound speed in the upper airways. Journal of Applied Physiology Respiratory Environmental and Exercise Physiology 49, 326-336.

Rice, D. A., Rice, J. C., 1987. Central to peripheral sound propagation in excised lung. Journal of the Acoustical Society of America 82, 1139-1144.

Riemann, B. 1860. Gesammelte mathematische Werke und wissenschaftlicher Nachlass. Leipzig, B.G. Teubner (ed.), (1876) 145–164 (originally published as Über die Fortpflanzung ebener Luftwellen von endlicher Schwingungsweite. Technical report, Göttingen 8 43)

Sarma, P. A., Pidaparti, R. M., Meiss, R. A., 2003. Anisotropic properties of tracheal smooth muscle tissue. Journal of Biomedical Materials Research - Part A 65, 1-8.

Sasaki, H., Takishima, T., Sasaki, T., 1977. Influence of Lung Parenchyma on Dynamic Bronchial Collapsibility of Excised Dog Lungs. Journal of Applied Physiology 42, 699-705.

Schmidt, M., Foitzik, B., Hochmuth, O., Schmalisch, G., 1998. Computer simulation of the measured respiratory impedance in newborn infants and the effect of the measurement equipment. Medical Engineering & Physics 20, 220-228.

Schroter, R. C., Sudlow, M. F., 1969. Flow patterns in models of the human bronchial airways. Respiration Physiology 7, 341-355.

Shalak, R. 1966 Wave propagation in blood flow.Asme Biomech 20-46.

Shapiro, A. H., 1954. The dynamics and thermodynamics of compressible fluid flow. Ronald Press, New York, .

Sherwin, S. J., Franke, V., Peiró, J., Parker, K., 2003. One-dimensional modelling of a vascular network in space-time variables. Journal of Engineering Mathematics 47, 217-250.

Sidell, R. S., Fredberg, J. J., 1978. Noninvasive Inference of Airway Network Geometry from Broad-Band Lung Reflection Data. Journal of Biomechanical Engineering-Transactions of the Asme 100, 131-138.

Smith, H. J., Reinhold, P., Goldman, M. D., 2005. Lung Function Testing. European Respiratory Society Journals Ltd, pp. 72-105.

Smith, N. P., Pullan, A. J., Hunter, P. J., 2002. An anatomically based model of transient coronary blood flow in the heart. SIAM Journal on Applied Mathematics 62, 990-1018.

Smolich, J. J., Mynard, J. P., Penny, D. J., 2008. Simultaneous pulmonary trunk and pulmonary arterial wave intensity analysis in fetal lambs: Evidence for cyclical, midsystolic pulmonary vasoconstriction. American Journal of Physiology - Regulatory Integrative and Comparative Physiology 294, R1554-R1562.

Strahler, A. N. 1957. Quantitative analysis of watershed geomorphology. Trans. Am. Geophys. Union 38, 913-920.

Suki, B., Habib, R. H., Jackson, A. C., 1993. Wave propagation, input impedance, and wall mechanics of the calf trachea from 16 to 1,600 Hz. Journal of Applied Physiology 75, 2755-2766.

Tiddens, H. A. W. M., Hofhuis, W., Bogaard, J. M., Hop, W. C. J., De Bruin, H., Willems, L. N. A., De Jongste, J. C., 1999. Compliance, hysteresis, and collapsibility of human small airways. American Journal of Respiratory and Critical Care Medicine 160, 1110-1118.

Wagner, E. M., Bleecker, E. R., Permutt, S., Liu, M. C., 1992. Peripheral airways resistance in smokers. American Review of Respiratory Disease 146, 92-95.

Wagner, E. M., Liu, M. C., Weinmann, G. G., Permutt, S., Bleecker, E. R., 1990. Peripheral lung resistance in normal and asthmatic subjects. American Review of Respiratory Disease 141, 584-588.

Wan, J., Steele, B., Spicer, S. A., Strohband, S., Feijoo, G. R., Hughes, T. J. R., Taylor, C. A., 2002. A one-dimensional finite element method for simulation-based medical planning for cardiovascular disease. Comput Methods Biomech Biomed Engin 5, 195-206.

Ward, J. P. T., 2002. The respiratory system at a glance. Blackwell Science, Oxford, pp. 100.

Ware ja, Aki k, 1969. continuous and discrete inverse-scattering problems in a stratified elastic medium-1. Acoustical Soc America-J 45, 911-921.

Weibel, E. R., 1963. Morphometry of the human lung. Berlin, .

West, J. B., 2005. Respiratory physiology : the essentials. Lippincott Williams & Wilkins, Philadelphia, pp. 186.

Wiggs, B. R., Moreno, R., Hogg, J. C., Hilliam, C., Pare, P. D., 1990. A model of the mechanics of airway narrowing. Journal of Applied Physiology 69, 849-860.

Winter, D. C., Pimmel, R. L., 1980. The influence of reflection artifacts on apparent phase velocity measurements in the trachea. Annals of Biomedical Engineering 8, 29-39.

Woolcock, A. J., Macklem, P. T., 1971. Mechanical factors influencing collateral ventilation in human, dog, and pig lungs. Journal of Applied Physiology 30, 99-115.

Yeh, H. C., 1979. Modeling of biological tree structures. Bulletin of Mathematical Biology 41, 893-898.

Websites

British Lung Foundation - www.lunguk.org (accessed on 08-04-2011)

Conference Board of Canada - www.conferenceboard.ca (accessed on 07-05-2011)

Dantec Dynamic website - http://www.dantecdynamics.com/ (accessed on 20-06-2011)

List of Figures

List of Tables